



HAL
open science

Density of states, band offset and charge injection in one-dimensional semiconductor nanostructures studied with multiple probes scanning tunneling microscopy

Nemanja Peric

► **To cite this version:**

Nemanja Peric. Density of states, band offset and charge injection in one-dimensional semiconductor nanostructures studied with multiple probes scanning tunneling microscopy. Micro and nanotechnologies/Microelectronics. Université de Lille, 2021. English. NNT : 2021LILUI025 . tel-03430762

HAL Id: tel-03430762

<https://theses.hal.science/tel-03430762v1>

Submitted on 16 Nov 2021

HAL is a multi-disciplinary open access archive for the deposit and dissemination of scientific research documents, whether they are published or not. The documents may come from teaching and research institutions in France or abroad, or from public or private research centers.

L'archive ouverte pluridisciplinaire **HAL**, est destinée au dépôt et à la diffusion de documents scientifiques de niveau recherche, publiés ou non, émanant des établissements d'enseignement et de recherche français ou étrangers, des laboratoires publics ou privés.

UNIVERSITÉ DE LILLE

École Doctorale Sciences Pour l'Ingénieur

IEMN - Institut d'électronique de microélectronique et de nanotechnologie

Thesis defended by **Nemanja PERIC**

Defended on **27th January, 2021**

In order to become Doctor from Université de Lille

Academic Field **Electronics, microelectronics, nanoelectronics and micro-waves**

**Density of states, band offset and charge injection in
one-dimensional semiconductor nanostructures
studied with multiple probes scanning tunneling
microscopy**

*Densité d'états, alignement de bande et injection de charges dans des nanostructures
semiconductrices uni-dimensionnelles étudiées par microscopie à effet tunnel à
pointes multiples.*

Thesis supervised by Bruno GRANDIDIER Supervisor
Louis BIADALA Co-Supervisor

Committee members

<i>Referees</i>	Bassem SALEM	Senior Researcher at LTM	
	Hervé AUBIN	Senior Researcher at C2N	
<i>Examiners</i>	Sandrine ITHURRIA	Professor at ESPCI	Committee President
	Xavier WALLART	Senior Researcher at IEMN	
<i>Supervisors</i>	Bruno GRANDIDIER	Senior Researcher at IEMN	
	Louis BIADALA	Senior Researcher at IEMN	

Abstract

The traditional transistor miniaturization is resulting in devices experiencing quantum effects. Rather than fighting these effects by developing new architectures of conventional silicon-based devices, the long-term solution might be in revisiting existing knowledge of these fundamental concepts and studying them in a well-controlled and methodological manner. Consequently, the newly emergent insights could be applied to the keystones of modern-day electronic devices, such as one-dimensional shape and the presence of heterointerface, but on different materials. This, in fact, has a potential to yield an alternative approach to information processing and computation.

Nowadays, it is possible to obtain nanostructures of any shape and size due to recent breakthroughs in nanofabrication. This thesis aims to exploit such possibilities to simulate an experimental environment in which quantum confinement effect can be studied in a controlled manner on different one-dimensional semiconductor nano-heterostructures. At first, a reliable methodology will be developed to accurately determine the band alignment between two dissimilar semiconductors comprising a heterointerface. This will be achieved on planar one-dimensional InGaAs nanostructures grown on InP by selective area molecular beam epitaxy, a nanofabrication method which, to date, offers the best control of nanostructure shape, size, position, and orientation in ultrahigh vacuum. The surface reconstruction, as well as the entire structure morphology will be investigated in great detail by means of atomic force microscopy and scanning tunneling microscopy, while the aforementioned growth will be described by modeling the diffusion dynamics. A combination of low-temperature two-probe scanning tunneling spectroscopy and room-temperature four-probe contact measurements will be utilized to obtain accurate information about the band alignment and charge transport of the heterosystem.

Once proven successful, the approach will be employed to study nanostructures of much smaller dimensions, where quantum size effect is ever-present: colloidal CdSe nanoplatelets, which imitate the typical optical characteristics of epitaxial quantum wells, but, due to anisotropic lateral dimensions, make the understanding of the impact of finite lateral confinement on the behavior of the free charge carriers more complex. In addition to the study of the morphology of the nanoplatelets and of their optical transitions, low-temperature scanning tunneling microscopy and spectroscopy investigations will be performed. Once drop-casted onto the gold substrate, the density of states of the nanoplatelets will be directly probed in order to accurately determine the extent of quantum confinement experienced by the carriers as a function of the nanoplatelets thickness, temperature and spatial configuration. The results which are, on one hand, inconsistent with foregoing quantum well-like perception found in literature, while on the other, perfectly in line with our tight binding calculations, will establish a solid baseline for the follow-up study CdSe/CdS core-crown nanoplatelets.

Résumé

La miniaturisation continue des composants électroniques a atteint un seuil au-delà duquel les effets quantiques deviendront prépondérants. Plutôt que de vouloir supprimer ces effets, il peut être intéressant de les mettre à profit. Mais ce changement de perspective nécessite d'avoir une compréhension plus fine des propriétés électroniques de nanostructures semi-conductrices considérées comme de potentiels éléments actifs dans des dispositifs futurs. Au cours de cette thèse, deux types de structures dont la géométrie s'apparente plus ou moins à un système uni-dimensionnel ont été considérés: des nanofils semi-conducteurs III-V fabriqués par croissance épitaxiale en ultravide et des nanoplatelets semi-conducteurs II-VI synthétisés chimiquement.

Dans le premier cas, l'épitaxie par jets moléculaires sélective de nanofils planaires composés d'InGaAs permet d'élaborer des nano-cristaux localisés précisément à la surface d'un substrat d'InP grâce à l'utilisation d'un masque diélectrique. L'analyse de la morphologie de ces nanofils par microscopie à champ proche a révélé une anisotropie de forme en fonction de l'orientation des nanofils. En modélisant la cinétique de croissance, nous avons montré que cette variation de forme s'explique par une différence de diffusion des adatoms liée à la reconstruction (2x4) de la surface (001) des nanofils. Les propriétés de transport dans ces hétérostructures uni-dimensionnelles $\text{In}_{0.53}\text{Ga}_{0.46}\text{As}/\text{InP}$ ont ensuite été caractérisées par microscopie à effet tunnel à pointes multiples. Deux approches expérimentales basées l'une sur la spectroscopie tunnel à deux contacts, l'autre sur des mesures à quatre pointes en contact ont été conçues pour remonter à la mesure des discontinuités de bande entre le substrat d'InP et les nanofils d'InGaAs. L'obtention des discontinuités de bande est directe et ne requiert ni fabrication d'électrodes, ni modélisation des caractéristiques $I(V)$, contrairement aux techniques électriques conventionnelles.

Dans un second temps, nous avons considéré des nanoplaquettes de CdSe, qui s'apparentent à des puits quantiques colloïdaux d'épaisseur limitée à quelques plans atomiques pour des dimensions latérales comprises entre plusieurs nanomètres et quelques dizaines de nanomètres. Bien que les propriétés excitoniques des nanoplaquettes aient fait l'objet de nombreuses études, le rôle du confinement quantique latéral sur la localisation des porteurs de charge est encore mal connu. En utilisant la microscopie à effet tunnel, nous avons caractérisé des nanoplaquettes individuelles et des nanoplaquettes assemblées en paquet pour déterminer la densité d'états en bande de conduction. Les mesures spectroscopiques montrent l'existence, d'une part, de singularités superposées à une oscillation de la densité d'états, en bon accord avec la densité d'états calculée par la méthode des liaisons fortes et, d'autre part, la présence de piège sur les parois latérales des plaquettes. Contrairement à l'exciton dont le confinement est plus important, la délocalisation de l'électron est fortement influencée par le confinement latéral et la présence de piège. A cet effet, des travaux préliminaires par spectroscopie optique de nanoplaquettes cœur-coquille permet d'entrevoir l'intérêt d'une couronne pour mieux contrôler le confinement des porteurs de charge dans ces objets.

Acknowledgements

This stands as one of the most important milestones in my personal and professional life. Few years ago, I have found myself facing another seemingly impossible challenge, as I came to the interview for this PhD position, armed with only three things: for a chemist, I have a decent background in surface science; also, I have just the very basics of operating STM systems; and finally, I am not very good at math. However, soon I realized that the challenge is only as difficult as the setting that surrounds it. Being at IEMN, as a part of physics group within it, made this PhD adventure just one more fun and memorable experience.

Development of this thesis under the supervision of Dr. Bruno Grandidier was interwoven with numerous big learning opportunities, with each one being more challenging and exciting than the last. With his guidance, patience, and endless drive for which I am profoundly grateful, I have managed to tackle them and take the most out of them. I am also thankful for the suppleness, dedication, and availability in his mentorship. Ever-present to ask a question but also to be asked one, to share incredible ideas, but also consider mine. Thank you for pulling the absolute best out of me.

I would like to express my sincere gratitude to Dr. Louis Biadala for being a cheat code for my PhD experience. On top of sharing the immense scientific knowledge, Louis had a unique approach in teaching me all the odds and ends of the academic world. While being backed up by his endless support and devotion to supervising, he intentionally placed me in situations in which he knew I would shine, but also the ones where that would not be the case. This hands-on approach gave me experiences which will most certainly prove to be priceless for my future career. Huge thank you for being a great co-supervisor, but even bigger one for being a true friend.

To Dr. Maxime Berthe - Thank you for teaching me the ways of SPM! My complete skillset and good laboratory practice I owe to him. He gave me the know-how, but even more importantly he gave me the confidence to work with highly sophisticated scientific equipment. Under his wing, these instruments became just a collection of big metal toys which I would use to explore the world of physics, and never feel limited by my technical abilities.

I would like to extend my sincere thanks to the other members of Physics group as well, Dr. Damien Canneson, Dr. Pascale Diener and Dr. Yannick Lambert, for welcoming me into the team and their support at every stage of my thesis development.

I also owe my sincere gratitude to the members of my defense committee, Dr. Bassem Salem, Dr. Hervé Aubin, Dr. Xavier Wallart, and Dr. Sandrine Ithurria for their very comprehensive evaluation of my work, as well as for their insightful comments and suggestions.

This PhD thesis has been developed within the framework of INDEED (Innovative Nanowire DEvice Design) network, a project funded from the European Union's Horizon 2020 research and innovation program under the Marie Skłodowska-Curie grant agreement No 722176. I am deeply grateful for being given this opportunity which strongly stimulated my professional and personal growth, all while allowing me to travel around the world and meet wonderful and knowledgeable people along the way.

Here, I would also like to dedicate a special thanks to all the members and collaborators inside and outside of the INDEED network for the scientific exploration which goes beyond political borders and any self-interest.

A big thank you also goes to Nora Benbahlouli, Laetitia Perquin, Florence Senez and Emmanuelle Gillmann for their administrative assistance and availability.

My dear PhD fellows, Dr. Nathali Alexandra Franchina Vergel, Dr. Damien Eschimese, Dr. Louis Thomas, Dr. Vincent Notot and Dr. Davide Sciacca, I would like to share with you that adding that “Dr.” honorary suffix before your names invoked immense feeling of pride and joy, especially knowing how hard we worked for it. We were a great team, always there for each other with unconditional support, plenty of valuable advice, and plenty more of memorable beers. Thank you for everything!

For me, doing a PhD was only one part of the challenge, the other part was being far from home. However, I never felt alone. This is all thanks to my small, but beautiful family! Their belief in me initiated this journey and whose love and support helped me reach the end. “Of course, mom... the biggest credit goes to you!” For the same reasons, a massive thank you goes to a very special group of great people, who also happen to be my biggest treasure: Nikola Raković, Ljiljana Mitrović, Marko Markov, Marko Salić, Nemanja Početak and Petar Keković.

As of today, I am far more knowledgeable in the physics behind nanoscience, and I found a strong passion for it. Furthermore, I became much more skilled in various SPM systems, on top of learning many other techniques. And finally, I still suck at math. Honestly, I would not have had it any other way and it is all thanks to all of you!

Ovaj uspeh posvećujem mom dedi, Draganu Burojeviću.

Contents

Abstract	iii
Acknowledgements	v
Contents	vii
Introduction	1
Chapter 1. State of the art	3
1.1 Semiconductors	3
1.2 Quantum structures	3
1.3 The appeal of one-dimensionality in nanotechnology	5
1.4 A broad definition of nanowires	7
1.5 What are the trends?	11
1.6 Heterointerfaces with the emphases on the 1D nanostructures	15
1.7 Planar 1D heterostructures by means of selective-area epitaxy	22
1.8 Quantum structures by means of colloidal synthesis	27
1.9 Take-away points and ensuing challenges	34
Chapter 2. Characterization techniques	35
2.1 Introduction to scanning probe microscopy	35
2.2 The theory behind scanning tunneling microscopy	37
2.3 The theory behind scanning tunneling spectroscopy	42
2.3.1 The lock-in amplifier	43
2.4 STM and STS on the Omicron LT-STM	45
2.4.1 STM and STS on selective area grown nanowires	48
2.4.1.1 Locating and identifying the nanowires on the surface	48
2.4.1.2 Performing STS measurements on semiconductor nanowires	50
2.4.2 STM and STS on colloidal nanocrystals	53
2.4.2.1 Locating and identifying the colloidal nanocrystals on the surface	53
2.4.2.2 Performing STS measurements on colloidal nanocrystals	53
2.5 The Omicron VT four-probe STM	59
2.6 Complementary techniques	63
2.6.1 Atomic force microscopy	63
2.6.2 Optical spectroscopy	65
Chapter 3. Morphology and electronic structure of SAG InGaAs nanowires	68

3.1	Introduction	68
3.2	Sample preparation	70
3.3	Nanowire morphology.....	73
3.3.1	SEM measurements	77
3.3.2	AFM measurements.....	78
3.3.3	STM measurements	88
3.3.4	Diffusion kinetics model.....	93
3.4	Electronic properties of heterostructures.....	98
3.4.1	STS measurements of the $\text{In}_{0.53}\text{Ga}_{0.47}\text{As}$ cross-shaped nano-heterostructure.....	101
3.4.1.1	$\text{In}_{0.53}\text{Ga}_{0.47}\text{As}$ / InP band alignment from STS	105
3.4.2	Charge transport in the $\text{In}_{0.53}\text{Ga}_{0.47}\text{As}$ cross-shaped nano-heterostructure.....	107
3.4.2.1	Two-probe configuration	107
3.4.2.2	Four-probe configuration	109
3.5	Conclusions.....	113
Chapter 4. Quantum confinement and band alignment in CdSe NPL-based heterostructures.....		114
4.1	Introduction	114
4.2	Growth of CdSe NPLs.....	115
4.3	Bare cadmium-selenide nanoplatelets.....	117
4.3.1	STM investigation of the structure morphology.....	122
4.3.1.1	LT-STM on 5.5 ML-thick NPLs.....	122
4.3.1.2	LT-STM on 7.5 ML-thick NPLs.....	126
4.3.2	STS study of the electronic properties.....	127
4.3.2.1	LT-STs on individual flat-lying NPLs	129
4.3.2.2	LT-STs on stacked up NPLs.....	131
4.4	Extensive “pre-STM” study of CdSe/CdS Core/crown NPLs.....	140
4.4.1	Influence of the crown size on optical properties.....	141
4.4.2	CdSe exciton fine structure	144
4.4.3	Recombination dynamics of the exciton complex	146
4.4.4	Optical properties of CdSe/CdS core/crown NPLs in high magnetic field.....	148
4.5	Conclusions.....	153
Conclusion and future work		154
Bibliography		156
List of publication		177

Introduction

Based upon the everyday carry-on electronic devices, it is clear that the growing momentum behind the integration of nanostructures into semiconductor technologies has established a healthy collaboration of academia and industry. Yet, there are plenty of concepts which are readily utilized, but not thoroughly understood and/or measured. For example, the cross-correlation between electronic and optical properties of nano-heterostructures with the extent of quantum confinement, the type of band alignment, their geometry, composition, surface characteristics, growth mechanisms, etc. It is needless to say that to stimulate further technological development, these knowledge gaps need to be filled with as less as possible experimental uncertainty. In fact, accomplishing this in the framework of one-dimensional semiconductor nanostructures is the main objective of this thesis.

At its core, the experimental research is reliant on the development of the logical strategies to expose, in most cases, the complex and dynamic nature of a given physical phenomenon. Different layers will demand for different instrumental requirements or even, completely different forms of strategies. Tailoring the logic behind a certain study necessitates the precise determination of the experimental approach, by linking it to the set of peculiar sample properties, whilst facilitating its effectiveness and reach. However, in the adolescent fields, such as nanotechnology, this task can be far from straightforward.

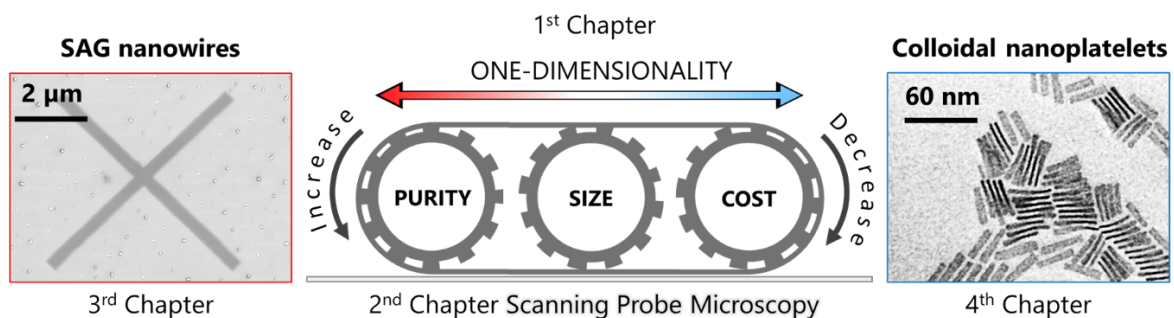


Figure 1.1 Context of the thesis as envisioned. Schematic representation of the experimental outline with the samples involved. Using scanning probe microscopy to find answers at the boundaries of the bottom-up approach. Illustration is also designed to highlight one or the other nanofabrication method based on increase/decrease of production cost, sample purity and minimal nanostructure dimensions.

In this respect, the experimental strategy employed during the development of this thesis, facilitates a context-neutral environment in terms of nanofabrication, to study fundamental notions which are shared among most of the semiconductor nano-heterosystems. In other words, focusing on the behavior rather than the origin, allows for the creation of the robust and controlled environments in which a specific physical and chemical characteristic can be well-isolated and explored. This, if combined with the direct nature of scanning probe microscopy techniques effectively eradicates most of the analytical uncertainties.

In a pragmatic sense, the sectioning of the thesis is done in four chapters, whereas contextually, only in two, each one sited at the opposite boundaries of the bottom-up growth method (please refer to the schematic layout in Figure 1.1). As it will be discussed in greater detail later down in the text, this nanofabrication approach allows for designing and reliably constructing a semiconductor nanostructure of any shape and size. However, depending on what would be the focus of the fundamental study or application, the choice of which flavor of the bottom-up method will be used becomes crucial. There are couple of tightly linked parameters to consider: fabrication cost, sample cleanliness and nanostructure dimensions. Taking these into the account, two methods stand at the extremes, selective area epitaxy and colloidal synthesis. Regardless of their respective advantages and shortcomings, both are characterized by having outstanding growth control, capable of yielding highly anisotropic nanostructures with exceptional crystalline quality, which is a key for the attainment of the morphological or electronic one-dimensionality. Another impactful variable is bound to the fact that most of the material property-defining phenomena take place at the nanostructure interfaces and surfaces. With respect to the former, having atomically sharp compositional variations within a given nano-heterosystems is a valuable resource to study a plethora of effects, which will be discussed further down in this chapter. Whereas for the latter, having a possibility of preserving the samples before, but also during the measurements is essential, which can be accomplished with the effective surface passivation and ultra-high vacuum working environment. This further develops the discussion towards Chapter 2, where the general outlook of the instruments used in this thesis is given. Aside from complementary techniques, such as optical spectroscopies and electron microscopies, the other instruments can fit into the group of scanning probe microscopies. These tools have been successfully used for probing samples obtained by means of selective area epitaxy and colloidal synthesis. Starting from the first, the experiment was performed on the InGaAs nanowires grown on InP. The results of this study contain couple of major highlights, such as accurate measurement of band offsets between the two materials, electronic transport properties and morphological characteristics of nanowire structures of various shapes. These findings are described in detail in the third chapter. On the other side of the spectrum, the quasi two-dimensional CdSe nanoplatelets were probed with the same technique to reveal the true extent of quantum confinement, by performing scanning tunneling spectroscopy on individual nanocrystals, but also when in an ensemble. To further extend our studies towards nano-heterostructures of the same origin, we initiated the work by exploring optical properties of CdSe/CdS core/crown nanoplatelets at cryogenic temperatures and in a high magnetic field. The results of these studies are presented and discussed in the last chapter.

Chapter 1. State of the art

1.1 Semiconductors

Reflected by the abundance of silicon in the current electronic industry, the ubiquity of semiconductor materials is evident. From light-emitting diodes, transistors, sensors, cameras, gas detectors, lasers, solar cells, it is clear that semiconductor devices are deeply integrated in the modern-day society. Simply put, and referring to their electronic characteristics, semiconductors can be placed somewhere between metals and insulators. This is a direct result of a unique band structure which dictates their optical and electronic properties. The presence of the band gap which is narrower than 3 eV is usually a defining parameter to classify a certain material as a semiconductor, instead of an insulator.[1] The width of the band gap plays an important role in designing the functionality of the future semiconductor-based devices.

1.2 Quantum structures

As the dimensions of the materials reach nanometric scale, one of the most pressing effects is the confinement of the motion of the charge carriers (electrons and holes) and in the case of semiconductors, also excitons (electron-hole quasiparticles). This phenomenon is known as quantum confinement effect and it causes heavy modification of the band structure by shifting and degeneracy splitting of the energy levels. As it is a quantum mechanical effect, the size threshold at which the nanostructures are susceptible to it is generally determined by the properties of the quantum particles involved. In the case of the electrons when the size of the nano-object is comparable to spatial extension of electronic wave function, electrons will start to “feel” the presence of the nano-boundaries and accommodate by the quantization of their energy and momentum. In practice, if at least one of the dimensions of the nanostructure is smaller, comparable or larger to the exciton Bohr radius of its material, the system can be portrayed to be experiencing strong, weak or no confinement at all, respectively.[2] Depending in which geometry the motion of the carriers is impeded, the classification of the nanostructures is the following:

- 2D quantum well: here, the carriers are confined in a potential such that their motion is restricted in one dimension, leaving only a free movement in other two directions perpendicular to the confining potential.
- 1D quantum wire: the carriers are experiencing the confinement in two dimensions, yet they freely propagate in the third dimension.
- 0D quantum dots: the motion of the carriers is limited in all three directions.

Following on the classification listed above, the key to discriminate between these confined systems is to examine the changes they experience with respect to their bulk counterparts. Most generally, these

can be found in the altered values of the band gap energy, band edge positions and finally, in the density of states. The increase of the band gap energy, as the nanostructures get smaller was described by Brus.[3] If one considers weakly correlated electron-hole bound pair, solving the Schrödinger equation for the first excited state while considering the particle with radius R , within the effective mass approximation for the kinetic energy and an effective medium approach with dielectric screening for the potential energy, the band gap can be expressed as

$$E_g = E_{g,\text{bulk}} + \frac{\hbar^2 \pi^2}{2R^2} \left(\frac{1}{m_e^*} + \frac{1}{m_h^*} \right) - \frac{1.8e^2}{\epsilon R} + \frac{e^2}{R} \sum_{n=1}^{\infty} \alpha_n \left(\frac{r_e + r_h}{R} \right)^{2n} \quad (1.1)$$

where, \hbar is Planck's reduced constant, n quantum number, ϵ the dielectric constant, α the polarizability, r_e and r_h are the position for the electron and the hole within the particle, R is the nanocrystal radius, and m_e^* and m_h^* are the effective masses for the electron and hole, respectively.[4], [5] Experimentally, this trend is the most evident in optical spectroscopies, where absorption/emission energies are becoming more and more blue shifted as the confinement in any given dimension of the nanocrystals is increasing.

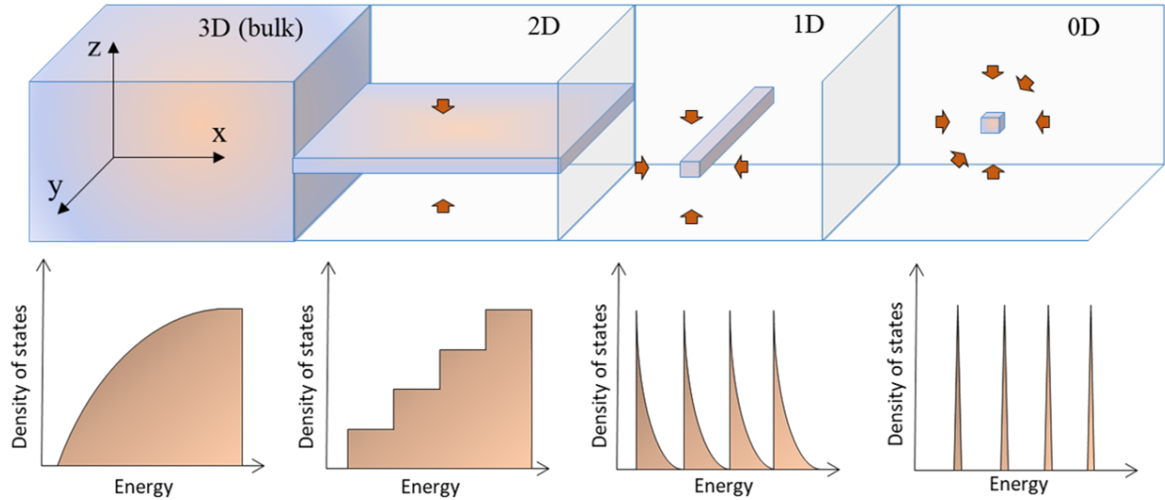


Figure 1.1. Schematic representation of density of states as function of energy in bulk semiconductors (3D), quantum wells (2D), quantum wires (1D) and quantum dots (0D).

As stated above, depending on the shape and size of a confined semiconductor, the density of states will strongly differ when compared to bulk. These variations are depicted schematically in Figure 1.1. In practice, this behavior can affect level occupancies, interband transitions, carrier density and mobility of the confined system, and thus have great impact on its optical and electronic properties.

1.3 The appeal of one-dimensionality in nanotechnology

In solid-state physics there are many exotic fundamental phenomena tied to the concept of one-dimensionality, such as metal-insulator phase transition, superconductivity, and giant magnetoresistance.[6]–[8]

In fact, electronic properties of solids of higher dimensionality can be successfully described by using Landau Fermi liquid theory. In this way the many-body interaction problem is avoided by embracing the notion of free particles. However, with the size reduction of bulk materials, the electron-electron interactions become increasingly hard to neglect. The breaking point is reached with the one-dimensionality.[9] Because of collective electron motion in a strongly confined environment, individual excitations become no longer possible and the system is better portrayed by Luttinger liquid model. The key feature of these systems is spin-charge separation and density of states suppression at the Fermi level.[10] Such remarkable behaviors have been even observed experimentally.[11]–[13]

Furthermore, whilst staying within realm of quantum size effect (apart from zero-dimensionality), electronic transport will most likely differ from bulk diffusion one. This distinct electron motion is identified as ballistic transport and is a common appearance in 1D systems. It occurs if the channel dimensions are smaller than the electron mean-free-path and it is characterized by the absence of electron momentum relaxation through scattering events.[14] In this instance the transport will take place through 1D subbands with each one contributing a quantum unit of conductance $G_0 = 2e^2/h$. Thus, the conductance of the whole 1D system can be estimated by $G = G_0 T/R$, where T and R are transmission and reflection coefficients of the barriers with $T + R = 1$. [15] With InAs having long electron mean-free-path in bulk, the prototypical example for this behavior are InAs nanowires.[16] Possession of this characteristic, certainly contributes to them being an ideal candidates for applications in quantum computing.[17]

Notably, the electronic perception of one-dimensionality discussed above is not the only one. This concept can be also employed in terms of morphological characteristics, regardless of the extent of quantum confinement. The key feature of one-dimensional geometry lies in large surface-to-volume ratios. On the nanoscale, the objects which fit this description are nanowires, -tubes, -rods, -belts, -filaments, -pillars etc. If the immense surface presence is combined with extremely small dimensions of nanostructures, their material properties and applicability will vastly differ from their respective macroscopic forms.[18] For starters, it has been shown that one-dimensional shape can offer improvements in structural qualities of nano-objects, by increasing their defect and stress tolerance, a highly desired trait for flexible-electronics.[19], [20] In addition, accommodating a material into a one-dimensional shape can be a convenient way to increase its active area. For instance, in photovoltaics nanopillar arrays were successfully utilized to both increase the absorption efficiency across a large wavelength range and minimize reflectance.[21] The publications reporting similar feats for energy applications are plentiful.[22], [23]

It is, however, worth pointing out that most of the scientific publications covering any of the above-listed traits which are strongly tied to the concept of one-dimensionality in nanotechnology, have a reoccurring keyword: “nanowire”.

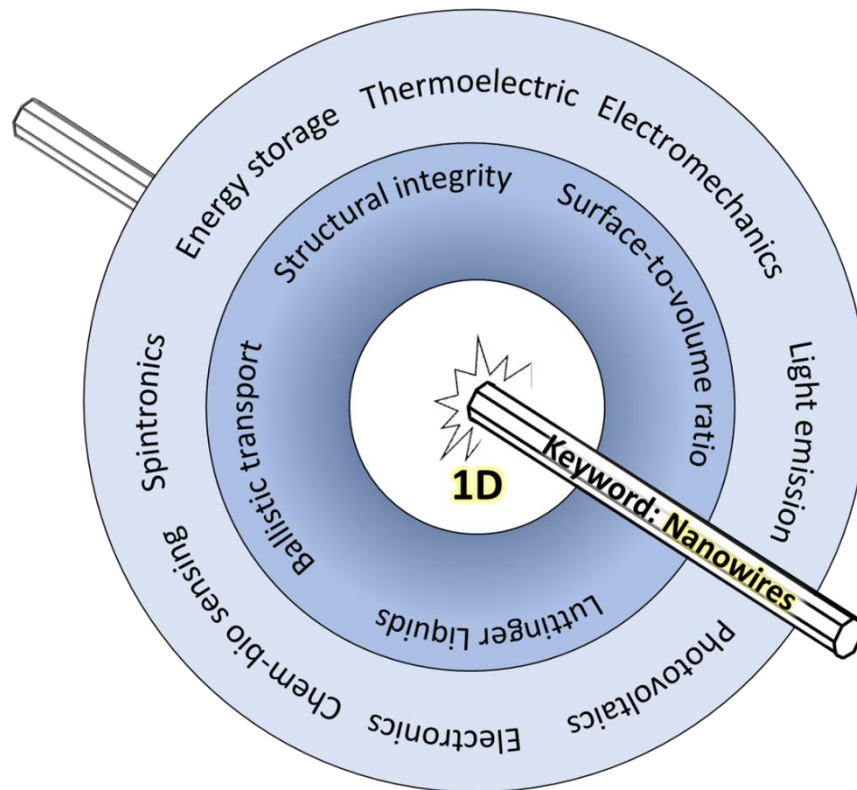


Figure 1.2 Nanowires within the context of the one-dimensionality.

1.4 A broad definition of nanowires

Nanowires are best described as filament-shaped nanostructures which are only defined by their diameter ranging from just a few to couple of hundreds of nanometers. They can be made of metals (Ni, Pt, Au, etc.), insulating materials in the form of various metal oxides, organic/inorganic molecules and most commonly, out of semiconductors, such as silicon, germanium, III-V, II-VI, III-N.[24] For the crystalline semiconductor nanowires, there is a causal relationship between their distinct anisotropic shape and crystal structure.

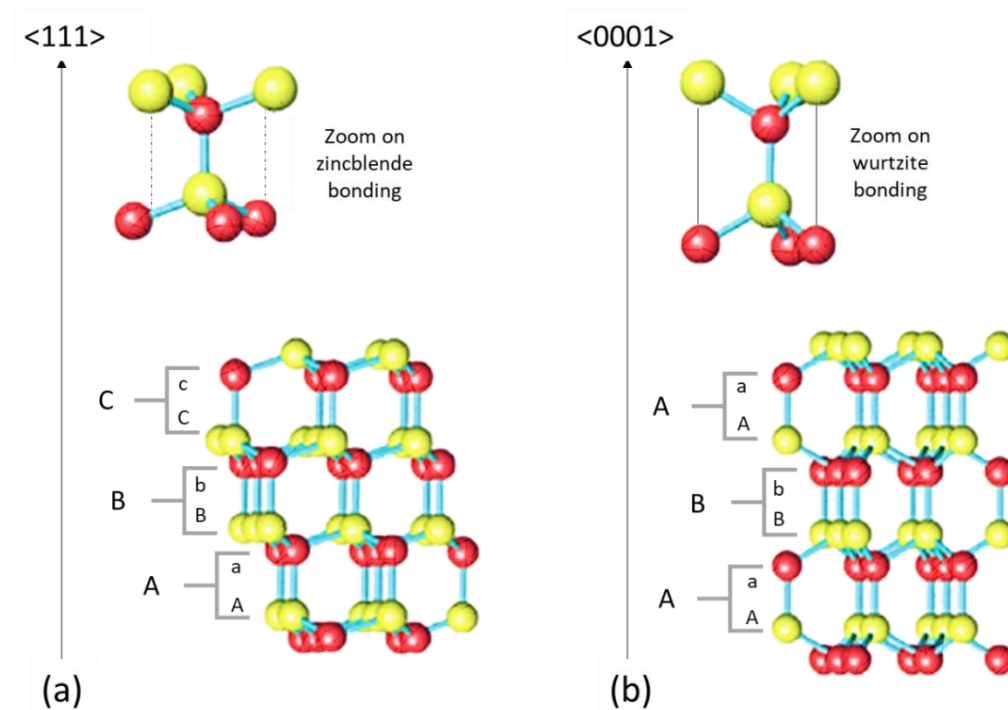


Figure 1.3 3D models of (a) zincblende and (b) wurtzite crystal structures. Different atom colors represent two different atomic species originating from III-V group. Their stacking sequence is denoted with Aa, Bb and Cc, signifying a layering order. Figure taken and adopted from reference[25].

In crystallography, the crystal structure refers to 3D-lattice formed of identical blocks (unit cells) following the periodic arrangement of the atoms building a crystal in three-dimensional space. With the exception of nitrides, in bulk all III-V semiconductors exhibit zinc-blende crystal structure.

During their growth most of them have the tendency to adopt the crystal structure of their substrate. However, that can be changed by controlling the growth parameters. In general, nanowires crystallize in cubic zincblende (ZB) or hexagonal wurtzite (WZ) crystal structure, with ZB being the preferential one for most of them. Side by side comparison of the two structures along the close-packed $\langle 111 \rangle$ and

$\langle 0001 \rangle$ directions, respectively, reveals that they are quite similar with the only differentiating feature being the stacking sequence of the atomic bilayers. For the purpose of illustrating the stacking of the bilayers the common denotation of A, B and C is used.[26] As shown in Figure 1.3, the stacking of the bilayers along the previously mentioned directions is represented with ABCABCABC... for ZB (inset (a)) and ABABAB... for WZ (inset (b)). Notably, as it is generally not the case with their bulk counterparts, the polytypism is a common occurrence for most of the III–V semiconductor nanowires, where it is possible to have an alternation of ZB and WZ phases along the single nanowire.[27], [28] The intermixing between the two phases is a direct result of the III-V nanowire growth. In specific, their extension is along the [111] direction for the cubic cell and the [0001] direction for the hexagonal one. As these two are closely related, the end crystal structures will exhibit some resemblance as well. From energetic point of view, the difference between the two structures lies in the third-nearest atom spacing and can be responsible for the switch between the two.[25]

The first nanowire growth was reported by Wagner and Ellis in 1964.[29] With that historical leap in nanotechnology, the today most widely used nanowire growth mechanism was defined. Starting from nomenclature, “VLS” refers to three phases involved during the nanowire growth (vapor, liquid, solid). In specific, from introduction of gaseous semiconductor material into the reaction chamber, followed by its incorporation and alloying with metal droplet in liquid phase and finally, the formation of the solid semiconductor nanowire. The growth of the nanowire utilizes catalytic effect of liquid metal droplet to achieve the anisotropic extension usually along [111] direction.[30] This, together with the suppression of parasitic growth is a consequence of semiconductor material being more efficiently incorporated in the droplet than at the surface of the substrate. Using the well-established gold-seeded Si nanowire growth for explanation purposes, the whole process can be chronologically divided up into the following steps (see Figure 1.4):

- i. Catalyst formation
- ii. Eutectic formation
- iii. Nucleation and growth

First step involves formation of catalytic layer or Au particle, in this case, on the desired substrate where the nanowires will be grown. Step (ii) entails for the temperature in the reactor to be raised to the eutectic point (approximately 800K), at which the silicon will start alloying with gold particles. Lastly, the introduction of the material gasses will feed the growth of the nanowires, at sites where gold seed particles are located. The diameter and the length of the end nanowire will develop by closely following the size of the initial seed particle, but it will also depend on the deposition conditions. These include pressure and temperature. VLS mechanism usually yields identical nanowires once the process has been completed. For this very reason methodologies based on this mechanism are highly utilized.

Nowadays, the core principle of bottom-up nanowire growth is well established and largely understood. However, there are some variations on the topic, which will give rise to completely different nanowires. In the following, we will briefly touch upon three more mechanisms (VSS, VS, SLS) that have been successfully utilized to grow plethora of nanowires known to this day.

Vapor-solid-solid (VSS)-based growth has a similar notion as VLS-based growth of nanowires with the differentiating characteristic being in the lack of phase transformation of the seed particle during growth.

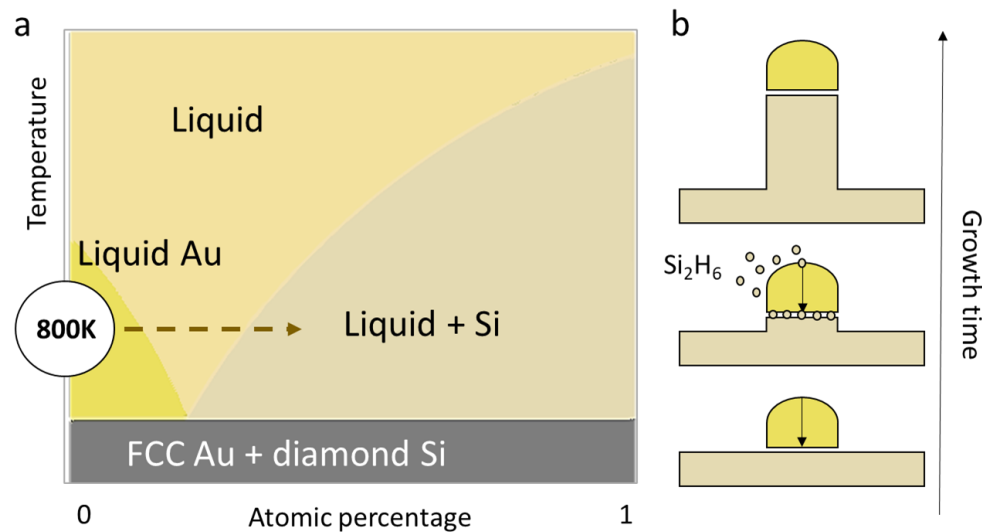


Figure 1.4 (a) Binary phase diagram with (b) schematic representation of Si nanowire gold seeded VLS growth. Figure inspired by the ref.[31]

Since the growth temperature is lower than the eutectic temperature, the metal droplet will remain solid throughout the whole growth process.[32]–[34] Firstly, the reactant gasses are introduced into the growth chamber and start propagating towards the seed particle. Depending on if it is the very beginning of the growth or the nanowire has been partially grown, the reactant molecules will attach to the surface of seed particle or both seed particle and a nanowire, which would be followed up with their diffusion in the solid catalyst particle. Finally, the material deposits will start to incorporate into the nanostructure at the nanowire/catalyst interface.[35] Due to the fact that the diffusion of the reacting species through the solid seed particle is slow and additionally, the surface reactivity is weaker, the reaction time of VSS can be up to hundred-fold longer than in the case of VLS.[36] Despite the longer growth times, VSS offers higher growth control, with a premise of reaching atomic monolayer accuracy. Thus, this growth technique is particularly interesting for the fabrication of nano-heterosystems as their properties highly depend on the sharpness of the heterointerface. Another growth mechanism relies on the shared composition of both seed-particles and grown nanowires. If the growth process can be described as auto-catalytic, then it is governed by vapor-solid (VS) growth mechanism. The main appeal here lies in the lack of metal-seed particles, which helps to minimize the quantity of metal-induced surface states, that are unfortunately a commonality for metal-semiconductor heterojunctions.[37] To achieve the anisotropy of the grown nanowires, the mechanism heavily relies on different growth rates in different crystal orientations.[38] And finally, solution-liquid-solid (SLS) mechanism involves chemical reaction of seed particles dispersed in a solution with metallo-organic

precursors, from which the crystalline nanowires can grow.[39], [40] The use of this mechanism comes with couple of main advantages: it inherently allows for in-situ ligand passivation of products, it can yield quantum structures of much smaller dimensions with respect to the mechanisms described above, and most importantly, it has immense potential for industrial scalability.

1.5 What are the trends?

Judging by the present interest of scientific community, semiconductor nanowires have clearly received recognition as key components of future devices. This is mainly due to their unique properties originating from their small size, one-dimensional shape, and resulting high surface-to-volume ratio. In that regard, and with respect to their bulk counterparts, nanowires can exhibit very interesting mechanical,[41]–[44] thermoelectric,[45], [46] optical,[47]–[50] and electronic properties.[16], [51] Initially carbon nanotubes were viewed as an ideal material to explore and exploit the effects of one-dimensionality, yet due to the difficulties in attaining morphological variety and industrial scaling, their applicability was hindered. In contrast, nanowires certainly overcome this issue as they can be grown in a very reproducible, cost-effective, and most importantly, controlled manner. This possibility firmly places them as building blocks of future nanosized devices.[52] From solar cells, light emitting diodes, lasers, integrated electronic/photonic circuits all the way up to quantum devices and extremely sensitive biological and chemical sensors.[53]–[59] However, there were some key discoveries over the years which tailored the assessment of nanowires closer to some applications more than the others.

As a result of collaborative relationship with Leonid Chechurin's group from Lappeenranta University of Technology, we had an early access to a novel trend analysis platform. By means of natural language processing and machine learning, the semantic analysis of 50,000 scientific publications and 8,000 patents, published between 1993 and 2019 was conducted with the accent on nanowires. The underlying engine of this method is concept extraction. Concept is defined as a cluster of topics, whereas topics are constructed by TF-IDF metric (Term Frequency – Inverse Document Frequency)[60] by measuring the relations between the individual words in the individual documents. From there the concepts can be built using LDA algorithm (Latent Dirichlet Allocation)[61]. This allowed us to gain insight in the evolution of topical nanowire-based reports over the years, a highly accurate reflection of academic and industrial trends. The results of this analysis applied to three different topics (solar cells, lithography, and transistors) are presented in Figure 1.5a,b,c with patent quantities presented in purple and scientific publications in blue. Two observations immediately stand out. First, quantitatively, distributions for both patents and publications are exceptionally low until early 2000s. This is most probably an inaccurate depiction of the work done in that period, since scientific community used to refer to “nanowires” as “nanowhiskers” and thus, a significant number of older reports would slip from the analysis. Second, the distribution maxima between two document classes are quite different, a consequence of larger initial number of scientific reports within the data pool. With this in mind, and focusing on the topic of solar cells, the distribution seems to exhibit linear upward progression for both patents and publication. Yet, the same behavior cannot be seen for other two topics. Side-by-side comparison of lithography and transistor topics reveals a coherent and fluctuating evolution throughout the years. Interestingly, this non-linear progression can be well described with having the S-curve character, a common feature of all emerging technologies. [62]

The initial upwards trend represents the acceptance of novelty and the pursuit for further improvements and applicability, until reaching a peak, or better known as point of maturity. From here the negative dips are likely to occur, as the technology has reached a blockade in terms of development, from which it can diminish or be re-excited again with an innovation.

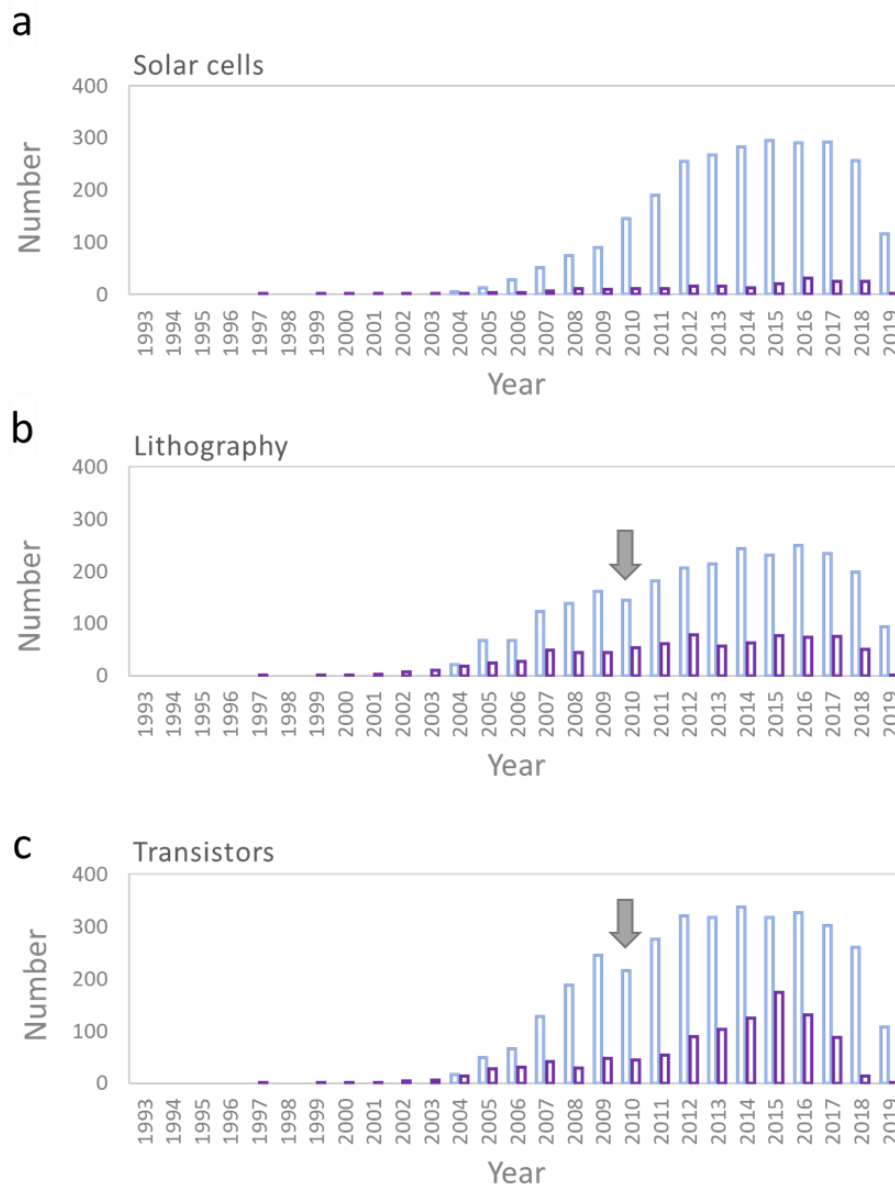


Figure 1.5 Conceptual trend analysis of patents (purple) and publications (blue) with respect to the nanowire (a) solar cells, (b) lithography and (c) transistors.

Remarkably, both lithography and transistor concepts have reached the bottom of the dip in 2010, followed by parallel uprising again. This is a clear indication of the tight links between the fields. Another observation is related to the total ratios of scientific and patent reports within a year. Despite the above-mentioned inconsistencies in the data pool, this ratio should still represent well the relationships between the industrial and academic sectors. And indeed, while taking into consideration

the time necessary to transfer laboratory samples into manufacturable devices, and the resulting chronological dephasing of the maxima between patents and publications, the ratios of lithography/transistor combination are much lower than the one for solar cells. To better understand these trends, one should refer to current state-of-the-art of the technologies involved.

- “Solar cell” concept:

The one-dimensionality of nanowires (Section 1.3) is certainly a driving force behind tremendous efforts invested over the years for their application in photovoltaics. However, if the price-to-performance relationship was to be evaluated for the case of nanowire-based solar cells, they will still fall short when compared with their thin film counterparts.[63] This can be accredited to a lack of control in some key areas, such as: surface/interface quality, doping and passivation, nanowire spatial positioning and overall morphology. Any advancements in that regard have potential to improve device performance, industrial scalability, mechanical and chemical stability.[64], [65] As it is clear from the statistics in Figure 1.5a, the breakthrough is still missing since the industrial sector is mostly slacking behind academic one.

- “Transistor” concept:

In contrast, the development of the nanowire-based transistors has been blooming over the past couple of decades, as a result of the global demand for higher device densities, clock speeds and power efficiencies within integrated circuit technologies, following the trend predicted by Moore’s law. [66] However, in order to maintain such progression of novel device design and their manufacturing, the down-scaling issue of conventional silicon-based technologies needs to be surmounted and this is where nanowires come into play. The most recent International Technology Roadmap for Semiconductors (ITRS) report claims that Moore’s law trend though traditional transistor scaling is expected to falter in the next few years. Thus, monolithic integration of semiconductor nanowire-based active components and interconnects (e.g. fast channels, steep-slope switches and vertical high-electron mobility transistors [67]) into existing silicon technologies has been recognized as one of the ways to keep up the pace. [68]

- “Lithography” concept:

Regardless of the application, from the nanofabrication standpoint, there are two main strategies, top-down and bottom-up one. In its core, top-down methodology most often entails selective chemical “carving” of an excessive volume of the material into the desired shape, while bottom-up is reliant on inducing the self-assembly of the material with atomic-scale precision.[69] Since the prerequisites for fabricating a nanowire-based heterostructure (applicable for energy harvesting and integrated circuit technologies) are very small dimensions and atomically sharp variations of composition, in most cases the top-down approach will not be suitable for the task. Directly etching out the materials is inherently a highly invasive process which can easily damage the device. Moreover, the installment of the additional heterojunction will require a regrowth stage. It has been shown that this process will yield lower crystalline quality if compared to the structures obtained by bottom-up method, where in-situ switching of the precursors is quite straightforward.[70] It is worth pointing out that the lithography has been successfully utilized in both ways, either for etching out bulk crystals as a part of purely top-

down method or as a supplement to bottom-up one to achieve position controlled nanowire growth by patterning.[71]

Remarkably, the scientific community has experienced the gradual shift of interest towards bottom-up method in the period of 2007-2010. Many reports can be found pointing out the necessity for the change of approach in nanofabrication.[72]–[74] In the words of Wei Lu and Charles M. Lieber[75]: “This ‘bottom-up’ paradigm, analogous to the way that biology so successfully works, may prove to be a solution to the technological challenges faced by the semiconductor industry, and could open up new strategies for increasing overall device density by allowing aggressive scaling in three dimensions”. On the timescale this line up perfectly with downwards trending, just before reaching the base of the dip, as seen in Figure 1.5b,c. It is indeed likely that this was the spark that reignited the interest and caused the parallel up-rise of nanowire-related lithography and transistor research. Nonetheless, the best option is to exploit the combined benefits of both bottom-up and top-down processes.[76]

1.6 Heterointerfaces with the emphases on the 1D nanostructures

As mentioned before, the use of silicon in the electronics industry is dominant. Thus, any integration of nanostructures into existing technologies demands for fine control of the interfaces between the materials. The potential of nanowire heterostructures for future applications is boundless, as it allows for fine tuning and installing specific physical and chemical properties through means of controlling the selection of materials that form the nanowire composites and the shape of the interfaces between them. Hiruma's group described why is this a case, characteristic only for the nanowires.[77] In specific, the lattice-mismatch strain can be mediated radially without introducing dislocations throughout the nanowire, thus avoiding any undesired modifications to the band structure. As a result, various material combinations can be exploited with even 10% lattice mismatch,[78], [79] with outstanding crystallographic and optical qualities. Some of the most popular material combinations are InAs / InP and GaAs / InAs. The three most known architectures of nanowire-based heterosystems are substrate-based, axial and radial heterostructures. If we assume certain materials A and B, first configuration will involve the growth of the A nanowires on the B substrate. Second configuration is obtained by growing nanowires which are comprised of different sections of different materials. Lastly, the radial configuration can be best described as a nanowire of material A surrounded by material B, or A / B core / shell nanowire. Whatever the configuration is, the interface of between the materials A and B will highly reflect on hetero-nanowire end properties.[80]

- Substrate-based nanowire heterostructures:

Of all the possible architectures, the substrate-based configuration of nanowire heterostructures was the quickest to gain traction in the research and development in both academic and industrial sectors. The main appeal was found in the intuitiveness of layering different materials on top of each other for added functionality. In the early works, it is easy to grasp the general theme, where the biggest selling point lies in the integrating different semiconductor technologies into existing and most abundant silicon-based ones. Just based upon the fact that the silicon is an indirect band gap material, while most of the semiconductors from III-V group are characterized by having direct band gaps, the opportunities for new applications in optoelectronics which could emerge from their union are plentiful.[67], [81]

- Radial nanowire heterostructures:

When referring to radially "heterostructured" nanowires, the core/shell architecture is the most abundant. The motivation for the research and development of these nanostructures can be mainly found in the ease of tunability of their fundamental properties and surface passivation. In fact, early theoretical work has shown that there are potentially multiple degrees of freedom during the synthesis stage, with which the band gap energies could be altered, starting from variations in composition, core diameter and shell thickness.[82] Literature also contains plenty of experimental reports with similar conclusions, which further showcases the promising perspective of these nano-heterostructure for optoelectronic applications by exploiting structure-property relationships.[82]–[84]

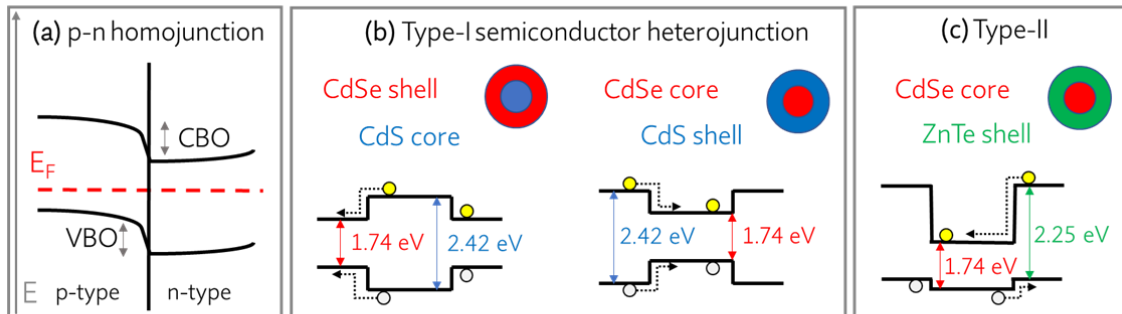
- Axial nanowire heterostructures:

Of all three, nanowire-based axial-heterostructures have been studied the most. Their fabrication relies on one-dimensional modulation of nanowire composition and/or anisotropic doping along the nanowire. [85]–[88] The main appeal for these nanostructures lies in better stress mediation when compared to other two morphological configurations. Interesting nonetheless, this architecture goes beyond the scope of this thesis, so it will not be discussed further.

Regardless of the architectural layout, combining different materials to tailor certain device functions is not straightforward, since any compositional changes will also directly reflect on the band structure. If an abrupt compositional section is created at any place of the nanowire, plenty of new phenomena may emerge. For example, starting from the “simplest” case, where the junction is formed of the same material species with different doping, a classical p-n homojunction (Figure 1.6a). Once the Fermi levels line-up, the discrepancies in the electron-hole ratios between the n- and p-type doped semiconductors, will be manifested as staggered, yet smooth potential variations between conduction and valence bands on both sides of the interface. However, completely changing the composition of the materials will certainly have a much greater impact on the electrostatic potential at a, now, heterointerface. To showcase such a scenario, the work of Goebel et al. done on core/shell nanowires comprised of CdSe, CdS and CdTe can serve as a great example.[89] In brief, this study involved the synthesis of the nanowires and detailed investigation of their morphological and optical properties. Three different nanowire samples were structured as in the schematics of the cross-sections (Figure 1.6b,c). Irrespective of the material used, the nanowire cores were uniformly coated with the shell with more than 90% coverage, and thus forming a crystalline heterointerface. This is significant, as the crystalline quality, material choice and its layering will directly reflect on the band structure of the heterosystem, which could in turn lead to unlocking additional positive attributes, such as increased quantum yields and charge separation. For example, bounding the larger band gap material with the smaller band gap one will result in easy migration of photogenerated electrons and holes into the core of the heterostructure. Such a scenario represents a good description of the type-I band alignment that exists in the CdSe/CdS core/shell nanowires in Figure 1.6b (left). Another example can be viewed in Figure 1.6b (right), where the material composition of the heterostructure has been interchanged. Here, the added benefit will be the increase of quantum yield, due to the isolation of photogenerated carriers from the surface trap states, by keeping them localized inside the core.

So far, in both examples, the high overlap of carrier wavefunctions characteristic for the type-I heterointerface was the key. Though, and in the final example, what happens if the type of band alignment is changed? By forming the CdSe/ZnTe type-II heterointerface, the wavefunction overlap between the two materials is constrained, which will result in spatial charge separation (Figure 1.6c), a highly desired feature for the photovoltaic applications. And indeed, through UV-vis, photoluminescence, and lifetime studies the authors of above mention paper have reported observations which are in line with such interactions, red shifts of both absorption and emission, composition dependent variations of quantum yield with respect to their bare counterparts and alternations in Auger kinetics for the case of CdSe/CdS core/shell nanowires.

Semiconductor-Semiconductor Interfaces



Metal-Semiconductor Interfaces

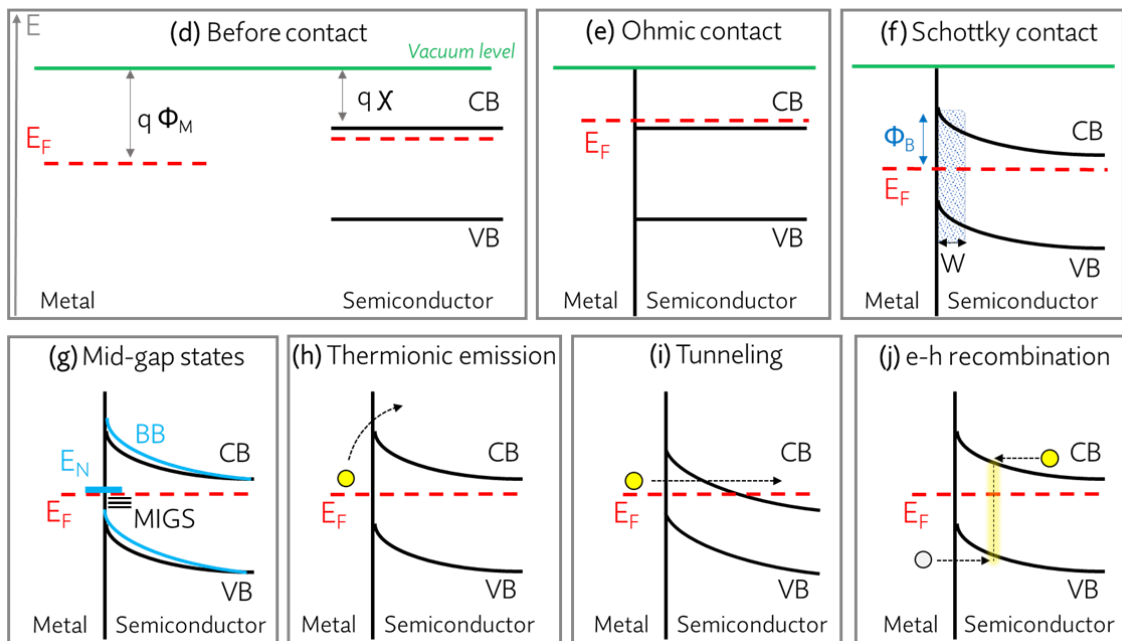


Figure 1.6 Energy band diagrams showcasing the (a) classical semiconductor p-n homojunction, (b) CdSe/CdS (left) and CdS/CdSe (right) core/shell nanowire Type-I heterojunctions (c) CdSe/CdS core/shell nanowire Type-II heterojunctions (insets taken and adopted from publication[89]), (d) simplified band structures of a metal and a semiconductor before contact (e) metal-semiconductor interface upon establishing Ohmic contact, (f) metal-semiconductor interface upon establishing Schottky contact, (g) MIGS (metal-induced in-gap states) and Fermi level pinning at the charge neutrality level, (h) electrons crossing the Schottky barrier by thermionic emission, (i) quantum tunnelling of electrons through the Schottky barrier and finally, (j) electron-hole recombination in the space-charge region. Legend: electrons and holes are schematically represented as yellow and gray balls, respectively. Notation: CBO and VBO are conduction and valence band offsets, q - charge, Φ_M -

metal work function, χ - semiconductor electron affinity, Φ_B - Schottky barrier height, W - width of the depletion region, E_N - charge neutrality level, E_F - Fermi level, BB - band bending.

This example had a two-fold benefit. For one, it is a good representative of what is to be expected once the heterojunction is formed, whereas for the other, it will be mentioned later in the text. Sadly, what is to be expected is not always what is experimentally observed. When it comes to band-alignment, there are still plenty of unknowns, due to the fact that any localized interface, or surface states, defects can act as donor/acceptor sites and thus create an unbalance in the carrier concentrations, modifying the optical or electronic outputs of a given heterosystems in an unpredictable manner. As a result, and despite the massive efforts invested over the years to accurately determine extents of band discontinuities for various material combinations, a reliable “go-to” experimental method is still missing.

With respect to semiconductor-semiconductor heterointerfaces, for device applications metal-semiconductor junctions are equally significant. As it is often the case with any evolving semiconductor technologies, the overall performance of the future electronic devices will be only as good as the contacts are.[90], [91] In other words, the voltage drop across the device should be significantly larger than the one at the contact point or otherwise, its functionality will be severely impeded or even nullified.[92] Judging only by the differences in the $I(V)$ characteristics, the metal-semiconductor contacts can be classified into Ohmic and Schottky contacts. First one has linear response of the current with respect to the voltage ramp, while the other has non-equivalent behaviors depending on whether the system is forward or backwards biased, respectively. When brought close together, the position of the Fermi level of the metal (Figure 1.6d), with respect to semiconductor CB and VB becomes essential in determining which type of contact will be established. In specific, if the energetic position of the metal Fermi level lines up either somewhere inside the valence or conduction band of the semiconductor, the contact will be classified as Ohmic (Figure 1.6e). In contrast, if the Fermi level is located within the gap of semiconductor, there will be a Schottky barrier at the interface (Figure 1.6f). In an ideal case, and by Schottky-Mott rule barrier height should only depend on the difference of semiconductor electron affinity (χ) and metal work function (Φ_M).[93] Unfortunately, in reality this does not stand because of defect- or impurity-induced in-gap states. Despite the fact that most of semiconductor materials are naturally free of in-gap states, the addition of any foreign elements at the surface will prevent its rearrangement and induce pinning of the Fermi level. If the Fermi level of the metal is not located at the same energy as charge neutrality level (E_N), a local charging of the semiconductor surface will be induced, while at the same time the image charge will appear on the side of metal. The resulting imbalance in electrostatic potential will be mediated by band bending in the semiconductor and pinning of the E_F at E_N (Figure 1.6g). As a result, and regardless of the metal work function the electronic properties of metal-semiconductor interface will be mainly characterized by the height of the Schottky barrier (Φ_B) and width of the depletion region (W), that can be expressed as: $W = \sqrt{2\epsilon\Phi_B/ne}$, where ϵ is a dielectric constant, n is the doping density and e is electron charge.[94]

Out of the two metal-semiconductor contact types, the Ohmic behavior is certainly more desirable for most of the applications. However, ohmic contacts are highly dependent on the contact resistance. With a clear goal of minimizing it, over the years much effort has been invested from both fundamental and

engineering side. The most common approach for fabricating contacts in the semiconductor industry is reliant on alloying method, even though there are many issues associated with this approach. To list some of them, an inherent high invasiveness which can damage or contaminate the device, large spacing between the contact points to avoid shortening, non-uniform wetting of the contact material, its faulty adhesion or even re-evaporation, etc.[90] Another issue is the rapid increase in parasitic resistance as source and drain junction depths are scaled. This effect can be alleviated by switching from Ohmic to low-barrier Schottky contacts, at which point lowering barrier height becomes a priority and a new challenge. There are three main mechanisms that govern charge transport across it: thermionic emission, quantum tunneling and electron-hole recombination in the depletion region. The first one assumes that the electrons in the metal will absorb enough thermal energy to cross over the barrier (Figure 1.6h). The next one involves quantum tunnelling of the electrons through the barrier (Figure 1.6i). And lastly, in the electron-hole recombination, simultaneously injected electrons and holes are recombining radiatively or non-radiatively in the depletion region through defect states (Figure 1.6j).[92] Interestingly, it has been demonstrated that insertion of a thin layer of high-k material between the metal and semiconductor, can lower it even down to 0.2 eV.[95] The I-V characteristics of such heterosystems will exhibit exponential current dependence on the thickness of the insulating layer as a result of charge injection being mediated through the tunneling of the electrons across the insulator.[96] Another way to improve charge transport is to lower the width of the depletion region by doping, and thus allow for more efficient electron tunnelling across it. However, this may not be suitable for all the applications. Another important factor is tied to position of the contacts. For the case of nanowires, the end-contact and side-contact configurations are available. The end-contact is the one where the nanostructure abruptly ends in with the contact, while the side contacts are generally formed by metal deposition across the nanowire.[94] Making the right choice for a given application is important, as it will determine the efficiency of the current flow. The crucial parameter here is the charge transfer length. It is defined as a length over which the current transfer from the semiconductor to the metal will take place.[97] The contact resistance will highly depend on its value, as it is defined by the square root value of the contact resistance/sheet resistance ratio.

Concerning the transport dynamics solely through a nanowire, its dimensions will play a decisive role. In the absence of ballistic transport, or in other words, if the nanowire length is greater than the mean-free-path of electrons the diffusion transport regime will take place, having a certain value of mobility depending on the material. With respect to bulk, the reduction of the channel diameter will most certainly have an influence on the mobility. [14] In that regard, the publication of Xiaocheng Jiang et al.[98] is not only a good example of such a scenario, but more importantly, it demonstrates how to exploit it. The sample investigated in this work was structured as follows: InAs forming a nanowire core, encapsulated in within a 3 nm-thick layer of InP acting as shell. The thought process behind the material choice for the nanowire was based on inherent high mobility of bulk InAs, a corollary of its small electron effective mass. However, at the time it was already well-known that the high mobility can be hampered if the material assumes the nanowire shape.[99] This behavior was accredited to numerous carrier scattering events that could be induced by defects or impurities mostly present at the nanowire surface. In fact, because of their shape, nanowires naturally have high surface-to-volume ratio and thus, the surface states play an important role in future device performance. Therefore, during the

device design one could encounter various efficiency hindering effects, with some of them being charge induced band bending and fluctuations of the applied potential, carrier trap states, etc.[31]

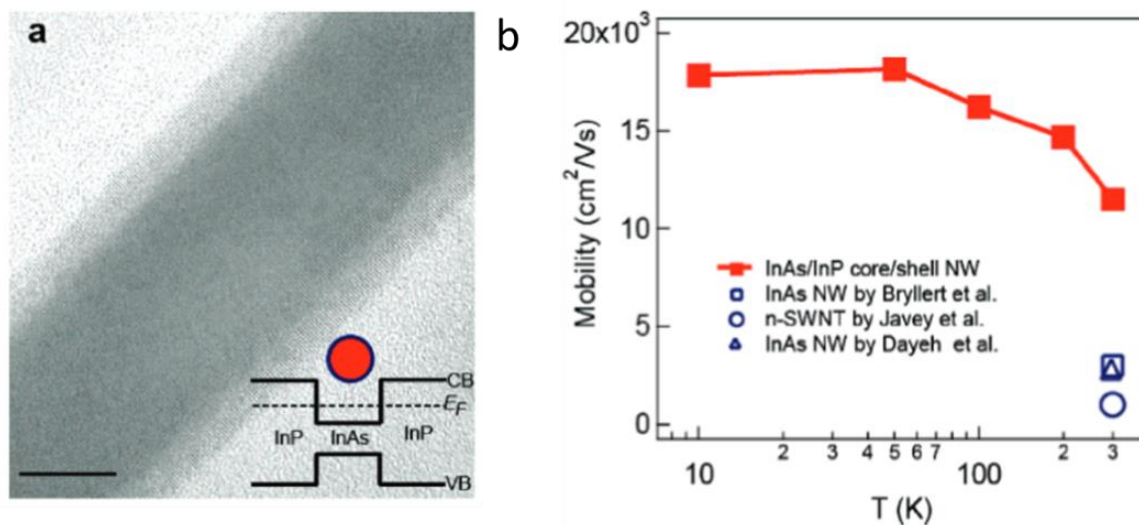


Figure 1.7 a HRTEM image of a representative InAs/InP NANOWIRE. Scale bar is 10 nm. Inset, cross-sectional schematic of an InAs/InP nanowire (red, InAs; blue, InP) and the corresponding band diagram. b Calculated electron mobility of the InAs/InP core/shell nanowire at different temperatures and its comparison with the state of the art of the period (early to mid-2000s).[100]–[103] Figure taken and adopted for reference[98].

To remedy such effects, the InAs nanowire can be passivated with protective shell, which allows for complete recovery or even, improvement of transport properties with respect to the InAs bulk ones. The two-fold benefit of growing the InP shell around the nanowire is immediately apparent and presented in Figure 1.7a. The uniform surface passivation was achieved, as it can be clearly seen from the TEM image and in addition, the type-I band alignment with sufficiently large band offsets between InAs and InP provided a good confinement of both electrons and thermally generated holes. Altogether, the results the authors have obtained from the transport measurements on this heterosystem undoubtedly confirmed their initial speculations, as the ensuing mobility values were much higher than the ones that could be found on bare InAs and even carbon nanotubes (See Figure 1.7b). This was an important demonstration, as it further highlighted the significance of atomically controlled surface passivation for the quality of future photonic and electronic nanowire-based devices.

Another interesting example originates from a group at Harvard University, which was successful in growing Si/Ge core/shell nanowires with atomically sharp hetero-interfaces (See Figure 1.8a).[104]

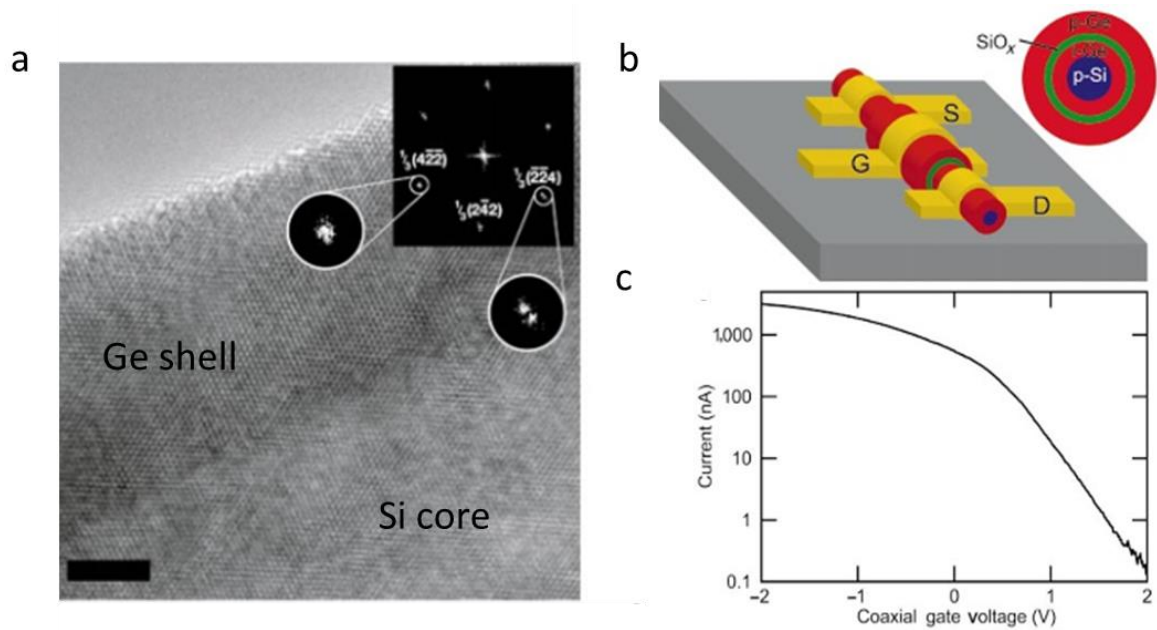


Figure 1.8 Si-Ge core/shell nanowires and a prototype coaxial FET. (a) High-resolution TEM image of a representative crystalline nanowire core and shell Si core 10-nm Ge shell and 1 nm interface. Inset, two-dimensional Fourier transform of the real-space image showing the [111] zone axis. (b) Coaxially gated nanowire transistor, with device schematic showing its structure. The inset shows the cross-section of the as-grown nanowire, starting with a p-doped Si core (blue, 10 nm) with subsequent layers of i-Ge (red, 10 nm), SiO_x (green, 4 nm), and p-Ge (5 nm). The source (S) and drain (D) electrodes are contacted to the inner i-Ge core, while the gate electrode (G) is in contact with the outer p-Ge shell and electrically isolated from the core by the SiO_x layer. (c) Gate response of the coaxial transistor at $V_{SD} = 1V$, showing a maximum transconductance of 1,500 nA/V. Figures taken and adopted from the publication [104].

They have used this system to explore the applicability of band gap engineering for the case of radial hetero nanowires. Indeed, this work reports the direct effects of band alignment between the two materials on the transport properties, by displaying favored hole carrier injection from p-type doped Si core to intrinsic Ge shell. In addition, and for demonstration purposes, they have fabricated a prototype of coaxial FET system (Figure 1.8b) and put it to the test. The trial measurements revealed outstanding performance for an unoptimized device (in Figure 1.8c), which was on par with the carbon nanotube-based FETs[105] at the time. In this way, they have presented the lowest limit of device performance and more importantly, the potential for formation and exploitation of radial 2D electron/hole gas at the interface of core/shell nanowire-based heterosystems, which is certainly an exciting feature in terms of fundamental studies and applicability of quantum transport.

1.7 Planar 1D heterostructures by means of selective-area epitaxy

Not long after the paper showcasing the successful growth of InP nanowires on germanium substrate was published,[106] the first bottom-up synthesis of III-V nanowires on silicon wafer was done by Mårtensson et al.[107] For their demonstration they have used gold seeded MOVPE technique to vertically grow randomly distributed GaP nanowires on Si (111) and Si (001) substrates (see Figure 1.9a, b, c). This material combination was chosen for the low lattice mismatch of 0.4 %. However, it was not the only one, as they further extended their study by also growing GaAs and InP nanowires (Figure 1.9c,d; respectively) in a similar fashion.

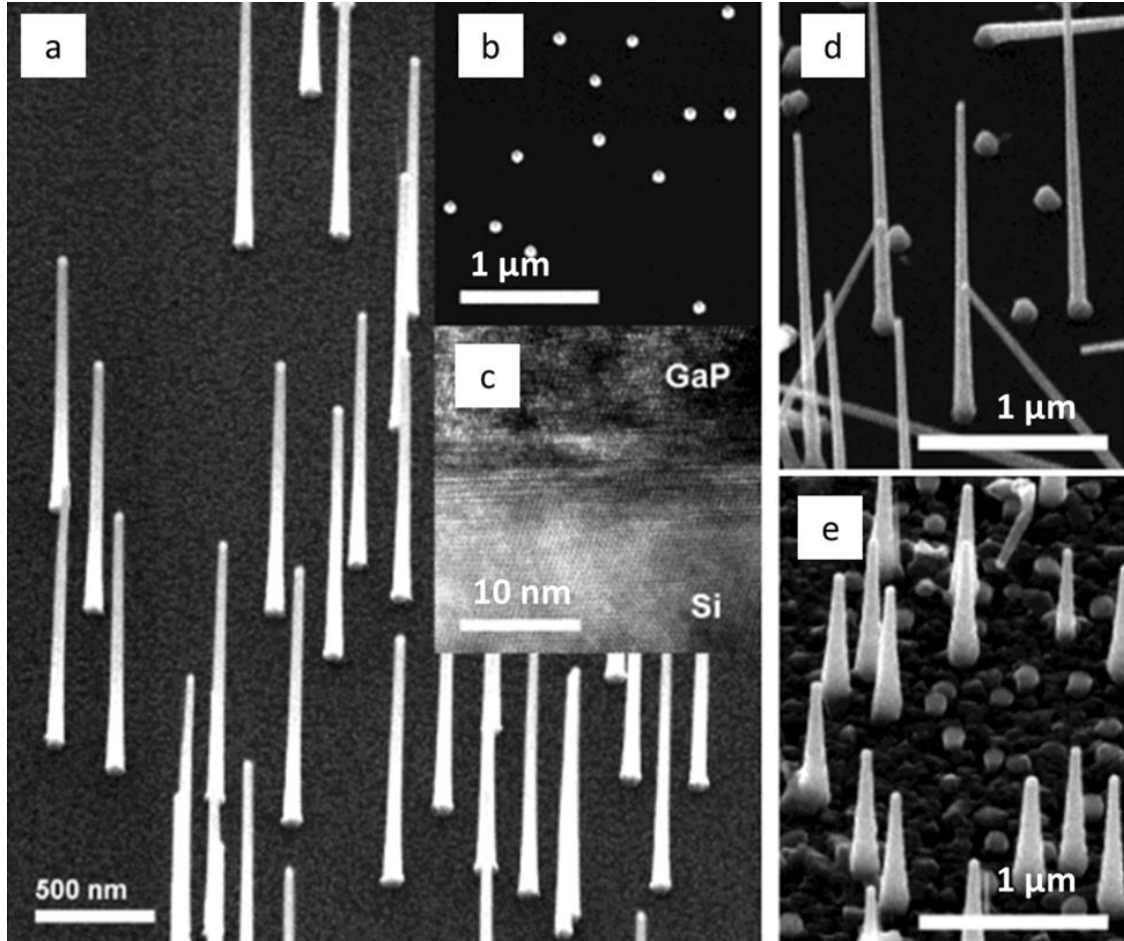


Figure 1.9 First growth of III-V semiconductor nanowires on the silicone substrates, accomplished by Mårtensson et al.[107] SEM images of GaP nanowire on Si(111) from a (a) tilted and (b) top view. (c) HRTEM of the interface between the two materials. (d) SEM image of vertical GaAs nanowires on Si(111) and (e) InP nanowires on the same substrate.

Nowadays, this work might seem a bit rudimentary, however the only reason for that lies in the efforts invested over the years to grow the nanowire-based heterostructures with ever-increasing control and complexity.

For high-speed electronics it is not enough to only fabricate close to perfect nanowire-based heterojunction, it also needs to be well positioned within a logic circuit. One way to achieve this is by means of nanomanipulation. This procedure involves growing the nanowires on separate substrate, from which they would be mechanically transferred and one-by-one integrated into a chosen circuit. However, there is a major flaw with this approach, as it lacks potential for industrial scalability. Nevertheless, there is an alternative path, in which the nanowires are grown directly into a desired system. If the bottom-up (nanowire growth) approach was to be complimented with top-down (nucleation site formation) the position-controlled growth will be achieved, more commonly referred to as selective area growth (SAG). Even though it is possible to have great results with metal-seeded growth by realizing the site formation done with nanoimprint lithography[108], [109], a very popular way has recently been to use electron beam lithography to pre-pattern the mask and grow the material within the mask cutouts. In specific, this method exploits the fact that the gaseous reactant materials in the reactor will tend to desorb on the surface of the mask rather than clusterize or diffuse, thus driving them to nucleate only within the mask openings. Naturally, the first step involves the mask formation. In most cases this is done by spin coating the substrate with the uniform layer of silicone-oxide or nitride, only to be covered with the resist afterwards. Lithography is used to draw the patterns in the resist, while etching methods are employed to form the openings in the marked spots. Once done, the growth of the nanowires will be initiated within them. Selective area growth of nanowires is generally performed at higher temperatures by vapor-solid mechanism (Section 1.4).[110] The two most common techniques for this task are metal organic vapor phase epitaxy (MOVPE) or molecular beam epitaxy (MBE). Regardless of the approach, MOVPE/MBE selective area growth offers fine control of the nanowire shape, orientation, and positioning on the substrate, all while attaining high degree of crystalline purity.

One of the earliest works done with selective area growth method on III-V semiconductor nanowires involved growth of bare GaAs nanowire and GaAs/AlGaAs core/shell nanowire heterostructures on silicone substrates.[111] The motivation behind this attempt was to further push for the growth flexibility and control, in terms of nanowire position and growth orientation. Starting from the former, the authors were successful in forming an array with equidistant spacing between the individual nanowires with the use of selective-area MOVPE. While concerning the latter, the natural affinity of cubic III-V materials to grow along $[111]_A$ and $[111]_B$ directions can cause inclination of the end nanowires when grown on $\text{Si}(111)$ substrates.[112] Such behavior is accredited to a nonpolar character of the silicone and results in three equivalent direction of $[111]_B$, as it was previously seen in the case of InAs nanowires and presented in Figure 1.10a.[113] By modifying the substrate surface from $\text{Si}(111)$ to $\text{Si}(111)_B$ they have managed to overcome this issue, and thus obtain perfectly vertical and aligned nanowires, as it can be clearly seen in the Figure 1.10b. This is important, since for some applications any additional tilt of the nanowires can jeopardize the density of devices due to larger space occupancy of a single nanowire.[37]

Thus far, the control of nanowire verticality has been considered, however for designing 3D channels for novel logic circuits with high degree of complexity, a growth control in horizontal direction is equally if not even more important. Moreover, the mostly planar form factor of currently highly trending devices, such as finFETs or gate-all-around FETs allows for the easy plug-in exchange of now aging processing technologies.[70] When it comes to the planar nanowire synthesis the work of Fortuna et al.[114] was the pioneering one in the field. They were successful in growing GaAs nanowires spreading horizontally on GaAs (100) substrates using MOCVD (see Figure 1.10c). The gold catalyzed growth along [110] direction would push the seed particle, leaving randomly distributed nanowires behind. This work is certainly impressive in terms of novelty, nanowire quality and reproducibility, yet for fabrication of planar nanowire-based devices there were some key points still to be addressed. There was no progress made regarding lateral heteroepitaxy, the growth was heavily reliant on metal seed particles as catalyst, and finally, the spatial positioning of the nanowires was still a challenge. Fortunately, it was soon to be discovered that MBE selective area growth is a methodology which can satisfy all the requirements.

Concerning the growth of nanostructures with higher degree of complexity, metal-seeded method has shown potential as it can yield nanowires of various materials with very interesting geometries. [115]–[117] However, for the particular case of silicone and III-V materials there are reports which showcase seed-induced degrading effects on device performance. For example, gold is the most commonly used material for this purpose mainly for its inertness and low melting point, yet its usage can come with some heavy compromises, such as deep level-trap states, high solid diffusivity and difficulties in cleaning the growth equipment.[118] Hence, the motivation for lowering the industrial reliance on it was major. The breakthrough came in 2006, when Mandl et al. were successful in fabricating vertical nanowires from the III-V group (InAs) on silicone substrate without gold seed particles, by using MOVPE method.[119] This demonstration has certainly opened up the field and inspired for more work to be done on other high-mobility materials composing structures with various spatial configurations.

Indeed, the fabrication of nanowire-based devices with a higher level of complexity demands for a good control of position and orientation. For this purpose, quite a few creative methodologies have emerged.[120], [121] For instance, it was demonstrated that with Langmuir-Blodgett technique nanowires could be assembled into parallel or crossed structures, as seen in Figure 1.10d. The nanowires would be dispersed in the surfactant and with uniaxially applied compression orientate themselves in different spatial configurations. Based on the intensity of the compression the separation between the nanowires would be controlled.[122] However, what this method offers in terms of industrial scalability, it loses in relatively low precision and lack of solid substructure connections. In contrast, structures grown by selective area epitaxy are formed integrally following the design of the patterns with remarkably high selectivity. For example, with the case of InGaAs nano-pillar arrays grown on InP (111)B substrate it was shown that the design created for 2D photonic crystal applications, can be transferred by using silicone-oxide as a material for the mask and electron beam lithography to form patterning while the final structure realization can be done with the use of selective area MOVPE.[123] By keeping the same patterning strategy, while switching the growth methodology, Akabori et al. (2012) introduced the SA-MBE method as useful tool for growing planar nanowires. They have grown InAs on GaAs(001), (111)B and (110) positive resist HSQ-masked substrates.[124] From

there, MBE selective area growth method has received much more attention due to its better industrial scalability, all while striving for MOVPE level of crystalline quality.

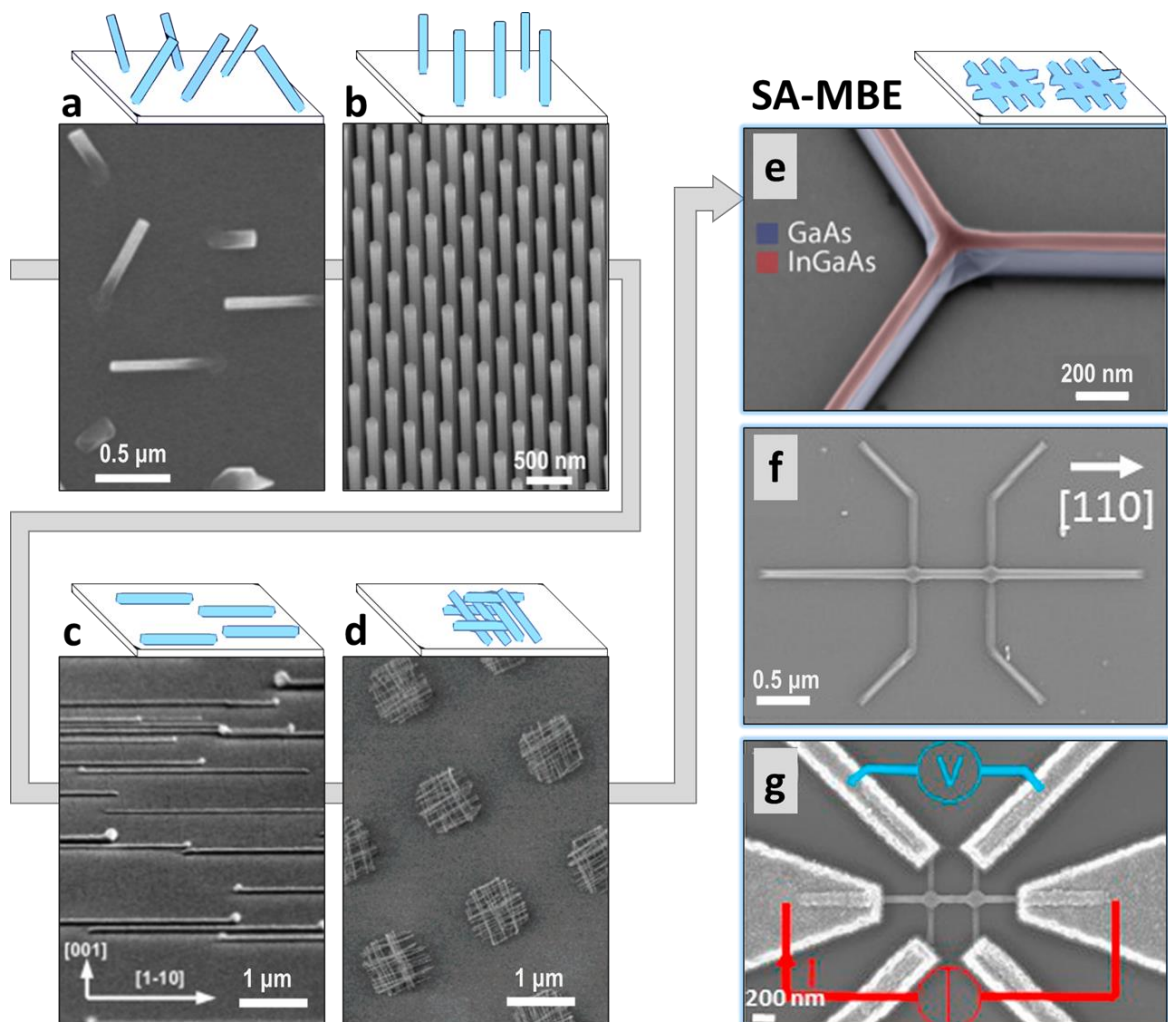


Figure 1.10 From simple vertical to complex planar nanowires. (a) SEM image of InAs nanowires grown on InAs(111)B substrate (top-view). (b) SEM image of GaAs/AlGaAs core-shell nanowires grown on Si(111) substrate. (c) SEM image of planar GaAs nanowires grown on a GaAs(100) substrate. (d) SEM image of aligned and intercrossed silicone nanowires by utilizing Langmuir-Blodgett method. (e) SEM image of a single Y-shaped InGaAs/GaAs compound nanowire grown by SA-MBE. (f) SEM image of InGaAs branched nanowires grown by hydrogen-assisted SA-MBE. (g) Configuration used for transport measurements on the branched nanowire from the previous inset. Figures taken and adopted from the ref. [111], [113], [114], [122], [125], [126], in their respective order.

As mentioned before (in Section 1.4), epitaxial growth usually implies that the nanowires will adopt the substrate crystal structure. However, heteroepitaxy process will regularly be accompanied with defect formation, resulting from the differences in thermal expansion, polarity or the lattice mismatch between the materials involved. When growing hetero-nanowires the defects which are most observed are stacking-faults, threading dislocations, twinning and antiphase domains, and they can certainly have a negative impact on the end device performance (e.g. decrease of carrier diffusion length and lifetime).[67], [127] Again, growing nanowires vertically allows for the strain mediation to be governed through its sidewalls, allowing for wider palette of materials which could be used in forming a heterostructure with good crystalline quality. Sadly, this is not the case for the growth of planar heterostructures due to their larger footprint and smaller aspect-ratio. Thus, in order to avoid defect formation, special care must be taken with respect to the material composition, as it has been shown for the case of planar InGaAs heterostructures where the material combination is constrained to nearly lattice-matched substrates (e.g. $\text{In}_{0.53}\text{Ga}_{0.47}\text{As}$ on InP).[128] Nevertheless, there has been a lot of progress made towards minimizing this issue by understanding and exploiting different growth kinetics and thermodynamics. These feats can be clearly seen by following the advancements starting from defect-free 3D homoepitaxy done by low-pressure SA-MOCVD for the case of GaAs nanosheets,[110] over to GaAs nanomembranes of the same quality obtained by SA-MBE[129] and finally, towards near crystalline perfection of highly complex SA-MBE grown InGaAs/GaAs nanowire networks.[130] With a focus on the lastly cited, clever choice of nanostructure topology and composition (see Figure 1.10e) makes these heterosystems extremely compelling for potential applications for quantum computing. In particular, the remote doping, a direct consequence of the band alignment between InGaAs and GaAs, has shown to have a positive effect on the electrical transport properties (increase of electron mean free path and the strength of spin-orbit interaction) of this nano-heterosystem.[125]

Another similar and quite recent example was the paper published by Bucamp et al.[131] which focused on MBE selective area growth of different $\text{In}_{0.53}\text{Ga}_{0.47}\text{As}$ nanostructures on InP(001) substrate. The goal was to overcome the disparities in optimal growth temperatures of InGaAs constituents. In other words, temperature should be high enough to stimulate a re-evaporation of Gallium, yet low enough to avert the same process for Indium. They have achieved growth at 470 °C with remarkably high selectivity with respect to the silicone-oxide mask, by introducing atomic hydrogen flux during the InP deoxidation process, but also during the growth. The addition of this step had a positive effect on the morphological quality of grown nanostructures. As it can be seen in the Figure 1.10f, the outcomes were the nanowires of various shapes and dimensions (widths ranging from 50 to a 500 nm), following desired form and well-defined facets for the entirety of their length. These observations certainly confirm the viability of the hydrogen assisted SA-MBE technique for the growth of the nanowire-based heterostructures. As in the previous example, the authors of this work have also performed transport measurements with four points of contact (Figure 1.10g) and obtained values for the bulk mobility at room temperature of $8800 \text{ cm}^2\text{V}^{-1}\text{s}^{-1}$. Impressive nonetheless, yet for both 3D nanostructures spoken above, the metallic contacts were deposited across the nanowires and thus, they remained in the fixed position. Moreover, the contact deposition has one more inherent disadvantage in the form of a greater contamination risk.

1.8 Quantum structures by means of colloidal synthesis

In today's semiconductor industry one of the most pressing challenges to overcome is the production of the nanostructures which could exhibit all the trademarks of quantum confinement, but at a low cost and with a high reproducibility. In this regard, the favorable candidates could be found in the solution-based synthesis. As mentioned in Section 1.4, the SLS mechanism has proven to be capable of offering an atomic monolayer control of nanostructure crystallization in a reproducible manner. Colloidal nanocrystals are particles with dimensions not larger than one hundred nanometers, which are obtained by means of wet chemistry. Their ultra-small size is responsible for their electronic properties to be quite different from the ones found in bulk crystals. This is mainly due to the alternation of their band structure being instigated by a strongly confined environment. As discussed in Section 1.2, with the reduction of the nanocrystal size and/or change in shape, quantum confinement effect will be manifested through the variation of the band gap energy, discretization, and separation of supra-bandgap energy levels. Because these effects are so prominent in colloidal nanostructures, they have been regarded as ideal nano-objects for their exploration, but also their exploitation for various applications. This is further prompted by the advances in colloidal synthesis, which have made growth of nanostructures of different dimensionalities attainable. As a result, over the past two decades a significant bibliography was produced on the bases of colloidal quantum dots (QD), quantum wells (QW) and quantum rods (QR) and various other colloidal semiconductor nanostructures.

There are two main steps in colloidal nanocrystal synthesis: nucleation, and growth. Starting from the nucleation. It occurs spontaneously in a supersaturated solution of precursors and is driven by the reduction of surface energy and the gain of chemical potential, which is energy freed by the bond formation in a given nanocrystal. Once nuclei have formed, the growth is follow-through by further attachment of precursors. This process is driven by the minimization of Gibbs free energy and can be expressed as:

$$\Delta G = -\frac{4}{3}\pi r^3 |\Delta G_V| + 4\pi^2 \gamma \quad (1.2)$$

Here, r stands for the radius of a spherical cluster, $|\Delta G_V|$ is the difference of Gibbs free energy per unit of volume and γ is surface energy per unit of area. As it can be clearly seen from the Eq. (1.2), in order to minimize Gibbs free energy a stable balance between two competing processes needs to be established, i.e. between volume decrease on one side and resulting surface energy increase on the other.[132] At this point and for making the best results, it is also important to avoid Oswald ripening effect[133] and consequent broad size-distribution of the nanocrystals in the product suspension. This can be achieved only by having good control over nucleation and growth stages. There are two main approaches which satisfy this requirement, "hot injection"[134] and "heating-up"[135] methods. In the first, a solution of reactive precursors is swiftly injected into the surfactant solution at the temperatures which regularly reach 300 °C or even higher. Upon injection, the reaction between the two species is extremely fast because of a sudden increase in the supersaturation level and thus the nanocrystal growth is triggered. The presence of the surfactant molecules in the solution allows for the surface passivation of the formed nanocrystals and thus prevent their agglomeration. Notably, one of the precursors is usually introduced in the excess to prevent Ostwald ripening and as a result, this method

typically yields products with very narrow size-distribution of the nanocrystals.[136] Whereas for the second approach, the mixture of reactive precursor and ligand solution is stirred at low temperatures only to be heated-up to firstly initiate the nucleation stage and then with continued heating grow these nuclei into mature nanocrystals.[135] It is worth pointing out that regardless of their respective pros and cons, each method offers good control of nanocrystal size, shape, and composition. Yet, the real competitiveness of colloidal nanocrystal-based devices will not only depend on the cost of production, but also on prospective device performance. Naturally, the synthesis from the solution makes the fabrication costs low and easily scalable, whereas improving the performance was the reason which shifted the focus of the research towards radial nano-heterostructures. The hereby motivation had a two-fold character, surface passivation and band gap engineering. Starting from the former, the goal is to minimize the area capable for hosting trap states and consequently, limit the possibility of having non-radiative recombination events.[137], [138] The most common way to achieve relatively complete and stable surface passivation is to cap inorganic nanocrystals with organic molecules, usually referred to as ligands. However, the use of word relatively in this context is not purposeless. Because of the steric spatial occupancy, the ligands are not able to completely cover the surface and thus, satisfy all the dangling bonds. Whereas for the latter, I will refer to the example of colloidal II-VI core/shell nanowires given in Section 1.6, where the overwhelming benefits of layering one semiconductor material with another are discussed in detail. Because of effective surface passivation and instalment of additional properties through band alignment, the core/shell morphology was quick to gain traction.

This is important, as colloidal nanocrystals have found their applications in various fields. To list some of them, photodetectors,[139]-[141] lasers,[142]-[144] biological cell markers,[145]-[147] solar cells,[148], [149] electronics,[150], [151] and many more. Notably, for the past two decades, in one area they have particularly stood out, in flexible optoelectronics with a strong focus on LED (light-emitting diode) display technologies. If the reference was to be made on the relationship between nanocrystal size and the color of emitted light (Figure 1.11a), this is not surprising. In addition to wide and tunable emission (from UV to near-IR) the colloidal nanocrystal-based LEDs are known to exhibit exceptionally good color accuracy and almost 100% luminescence quantum yield (Figure 1.11b).[152] Still, in the current state of the commercial electronic device industry, most of the high-end products are reliant on foldable AMOLED technologies (active-matrix organic light-emitting diode), e.g. Samsung Galaxy Fold smartphone (Figure 1.11c). [153], [154] However, AMOLED displays lack multi-axial flexibility and are extremely sensitive to stretching.[155] In contrast, the films formed by embedding the colloidal nanocrystals in polymers are able to retain their high optical performance, regardless of the direction in which the mechanical stress is applied.

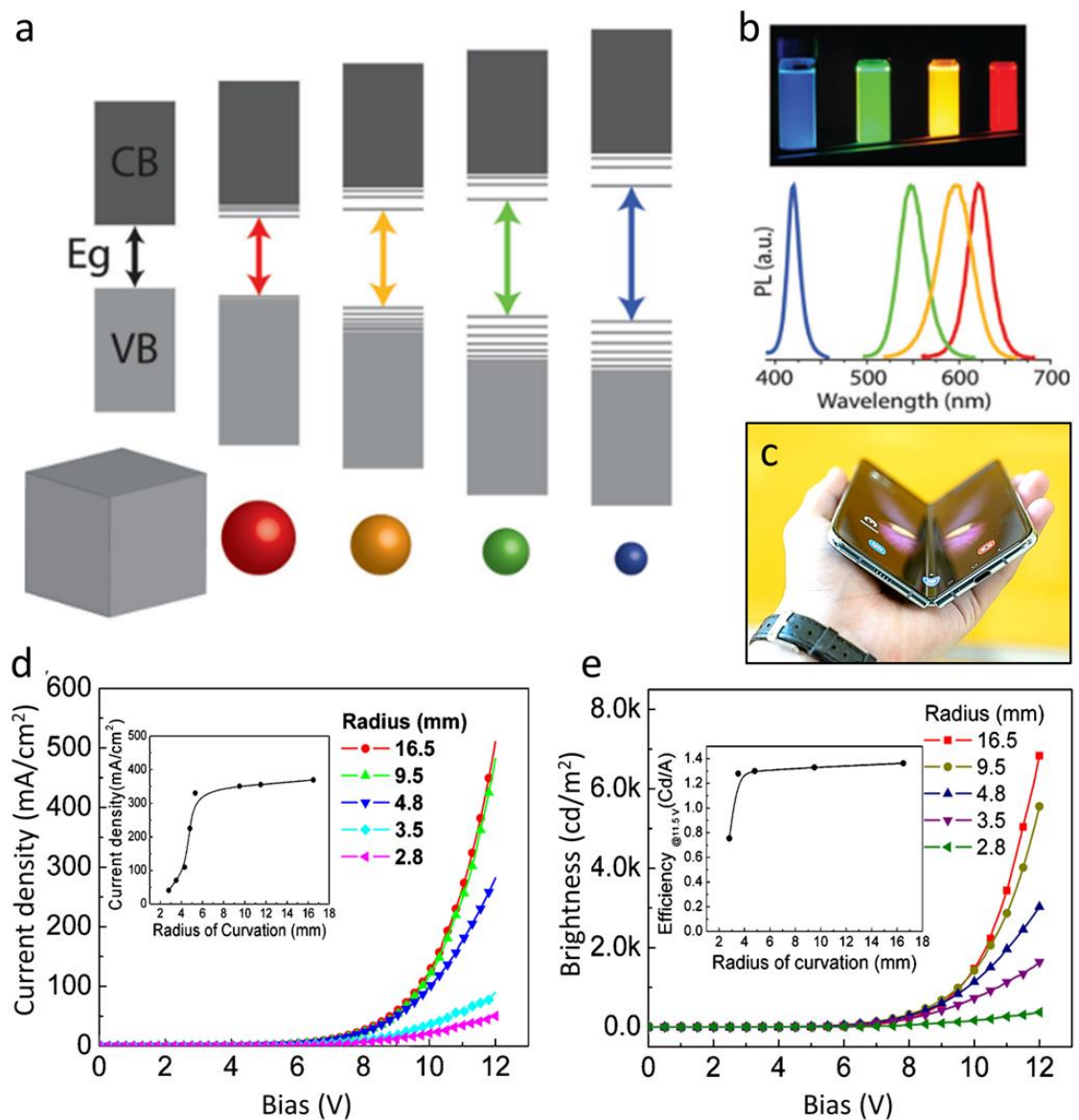


Figure 1.11 Colloidal nanocrystals as building blocks of future flexible display technologies. (a) Evolution of the colloidal nanocrystal band structure with the decrease in size. (b) UV-induced fluorescence of different sized colloidal nanocrystals with corresponding PL spectra. Figures taken and adopted from ref.[156] (c) Samsung Galaxy Fold (released: Sept. 2019) smartphone with Foldable Dynamic AMOLED touchscreen display. This image abides to the CC0 license. (e) Current-voltage and (f) luminescence-voltage characteristics of flexible QD-LED bent into different states of curvature. Insets (e) and (f) adopted from ref.[157]

For instance, in Figure 1.11 one can see the results of “flexibility” study on QD-LEDs fabricated over indium tin oxide (ITO)-coated poly(ethylene terephthalate) (PET) substrate. Judging by the current-voltage (see Figure 1.11d) and brightness-voltage (Figure 1.11e) response to the applied stress, LED did not exhibit any signs of performance degradation, until the 5 mm compression mark was reached at which point ITO film was the first one to give.[157] Moreover, unlike complex organic compounds, nanocrystals are generally much more robust as they can withstand multiple cycles of excitation and fluorescence without any permanent damage or change in chemical properties. The superiority of inorganic nanocrystals becomes even more pronounced if the made comparison is centered on the electronic performances. In terms of charge carrier mobilities colloidal nanocrystal-based devices far surpass organic FETs.[158], [159] With the combination of a colloidal synthesis, drop-casting/spin-coating, and electron beam/atomic-layer deposition the colloidal nanocrystals can be easily integrated into the top-/bottom-gated standard triple-terminal FET layout, i.e. source, gate, drain.[152] In this configuration, the nanocrystals regularly play a role of semiconducting channel, either by being self-assembled into networks or imbedded in the conductive polymer.[160], [161] Regardless of the approach, it is worth noting that the previous studies have shown that the charge transport through these devices is a multiscale process.[162] In specific, on the nanometric scale the hopping transport will be the predominant mechanism, whereas percolative transport is a better fitting description for the larger scales. Hence, it is necessary to have good grasp on two key parameters: the magnitude of the interparticle tunnel barrier and the type of large-scale ordering.[151] A conventional way of controlling both is via ligand engineering. In specific, performing ligand exchange process with the interest of having molecules with the shorter chain length, will result in an improved wavefunction overlap and a consequent increase of carrier mobility.[163] In order to push these results even further, one could utilize the different nanocrystal morphologies. For instance, nanoplatelets (NPLs) are considered to be a superior alternative to quantum dots in more ways than one. Owing to their flatter and highly anisotropic shape, a better electron (hole) wave function overlap between neighboring NPLs can be realized, whilst their larger dimensions bring down the number of hopping steps necessary to reach the electrodes. Interestingly, the publication by Lhuillier et al.[162], has showcased a creative way to completely avoid any efficiency losses in charge transport caused by hopping events. In this work they were successful in fabricating high aspect ratio interconnects made of wide electrodes bridged by nanoplatelets. Due to the absence of hopping transport and intrinsically short transport length of the system, the photoconductivity was shown to be experiencing eight-decade enhancement. Another equally interesting strategy was again developed by the same group, where the viability of the ion-gel-gating was put to the test.[164] For this study the prototype transistor-based device was structured as in Figure 1.12. The CdSe/CdS core/shell nanoplatelets were deposited between the contacts Au/Cu, only to be covered with a mixture of polyethylene glycol and LiClO_4 , acting as an electrolyte. The system in question exhibited outstanding performances (see Figure 1.12, bottom): 10^8 on/off ratio for the drain and gate voltages of 0.5 V and 2 V, respectively; and the sub-threshold slope of 78 mV/decade. Moreover, the authors proposed that the slight disparity from thermodynamic limit of 60 mV/decade (at room temperature) can be caused by defect states originating from the formation of the heterointerface. At this point, it should be stressed out that in both examples given above, the core/shell NPL architecture was employed.

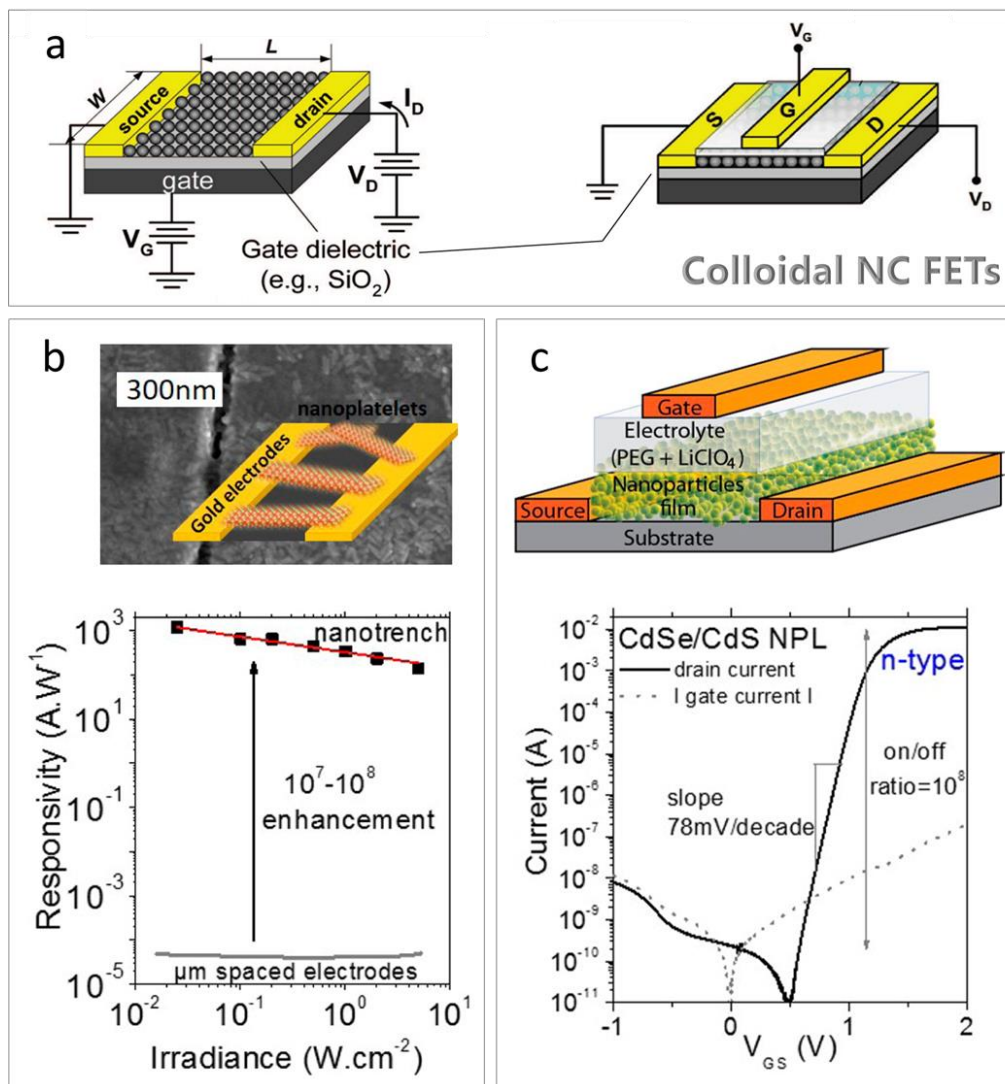


Figure 1.12 Electronic devices based on colloidal nanocrystals. (a) Simple schematic representation of the bottom-gated (left) and top-gated (right) colloidal nanocrystal field-effect transistors, where V_G , V_D and I_D stand for gate voltage, drain-source voltage, and source-drain current, respectively. The image taken and adopted from ref.[152] (b) At the top: SEM image of a nanotrench decorated with CdSe/CdS nanoplatelets of the NPLs bridging the gold contacts, with the overlaid 3D model. At the bottom: Responsivity as a function of the irradiance for a film of CdSe nanoplatelets under a 2 V bias illuminated by a laser at 405 nm. Figure taken from ref.[162] (c) Schematic representation (top) and measured performance (bottom) of the CdSe/CdS nanoplatelet(NPL)-based electrolytic transistor fabricated by Lhuillier et al.[164]

Yet, there is another way. In contrast to the complete and uniform passivation which is characteristic for core/shell morphology, core/crown nanocrystals present a different radial architecture, which is

becoming a focal point of interest in the field of II-VI colloidal nano-heterostructures. All has started from above-mentioned bare colloidal CdSe nanoplatelet and their exceptional optical characteristics, such as absence of photon antibunching, fast radiative lifetimes, narrow and most importantly, highly tunable emission wavelength. Moreover, from the first appearance of bare CdSe nanoplatelets in the literature[165]. The development of synthesis methods has come a long way and as a result their dimensions, general shape and composition can be easily modified with atomic-scale precision, while still preserving their crystalline purity.

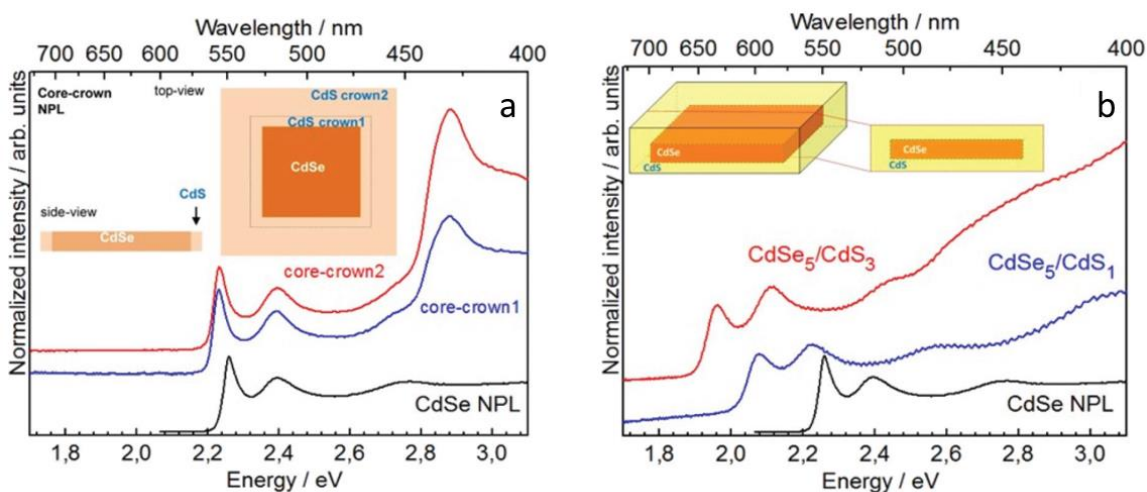


Figure 1.13 The difference in optical responses of (a) core/crown and (b) core/shell nanoplatelets with respect to the increase of crown or shell size or the lack thereof. Figure taken and adopted from reference [166].

Side-by-side morphological comparison of the nanowires and nanoplatelets, does highlight the more cuboidal shape of nanoplatelets. However, they still retain the high surface to volume ratio as their narrow width, a thickness of few monolayers and long lateral extension shape them into long and slender objects, setting them somewhere in between quantum wells and quantum wires. Again, due to the large surface area, passivation plays an important role on excitonic properties. Therefore, surrounding the nanoplatelets with a shell should result in the improvement of quantum yield, which was indeed observed even upon the principal synthesis performed by Mahler et al.[167]. In this study, the quantum yield of CdSe/CdZnS core/shell nanoplatelets was measured to be as high as 60%. However, growing a shell around the nanoplatelet can also come with some concessions. For instance, growing CdS uniformly in both vertical and horizontal direction around CdSe nanoplatelets will result in the change of the exciton dielectric environment and a consequent decrease in exciton binding energy. In contrast, if the growth of CdS is promoted only in the horizontal plane with respect to the CdSe nanoplatelet, the resulting core/crown nanostructure will have similar value of exciton binding energy if compared with a bare nanoplatelet of the same material. This is linked to smaller dielectric constant of the outside media, as the coverage is not complete.[168]

The comparison of optical properties of core/shell and core/crown nanoplatelets is most obvious when observing the evolution of absorption lines with respect to variations of shell/crown dimensions. In Figure 1.13, the absorption spectra of bare, (a) core/crown and (b) core/shell nanoplatelets are presented. This experiment was performed by Dzhagan et al.[166] and it clearly demonstrates the behavioral difference between the two morphological configurations. Unlike core/shell nanoplatelets, where the weakening of the confinement results in gradual redshifts as the shell thickness is increased, the core/crown species remain optically indifferent to the changes in crown size. As a direct consequence of band alignment and greater exciton binding energies, the crown-generated excitons can quickly and efficiently funnel into the nanocrystal core.[168] For this reason, core/crown nanoplatelets have been widely recognized for their applicability as photon collectors and concentrators. However, there are still plenty of unknowns concerning the effect of crown size, passivation efficacy and general influence on excitonic structure of these nanocrystals.

1.9 Take-away points and ensuing challenges

Overviewing the literature to the date, the works published constitute a couple of key conclusions:

- Whether it is for energy harvesting or scaling or any other application in that regard, the remaining challenges are mutual. The carry-on message lies in the urgent need for understanding and controlling the processes that occur at the surfaces and interfaces of one-dimensional nano-heterostructures and thus, prevent further bottlenecking of the development and industrial upscaling towards the future devices.
- Together, colloidal, and selective area growth techniques are capable of yielding nanostructures of high quality and of any shape and size in a very reproducible manner.
- Planar substrate-based architecture presents itself as a worthwhile foundation for high-speed electronics and quantum computing. In addition, it is a convenient platform to study the effects of nanostructure morphology and composition on the electronic properties of the heterointerface.
- Colloidal semiconductors can be viewed as building blocks of future flexible optoelectronic devices, but also as an ideal test subjects to study how quantum mechanical phenomena are exhibited on the electronic and optical nature of the nano-heterosystems.
- Conclusively, a methodological experimental approach should be formulated and applied to study the defect-resilient 1D nanoscale heterosystems.

However, this task involves overcoming the following challenges:

- Devise an experimental setting which can ensure sample preservation before and during the measurements. Multiple instrumental techniques should be utilized to explore all the angles of certain property, preferably in a well-controlled and non-invasive manner.
- Develop a reliable methodology to study band alignment and charge transport in nano-heterostructures.
- Investigate the correlation between band alignment and quantum confinement on one side, and nanostructure optical and electronic characteristics on the other.

Chapter 2. Characterization techniques

2.1 Introduction to scanning probe microscopy

As discussed in the previous chapter, electronic components, sensors, energy harvesters, and biological systems integrate an increasing number of nano-devices. To predict their behavior and ensure the highest possible performance, a thorough characterization of physical and chemical properties of their nano-sized components is essential. Far-field techniques such as optical or electron microscopies have been widely used to characterize the morphology and crystalline structure of nanomaterials, however these techniques are limited by the thickness of the samples, conductivity and most importantly, resolution (half a wavelength of the photons or electrons, respectively). As a result of their small sizes and technical challenges related to nanofabrication and manipulation, new scanning probe microscopy (SPM) instruments with high resolution and sensitivity have been developed for their prompt and accurate characterization.[169], [170]

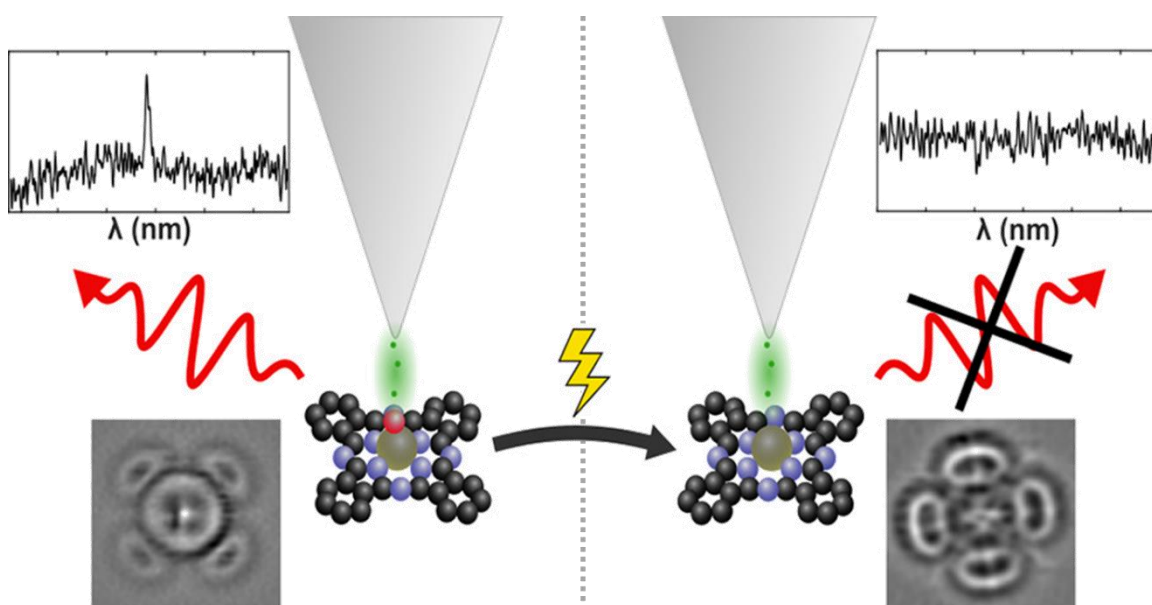


Figure 2.1 Schematic illustration of the experiment, STM-LE spectra, and AFM images of the vanadyl-phthalocyanine (peak at 682 nm) reduction to vanadium-phthalocyanine (no peak present). Figure taken and adopted from ref.[171]

In this regard, scanning probe microscopy has become an essential tool in the growing field of nanoscience. Since its working principle is based on the near-field interaction between the scanning probe and the sample, these techniques can easily overcome the afro-mentioned resolution limitations of the far-field approach. Hence, the SPM resolution is constrained only by the geometrical shape of the probe and the amplitude of the corrugations on the sample surface.[172] To briefly illustrate the remarkable capabilities of scanning probe microscopy I will refer to the recent work done by Kaiser et al.[171] The authors of this paper have successfully utilized a combination of atomic force microscope (AFM) and scanning tunnelling microscope induced light emission (STM-LE) to explore both structural and optical properties of a single-molecule chemical reaction triggered by means of atom manipulation. The best demonstration of such a broad range of capabilities sourced only from two techniques is shown from the results of the experiment which are summarized in Figure 2.1. Here, the AFM images and emission spectra of before (on the left) and after (on the right) central atom removal are shown. As it is clearly visible from the AFM images, the vanadyl-phthalocyanine was reduced to vanadium-phthalocyanine and as a result, the previously present emission at 682 nm was not detected.

In its core, the aim of this thesis is to explore the relations between the surface morphology of the semiconductor nanostructures and their electronic and optical properties. The only way to obtain the truthful picture is to characterize them in the conditions as close to the ones right after the nanostructures have been grown. For this reason, most of the measurements were performed in ultra-high vacuum (UHV). Scanning tunneling microscope (STM) has proven to be a valuable tool and was a central instrument for the development of this thesis. Other complementary techniques were used as well, such as electron microscopies (SEM, TEM), AFM and optical spectroscopies under magnetic field.

2.2 The theory behind scanning tunneling microscopy

Essentially, the starting point of SPM was the invention of STM in 1981 by Gerd Binnig and Heinrich Rohrer. This technique was firstly utilized by Binnig, Rohrer, Gerber, and Weibel.[173], [174] Since then, it has led to the creation of various new probe microscopes (e.g. AFM) and has been a widely used tool in surface science. This is to be expected, as these instruments are able to provide a topography with atomic resolution,[175] but also information on the local electronic structure.[176]

The operation mechanism is based on the quantum mechanical tunnelling effect. It makes use of a sharp metallic tip that is positioned just a few angstroms above a conductive surface whilst applying a voltage. Here, the potential barrier between the tip and the surface is larger than the available electron energy so that no current can flow based on classical mechanics. However, quantum mechanically, the overlap of the electron wave functions of the sample and the STM tip allows a tunnelling current to occur. For a better comprehension of this phenomenon, in the following a brief overview of the main concepts is given. The simplest form of the one-dimensional potential barrier scenario (illustrated in the top part of the Figure 2.2) is the most convenient way to understand the concept of quantum mechanical tunneling.[177] Here, an electron having some energy E is moving in the potential $U(z)$ and can be described by the wavefunction $\Psi(z)$ following the time-independent Schrödinger's equation in one dimension[178]:

$$-\frac{\hbar^2}{2m} \frac{d^2}{dz^2} \Psi(z) + U(z)\Psi(z) = E\Psi(z) \quad (2.1)$$

Where m is the electron mass, \hbar is the reduced Planck's constant and $U(z)$ is the height of the potential barrier. Now, since the regions I and III are outside the potential barrier, where the potential $U = 0$, by the scattering theory the solution for Eq.2.1 will be:

$$\Psi_I(z) = Ae^{ik_1z} + Be^{-ik_1z} \quad (2.2)$$

$$\Psi_{III}(z) = Fe^{ik_1z} \quad (2.3)$$

Here, A , B and F are coefficients and $k_1 = \frac{\sqrt{2mE}}{\hbar}$.

The first solution describes the electron in the Region I, which can be either moving towards the potential barrier or be reflected from it in the opposite direction. Whereas the second solution describes electron which is transmitted in the Region III and is only moving in one (positive) direction.

Regarding the Region II, with a non-zero potential, the solution for the Schrödinger's equation will be the following:

$$\Psi_{II}(z) = Ce^{ik_2z} + De^{-ik_2z} \quad (2.4)$$

Where: C and D are coefficients, $k_2 = \frac{\sqrt{2m(E-U(z))}}{\hbar}$.

Substituting k_2 with ik , one gets: $k = \frac{\sqrt{2m(U(z)-E)}}{\hbar}$. At which point the wavefunction in the Region II can be written as:

$$\Psi_{II}(z) = Ce^{-kz} + De^{kz} \quad (2.5)$$

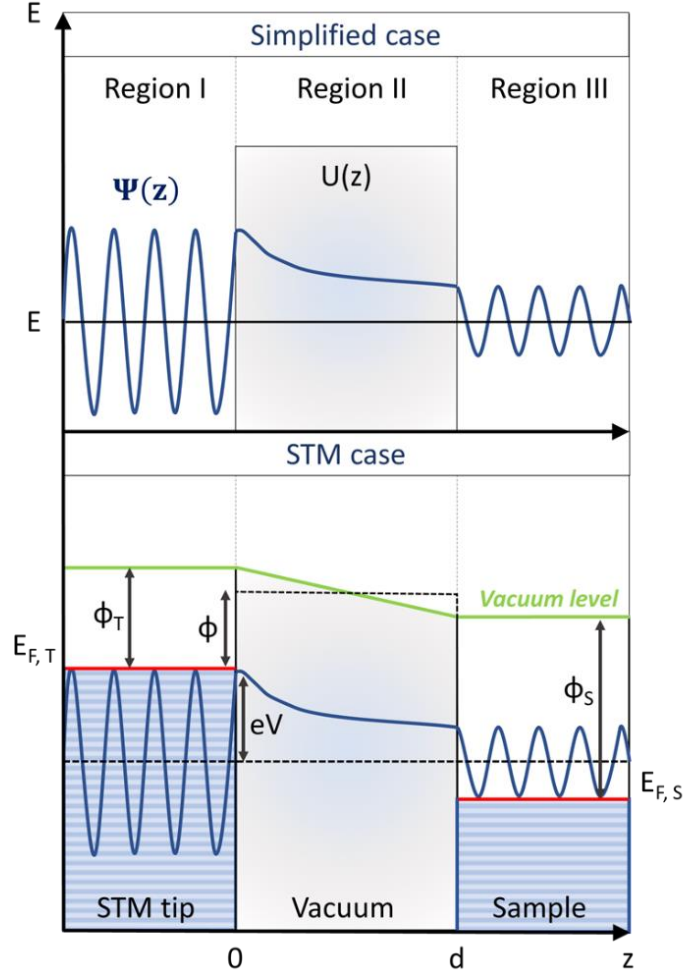


Figure 2.2 Split energy diagrams for the simplified potential barrier case (top) and the STM case (bottom).

The last equation describes the exponentially decaying character of the electron wavefunction inside the Region II, for an energy smaller than the potential U . For the following boundary conditions $z = 0$ and $z = d$, the transmission coefficient (Γ , defined by the F/A ratio) can be expressed as:

$$\Gamma \approx \frac{16E(U(z) - E)}{U(z)^2} e^{-2kd} \quad (2.6)$$

In other words, the probability of finding an electron on the other side of the barrier is proportional to e^{-2kd} .

This model could be very well applied also to the STM case (see the energy diagram at the bottom of the Figure 2.2), where we define a barrier height (ϕ) as the average between the work function of the tip and the work function of the sample:

$$\phi = \frac{\Phi_T + \Phi_S}{2} - \frac{eV}{2} \quad (2.7)$$

where Φ_T and Φ_S are work functions of the STM tip and sample, respectively. We also assume a small bias, which allows to consider a rectangular shape for the potential barrier. When the small bias voltage is applied between the two, a tunneling current will start to flow. Herein, the probability of an electron of the n^{th} tip state Ψ_n having energy E_n somewhere within the range between E_F and $(E_F - eV)$ on the other side of the barrier, is proportional to the wave function squared:

$$P = |\Psi_n(0)|^2 e^{-2kd} \quad (2.8)$$

Where $\Psi_n(0)$ is the wavefunction which describes n^{th} tip state at the tip surface and 0 indicates the location on the tip surface, and $k = \frac{\sqrt{2m\phi}}{\hbar}$. From here, the total tunneling current will be proportional to the number of states in the energy interval eV and can be expressed as:

$$I_T \propto \sum_{E_n=E_F-eV}^{E_F} |\Psi_n(0)|^2 e^{-2kd} \quad (2.9)$$

For small bias voltages, this equation can be re-written in terms of local density of states (ρ_s) near the Fermi level. For a given location z and energy E , the expression would be:

$$\rho(z, E) \propto \frac{1}{eV} \sum_{E_n=E-eV}^E |\Psi_n(z)|^2 \quad (2.10)$$

Consequently, the tunneling current can be written with respect to LDOS near the Fermi level:

$$I \propto V \rho_s(0, E_F) e^{-2kd} \quad (2.11)$$

From here, it is clear that the tunneling current is directly proportional to the bias voltage and LDOS of the sample surface and it exponentially depends on the tip sample distance.

Tersoff and Hamann model was one of the first to successfully describe the electron tunneling at the STM tip-sample junction, assuming a spherically-shaped apex of the STM tip.[179] By Bardeen's formalism[180] the magnitude of the tunneling current that flows between two electrodes in the first order perturbation theory can be expressed as:

$$I = \frac{2\pi e}{\hbar} \sum_{\mu\nu} f(E_\mu) [1 - f(E_\nu + eV)] |M_{\mu\nu}|^2 \delta(E_\mu - E_\nu) \quad (2.12)$$

Here $f(E)$ is Fermi function, $M_{\mu\nu}$ is tunneling matrix element between the tip wave function Ψ_μ and the one of the sample Ψ_ν of the energies E_μ and E_ν , respectively. The term $\delta(E_\mu - E_\nu)$ is related to the energy conservation for the case of elastic tunneling. This equation is further reduced in the low-temperature conditions and when a small bias voltage is applied:

$$I = \frac{2\pi e^2 V}{\hbar} \sum_{\mu\nu} |M_{\mu\nu}|^2 \delta(E_\mu - E_\nu) \delta(E_\nu - E_F) \quad (2.13)$$

Where E_F stands for Fermi energy.

To determine the tunneling current, the matrix element should be obtained via surface integral. Hence it is given by the Fermi golden rule:

$$M_{\mu\nu} = \frac{\hbar^2}{2m} \int (\Psi_\mu^* \nabla \Psi_\nu - \Psi_\nu \nabla \Psi_\mu^*) dS \quad (2.14)$$

As such to derive $M_{\mu\nu}$ the expressions for Ψ_ν and Ψ_μ are needed. However, in practice the exact shape of the STM tip is difficult to know. To overcome this J. Tersoff and D.R. Hamann developed a theoretical model in which the tip apex is approximated to be a sphere with s-type wave functions, which allows for the Eq. ((2.13) to be further simplified to:

$$I \propto \sum_{\nu} |\Psi_\nu(r_T)|^2 \delta(E_\nu - E_F) \quad (2.15)$$

From here the current can be expressed in terms of the sum of the local density of sample electronic states at the Fermi energy, just centered below the curvature of the spherical tip apex with a radius r_s :

$$\rho_s(r_T, E_F) = \sum_{\nu} |\Psi_\nu(r_T)|^2 \delta(E_\nu - E_F) \quad (2.16)$$

However, in practice larger voltages (couple of volts) are used, hence greater number of states within this window can contribute to the tunneling current. Thus, there are two additional factors that need to be addressed. First one is tied to the relative shift of the Fermi level of the sample and the tip, and second the modification of the wave functions due to electric fields.[181] With this in mind and for a temperature of zero kelvin and voltages that are lesser than the work function of the tip the tunneling current can be approximated to be[182]:

$$I \propto \int_0^{eV} \rho_S(E) \rho_T(E - eV) T(E, eV) dE \quad (2.17)$$

Where, ρ_S and ρ_T are the density of states of the sample and tip, respectively at the energy E , measured with respect to their individual Fermi levels. $T(E, eV)$ is the barrier transmission coefficient and is given by:

$$T(E, eV) \approx \exp\left(-\frac{2d\sqrt{2m}}{\hbar} \sqrt{\phi + \frac{eV}{2} - E}\right) \quad (2.18)$$

Tungsten is the material most commonly used for the fabrication of the STM tips. With the tungsten work function being 4.5 eV, it is quite easy to evaluate the transmission coefficient from the Eq.(2.18). The wavevector that is obtained in such a way is around 1 \AA^{-1} , or more concretely, for the variation of the distance between the tip and the sample, the change in current will follow as $e^2 \approx 0.1$. This exactly what allows for the atomic level of sensitivity in the z-direction.

Whereas for the other two directions the spatial resolution of the STM can be evaluated from the probability distribution of the s-wave tip on the surface of the sample. If we consider that the tunneling occurs only between the sample and the outmost atom at the tip apex having an s-type wave function:

$$|\Psi|^2 = \frac{e^{-2kr}}{r^2}; \text{ with } r = \sqrt{x^2 + z^2} \quad (2.19)$$

For the case when z is much larger than x, r can be approximated to be:

$$r \approx z + \frac{x^2}{2z} \quad (2.20)$$

If plugged back in the Eq.(2.19), one gets:

$$|\Psi|^2 = \frac{e^{-2kr}}{z^2} e^{-k\frac{x^2}{z}} \quad (2.21)$$

The probability density on the surface can be approximated by the Gaussian function in x with a Full Width Half Maximum (FWHM) of:

$$\Delta x \approx \frac{2z}{k} \quad (2.22)$$

Assuming that the s-wave decay length (k) is around one ångström, the lateral resolution will be the following:

$$\Delta x \approx 1.4\sqrt{r} \quad (2.23)$$

In practice, the STM tip having a 100 \AA radius of the apex can be considered to be a decent tip, hence the lateral resolution would be just above 10 \AA . However, in most cases the apex of the tip would be decorated with atomic-sized protrusions which could be the tunneling points, allowing for the resolution to be lowered even down to 5 \AA .

2.3 The theory behind scanning tunneling spectroscopy

In STM experiments, spectroscopy mode differs from the topography one, as the tip is held static during the measurements while bias voltage is varied. With the use of lock-in amplifier it is possible to modulate the voltage and measure the differential conductance spectra. This is important, as these curves are proportional to the local density of states of the sample beneath the tip. [183]

Assuming a constant density of states for the tip, from the equation (2.17) one can obtain the following:

$$\frac{dI}{dV} \propto e\rho_T\rho_S(eV)T(eV, eV) + e\rho_T \int_0^{eV} \frac{d}{d(eV)} [T(E, eV)]\rho_S(E)dE \quad (2.24)$$

In large part, the limitation to the resolution of the STS is thermal broadening. When the temperature is not zero, the expression of the current is:

$$I \propto \int_{-\infty}^{+\infty} [f_S(E) - f_T(E - eV)]T(E, eV)\rho_T(E, eV)\rho_S(E)dE \quad (2.25)$$

f_n is the Fermi-Dirac distribution. It is defined by:

$$f_n(E) = \frac{1}{1 + \exp\left(\frac{E - E_{F_n}}{k_B T}\right)} \quad (2.26)$$

Where k_B and T are Boltzmann constant and the temperature. By neglecting the insignificant contribution of the $T(E, eV)$ and by assuming that the density of states of the STM tip is constant, the dI/dV relation can be expressed as:

$$\frac{dI}{dV} \propto \rho_T \int_{-\infty}^{+\infty} \frac{\partial}{\partial V} f_T(E - eV)\rho_S(E)dE \quad (2.27)$$

Bearing in mind the convolution between the derivative of the Fermi-Dirac distribution of the tip and LDOS of the sample at the given temperature, one can obtain:

$$\frac{\partial I}{\partial V} f_T(E - eV) \propto -\frac{1}{k_B T} \frac{\exp\left(\frac{E - eV - E_F}{k_B T}\right)}{\left[1 + \exp\left(\frac{E - eV - E_F}{k_B T}\right)\right]^2} \quad (2.28)$$

In Figure 2.3, the simulation of the differential conductance spectra at three different temperatures is presented. Considering the density of states of the sample as a Dirac function, the evident smoothing of the peaks with the increase of the temperature follows the expression (2.28). Therefore, to have the best possible spectral resolution, all of the STS experiments which will be discussed in this thesis were performed at cryogenic temperatures.

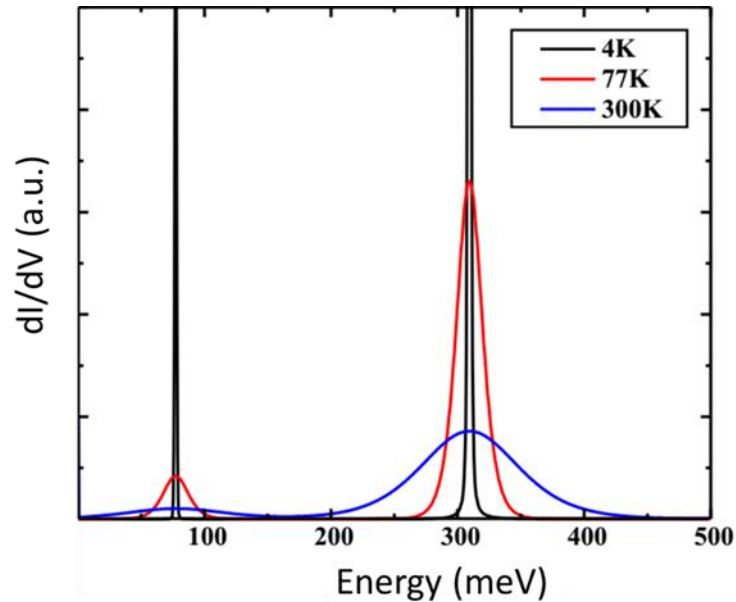


Figure 2.3 Illustration of temperature broadening in differential conductance spectra recorded at 4 K, 77 K and 300 K. Figure taken from ref.[184]

2.3.1 The lock-in amplifier

There are many potential noise sources in the STM systems, such as mechanical, thermal, amplifier induced and most commonly, flicker noise ($1/f$). [185] The last mentioned is present in most of the electronic devices and it results from slow resistance fluctuations caused by temperature variations in the system. In order to increase signal to noise ratio, but also obtain dI/dV curves while avoiding numerical differentiation, lock-in is used. The basic idea is to measure the derivative of the I-Vs, rather than compute it and in such a way obtain better signal-to-noise ratio. How this is accomplished is schematically presented in Figure 2.4. The STM tip is held stable at the set distance d from the sample. The bias voltage is ramped within a chosen range while the tunneling current is recorded. During the measurements, a small high-frequency (around 500Hz-10kHz) sinusoidal signal, $V_{\text{mod}} \sin(\omega t)$ is superimposed to the tunneling voltage. As a result, the tunneling current will oscillate at the same frequency. Next up, the tunneling current, along with the noise is converted to a voltage by transimpedance amplifier. Multiplying it with the reference signal will give a response at the sum and at the difference frequencies. Hence, only the signal oscillating at the same frequency as reference one will give a sinusoidal output, whereas everything else will be oscillating at the average value of zero. By tuning the phase with a phase shifter, one can effectively filter out only useful quantity of the signal by having it in the mixing product, which will be pushed to the dc value, while the noise will still have the ac character.

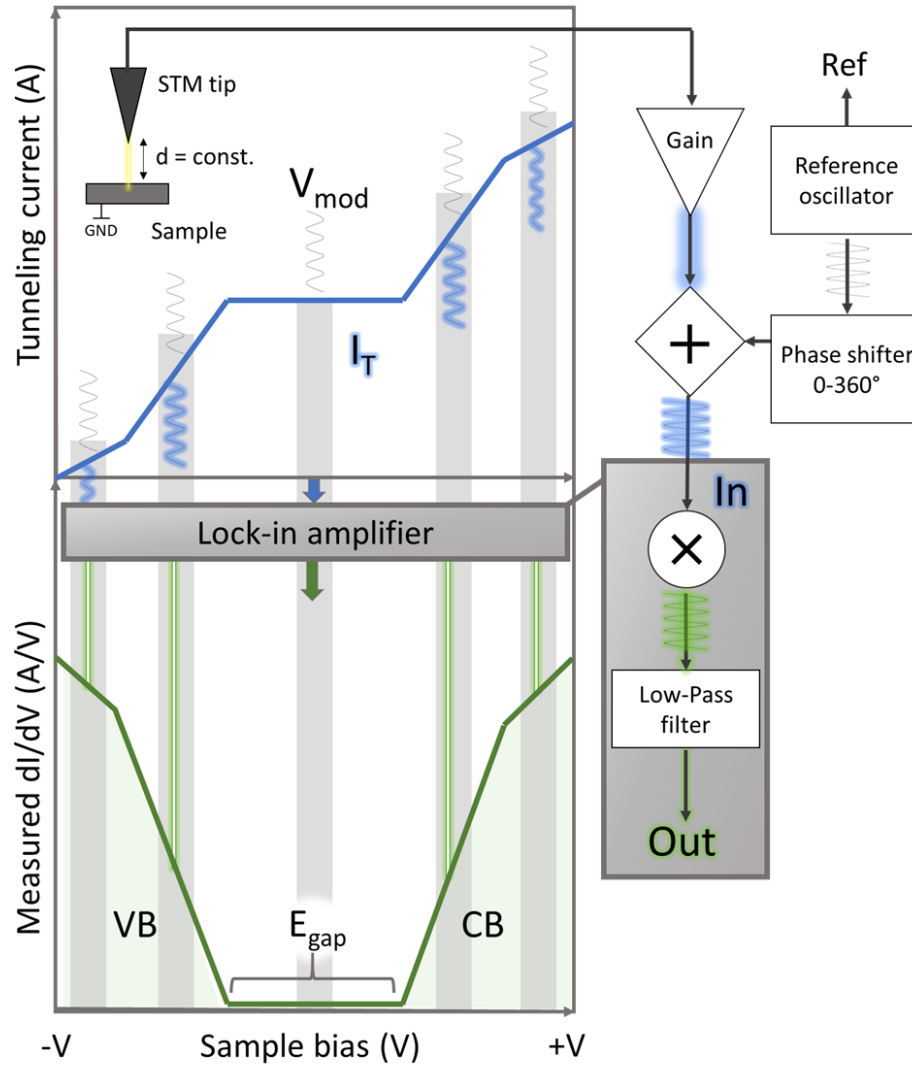


Figure 2.4 Schematic representation of the $I(V)$ and dI/dV spectra with a block diagram of the lock-in amplifier.

Using the low-pass filter, only the dc component is extracted from which the amplitude of the modulated current (sensitive to the slope of the I - V curve) can be measured. This is significant, since for small modulations, the tunneling current can be expanded in the Taylor series:

$$I(V_{bias} + V_{mod}\sin(\omega t)) \sim I(V_{bias}) + \frac{d}{dV}I(V_{bias}) \cdot V_{mod} \sin(\omega t) + \frac{d^2}{dV^2}I(V_{bias}) \cdot V_{mod}^2 \sin(\omega t) + \dots \quad (2.29)$$

where the first harmonic frequency is proportional to the differential conductance signal (dI/dV).

2.4 STM and STS on the Omicron LT-STM

The single-probe low-temperature STM system (LT-STM) developed by Omicron GmbH, that was used during this thesis is an instrument of the Physics group at IEMN and is located at the Institut Supérieur d'Électronique et du Numérique (ISEN) in Lille, France.

The whole system is kept in ultra-high vacuum (UHV) and comprises of two main chambers, analysis and preparation ones, as it can be seen in Figure 2.5. To reach and maintain the UHV conditions ($\sim 10^{-11}$ Torr), a set of different pumping tools is required. Aside from mechanical pumping this system relies on ion getter pumps and titanium sublimation pumps (TSP). Both chambers can be pumped separately since they are isolated from each other with a gate valve. In fact, the easiest way to describe the system layout and operation, whilst staying in the context of this thesis, is to follow the path of some archetypal colloidal nanocrystal (NC) and selective area grown nanowire (NW) samples from their arrival to their first STM image and STS curve. Before the measurements, both samples are protected from atmospheric conditions in their own respective ways. The sample NC is a suspension of ligand-passivated nanocrystals and the NW sample is a one-centimeter squared piece of wafer with nanowires capped with a thin layer of arsenic.

The starting point of any STM measurements, is to have a high-quality probe, which can be reliably done by electro-chemical etching of a tungsten wire. In practice, the wire is dipped below the surface of a sodium hydroxide (NaOH) solution and the voltage is applied between it and the cathode. After 10-20 minutes the lower part of the wire falls off, while the leftover part is sharp enough to be used as the STM tip. Both NW and NC samples are stored and transported in a way to prevent oxidation and contamination. If not stored inside the UHV systems, semiconductor nanowire samples are usually held in highly portable vacuum containers (Figure 2.5a), while air-tight vials containing liquid suspensions of colloidal nanocrystals are preserved in a cold and dark environment. The next step is to prepare the samples. The NW sample will be cut to size, whereas for NC sample the suspension will be drop-casted on chosen substrates and dried with nitrogen flux. Subsequently, both samples will be mounted on the sample holders. Depending on the type of the sample and the measurements needed to be done, different configurations of the sample holders can be used (simple plate, bridged, spring loaded, angled etc.). Once mounted the following step is their introduction to the UHV conditions without breaking the vacuum of the whole LT-STM system.

This is done through the load-lock compartment located on the side of the preparation chamber (layout in the inset of Figure 2.5). Both samples are placed on a short transfer rod and the compartment is sealed shut by screwing it tightly with a copper gasket at the joint. The follow-up bake-out procedure is done at 120 °C for several hours to remove any residual water from the inner chamber surfaces, but also the samples. After that, the valve between the load-lock and the preparation chamber can be opened and the samples can be safely transferred from one to the other. The preparation chamber contains all the necessary tools for the sample cleaning and other treatments, such as five-slotted storage bay, quadrupole mass analyzer (QMS), sputtering gun, evaporation stage, heating elements, thermocouple, and various electrical connections which allow for the sample polarization or for its isolated heating. All the maneuvering of the samples in the preparation chamber is done either with the transfer rod or with a manipulator with four degrees of freedom.

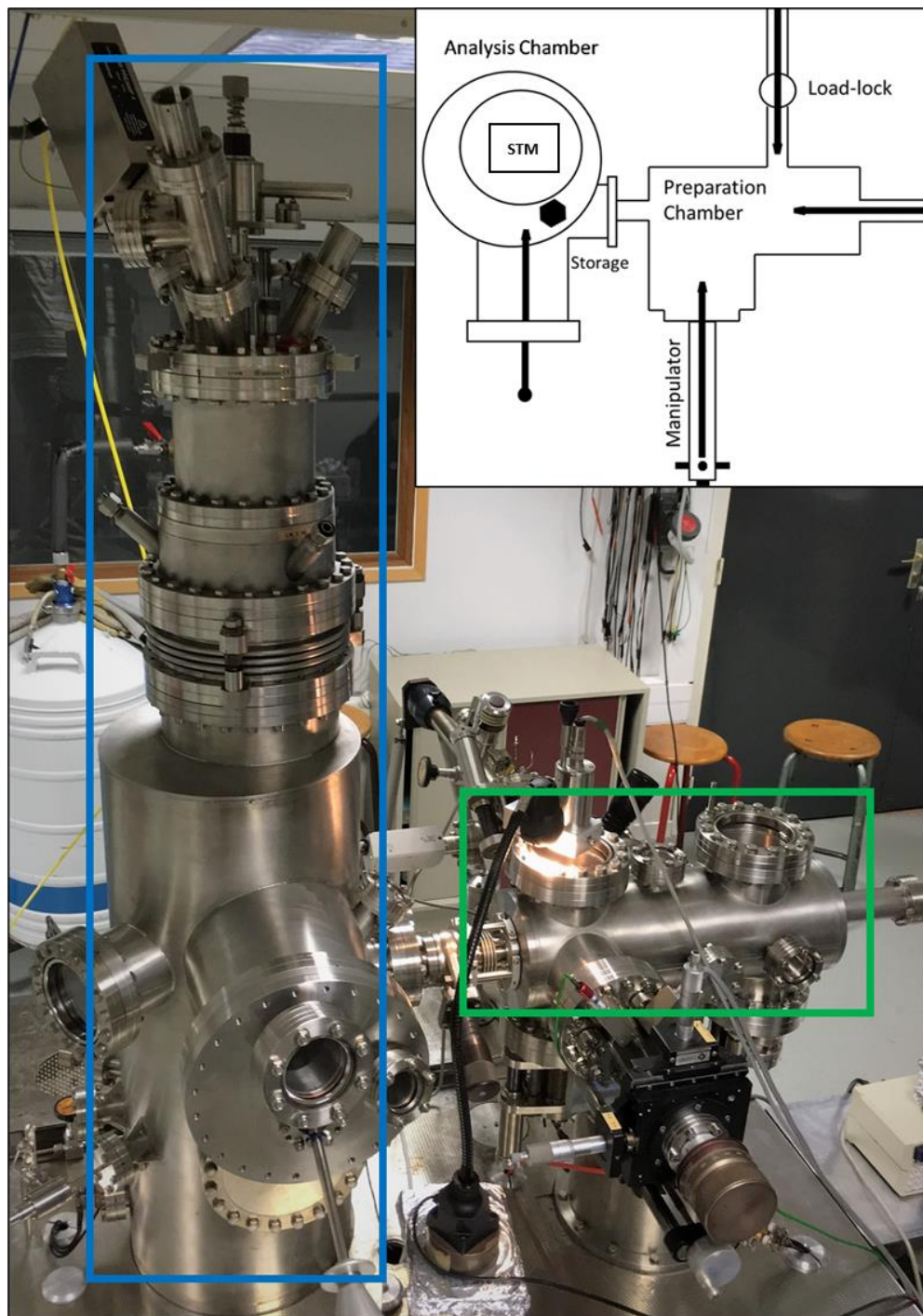


Figure 2.5 LT-STM system: The Omicron LT-STM analysis chamber (blue box) and preparation chamber (green box). Schematic of the system layout (inset).

Since no particular preparation is required for our prototypical NC sample, it can be immediately placed on the long transfer rod and moved to the analysis chamber. As for the NW sample, the arsenic decapping will be the next step. Arsenic layer is desorbed at 350 °C, by passing an electrical current through the sample substrate to heat it up for couple of hours, while the whole procedure is monitored with QMS. Once the arsenic peak has disappeared (as in Figure 2.6b) and the pressure of the chamber has recovered to its baseline value, the NW sample can be also transferred into the analysis chamber.

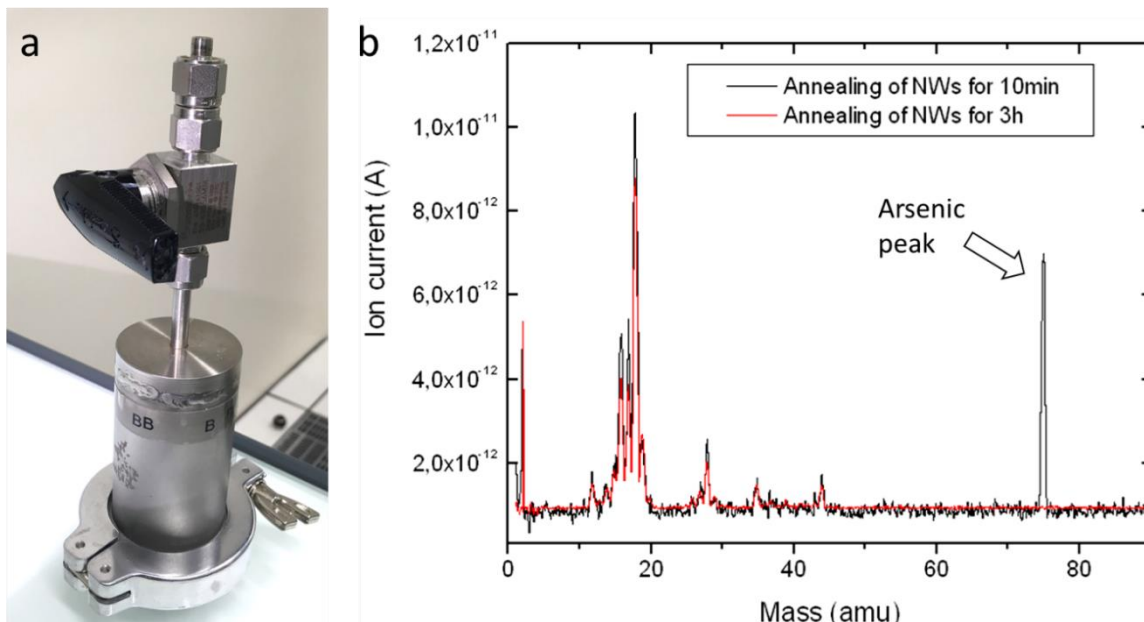


Figure 2.6 Handling the nanowire samples which are prawn to oxidation in the atmospheric environment. (a) Vacuum container for the sample transport. (b) QMS spectra captured at the beginning and at the end of NW arsenic decapping process.

There, the samples and spare STM tips can be stored on the six-slotted carousel before entering the microscope. Since the tunnelling conditions require the tip to be positioned just a few Å away from the sample, a high mechanical stability against oscillations is compulsory to avoid tip crashes and poorly resolved spectra and images. Hence, the STM has a very compact design and is mechanically decoupled from the rest of the UHV chamber. Indeed, during operation the STM hangs from the bottom of the cryostat to which it is connected by three soft springs. The cryostat consists of an outer tank for liquid nitrogen and a smaller inner tank for either liquid nitrogen (77K) or helium (4.2K). Having a STM kept at low temperatures has two key advantages. Firstly, it passively improves the vacuum conditions with screens acting as cold finger with respect to the base vacuum of the UHV chamber (usually up to one order of magnitude), thus allowing for the sample to stay clean for much longer periods. Secondly, it reduces thermal drift and noise, allowing for the measurements to be done on the same spot of the sample for several hours. This is particularly important for performing STS experiments as well as for the investigation of the bias dependence of one particular structure on the surface. Thermal stability is

insured by the presence of a double screen which completely shields the microscope from the external irradiation.

The sample holder inside the microscope has place for only one sample. Therefore, one at the time, our NC and NW will be picked up with a wobble stick and carefully placed inside the microscope and measured. Assuming that the measurements will be performed at low-temperatures, the samples will be left for some time to thermalize, before committing to tip-approach procedure. Once the sample and STM tip have cooled down, the values of bias voltage (usually couple of volts) and the setpoint current (couple of dozens of picoamps) would be set, at which point the automatic tip approach can be initiated. Since the STM is an instrument designed to work best for the case of atomically flat, conductive, and clean surfaces, doing experiments on either of our samples will be quite difficult. For example, there is a common challenge for both samples and is related to locating and identifying the nanostructures on the substrate. This process must not take too much time to avoid general inefficiency, but also potential contamination or degradation of both the sample and the tip. Moreover, these measurements will demand constant monitoring of scanning parameters (I_{setpoint} , V_{bias} , Feedback loop, etc.) and their real-time adjustment during the acquisition of the STM images or STS spectra.

2.4.1 STM and STS on selective area grown nanowires

The following section focuses on key points for characterizing selective area nanowires.

2.4.1.1 Locating and identifying the nanowires on the surface.

As mentioned before STM is an instrument designed for the samples with the surface roughness reaching no more than couple of dozens of nanometers. In that regard, most of the epitaxially grown nanowires are exceptionally large objects, by STM standards. Therefore, when acquiring STM images special care must be taken for inevitable and sudden height variations which could cause a tip to crash. The usual protocol which is used for these kinds of samples involves first finding and then, climbing the nanowire. Finding the nanowires in the absence of SEM, entails for the initial scanning to be done on a large scale with an exceptionally low speed, setpoint current, resolution, and with a fast feedback loop. Once a sudden change in height is detected, the scan is stopped and rotated in a direction parallel to the nanowire. Climbing the nanowire is done mostly with the same parameters with the only optional improvement being the resolution. When the tip has reached the top of the nanowire, the scanning parameters can be changed to favor the quality of the image (e.g. lower bias voltage, higher setpoint current, stiffer feedback loop, smaller scan area, increased number of pixels, etc.). From the noise levels and drift traces in the STM images one can know when the tip has reached the adequate level of thermal and mechanical stability (see Figure 2.7).

Only then, the scanning tunneling spectroscopy can be performed. However, for selective area grown nanowire samples, only second half of this protocol is applicable. Because the distribution of the nanowires will be dictated by the initial patterning of the mask, finding a nanowire should be in theory,

simpler. However, this is not true since the mask itself presents another more severe problem. Due to its non-conductive nature it renders the possibility of having a successful blind automatic approach next to impossible. In fact, this is more an instrumental challenge, rather than the one for the operator.

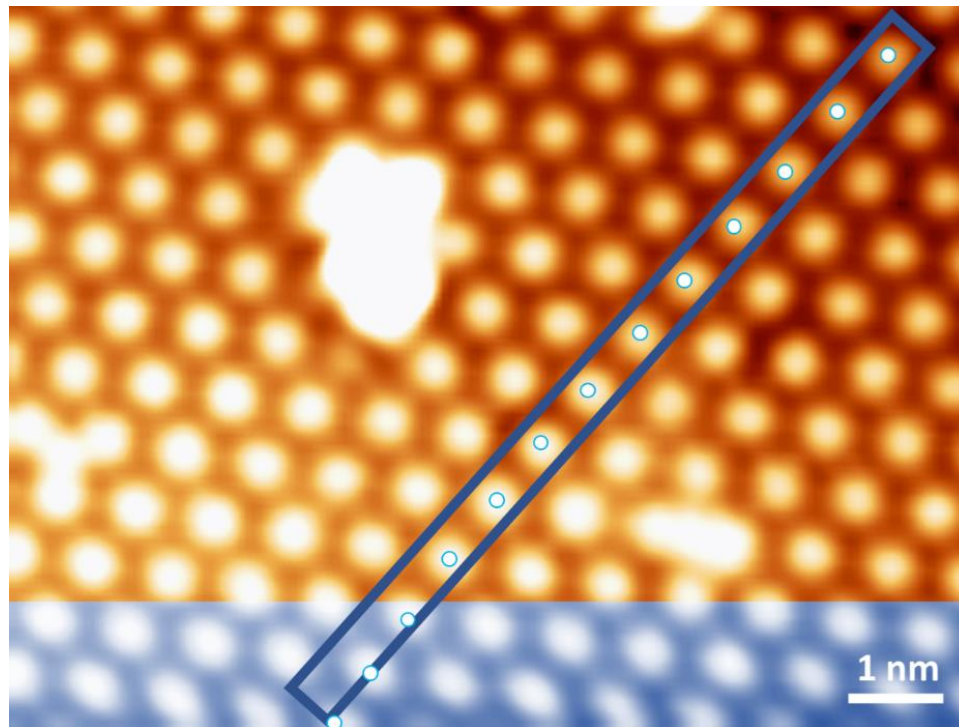


Figure 2.7 STM image with atomic resolution showcasing the mechanical drift of the piezo drivers (area shaded in blue). The scan was initiated from the bottom of the image and only after approximately 100 lines the system was stable, as it can be seen by the highlighted atomic periodicity. This example STM image was acquired on the germanene surface at 77 K and with the feedback parameters: $V_{\text{bias}} = -0.5$ V, $I_{\text{setpoint}} = 0.1$ nA.

Fortunately, the latest generations of STMs can surmount this issue as they have high-resolution UHV-SEM integrated, and as an added benefit, they are also capable of multi-probe LT-STM, STS and transport measurements with atomic resolution, all while having remarkable degree of thermal and mechanical stability. One of such systems was developed by ScientaOmicron and is equipped with four probes exhibiting equal level of performance. The probes can move and scan independently from each other, and are monitored by UHV-SEM.[186], [187] One such system was utilized to study one of our samples at CEMES/CNRS in Toulouse, France. However, what this system offers in terms of atomic resolution and low-temperature spectroscopy, it loses in flexibility when it comes to the electrical transport measurements, as it is unable to probe four-point DC electrical characteristics of the samples. For that purpose, a different variable temperature (VT) four-probe system at the home institute was utilized.

2.4.1.2 Performing STS measurements on semiconductor nanowires.

STS on semiconductor nanowires is usually not as demanding as for the case of colloidal nanocrystals, due to the larger size, but also because the nanostructure surfaces are much cleaner and more exposed (absence of ligands). However, it is noteworthy that defect, charge, or tip-induced band bending effects introduce misperceptions regarding the potential distribution across the tunneling junction.

In metallic systems, a polarized probe at the tunneling distance from the sample, involves charge redistribution on both sides of the tunneling junction. In the sample the charge will migrate to its surface in order to suppress the generated electric field and keep its net potential zeroed. On the other side of the junction, the probe will react by screening the surface charges to keep the polarizing voltage at the set value. However, if the sample is a semiconductor as in Figure 2.8a, the narrative is different. The formed electric field partially drops inside the near surface region of the semiconductor. This is a consequence of the low concentration of free carriers present in the semiconductor which could screen the voltage. The band diagram illustrating this effect is shown in Figure 2.8b, for a p-type doped semiconductor. Here, the negative bias voltage is applied to the sample. If the assumption is made that the semiconductor is clean and without surface states, the formed electric field causes electron accumulation near the surface and bends the band downwards. Yet, if the positive voltage is applied the upward band bending is expected. Either way, the energetic positions of the semiconductor surface states will be shifted. This effect is called tip-induced band bending (TIBB) and can alter the interpretation of STS spectra.

To quantify the extent of TIBB, in 2007 Feenstra et al.[188] have defined which are the important parameters to consider: sample doping concentration, effective masses, tip-sample separation and tip radius and finally, the electrostatic potential energy difference between the probe and a point deep within the semiconductor (ϕ_T). This quantity can be expressed as:

$$\phi_T = eV + \Delta\phi \quad (2.30)$$

where the contact potential $\Delta\phi$ is given by the work function difference between the tip and the sample:

$$\Delta\phi = \phi_m - \chi - (E_C - E_F) \quad (2.31)$$

Here, ϕ_m is the work function of the metallic tip, χ is the electron affinity of the semiconductor sample, E_C is the energy which corresponds to conduction band minimum and E_F is the Fermi level of the sample. Depending on the sign of the contact potential, the downwards band bending will be induced for the negative values and upwards for positive.

Furthermore, it was demonstrated that it is possible to obtain fairly accurate voltage distribution maps of a given tip-semiconductor system by solving the Poisson's equation in the 3D geometry within the boundaries of ϕ_T and Fermi level position in bulk of the semiconductor, as showcased in Figure 2.8c.[189] Here, the equipotential lines indicate that the potential penetrates well beyond the atomic sites at the surface of the semiconductor, with the maximum located at the point right beneath the apex of the STM tip (ϕ_0). In other words, the potential energy at this point is deterministic for the shape of STS curves which are obtained experimentally.

When there is no band bending the simple relation between the energy of some state and the applied voltage is valid:

$$E - E_F = eV \quad (2.32)$$

However, for the $\phi_0 \neq 0$, a slight modification needs to be applied[190]:

$$E - E_F = eV - \phi_0 \quad (2.33)$$

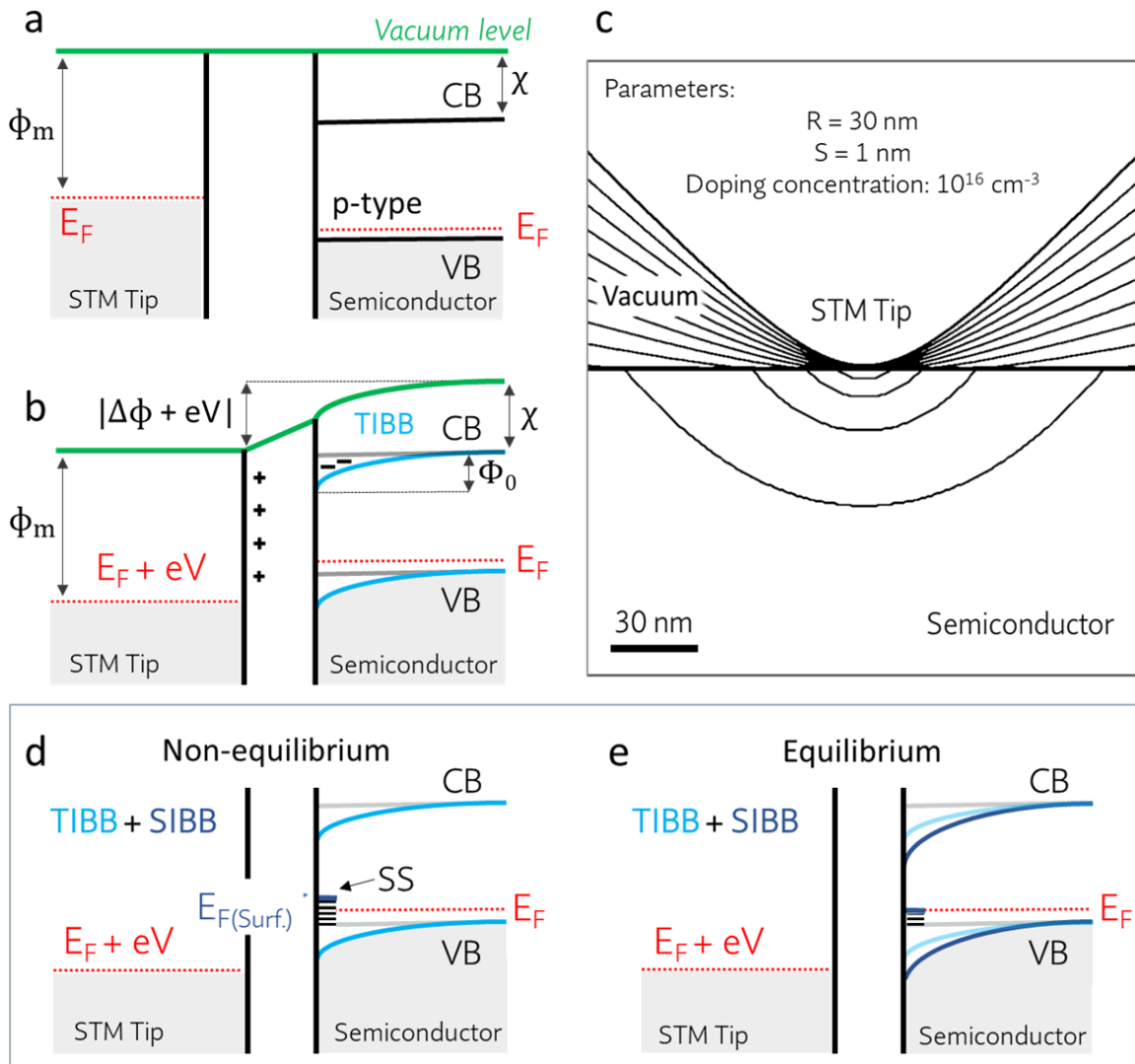


Figure 2.8 Tip induced band bending (TIBB) in semiconductors. (a) An example of an energy diagram for the STM tip-vacuum-p-type semiconductor tunneling junction of a width much larger than the tunneling distance. (b) Energy diagram of the same system (in the absence of surface states) when the

tip is brought in the tunneling distance from the semiconductor surface and when both values of both sample voltage and contact potential are negative. (c) Simulation of the potential distribution, for a tip-sample separation of 1 nm, tip radius of 30 nm, and tip position 1 nm inside the InGaP layer. A situation of depletion in the semiconductor is shown, with potential energy contours separated by one tenth of the potential difference between tip and semiconductor (e.g. with the electrostatic potential energy of the tip being 1 eV relative to a point far inside the semiconductor). The contours are at energies of 0.1, 0.2..., 0.9 eV). Figures (b) and (c) taken and adopted from ref.[188] (d) An example of a similar system as in insets (a) and (c), with a differentiating feature being the presence of surface states (SS). The added contribution of the surface states to band bending is denoted with SIBB. The system is portrayed in a non-equilibrium state. (e) System is in equilibrium. Figures (d) and (e) from ref.[191]

Notably, having any type of surface-localized charge imbalance with respect to the bulk of the material can result in the perturbations in the electronic structure of semiconductors, leading to possible errors in the experimental estimation of the TIBB.[192] For instance, the dangling bonds of exposed surface atoms which host an electron pair, form an electronic state usually within the band gap of the semiconductor. To exemplify this scenario and its correlation with TIBB, the band diagrams in Figure 2.8d,e are presented. Here, the same tip and p-type semiconductor system as in previous panels is shown, but with the semiconductor having midgap surface states which are half filled. Because the semiconductor doping is of p-type, its Fermi level will be located close to VB. This energetic position is much lower than the surface Fermi level, signifying that the system is in the disequilibrium state (inset d). To retain charge balance the electrons will transfer from the surface to the bulk, pinning the Fermi level midgap and causing further downward band bending, as demonstrated in the inset (e).[191] However, depending on the material an opposite effect can occur, in which the TIBB will be reduced by having large amounts of surface states, i.e. available charge to screen the electric field produced by the STM tip. Altogether, the conclusion can be drawn that special care must be taken when interpreting the STS data for even the simplest semiconductor samples, since practice has shown that the technique itself can be electronically intrusive.[192]–[194]

2.4.2 STM and STS on colloidal nanocrystals

In the following the same point from the previous section will be again addressed, but for the generic case of colloidal nanocrystal-based samples.

2.4.2.1 Locating and identifying the colloidal nanocrystals on the surface.

To ensure the best efficiency of the experiment, it is crucial to attain the optimal density of the nanocrystals deposited on the substrate (ideally, 1-10 per 500 nm²) during the drop-casting procedure. Having the bottom limit is obvious for the above stated reason, but it is also just as imperative to define the top one. Indeed, very high densities of nanocrystals deposited on the substrate can introduce couple of issues: higher probability for the STM tip to become contaminated, lesser number of suitable zones on the substrate for tip-forming maneuvers, and difficulties in finding an isolated nanostructures. The last is especially important for the spectroscopy, as having tip-nanocrystal junction on one side, and nanocrystal-substrate on the other is the only way to have true information about their electronic nature, which may not be the case if they are clustered together. Another problem is tied to the fact that the nanocrystals are generally exceedingly small and have their surfaces completely covered with ligands. Regardless of the set measuring mode, if the electric field induced by the STM tip is potent enough it can certainly push the nanocrystals away. However, reducing tip influence by lowering the feedback parameters will increase the likelihood of its interaction with ligand molecules. It is possible to clean and completely recover the tip with field emission and controlled contacting with the metallic substrate. Yet, this is to be avoided, since it can be a very time-consuming process, and not always with a successful outcome. Hence, to minimize the deleterious effects, assessing the polarity and the “just right” value of the applied voltage becomes crucial.

2.4.2.2 Performing STS measurements on colloidal nanocrystals.

Even when everything is done properly, i.e. the single nanocrystal is located and identified, the tip positioned and stabilized, and the STS data acquired with adequate statistics, it is likely that its follow-up interpretation may not be straightforward. If not thermally or chemically pre-treated, it is expected for the colloidal nanocrystals to be passivated with ligand molecules, effectively forming a mostly homogeneous dielectric shell. If the shell thickness is comparable to the tip-sample tunneling distance, the system is best described with a double-barrier tunneling junction (DBTJ) model (shown in Figure 2.9).

In this model, the tip-nanocrystal and nanocrystal-substrate junctions can be portrayed as two parallel-plate capacitors connected in series, with their respective values of capacitance C_{TN} and C_{NS} . Hence, the potential drop across each junction can be expressed as:

$$V_{TN} = V_{\text{bias}} \frac{C_{TN}}{C_{TN} + C_{NS}} \quad (2.34)$$

for the tip-nanocrystal junction, and

$$V_{TN} = V_{bias} \frac{C_{NS}}{C_{NS} + C_{TN}} \quad (2.35)$$

for nanocrystal-substrate one, where V_{bias} is the applied bias voltage.[195]

For each junction, the capacitances are:

$$C_{TN} = \frac{\epsilon A}{d_{TN}} \quad (2.36)$$

$$C_{NS} = \frac{\epsilon A}{d_{NS}} \quad (2.37)$$

, respectively. Here, A is the area of the capacitor, ϵ is a dielectric constant, d_{TN} is the distance between the tip and the nanocrystal and likewise, d_{NS} is the physical gap between the nanocrystal core and the conductive substrate. The STS voltage sweeps entail lifting and dropping of the tip Fermi level in energy.

As long as its energetic position is within the band gap of the nanocrystal, no tunneling current will flow. However, once it becomes resonant with either CB or VB states of the nanocrystal, the probability for electrons (holes) to tunnel across the nanocrystal to the substrate becomes favorable.

Let us first consider a scenario in which the nanocrystal is passivated with short-chained ligands. In this geometry the noteworthy condition is that the nanocrystal-substrate distance is significantly smaller than the tip-nanocrystal one, as shown in Figure 2.9a. Therefore, the value of C_{TN} will be much smaller than C_{NS} . Moreover, as a result of significant variation in tunneling resistances between the two junctions, the electron tunneling rates from the tip to nanocrystal (Γ_{in}) and from nanocrystal to the substrate (Γ_{out}) will also be different.

In specific, Γ_{in} will be much smaller than Γ_{out} hence, the DBTJ system will be devoid of any charging effects, because no more than one electron will be added to the nanocrystal at any given time. This is better known as shell-tunneling.[196] In other terms, the potential drop across tip-nanocrystal junction will be far more substantial when compared to nanocrystal-substrate one, hence the DBTJ can be described with having an asymmetric character.

To estimate the extent of this effect, the ratio of potential drop and the applied bias voltage can be expressed as:

$$\eta = \frac{V_{TN}}{V_{bias}} \quad (2.38)$$

and is defined as the lever-arm. In Figure 2.9b, one STS voltage sweep is represented in the form of energy diagram for the shell-tunneling case, where the lever-arm is very close to 1.

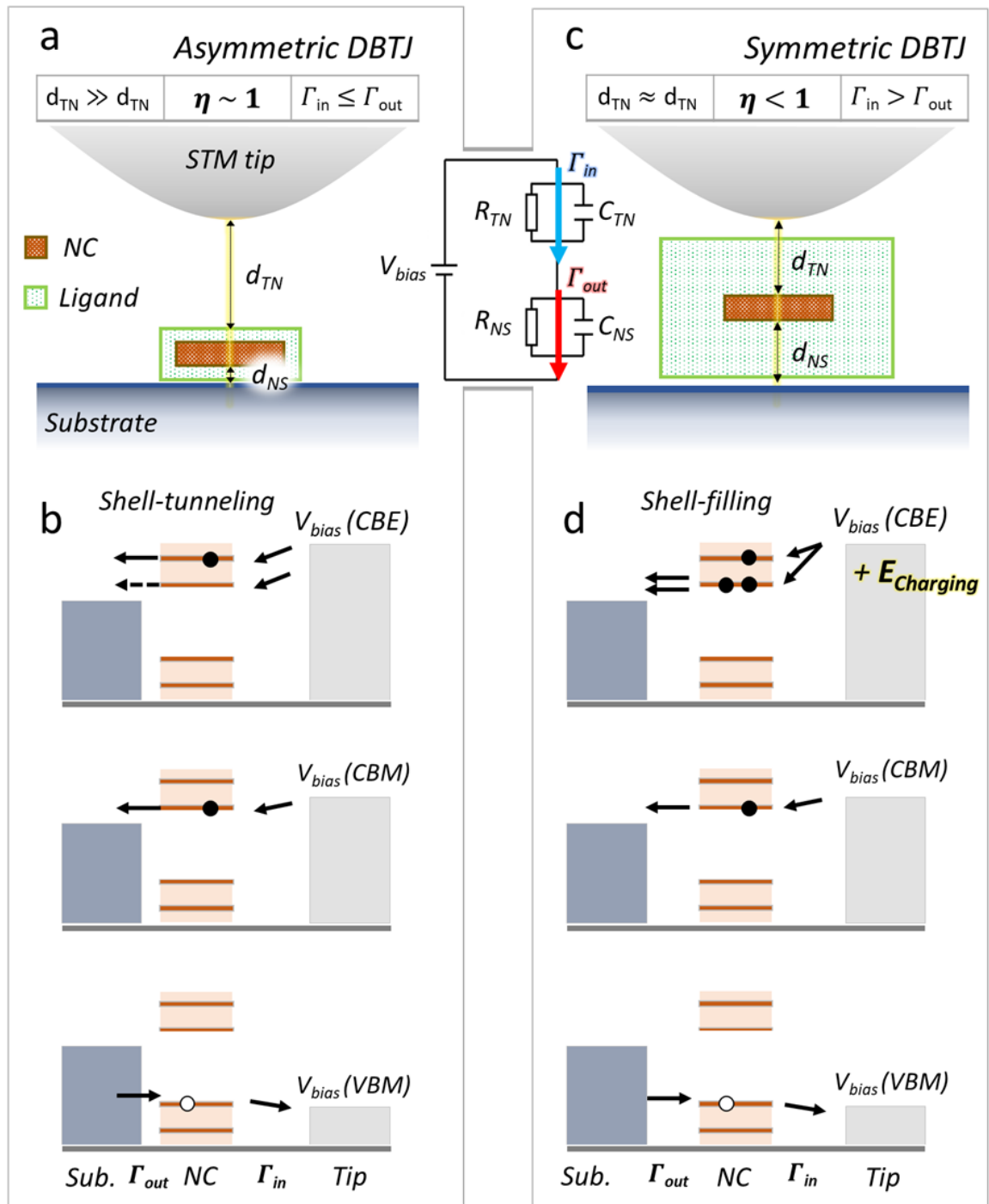


Figure 2.9 Scanning tunneling spectroscopy on colloidal nanocrystals. (a) The schematic depiction of the asymmetric (left) and symmetric (right) double-barrier tunneling junctions. Inset in the middle is

block diagram representation of the DBTJ. Figure inspired by the topical review of Swart et al.[195] Energy diagrams showing charge transport in the systems where lever-arm is (b) $\eta \sim 1$ and (c) $\eta < 1$. Figures taken and adopted from the ref.[197] Notation: $d(R,C)_{NS}$ and $d(R,C)_{TN}$ are nanocrystal-substrate and tip-nanocrystal distances, resistances and capacitances, respectively; Γ_{in} and Γ_{out} are electron tunneling rates, and in their respective order, VBM, CBM, CBE are valence band maxima, conduction band minima and excited energy level in the conduction band. Small, filled circles stand for electrons and empty ones for holes.

In this layout, the carrier transport through first hole level (VBM), first electron level (CBM) and first electron excited state (CBE) is governed in the one-by-one manner:

$$\eta eV_{bias} = E_{CBM} + \Sigma_{e1} \quad (2.39)$$

$$\eta eV_{bias} = E_{CBE} + \Sigma_{e2} \quad (2.40)$$

$$\eta eV_{bias} = E_{VBM} - \Sigma_{h1} \quad (2.41)$$

Here, Σ_{e1} , Σ_{e2} , and Σ_{h1} are first electron, second electron, and first hole electrostatic polarization (charging) energies, respectively. This quantity is correlated to the addition of a single charge into the nanocrystal. As a result, when the bias voltage is applied, the energy levels of the probed nanocrystal will be shifted a bit with respect to their zero-bias position. From here, the width of the apparent STM band gap (V_G^{STM}) can be expressed as:

$$\eta eV_G^{STM} = E_{CBM} - E_{VBM} + \Sigma_{e1} + \Sigma_{h1} \quad (2.42)$$

Since polarization energy does not depend on the exact shape of the wavefunction, one can assume values for the electron and hole are more or less the same:

$$\eta eV_G^{STM} \approx E_{CBM} - E_{VBM} + 2\Sigma \quad (2.43)$$

To summarize, in the absence of charging and for the case of asymmetric DBTJ, the acquired spectra should give out accurate information about the nanocrystal electronic structure (width of the band gap, level spacing, etc.), since individual electrons and holes will contribute to the tunneling current by tunneling through CB and VB states of the nanocrystal, respectively. However, this is not always the case. In Figure 2.9c, the schematic of symmetric DBTJ is shown. We assume the ligands are much longer than in the first case causing the capacitance for each junction to be comparable, due to weaker coupling of the nanocrystal with the substrate. The same can be said for tunneling resistance, which will also reflect on tunneling rates with now, Γ_{in} being similar to Γ_{out} . This scenario is an ideal platform for the shell-filling carrier transport to take place, which can affect both the measured width of the band gap, but also supra-gap level spacing. For the first injected electron, nothing will change with respect to shell-tunneling regime. However, due to the tunneling rates defined above, the second electron is added before the first one managed to escape the nanocrystal. For this reason, an additional electron-electron repulsion term (J_{e-e}) needs to be considered for each other carrier:

$$\eta eV_{bias} = E_{CBE} + \Sigma_{e1} + J_{e-e} \quad (2.44)$$

Due to the less stable nature of the symmetric DBTJ and strong charge screening by the tip, one could expect the lever-arm to decrease even as far as 0.5, which can cause the tunneling of electrons (holes) on both sides of the zero-conductance region. This implies that experimentally measured band gap no longer coincides with the real HOMO-LUMO gap. Instead, for example of electron tunneling on both sides, the apparent STM gap will be:

$$V_G^{\text{STM}} = \frac{1}{\eta(1-\eta)} (E_{\text{CBM}} + \Sigma_{e1} - E_F) \quad (2.45)$$

where the E_F is the Fermi level. While for the hole tunneling:

$$V_G^{\text{STM}} = \frac{1}{\eta(1-\eta)} (E_{\text{VBM}} + \Sigma_{h1} - E_F) \quad (2.46)$$

Even though the above discussed effects introduce lots of difficulties in interpreting STM data, at least they are experimentally identifiable, by performing subsequent STS cycles with increasing/decreasing values of setpoint current, with the aim of altering the tip-nanocrystal distance.

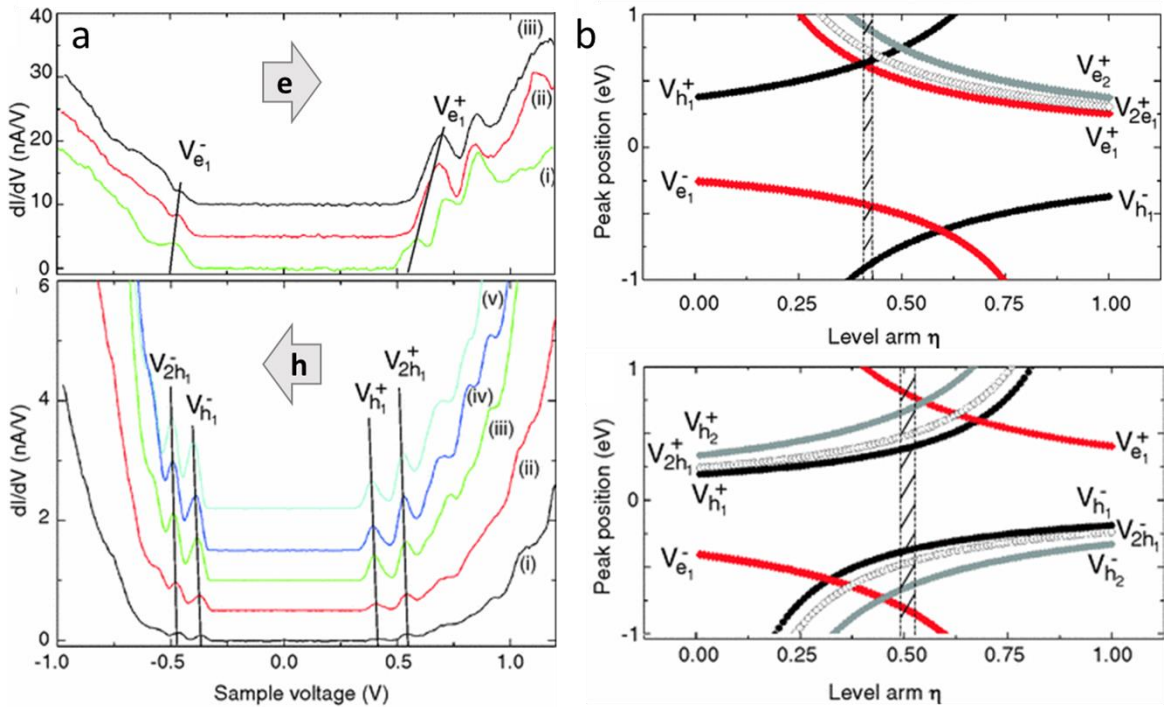


Figure 2.10 (a) Sets of differential conductance spectra acquired at different values of setpoint current on two different colloidal PbSe/CdSe nanocrystals, where the contribution to the tunneling current at both negative and positive voltages is given solely by the electron (top) and hole (bottom) ground states. (b) Variation of the peak position as function of the lever-arm, for the case shown in (a), in their respective top-to-bottom order. The shaded regions correspond to the measured range of lever-arms in (a). Figures taken and adopted from ref.[198]

This was well demonstrated by Nguyen et al. [198] on colloidal PbSe/CdSe colloidal nanocrystals. Some of the examples from this study are presented in Figure 2.10. In (a) panel, two different sets of differential conductance spectra taken with increasing values of setpoint currents are presented, where DBTJ was symmetric with the value of lever-arm around 0.5 in both cases. Following the peak evolution throughout the cycles, their shifts to higher absolute values of positive (top) and negative (bottom) voltages becomes evident. As a result, one could identify the former trend as a consequence of electron ground state contribution to the tunneling current on both positive and negative values of sample voltage, whereas for the latter this role is taken by the hole ground state. Taking the peak positions from the experimental data for a given value of lever-arm and with further extrapolation using Eq. (2.45) and Eq. (2.46) valuable trends as shown in Figure 2.10b can be obtained.

2.5 The Omicron VT four-probe STM

As it was described in the previous sections, a conventional single probe STM is a particularly useful tool in nanotechnology, as it is capable of imaging the topology and local electronic structure of various conductive samples. Unfortunately, its characterization-based functionality largely ends there. However, expanding upon it can be as simple as just adding another probe. With two probes, it is possible to measure the local lateral electrical conductivity of the sample by utilizing each one as a contact electrode. One such study which I conducted can serve as a helpful example of the potential benefits and hurdles one could expect from these kinds of experiments. The two-tip measurements were performed on the free-standing core/shell GaAs/SrTiO₃ nanowires with a premise of investigating their electronic properties.

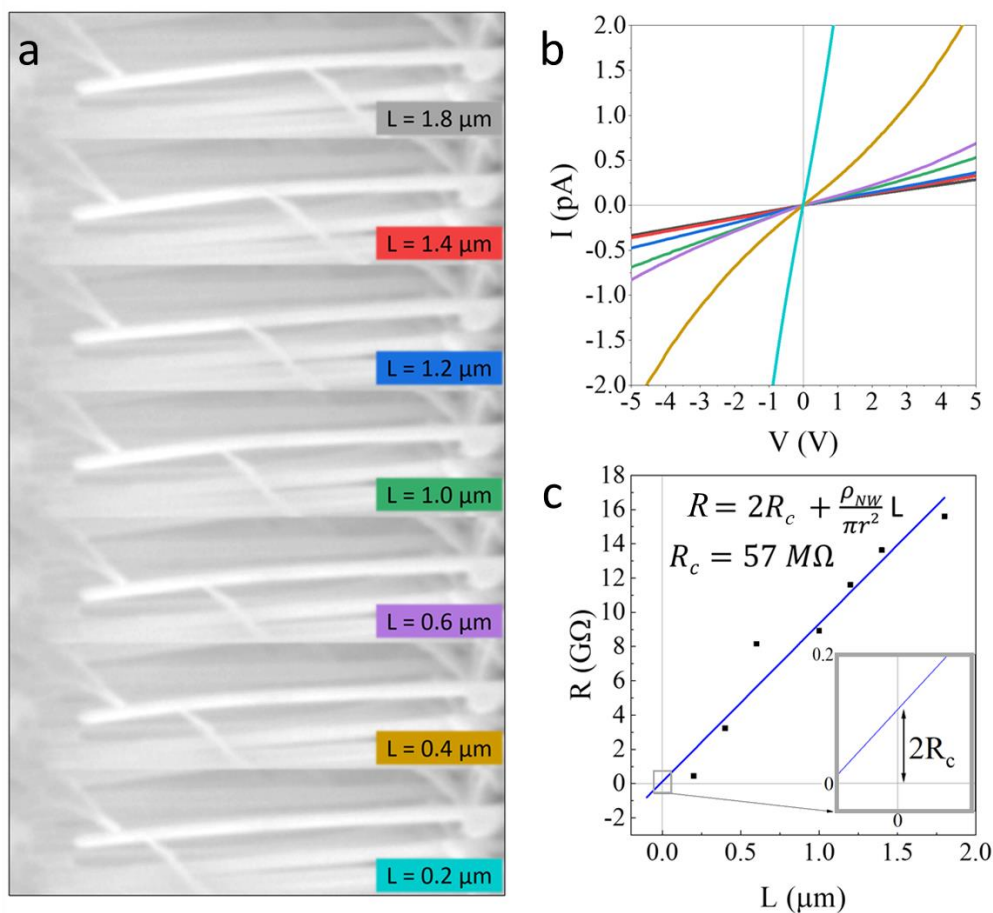


Figure 2.11 Series of scanning electron micrograph SEM images of free-standing GaAs/SrTiO₃ core/shell nanowires, with the brightest nanowire contacted with two W tips. The distance L between the STM tips is indicated in each frame. (b) I(V) curves measured for the different tip spacings shown in (a). (c) Resistance R measured from the I(V) measurements as a function of L. R_c, r and ρ_{NW}

correspond to the contact resistance, the radius of the nanowire and the nanowire resistivity, respectively. Inset: Close-up view of the intercept of the fitted $R(L)$ line with the y -axis to determine R_c .

Without going too deep into details concerning the study itself, the results which are presented in Figure 2.11, clearly showcase the potential of the dual-probe measurements. With a possibility of moving each of the tips freely, they could be positioned at any place along the nanowire (see Figure 2.11a). Once a good contact is established the $I(V)$ characteristics of the nanowires is probed (as in Figure 2.11b). With the transfer length method, one obtains the total resistance of the nanowire with respect to the probe separation. However, in this configuration the contact resistance plays an important role. It is estimated from the intercept of the fitted line with the y -axis (Figure 2.11c). Still, it is worth pointing out that for some experiments the contact resistance can induce some unnecessary ambiguities. This can be avoided by completely eliminating its effect with a four-probe STM system.

The reason why this works is that the current injecting circuit is separated from the voltage sensing one, as illustrated in Figure 2.12. Hence, if the internal resistance of the voltage sensing part is exceedingly high, the influence of the contact resistance becomes insignificant.[199] Once the four-probe resistance (R_{3D}^{4P}) is obtained by dividing the measured potential drop by the injected current, the resistivity (ρ_{3D}) for the bulk materials can be further extracted. In its simplest form (for the ideal infinite-sized bulk material with four equally spaced and in-line contacts) the relation would be the following:

$$R_{3D}^{4P} = \frac{\rho_{3D}}{2\pi} \frac{1}{s} \quad (2.47)$$

However, as there are multiple spatial configurations (linear equidistant, linear non-equidistant, square, or even arbitrary) in which these measurements could be done on different sample geometries (3D, 2D and 1D) the expressions become more complex and specific. For our studies, these particularities will be discussed on a concrete case in the third Chapter.

The multi-probe STM used for transport measurements in this work was the Omicron Nanoprobe system and it is located at the IEMN, Villeneuve d'Ascq, Lille. As it can be seen from the picture in Figure 2.13a, the system is comprised of two main chambers, which have lots of analogous functionalities to the single-probe LT-STM described above.

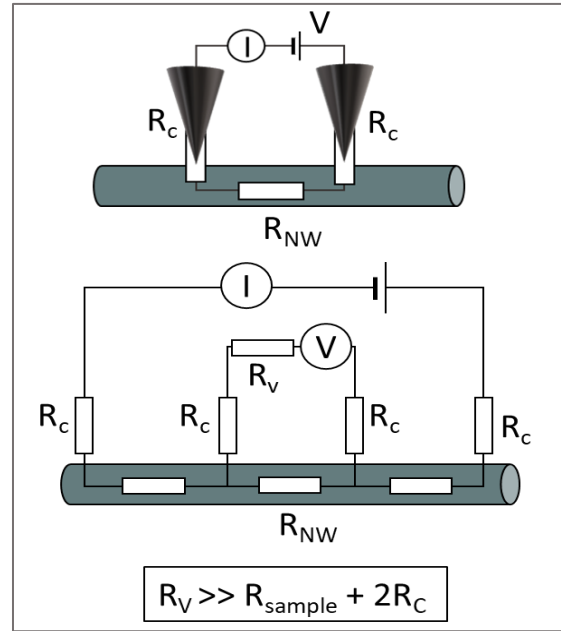


Figure 2.12 Top: Schematic representation of the two-probe resistance measurement. Bottom: Four-probe configuration for measuring resistance without any influence of the contact resistance. Figure taken and adopted from ref. [199]

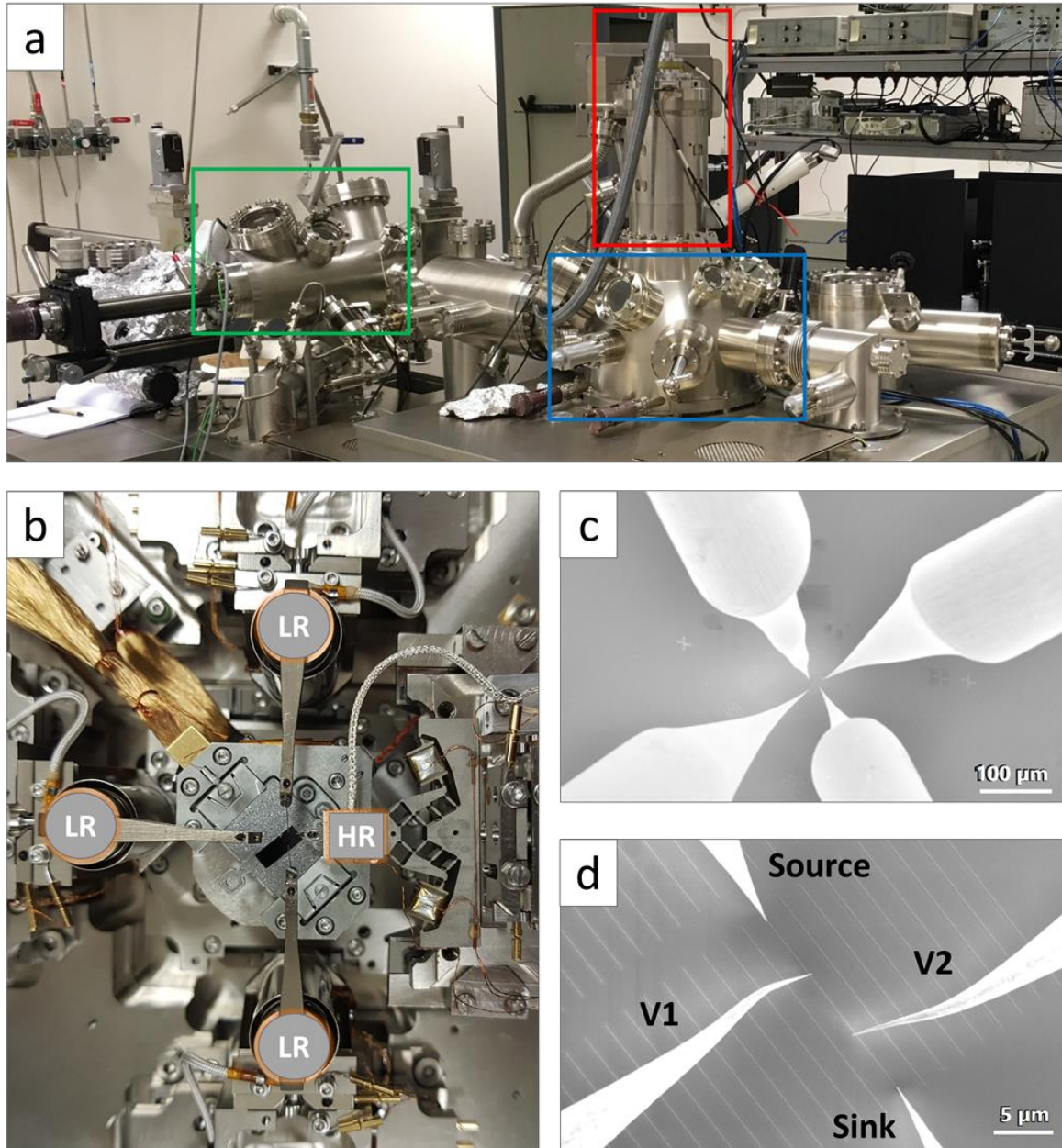


Figure 2.13 Omicron Nanoprobe four-probe VT-STM system. (a) The picture of the entire instrument with its main segments highlighted in green (preparation chamber), blue (analysis chamber) and red (SEM column). (b) Inside the analysis chamber. The sample (black rectangle in the center) is surrounded with four STM tips, out which three are low-resolution and one is high-resolution (HR) tip. (c) SEM image of the four tips above a planar nanowire sample. (d) SEM image of four tips contacting a

semiconductor nanowire in the most common, linear-equidistant configuration, where V_1 and V_2 probes measure the potential drop.

The main similarities are in the UHV environment, mechanical isolation, sample loading systems, tools for sample preparation and storage. However, instead of the cryostats, this instrument has a high-resolution UHV-SEM located just above the analysis chamber. As it is a VT system, the temperature control is achieved with a combination of heating element and cold finger which are in contact with the sample stage, located inside the analysis chamber. The available temperature range spreads from 30 K to 500 K. Another obvious difference is in the number of probes, as this instrument has high-resolution and three low-resolution probes (see Figure 2.13b,c). Each one possesses STM/STS capabilities and can be moved independently from one another. This allows for the tips to be navigated with the SEM and positioned in spatial configurations such as the one shown in Figure 2.13d. This is a prototypical example of the four-probe measurements done on planar nanowires. Here, the two tips which are in electrical contact with far ends of the nanowire are used as source and ground electrodes for driving the current through it, whereas the two inner tips act as potential probes. When a current is passed through the nanowire, the potential drop is measured. The gradient of the obtained I-V curves yields the four-probe resistance of the nanowire for a given separation between the inner probes. By moving the probes toward the center of the nanowire, a set of measurements for different tip separations is acquired. The probe movement is limited only by their size. In practice, with very sharp tips it is possible to achieve probe separation of around 100 nm. In addition, the precision with which these tips can be operated allows for establishing light and stable contacts with the samples. As a result, this technique far surpasses the traditional transport measurements based on contact deposition in three important areas: non-invasiveness, operation cost and flexibility.

2.6 Complementary techniques

In the following the two main complementary techniques used for the development of this thesis will be discussed. These include room-temperature atomic force microscopy and variable-temperature optical spectroscopy with and without applied magnetic field.

2.6.1 Atomic force microscopy

The atomic force microscopy (AFM) is one of the oldest techniques in the family of scanning probe microscopies.[200] In similarity to STM, it also utilizes sharp metallic tips and has capability to map the topography at the nanoscale, but with one big advantage. AFM can work with non-conductive samples, a particularly useful ability which originates from its design and working principle. The tip is attached to a spring-like cantilever which interacts with the surface of the samples. Depending on the tip-sample distance this interaction can be either repulsive or attractive, most commonly linked to van der Waals, electrostatic or capillary forces.

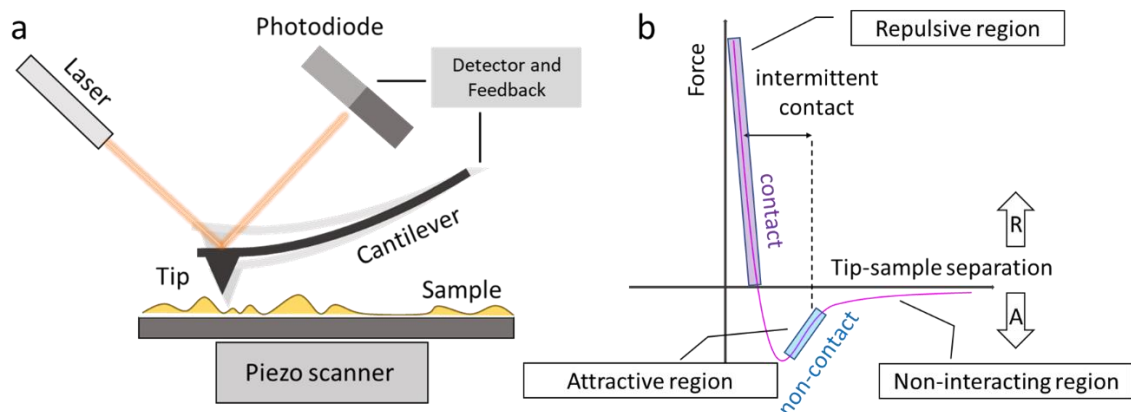


Figure 2.14 The working principle behind AFM. (a) Main parts comprising a conventional AFM system. (b) Illustration of a typical force-separation curve, where R and A arrows represent the directionality of the repulsive and attractive force.

Assuming the case in which the first is dominant and where the tip is far from the sample, the cantilever is not affected by interatomic forces and is in its free equilibrium position. Bringing the tip closer to the sample the attractive force will deflect the cantilever downwards until reaching the point of contact. Once in contact, the tip feels the repulsive forces which deform the cantilever in the upward direction. In other words, the cantilever acts as a force sensor. Any change in motion of the cantilever is tracked using the laser, which is focused on its far end, close to the tip. The incident laser beam is reflected off the surface of the cantilever, effectively mirroring any deflection caused by tip-sample interaction.[201] A position sensitive detector is used to record these variations, while the feedback loop is used to maintain a predefined setpoint parameters. The three-directional piezoelectric scanner is used to

control the movement between the sample and the tip. Bending of the cantilever which is recorded by the photodetector is converted into an electrical signal and processed into a topographical image. Among many, there are three main operational modes of the instrument. These are classified according to the separation between the cantilever and the surface, and the cantilever's oscillation amplitude. In specific, the contact, non-contact, and intermittent contact modes. In their respective order, first involves the tip "touching" the sample, i.e., the distance tip-sample is lower than the average size of an atomic radius, for the next the tip-to-sample separation is larger than 5 nm, and in the last a forced oscillation is applied to the cantilever at a frequency close to the resonant one. The oscillation is maintained by a feedback loop and any deviation of the frequency is used to map the surface.

Most of the commercially available AFMs are multi-scale instruments, as their dynamic range spreads from micrometric to sub-nanometric scale.[202] Regarding the vertical resolution, the instrument is mainly limited by the thermal noise of the deflection detection system.[203] The resolution can be estimated using the following expression:

$$\Delta z = \sqrt{\frac{4k_B T}{3k}} \quad (2.48)$$

Where B is the Boltzmann constant, k the spring constant of the cantilever, T the absolute temperature. For a free cantilever of $k = 1 \text{ N/m}$ and at room temperature this corresponds to 0.074 nm. Regarding the lateral resolution it is given by the minimum detectable distance between two sharp spikes of different heights:

$$d = \sqrt{2R}(\sqrt{\Delta z} + \sqrt{\Delta z + \Delta h}) \quad (2.49)$$

With d being the lowest detectable distance, R the radius of curvature of the tip (R) and Δh the small height difference between the spikes. From the expression above it is clear that the lateral resolution mostly depends on the quality of the tips. Therefore, the main technical challenge is to obtain as sharp as possible probes, without compromising their rigidity. The tips which were used in our experiments usually did not exceed the apex larger than 20 nm, allowing us to have a resolution of just a few nanometers for mostly flat samples.

The AFM which was used in this thesis was the Veeco Dimension 3100. The high-resolution, non-invasiveness and overall convenience of the work in atmospheric environment made this instrument an ideal tool to study the morphology of both the colloidal nanocrystal-based samples and epitaxial nanowire samples.

2.6.2 Optical spectroscopy

From the very beginnings of nanoscience, the luminescence-based spectroscopy has been an indispensable tool for the characterization of semiconductor nanostructures. This is also true within the context of this thesis since performing measurements in the UHV environment is an expensive and time-consuming process. In contrast, the main appeal of the optical spectroscopy lies in its time- and cost-effective, non-invasive, and fundamental nature. Concerning the last, due to its operating principle, it is inherently capable of giving valuable insight into the electronic structure of the luminescent materials. Inducing excitation/emission cycles can be done in a number of ways, yet for the case of semiconductor nanostructures, the most common approach is photoluminescence.[204] This method entails that the material is excited with light of higher energy than its band gap energy. The whole process is best described in three steps, excitation, thermalization and recombination. The excitation stimulates the formation of electron-hole pairs, a consequence of electrons absorbing the energy of the incident light. Subsequent carrier relaxation within their respective bands is called thermalization and it occurs through emission or absorption of phonons, thus establishing a quasi-equilibrium distribution of electrons and holes.[205] Now thermalized electrons and holes can recombine either in a radiative or non-radiative manner. In the outcome when a carrier relaxation is necessitated with the emission of a photon, its characteristics can be causally linked to the material properties (width of the band gap, crystal quality, purity, etc.). There are a couple of most prevalent routes the excited electron can take during the recombination. In pure and direct band gap semiconductors, one could expect a radiative band-to-band transition, whereas for the case of indirect band gap materials the photon emission will be aided by phonons, responsible for momentum conservation.[206] However, if the system contains impurities (dopants, defects, foreign atoms) the recombination can be mediated through in-gap states.

By and large, the investigation of optical properties relies on the analysis of excitonic complexes which define the emission of a given sample. A common methodology used for the identification of the excited states is to perform optical studies in the magnetic field. Depending on the orientation of the magnetic field with respect to the wave vector of the light (k), the system can be portrayed of being in one of the two magneto-optical geometries: Faraday and Voigt geometry.[207] In the first one, the light propagates along the direction of the magnetic field, whereas in the second the trajectory of the light is perpendicular to it. This classification is based on the differences in the eigen-modes of the propagation state of the passing light through a given medium. In practical terms, the specific effects of each geometry can be demonstrated by the setup illustrated in Figure 2.15. In Faraday geometry, the light which passes through the linear polarizer enters the medium which is longitudinally magnetized ($B_{||}$). The linearly polarized light is a superposition of left- and right-circularly polarized components, however, once it enters the medium the magnetic field induces the inequalities in propagation velocities between the two.[208]

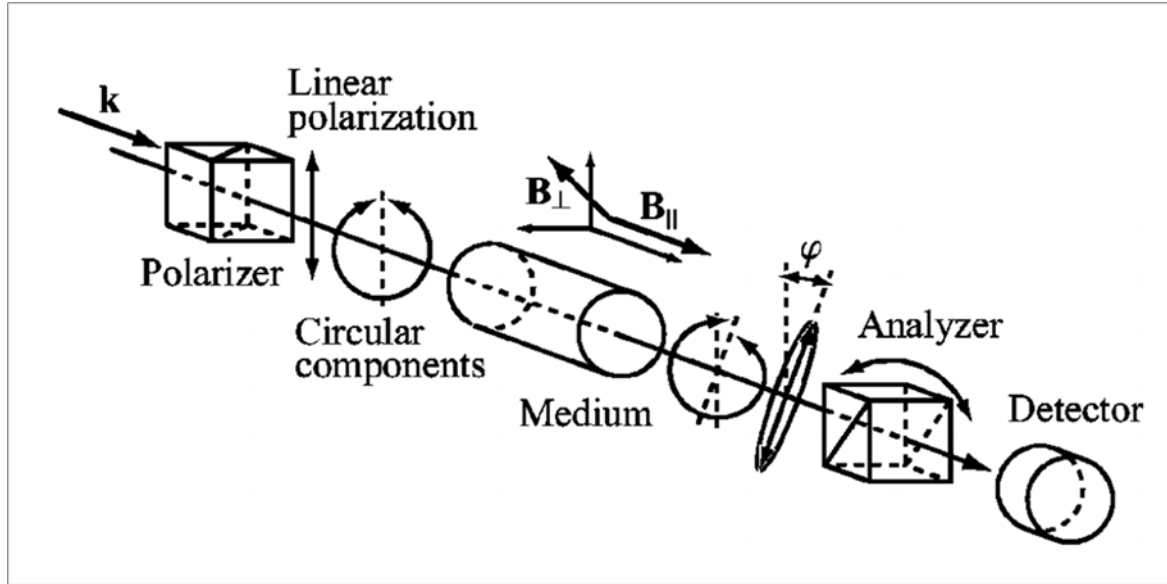


Figure 2.15 Schematic illustrating the effect of magnetic field on the light passing through medium in a Faraday and Voigt geometry. Notation: k is the light wave vector, ϕ is the angle of rotation of the polarization, B_{\parallel} and B_{\perp} are longitudinal and transverse magnetic fields, respectively. Figure extracted from ref.[207]

The resulting phase shift between two circular modes causes the light leaving the medium to have the plane of polarization rotated (ϕ) with respect to the original direction.[209] The intensity of the output light with specific polarization (depending on the orientation of the polarizer with respect to the analyzer) is measured. Whereas for the measurements of the Voigt effect, the external magnetic field is rotated by 90° (B_{\perp}) with respect to the Faraday case, which causes the magnetic linear dichroism of the light. The components of the incident light which are parallel to the direction of the magnetic field remain unaffected, while the orthogonal linearly polarized components are experiencing differential absorption and phase shifts, responsible for the optical rotation and induced ellipticity of the exiting light.[207]

Since the simple notion “the stronger the magnetic field, the stronger the effect” is valid for both geometries, the Florida-Bitter electromagnet at the High Field Magnet Laboratory in Nijmegen (see Figure 2.16a) was used for magneto-optical experiments during the development of this thesis. The magnet has a 32-mm bore and is capable of reaching 37.5 T, by consuming 20.5 MW of power at 40 kA.[210] Being a resistive and not a hybrid magnet design, such high magnetic field is achieved by stacking five Florida-Bitter coils (CuAg) and one outer 1 m-wide Bitter coil (Cu), as shown by the 3D schematic in Figure 2.16b. The length of this coil is around 670 mm and it weighs close to 3000 kg.[211] The samples is mounted on the titanium sample holder which rests on the three-axis piezo-positioner (Attocube) and placed onto optical probe made of titanium and carbon. Next, the probe is placed into liquid helium bath cryostat and secured inside of the magnet.

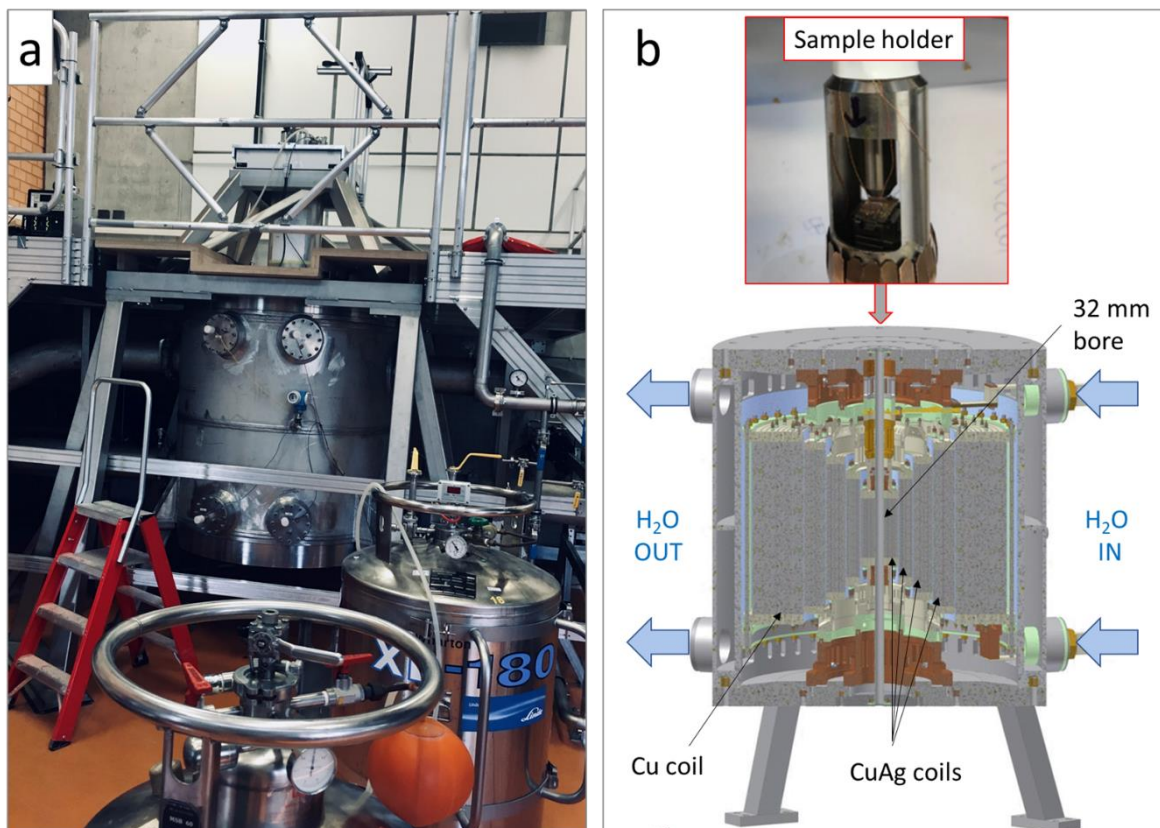


Figure 2.16 37.5 T Florida-Bitter electromagnet located at High Field Magnet Laboratory in Nijmegen. (a) The picture of the magnet. (b) 3D schematic of vertical cross-section of the magnet showing the housing incorporating the coils and the structural elements. Figures taken and adopted from ref.[211], [212]

The instrumental setup for the optical part of our magneto-optical experiments was quite similar to the one provided in the ref.[213] For non-resonant excitation measurements, the NPLs were excited using a pulsed diode laser with a weak average excitation power density $<0.02 \text{ W cm}^{-2}$. The PL detected in backscattering geometry was filtered from the scattered laser light with a 0.55 m spectrometer and detected either by a liquid-nitrogen-cooled charge-coupled-device (CCD) camera or by an avalanche Si-photodiode. For polarization-resolved measurements, PL was analyzed by a combination of a quarter-wave plate and a linear polarizer. The excitation and detection of the light was guided through a lens and filter system to the sample and the photoluminescence is sent back to the measurement system.

Chapter 3. Morphology and electronic structure of SAG InGaAs nanowires

3.1 Introduction

The interest of society for advancement into the technological era of quantum information had a major impact on accelerating the fundamental research in the field of semiconductor nano-heterosystems. The development of functional quantum information-based devices such as quantum computers and quantum communication systems requires fabrication and manipulation of the materials to be done at the atomic scale, where quantum mechanical effects are ever-present.[214] Nowadays and for this function, the advances in various crystal epitaxy growth operations have made the nanoarchitecture and nanofabrication a reproducible and flexible process. Among plethora of techniques which fit in this category, selective area growth method certainly stands out, as it offers a fine composition, dimension, and orientation control of the end nanostructures.[123], [215]–[219] Hence, in this work we exploit all three of these degrees of freedom to create an ideal playground to study fundamental properties of nano-heterosystems.

Among countless of possible geometries, nanowires have caught our interest, since their 1D shape offers improvements in material quality and consequently, future device performance.[220]–[223] As it was highlighted in the first chapter, this can be accredited to relaxation of elastic stress through nanowire sidewalls, which in return will reduce density of structural defects in lattice-mismatched heterosystems. Moreover, as an added advantage, with selective area growth it is possible to precisely define nucleation sites within the mask cutouts mirroring the predesigned patterns, effectively overcoming position and orientation randomness commonly associated with other nanowire growth methods.[224] Regarding the material preference, III-V compound semiconductors present themselves as a straightforward choice, mainly due to their ease of integration with Ge or Si substrates without lattice or thermal expansion induced mismatch.[219] In particular, we have opted for the material combination of InGaAs and InP, since over the decades of intense research, it has been recognized for its potential applicability in highspeed electronics and optical communication systems, due to high electron mobility and optical band gap of 1.3 – 1.6 μm , inherent to its resulting heterostructures.[225] However, to take a full advantage of these outstanding optical and electronic properties and bring them towards engineering and fabrication of future quantum devices, it is crucial that one has a good understanding of the underlying processes at the heterointerface from which those characteristics originate. For instance, the information concerning the valence and conduction band offsets.

Defined by the band alignment between two different semiconductor materials which comprise a heterostructure, the band offsets can be portrayed as a discontinuity among their respective band edges at the interface. In general, the band alignment in semiconductors is classified into type-I, type-II, and type-III. Starting from the first, the band gap of one semiconductor completely incorporates the band gap of the other. Whereas for Type-II, the gap overlaps between the two exists, but it is not complete.

And finally, in the case of Type-III the gap overlap in energy is not present at all. However, accurate determination of band offsets is still not straightforward. This becomes quickly apparent if one reflects on the present literature, as the extensive comparison between experimental data acquired across various techniques and theoretical predictions reveals major inconsistencies among the reported values for band offsets for many heterosystems, including InGaAs / InP ones. Thus, the task of device designing based on heterojunction engineering requires a more reproducible characterization approach to be established.

For this purpose, we have engaged scanning probe microscopy to study InGaAs nanowires selective area grown on the p-type doped InP (001) surface. With the use of single-probe low-temperature scanning tunnelling microscope (LT-STM) we started by focusing on the topography of the nanowires. This study included thorough investigation of the surface reconstruction on both nanowire top and side facets. With the heterointerface being so sensitive to the even slightest changes of chemical and physical parameters that define it, understanding the relation between the shape of the band offsets between two dissimilar semiconductors and the heterointerface morphology is essential. For this very reason, we have addressed the nanowire growth mechanics by complementing our work with a large-scale AFM study. And lastly, by combining the low-temperature single- and multi-probe scanning tunnelling spectroscopy (STS) with the two-tip and four-tip transport measurements we have managed to accurately determine values for both conduction and valence band offsets.

3.2 Sample preparation

The following section describes the technological processes (step-by-step schematic in Figure 3.2) behind the fabrication of $\text{In}_{0.53}\text{Ga}_{0.47}\text{As}$ nanowire-based structures on InP, starting from the initial design created in the LayoutEditor software (see Figure 3.1) all the way up to the “STM-ready” sample. As this process is based on MBE selective area growth method, the formation of the patterned cutouts on the surface was the first step.

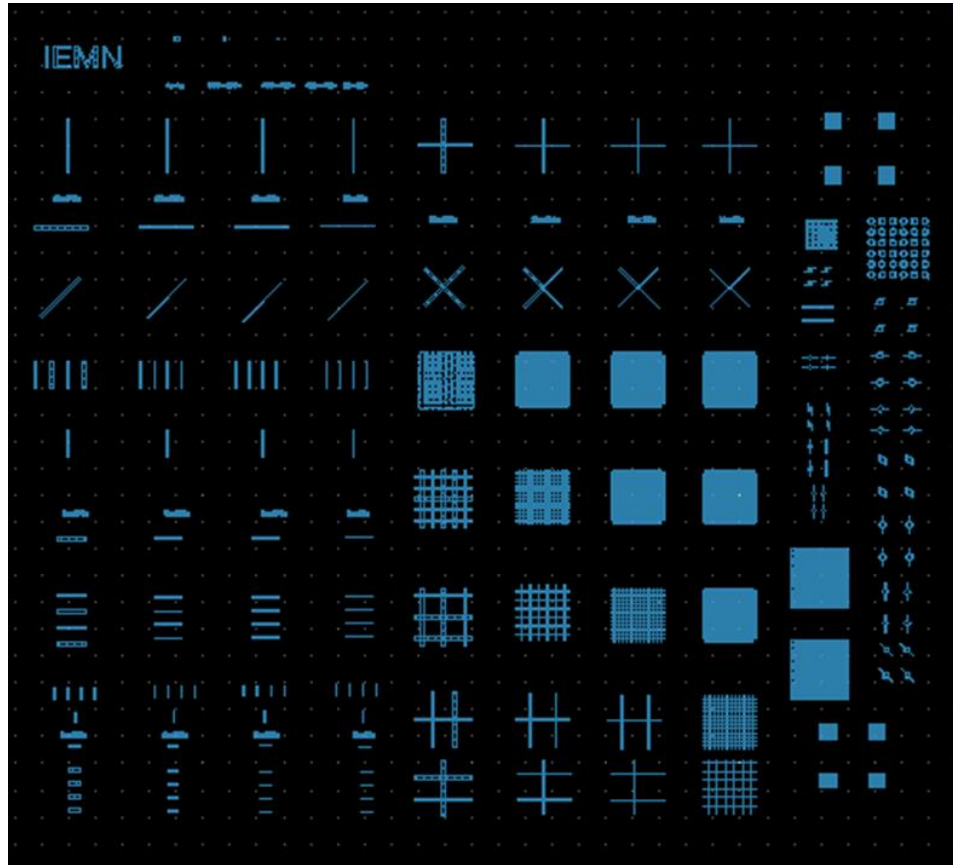


Figure 3.1 Detailed map created in LayoutEditor software showcasing various nanowire-based nanostructures grown for the LT-STM experiments.

This task is accomplished by firstly depositing 30 nm-thick SiO_2 on a InP (001) substrate by plasma-assisted chemical vapor deposition (PECVD) at 300 °C. Once the uniform mask is attained across the whole wafer, it was covered with 100 nm of positive resist by spin coating. In specific, polymethyl methacrylate (PMMA; 495K 3%).

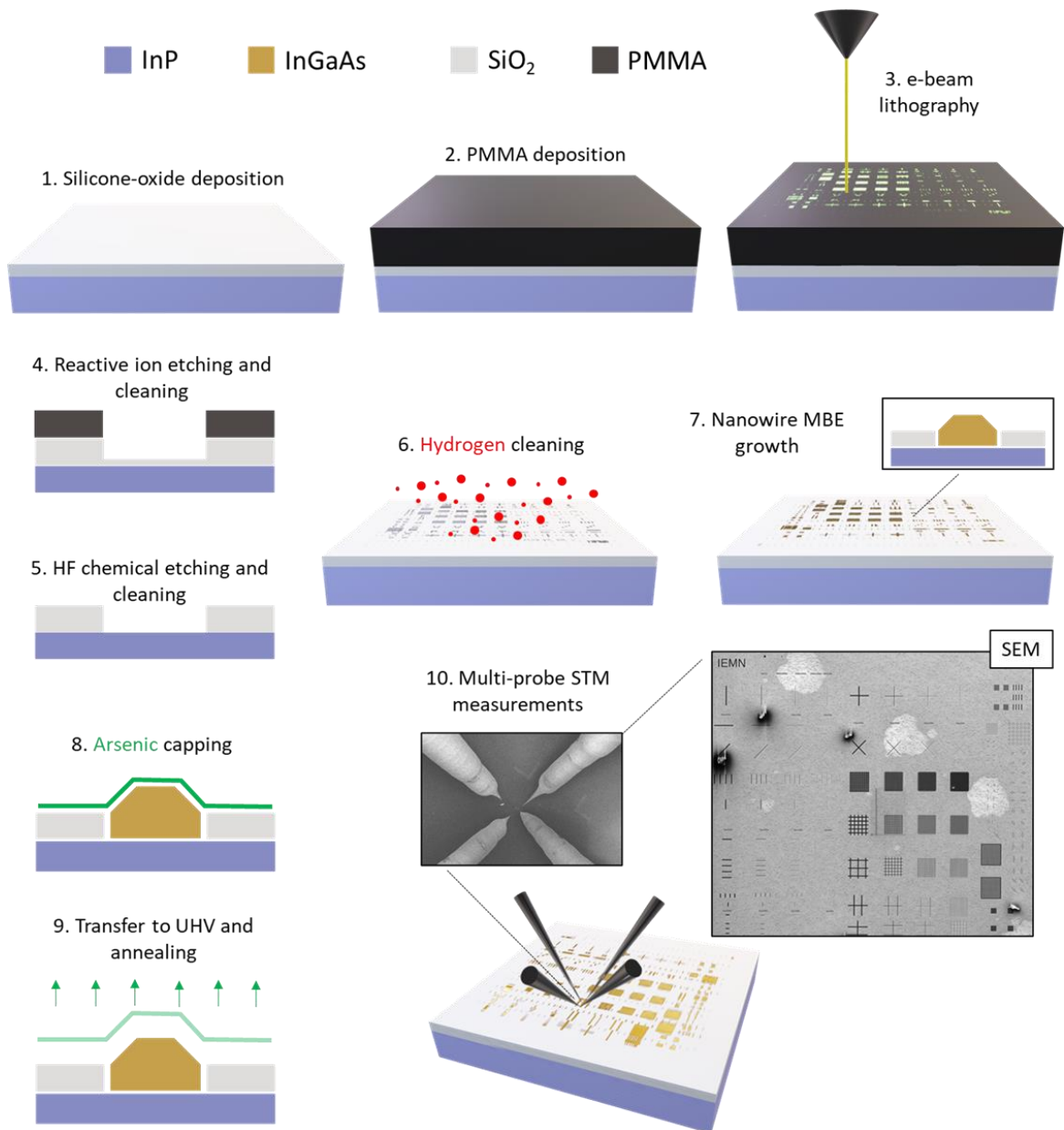


Figure 3.2 Schematic representation of the InGaAs nanowire sample preparation for the follow-up multiprobe LT- and VT-STM measurements presented in eight consecutive steps. Structures are not in scale.

The next step involved the combination of pattern writing with the electron beam and the successive development of the created patterns with the mixture of 30 mL of MIBK (methyl isobutyl ketone) and 60 mL of IPA (isopropyl alcohol) for 90 seconds. After that, the engraved patterns in the resist were transferred onto the mask below by reactive ion etching (RIE). The instrument assigned for this task

was Oxford Plasmalab 80 Plus, while the protocol consisted of the following steps: i) 6 seconds of O₂ plasma to clean the openings in the mask of any resist; ii) the etching of the mask was done with CHF₃ (20 sccm) / CF₄ (20 sccm) / Ar (10 sccm) plasma for 55 seconds with 100 W RF power and a chamber pressure of 50 mTorr; iii) the resist from the mask was removed after 10 minutes of UV exposure, subsequent acetone bath (50 °C) for the same duration and final cleaning with O₂ plasma for 30 seconds. The etching into silicon oxide mask was stopped 20 nm short of InP to avoid exposure of the semiconductor layer to plasma and chemical treatment involved in the follow-up resist removal process. For making the openings go all the way through to the InP surface, chemical etching was used. In this step, the sample was dipped in an 1% concentrated solution of hydrofluoric acid for 30 seconds and then, rinsed with water. At this point, the sample was ready for its transfer to the MBE, as the InP was covered with 10 nm-thick silicon-oxide mask having the desired patterned cutouts. Prior to the growth, the sample was subjected to deoxidation under arsenic and atomic hydrogen flux, while being stabilized at 470 °C. The importance of this step has been recently reported.[126] In particular, it has been demonstrated that hydrogen cleaning of the InP surface has significant impact in increasing the growth selectivity with respect to silicon-oxide mask. Finally, the hydrogen assisted nanowire growth under indium (0.106 ML/s (monolayer per second)), gallium (0.094 ML/s) and arsenic (1 ML/s, corresponding to V/III ratio of 5) flux was initiated. For the exact growth conditions please refer to the work done by Alexandre Bucamp.[131] To protect the sample from oxidation during its transfer to the STM system it was capped with around 20 nm of arsenic. Once inserted into ultra-high vacuum this protective layer was removed by annealing the sample at 340 °C for one hour. And with this last step, the sample was ready for the upcoming SPM studies.

3.3 Nanowire morphology

Because the realization of future devices based on 1D nanosystems demands for superb control of the structure quality, position, composition, shape and dimensions, a good understanding of the physical and chemical processes that govern the epitaxial growth is essential.[226], [227] Usually, the surface/interface energies and surface diffusion kinetics are considered to be the shape-determining parameters. Conveniently, it has been shown that both can be tuned by controlling the growth conditions.[228], [229] Reviewing the literature to the date revealed that there were couple of experimental feats which were aimed towards understanding the growth mechanics of selective area MBE/MOVPE grown nanostructures. Since the III-V semiconductor nanostructures which were studied in this thesis were grown on (001) substrates, the following discussion will mainly focus on similar compositional and geometric configurations.

For instance, the work of Fahed et al.[230] demonstrated that the flux ratio of the material constituents can affect the final shape of SA-MBE grown InP nanowires on InP substrate. The 200 nm-wide nanowires were grown on InP (001) along [1-10] and [110] directions. After the growth, the investigation of the nanowire morphology was carried out with FIB-STEM (focus ion beam preparation coupled with scanning transmission electron microscopy). The results of this study are presented in Figure 3.3a and showcase the evolution of the nanowire shape with respect to P/In ratio and nanowire orientation. For the nanowires spreading along [110] it was clear that (111)B can be controlled by the growth conditions, whereas for the [1-10]-oriented nanowires the flux ratio did not have significant effect. This discrepancy was linked to strong dependence of (111)B facets to phosphorus chemical potential. Another recent example would be InAs planar nanowires grown by selective area chemical epitaxy on InP (001), InP (111)B and InP (110) substrates.[231] This work revealed the effects of growing the nanowires in different orientations. For all the configurations the growth at 520 °C displayed excellent selectivity with respect to SiO₂ mask. Interestingly, on the (001) surfaces the grown nanowires were again of a radically different shapes depending on if they extend along [1-10] or along [110] directions. The nanowires along the [110] direction had rectangular cross-section with just small portion of the truncated edges of (111)B facets. While the nanowires stretching along [1-10] direction had been dominated with (111)A facets and, thus they had more trapezoidal cross-section. Likewise, for this growth study, the observed shape-dependences were accredited to the surface thermodynamics, as the formation of the facets with the lowest surface energy will be favorable. Throughout the years this has been a common narrative for description of growth mechanisms at the nanoscale. Indeed, with the decrease of the dimensions the surface to volume ratio becomes more prominent thus putting further emphasis on the effect of the surface energies, all while the effects of surface kinetics are expected to be reduced, since the diffusion length of, for example, group-III materials was determined to be in the micrometer range, which far exceeds the size of the nanostructures.[232], [233]

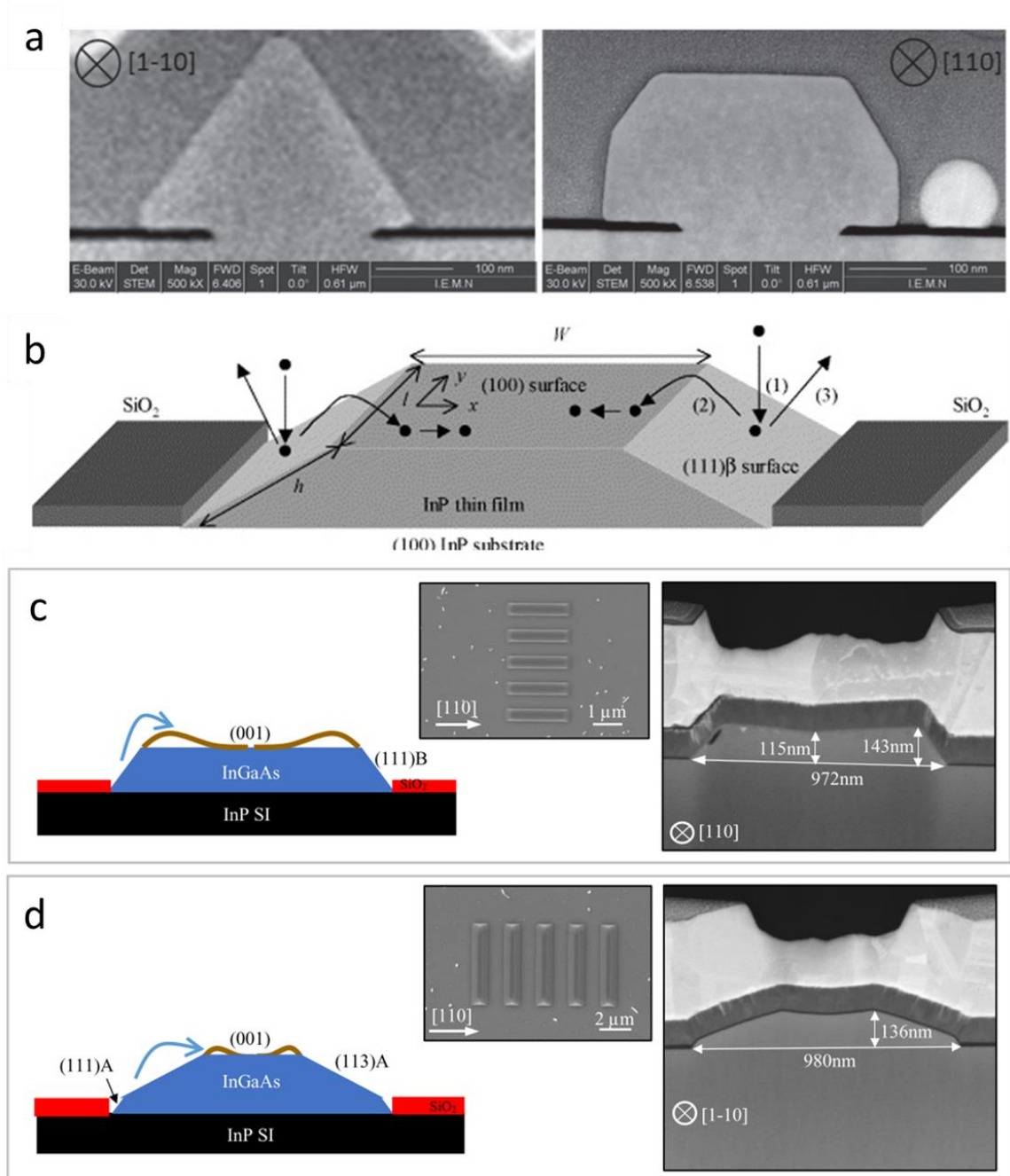


Figure 3.3 The role of surface migration in MBE selective area growth. (a) FIB-STEM images recorded after 200 nm InP growth in apertures directed along $[1-10]$ and $[110]$ for $P/In = 5$. Figure taken and adopted from ref.[230] (b) Schematic of the model describing three stages of precursor dynamics during the selective area growth of InP micro-strips. The black circles and arrows illustrate the surface

migration process. Initially, the adatoms are adsorbed onto the sidewalls (1), from there they can either migrate to the top facet (2) or desorb (3). Illustration taken from ref.[234] Insets (c) and (d) show selective area grown InGaAs nanowires on InP (001), which are oriented along [110] and [1-10] directions, respectively. Figure taken from ref.[131]

However, this might not always be the case. Even at the early stages of the microscale epitaxial growth, the importance of growth kinetics on the structure shape and quality was recognized.[235]–[238] For example, the work of Grandjean et al.[239] theoretically and experimentally demonstrated the effects of the diffusion length on the growth of the highly strained $\text{In}_x\text{Ga}_{1-x}\text{As}$ on GaAs(001). The authors have studied the effects of mass transport by observing the variation of the critical thickness at which the three-dimensional growth takes over the two-dimensional one. This transition in growth dynamics has been readily discussed in the earlier studies, with its driving force being linked to the decrease of the strain energy.[240], [241] Together, the Monte Carlo simulations of $\text{In}_{0.5}\text{Ga}_{0.5}\text{As}$ and RHEED (Reflection High-Energy Electron Diffraction) measurements of $\text{In}_{0.35}\text{Ga}_{0.65}\text{As}$ growth on GaAs (001) substrate clearly showcased the major effects of two main growth parameters on the diffusion length and thus, on the surface topography.[239] In specific, growth temperature and growth rate. The diffusion length can be defined as:

$$\lambda = \sqrt{\tau D} \quad (3.1)$$

, where τ is the mean residence time of the atoms on the surface and D is the surface diffusivity. The latter can be expressed as:

$$D = D_0 \exp\left(-\frac{E}{kT}\right) \quad (3.2)$$

with D_0 being the maximal diffusion coefficient and E activation energy for the diffusion of the atoms on the surface.[242] Since re-evaporation of the atoms in the MBE conditions can be neglected, the first of the two variables in Eq. (3.1) can be considered to be the time needed to grow one monolayer of material (growth rate). As an alternative, the diffusion length can also be controlled by either increasing the energy (E) of the barrier with the use of surfactants, or just simply by varying the growth temperature (see Eq. (3.2)). Naturally, the knowledge obtained from this, and similar studies was not only applicable for achieving the well-controlled two-dimensional layer-by-layer growth, but also for the one on planar patterned substrates towards the fabrication of advanced integrated devices. For instance, the selective area growth of InP micro-strips on SiO_2 by MOVPE was well described using a model which encompasses three key parameters: the diffusion length on the epilayer, the diffusion length on the mask, and the lifetime ratio of the mask and epilayer. In practical terms this is significant, as it was one of the first studies to demonstrate the surface migration as a relevant factor.[243] In particular, no prior selective area growth model was able to describe the ridge formations near the edge of the mask, as they were a product of the precursor migration from structure sidewalls to towards the top facet. Notably, this was not a lone example, as similar cross-sectional shapes were observed for various growth conditions and different microstructure compositions, dimensions and orientations.[244], [245] Interestingly, a nanoscale subject was recently reported.[131] Inset in (c) and (d) in Figure 3.3, show InGaAs nanowires grown in [110] and [1-10] directions on InP (001) substrate, respectively. The same selective area growth protocol described in Sample preparation section was

used, with the exception of having longer growth time. Regardless of the nanowire orientation, there is an evident presence of the ridge formations at the edges of the top facet which frame the depleted region in the center of the nanostructure. In general, not much is known about the selective area growth regime that takes place in the MBE chamber,[126] and even more so about the origin of the peculiar morphological features. To shed more light into the field, the following section showcases the results of the extensive scanning probe microscopy study of InGaAs nanowires grown on InP, by MBE selective area growth.

3.3.1 SEM measurements

The complex nano-heterostructures involved in this study have a shared building component. They are comprised of the interconnected individual InGaAs nanowires lying flat on the InP (001) substrate, as schematically shown in Figure 3.4a. Regardless of the shape of the nanostructure, the length of the individual nanowires within it appears to be the same, measuring up approximately $10\ \mu\text{m}$. The width and height, however, vary depending on the size of the patterned cutouts in the mask, but also on the nanowire orientation with respect to the substrate. The exact values of these dimensions will be discussed on the case-to-case basis later down in the text. Lastly, for all structures there are two prominent crystallographic directions $[110]$ and $[1-10]$.

In Figure 3.4b-f, the SEM images of different InGaAs nanowire-based structures, grown by the procedure described in Section 3.2, are presented.

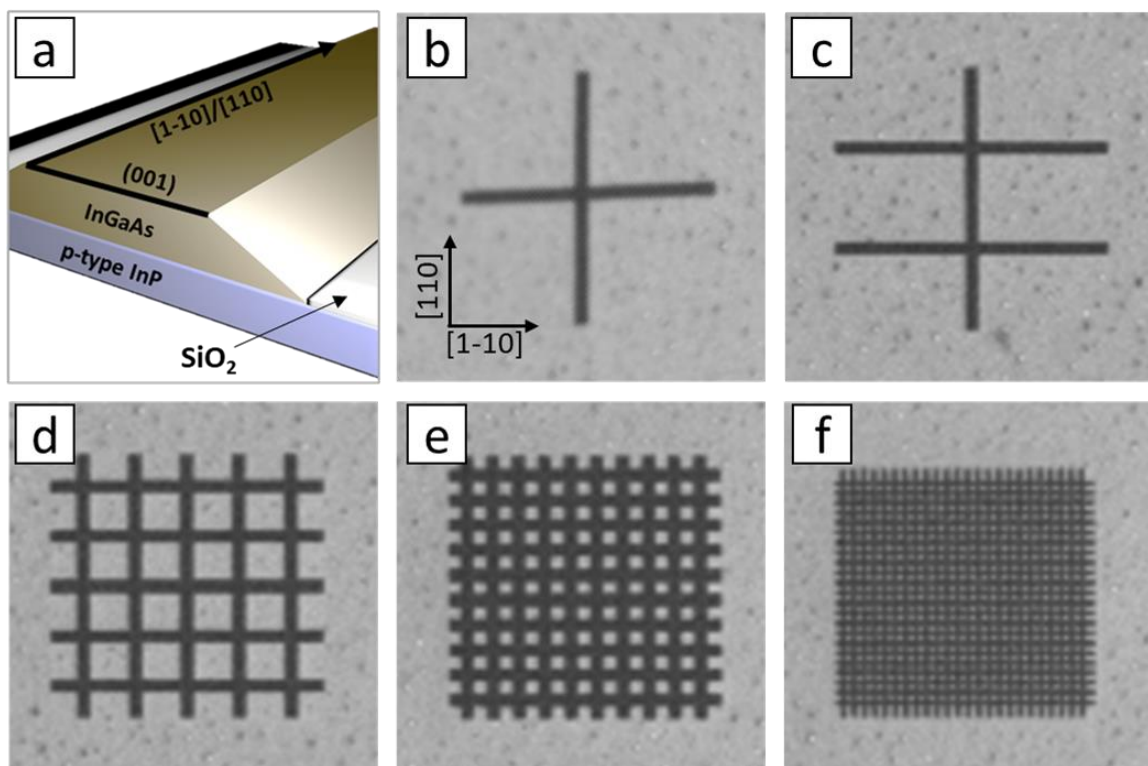


Figure 3.4 Zoology of the InGaAs nanowire-based structures grown on p-type doped InP, by selective area epitaxy. (a) Structural model of the nanowires which comprise the more complex nanostructures. (b) $14 \times 14\ \mu\text{m}^2$ SEM images of different InGaAs SAG nanowire-based structures which were studied during the development of this thesis. In the text these nanostructures are referenced as: (b) cross-shaped nanowires, (c) double-crossbar nanowires, (d) 5×5 grid nanowires, (e) 10×10 grid nanowires and (f) 23×24 grid nanowires.

As these were the subjects of the upcoming morphological study, for clarity, a specific notation will be used in their respective order: cross-shaped nanowires, double-crossbar nanowires, 5 x 5 grid nanowires, 10 x 10 grid nanowires and 23 x 24 grid nanowires.

3.3.2 AFM measurements

In the following, the discussion will focus on the AFM data acquired on various nanostructures, most of which were mentioned in the previous section.

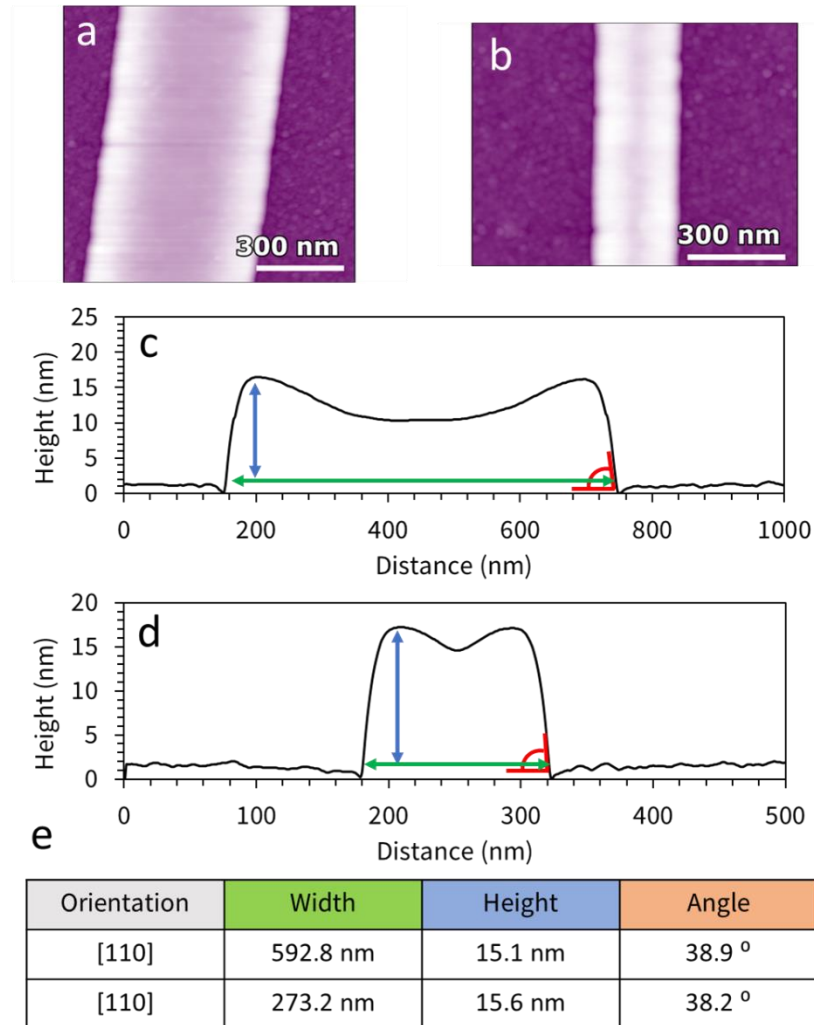


Figure 3.5 InGaAs SAG nanowires grown along [110] direction on InP. (a) AFM image of the 592.8 nm-wide nanowires. (b) AFM image of the 273.2 nm-wide nanowires. Insets (c) and (d) showcase cross-sectional height profiles of the nanowires in (a) and (b), respectively. (e) Table summarizing the dimensions measured from the height profiles in panels (c) and (d).

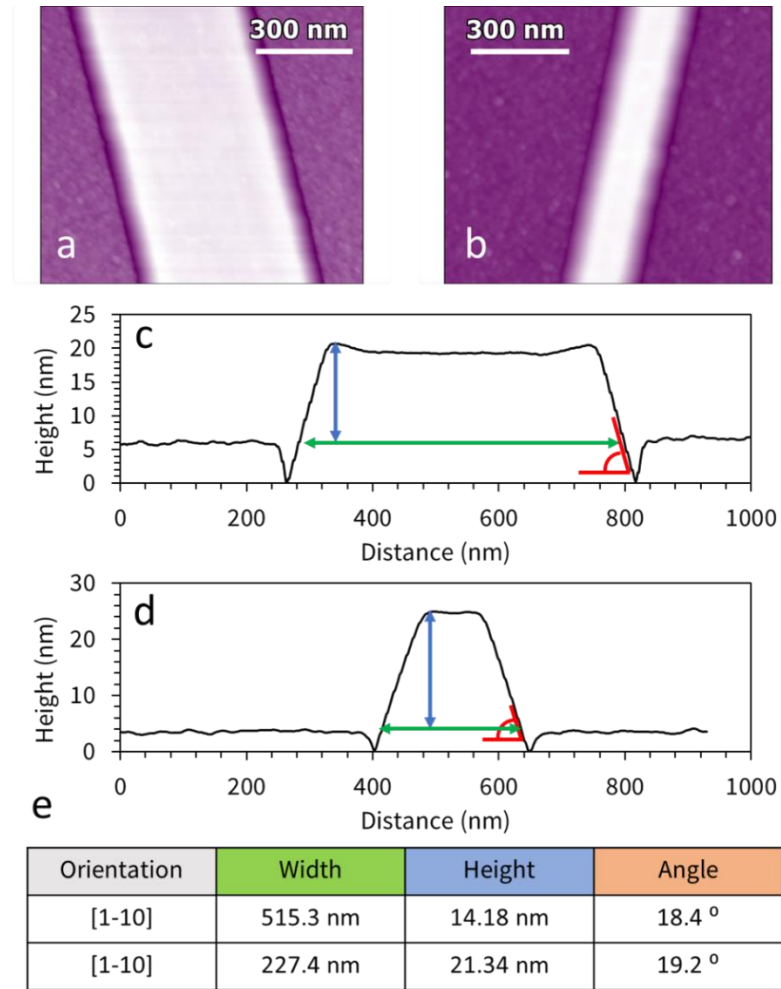


Figure 3.6 InGaAs SAG nanowires grown along $[1-10]$ direction on InP. (a) AFM image of the 517 nm-wide nanowires. (b) AFM image of the 229 nm-wide nanowires. The cross-sectional height profiles of the nanowires in (a) and (b), are presented in (c) and (d), respectively. (e) Table summarizing the dimensions measured from the height profiles in panels (c) and (d).

Starting with the simplest case of the individual nanowires of two different widths, spreading along $[110]$ and $[1-10]$ directions. In Figure 3.5, the results of the morphological AFM study of the individual $[110]$ -oriented nanowires are presented. The AFM images in the panels (a) and (b) showcase the nanowires grown inside mask openings of larger and smaller widths, with their corresponding height profiles presented in (c) and (d), respectively.

Focusing on the wider nanowire first (Figure 3.5a), it measures to be 592.8 nm-wide (see Figure 3.5c, and the corresponding row in the Table e). At its highest point (the interface between the top and side facets), the nanowire height is measured to be around 15 nm from the SiO_2 , whereas the angle that nanowire sidewall closes with the mask was measured to be 38.9 degrees. This value corresponds well

with the (112) side facet. Note that, all of the nanowire dimensions are, in fact, in a good agreement with the above mentioned study of Bucamp et al.[131] (for reference see Figure 3.3c,d).

As the growth time for our sample was significantly shorter, the nanowires are much thinner and have lower sidewall angle ((112) facet vs. (111)B) indicating a less complete nanowire formation. Another common and more interesting feature is that the height profile of the nanowire does not appear to be the same across the whole (001) nanowire top facet, as it is clear from the profile in panel (c) In particular, there is a gradual surface depression symmetrically leading towards the center of the nanowire from both sides. For simplicity, this feature in the future text will be further referred to as a “cusp”. Even though the angle of depression with respect to (001) facet is small ($1-3^\circ$), its presence is evident for both thick and thin nanowires (see Figure 3.5d). Indeed, as the nanowire width is reduced to 272 nm, the very slight increase in height is observed (15.6 nm with respect to the mask) and decrease of the (001) facet. This is an important observation by itself, however, it also had an impact on the determination of the other characteristics of the nanowire. In particular, the angle of the sidewall. The most reliable way to accurately estimate its value would be to measure it with respect to the plane-leveled (001) facet. However, since this was not possible for most of the nanowires, for the sake of consistency, the angle for all the nanowires within this study was estimated with respect to the SiO₂ mask. For instance, the angle of the thin nanowire extending along [110] direction was measured to be 38.2° . This value was attained with two considerations in mind. First one is tied to the fact that the nanowire sidewalls contain a small bump near the tip of the nanowire, and the second is the slight tilt of the whole structure with respect to the mask, but more on that later. To address the firstly mentioned, the angle was measured near the base of the structure where slope appears to be constant for the largest fraction of the sidewall. This step was performed on both sides of the nanowire and average value was taken, effectively negating the tilt of the mask.

Studying the morphological modifications with respect to the change of the nanowire orientation from [110] to [1-10] did not reveal any disappearance of the main features. However, it did showcase the slight modification of the overall nanowire dimensions and shape (see Figure 3.6). In the (a) panel, the AFM image of the wide nanowire is presented. From its height profile in panel (c), the following nanowire dimensions were estimated: height = 14.2 nm, width = 515.3 nm, and angle = 18.4° . Note that the values for the width and angle are significantly smaller than the ones measured on [110]-oriented nanowires. This is also true for its narrower counterpart presented in Figure 3.6b. Here, the nanowire can be characterized of being 227.4 nm-wide and 21.3 nm-tall and of having a sidewall angle of 19.2° (see panel (d)). This time around, the measured angle seems to be consistent between thick and thin nanowires, and it could be linked to (114) facet. Regarding the cusp, it is manifested to a much lesser extent than for the case of [110]-oriented nanowires. By taking a closer look at the cross-sectional profiles of all four nanowires described above, another orientation-dependent feature was revealed. In specific, for both thicknesses and on both sides of the [1-10]-oriented nanowires there are noticeable dips near the base of the nanowire. Their depth was measured to be approximately 6.2 nm. To identify these features, couple of considerations need to be made. First one is tied to the fact that the overall profile of the nanowires is quite flat since their width-to-high aspect ratio is exceedingly high. Next, the apex of a very sharp AFM tip is usually around 10 nm. And finally, the nanowire sidewall/substrate angle is generally small and even more so in the case of the [1-10]-oriented nanowires. Altogether, these

factors indicate that it would be possible to accurately resolve the interface between the SiO₂ mask and the nanowire sidewall. As a result, we can conclude that the [110]-oriented nanowires appear to be completely filling out the openings in the mask, which does not appear to be the case for the [1-10]-oriented ones. However, it is worth pointing out, that in all the cases the width of the [110]-oriented nanowires was smaller than the widths of the mask openings visible in Figure 3.6c,d. Thus, if one assumes that the process of fabricating the mask cutouts is independent of the crystallographic direction, this finding suggests that the overgrowth of [110]-oriented nanowires beyond the mask is not present. However, this certainly questions the accuracy with which the measuring of the height of the nanowires along [110] crystallographic direction can be done. One could assume that the mask thickness is 10 nm and just add it to the value measured from the top of the nanowire. This approach is the most convenient, but definitely not accurate, since from the previous attempts of sidewall angle measurements it was clear that the surface of the mask is not perfectly leveled with respect to (001) plane of the InP substrate below. To overcome the non-uniformity of the mask thickness, another approach would be to measure the depth of the dip for each individual nanowire structure in [1-10] direction and apply the correction to the measured value of the height of [110]-oriented nanowires. Less convenient, and still inaccurate, since the AFM tip becomes more and more blunt overtime which would result in plenty of inconsistencies in the data pool. Consequently, as the high-level of accuracy was difficult to reach, our approach focused on consistency, as it was the case for the measurements of the nanowire sidewall angle. The height of all the nanowire-based structures was done with respect to the mask itself. However, for a few specific cases which will be discussed later down in the text, the correction mentioned in the second approach was utilized. At this point, it seems that AFM might not be the best tool for the job, however, as it is a time-efficient and reproducible technique, it served purpose for preliminary characterization of a large number of different nanostructures before inevitable FIB-STEM measurements. Some of the highlights of the AFM statistics collected within this study will be the next topic of discussion. In order to understand the causality behind cusp formation, the strategy was to isolate the diffusion length as a parameter. On this basis, the criteria for the nanostructures which would be chosen for the measurements was set. The nanostructures would be comprised of interconnected nanowires having the same width (one exception), length, and orientation, with the only differentiating factor being the spacing between them. The simplest example abiding to these requirements was double-crossbar nanowire structure (see Figure 3.7). In panel (a) the AFM image of the whole nanostructure is presented.

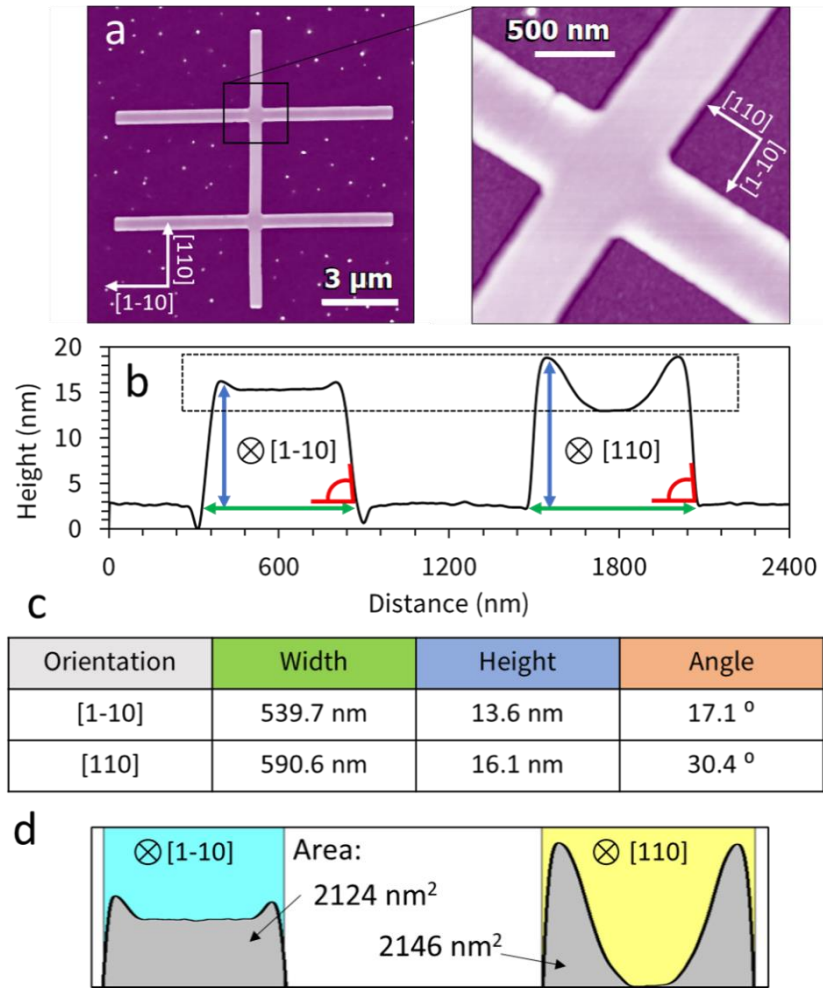


Figure 3.7 InGaAs SAG double-crossbar nanowires grown along [1-10] and [110] directions on the InP substrate. (a) A large AFM image of the whole nanostructure and high-resolution zoom-in on the area indicated by the black square. (b) Height profiles extracted along the directions across [1-10] (left) and [110] (right) crystallographic directions. (c) Table summarizing the nanowire dimensions extracted from the height profile in panel (b). (d) Zoom-ins on the cusp of the nanowire of two main orientations. The image is designed to highlight the material "displacement" around the cusp region.

The clearly visible nanowires forming a double-crossbar geometry are 5 μm apart and are of a lighter contrast with respect to the rest of the substrate. To achieve the best possible sensitivity in the vertical axis the scanning direction was rotated as shown by the zoom-in on the area highlighted by the black square. Before the detailed discussion of the nanostructure morphology, it is worth mentioning that prior to this zoom-in, a swift statistical analysis was conducted confirming that the nanowire shape is completely uniform throughout its length, with the first structural changes occurring just few dozens of nanometers prior to its end or intercept with other nanowires. Judging only by contrast variations

before and after the intercept, the nanowires spreading along [110] and [1-10] directions seem to be completely unaffected by it.

Furthermore, the [110]-oriented nanowires occupy a larger portion of the dynamic range of the color palette signifying the presence of more substantial height variations. This was expected, but also confirmed by the height profiles in panel (b), which were extracted across the nanowires of both orientations. In particular, along [110] direction the nanowires possess a much deeper cusp when compared to the [1-10]-oriented ones. In fact, this nanostructure is an ideal playground to investigate the difference in the cusp topography with respect to the nanowire orientation. There are two main reasons for this, and both have to do with the spacing between the [110] and [1-10] oriented nanowires. On one hand, the nanowires are far enough apart, so that they would not be affected by the 2D diffusion of the precursors. This is clearly the case, as the aforementioned statistical analysis revealed that the intercept-related topography is highly localized. On the other hand, the separation of the nanowires is still within the range of the nanostructure itself, as such the slight tilt of the mask will not have a significant enough effect to introduce ambiguities in the experimental findings. In Figure 3.7d, the section focused on the cusp region of the height profile in panel (b) (highlighted by the black dashed rectangle) is presented. This was done in order to point one striking observation revealed by this nanostructure. Measuring the areas occupied by each profile revealed that they are comparable, if not the same. This means that the same amount of the material is involved in the formation of the cusp for both orientations. Furthermore, this suggests that the directionality of the surface diffusion is the one starting from the nanowire sidewalls towards the center of the structures. The unequal material distribution leads to the depletion region in the center of the nanowire with the accumulation regions at the edges of the (001) facet. Just based on this alone we can conclude that the diffusion of group III atoms is more hindered in [110] direction. Finally, referencing back to the individual nanowires presented in Figure 3.5 and Figure 3.6, the dimensions and sidewall angles of double-crossbar nanowires are comparable in their respective crystallographic directions. Other previously seen significant features are present as well, such as the small dips near the bottom of the [1-10]-oriented nanowire sidewalls and smooth lobing near the top [110]-oriented nanowire sidewalls.

Moving on the discussion towards the nanostructures with a slightly higher degree of complexity (5 x 5-grid nanowires), these features and the overall nanowire shape remains the same, as it can be seen from the tables in Figure 3.8d. This certainly demonstrates a good growth selectivity with respect to the mask as well as growth reproducibility on the micro-scale. The structure is comprised of combined total of 20 nanowires forming a symmetric $10 \mu\text{m}^2$ grid. Again the height profiles were extracted across the nanowires spreading along [1-10] (see Figure 3.8b) and [110] directions (Figure 3.8c). The dimensions are summarized in the table in panel (d). Again, the nanowires do not seem to be affected by their neighbors indicating that the diffusion length must be lesser than the separation between them, which is approximately $1.6 \mu\text{m}$.

In order to investigate a scenario where this number will have a much lower value, we have also studied the same nanostructures but with a higher grid density. One such example is shown in Figure 3.9, where the separation between the nanowires was measured to be around 550 nm. And still, this 10×10 -grid nanowire structure has kept all the trademarks of the previously discussed examples.

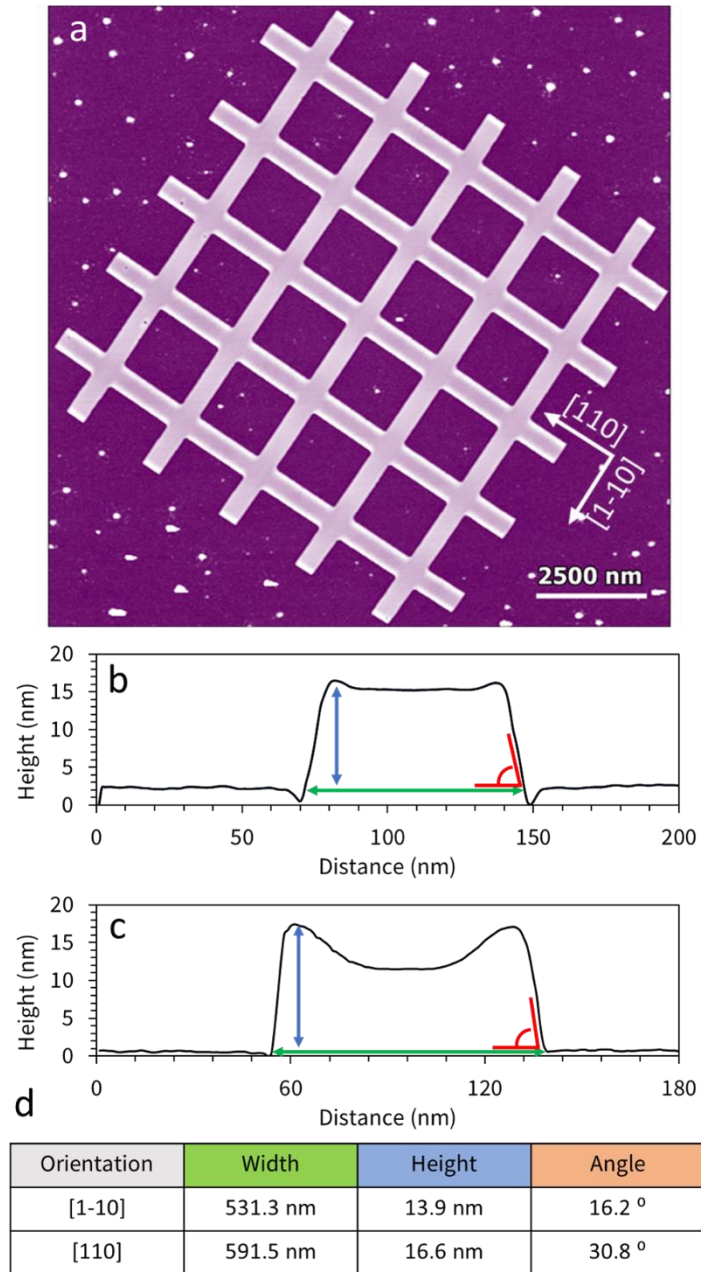


Figure 3.8 InGaAs SAG 5 x 5 grid-nanowires grown along [1-10] and [110] direction. (a) An AFM image of the whole nanostructure. Line profiles taken perpendicular to (b) [1-10] and (c) [110] directions. Table (d) summarizes the nanowire dimensions along two main crystallographic directions.

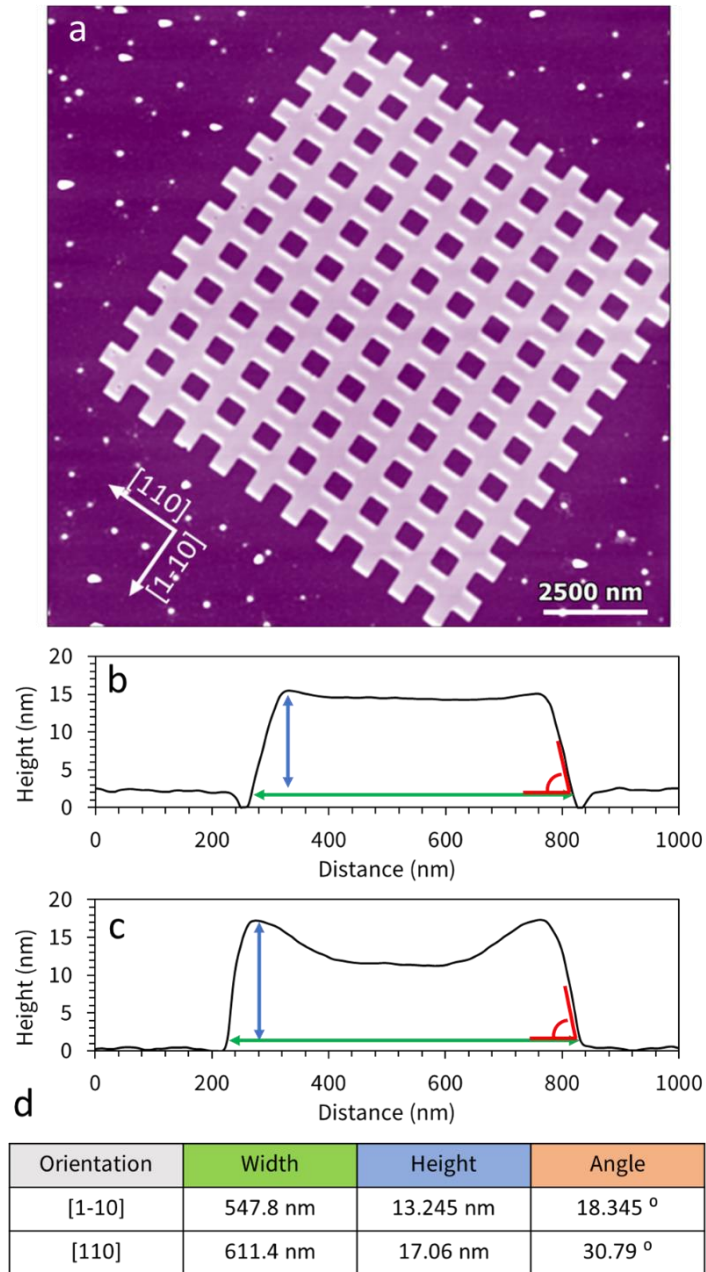


Figure 3.9 InGaAs SAG 10 x 10 grid-nanowires grown along [1-10] and [110] direction. (a) An AFM image of the whole nanostructure. Line profiles taken perpendicular to (b) [1-10] and (c) [110] directions. Table (d) summarizes the nanowire dimensions along two main crystallographic directions.

A further decrease of the spacing between the neighboring nanowires would require for the width of the mask cutouts to be decreased as well. For the next nanostructure the size of the openings was comparable to the “thin” nanowires presented in Figure 3.5b and Figure 3.6b. The spacing was measured to be 150 nm between [110]- and 200 nm between [1-10]-oriented nanowires. An AFM image of a whole 23 x 24-grid nanowire structure is shown in Figure 3.10a, with a zoom-in at the center of it in panel (b).

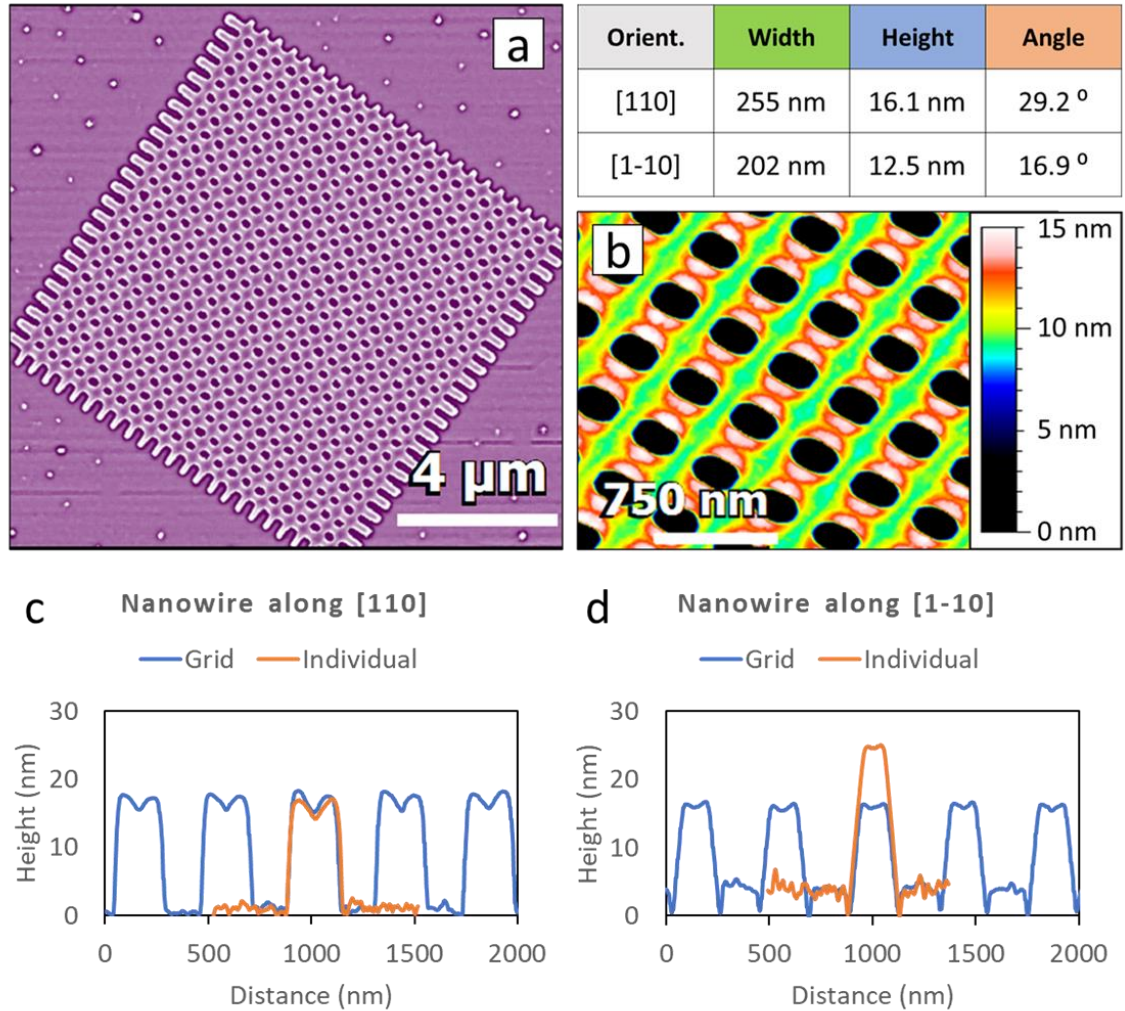


Figure 3.10 InGaAs SAG 23 x 24 grid-nanowires grown along [1-10] and [110] direction. (a) An AFM image of the whole nanostructure. The table in the top-right corner contains information about the nanowire crystallographic orientation and measured values of width, height, and the angle of its sidewall with respect to the substrate. (b) A high-resolution AFM image recorded near the middle of the nanostructure with its respective height palette. (c) Comparison of the height profiles extracted

from the individual [110]-oriented nanowire (from Figure 3.5) and the ones comprising a grid structure in panel (a). (d) Height profiles of the nanowire in Figure 3.6 and grid-nanowires, along [1-10] direction.

The dimensions of the nanowires comprising the structure in both crystallographic directions are given in the table above. They are in most part comparable to the ones measured on the standalone nanowires, with one striking exception being the height of the nanowires along the [1-10] direction. This can be better seen in the height profiles in panels (c) and (d). Here, the profiles from Figure 3.5d and Figure 3.6d (orange) are superimposed to the ones extracted across the grid-nanowires (blue) in both directions. The discussion concerning the origin of this phenomenon will continue later down in the text. However, what is immediately worth pointing out is that the overall shape of the nanowire reflects a proportional/uniform growth in [111] direction, as if an additional supply of the material was fed to the [1-10]-oriented nanowires.

3.3.3 STM measurements

The main instrument we used for this experiment is four tip low-temperature scanning tunneling microscope.

Figure 3.5b showed a cross-shaped InGaAs nanowire structure lying flat on InP substrate. Among other nanowire structures on the sample this one was chosen for the STM measurements due to its large size and spread across two crystallographic directions, [110] and [1-10]. This is important, as it allowed us to study different parts of the nanowire structures by positioning the STM tips accordingly. From the SEM image of the nanowire the following planar dimensions were estimated: 10 μm tip-to-tip length and 550 nm edge-to-edge width.

The LT-STM images in Figure 3.11a, b show the topography of the (001) top facet recorded on the [1-10]-oriented nanowire. The surface appears to be decorated with clearly resolved alternating dark and bright rows stretching along the [1-10] direction. These are atomic rows which are vertically broken up into jagged terraces. Upon closer inspection of the topography, two important bits of information were obtained from the surface profile in Figure 3.11c, extracted from the path indicated by red dashed arrow in (Figure 3.11a). First, showcases the periodicity between the bright rows of 1.63 nm, while the second indicates the terrace height of 0.28 nm. Both values are in good agreement with the ones found in literature[215] corresponding to $2\sqrt{2}a$ spacing between the atomic rows (InGaAs lattice constant $a = 0.587$) and the height of atomic bilayer, respectively. Together they lead to conclusion that the nanowire (001) facet is terminated with arsenic dimers as a part of (2 x 4) surface reconstruction, presented by a simple schematic in Figure 3.11(d). This does not come as a surprise as the nanowires were annealed at 340 $^{\circ}\text{C}$ for 1 hour, as a part of As-decapping process within a sample preparation procedure. At this temperature, As-rich surface will certainly accommodate the formerly mentioned reconstruction, as it was previously demonstrated by RHEED (Reflection High Energy Electron Diffraction) measurements.[215] In addition, there are two types of defects clearly visible on the surface, adatom and missing atom ones. Former are connected to bright lobes on the surface, which could be assigned to arsenic clusters. During the measurements they appeared to be loosely attached to the surface, as they could be easily moved by the electric field generated by the STM tip. The latter mentioned defects appear in the images as dark lines or spots, depending on the number of arsenic dimers missing from the surface. Notably, and regardless of which part of the top facet of the nanowire cross-structure was investigated (all four cross “arms” and the intercept in the center) the surface reconstruction, roughness and cleanliness were found to be the same.

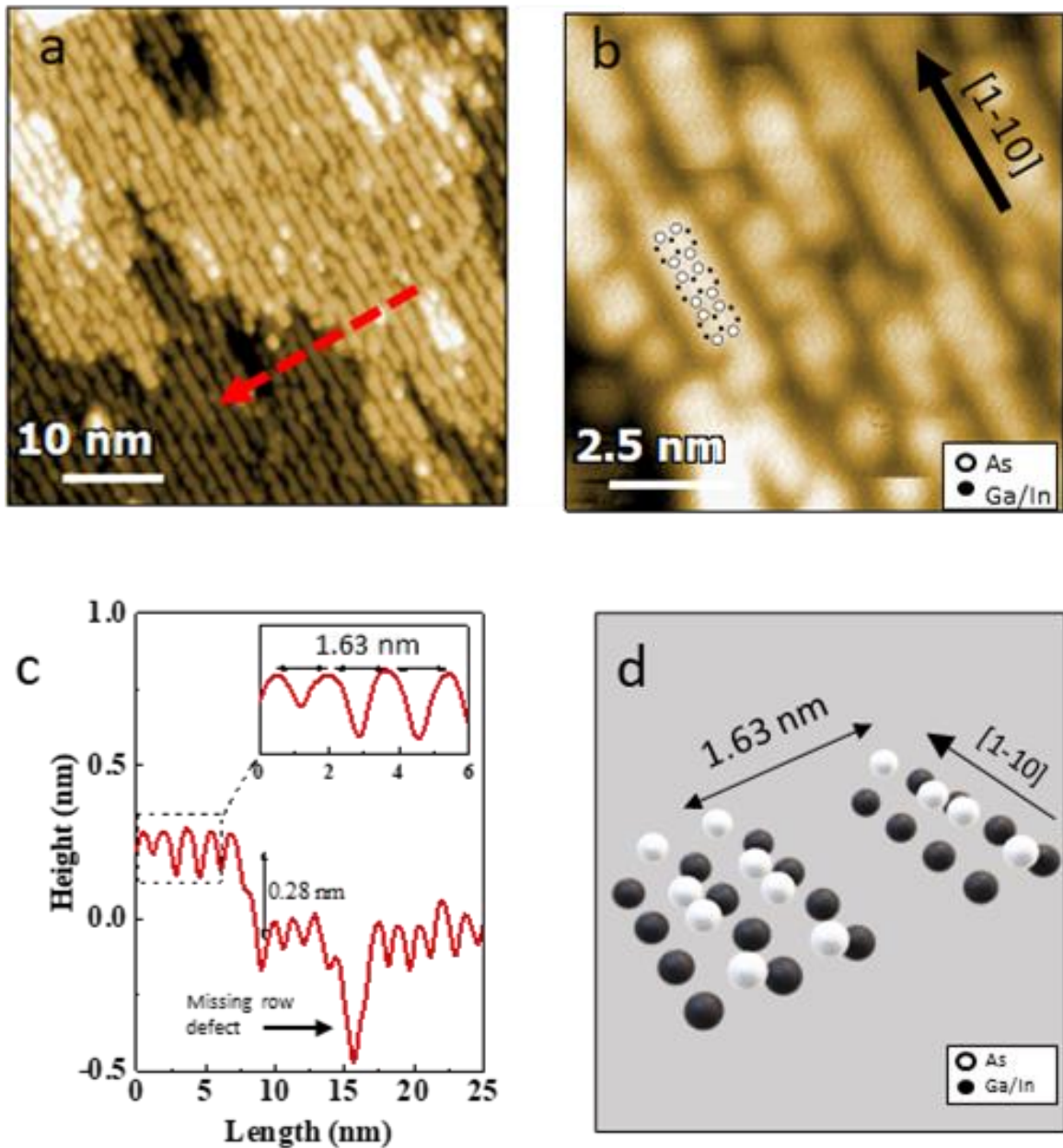


Figure 3.11 The LT-STM (4.2 K) study of InGaAs nanowire topography (a) Large STM overview of the (001) facet. Feedback parameters: $V_{\text{bias}} = -1.8$ V, $I_{\text{setpoint}} = 50$ pA (b) High resolution STM image highlighting the InGaAs (001) - (2x4) surface reconstruction with a superimposed simple 2D model of clearly resolved arsenic dimer rows. Feedback parameters: $V_{\text{bias}} = -2.0$ V, $I_{\text{setpoint}} = 50$ pA (c) Height profile acquired across the path indicated by red arrow in inset (a). (d) 3D structural model of the InGaAs (001) - (2x4) surface reconstruction.

With the clear picture of surface reconstruction on the top of the nanowire in mind, we have extended our study towards nanowire sidewalls. Since every nanowire structure on our sample is surrounded by silicon-oxide, this task was not as straightforward.

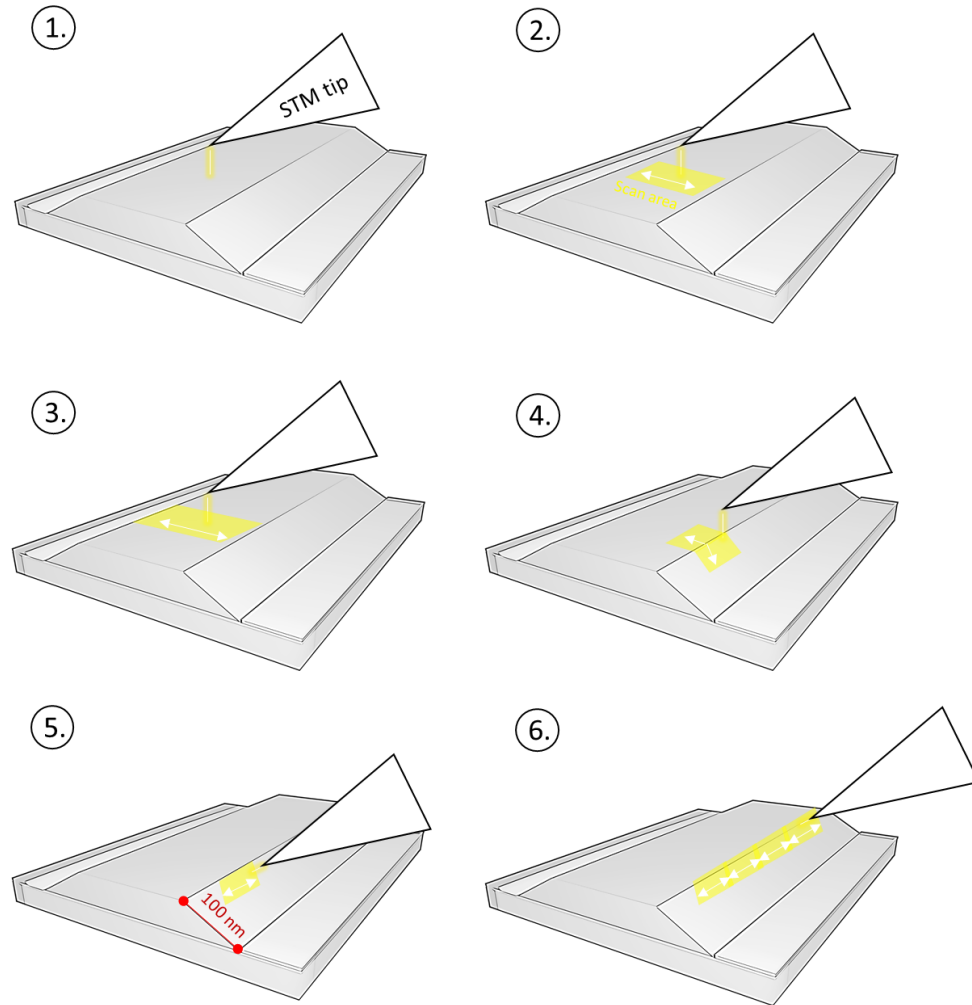


Figure 3.12 Schematic representation of the step-by-step procedure used for scanning the nanowire sidewalls with the LT-STM. Scan areas are presented in yellow, while scanning directions with white arrows. Structures are not in scale.

In specific, the scenario we wanted to avoid entails accidental overextension of the set scan area beyond the nanowire boundaries and consequent slipping of the STM tip from the nanowire sidewall towards the oxide. This will result in the probe crashing into the surface of the sample, as the typical value of

bias voltage ($V_s \approx \pm 2$ V) we used for scanning on the top of the nanowire would not be sufficient to support the tip in tunneling regime. In addition, due to technical restraint we could not rely solely on the SEM to navigate and monitor the movement of the probes once the scan has been initiated. This is because SEM electron beam can influence the tip-sample tunnelling junction resulting in much noisier STM images or even worse, the unwanted tip-sample contact. To overcome these challenges, we needed to come up with a different strategy.

Our approach can be broken up into couple of consecutive steps which are schematically presented in Figure 3.12. Firstly, with the use of SEM the tip was roughly positioned in the middle of nanowire (001) facet and the automatic approach was initiated. Once the tip-sample tunnelling current was established, the scan was started in the direction perpendicular to the nanowire and incorporated approximately 50 nm^2 of the surface area. This scanning direction was chosen as it could provide more contrasted output for the measured height variations within each linescan. With every subsequent scan the probed area would be gradually increased until the nanowire edges were reached. At this point the scanning window was reduced to increase the dynamic range and centered at the interface between the two facets. It is also worth mentioning that out of four existing tips in the system the one chosen for the measurements would be the one with the apex facing the nanowire sidewall. In such a way we exploited the 45° angled position of the tips to have a more perpendicular angle of attack and thus, reduce the tip convolution effect. Next, by referring to the AFM images above we estimated the approximately 100 nm-long extension of the nanowire (114) facet, and as a result we limited the scanning area to 50 nm^2 to integrate a comfortable safety margin. Lastly, the scanning direction was adjusted to follow along the nanowire as it, in this case, allowed for increased sensitivity for probing minor protrusions on the surface. In the end, the above described methodology was found to be effective as we managed to obtain additional morphological information on a larger scale without the risk of crashing the STM tip by misjudging its position. The main results of this experiment are presented in Figure 3.13.

Marked as a third step within the protocol described above (see Figure 3.12), the STM image shown in Figure 3.13a was recorded by scanning across the entire width of the (001) facet. On the top of the nanowire we observe the now familiar arsenic dimer rows stretching along [1-10] direction. Indeed, across all 340 nm (edge-to-edge width) the surface revealed the (2 x 4) reconstruction. Another observation consistent with previous measurements can be found in the height profile of the scanned area. The clearly visible depression in the middle of the nanowire undoubtedly indicates the existence of the cusp. The depth of the cusp at its lowest point is measured to be 2.8 nm with respect to the highest point of the nanowire. Moreover, it is also visible that it possesses a slightly asymmetric shape. In contrast to the top side of the nanowire, the surface of its sidewalls appears to be disordered. This can be clearly seen from the $30 \times 30 \text{ nm}^2$ 3D STM image in Figure 3.13b taken across the 20° -angled interface between the (001) and (114) nanowire facets. The final step in our methodological approach further confirms this, since crossing the very abrupt and well-defined boundary between the two planes to focus solely on the scanning of the (114) facet revealed images as the ones shown in Figure 3.13c. We suspect that this could be due to incomplete arsenic desorption during the sample preparation stage. Arsenic clusters, like the sparse and mobile ones already seen on the (001) facet (Figure 3.11a), could cover and mask the well-reconstructed nanowire surface below.

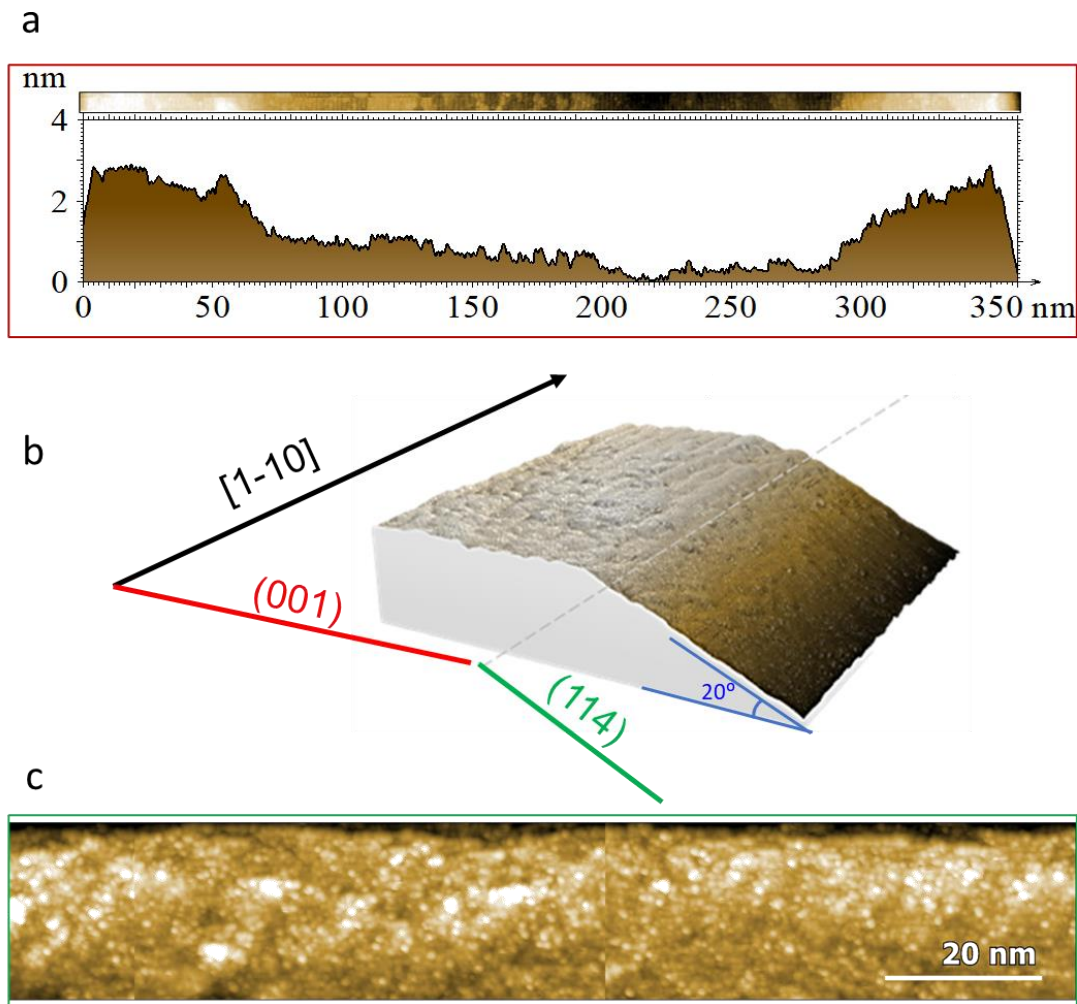


Figure 3.13 Large scale study of InGaAs nanowire morphology (a) Edge-to-edge STM image with its respective apparent height profile extracted across the entire nanowire (001) facet. Feedback parameters: $V_s = +2.6$ V, $I_{\text{setpoint}} = 10$ pA. (b) 30×30 nm² 3D view of the STM image acquired by scanning across the edge of the nanowire. Feedback parameters: $V_s = +2.1$ V, $I_{\text{setpoint}} = 10$ pA. (c) Panorama view assembled by patching together multiple STM images taken by scanning along (114) nanowire facet. Feedback parameters: $V_s = +2.1$ V, $I_{\text{setpoint}} = 1$ pA. For clarity, the plane subtraction was performed in vertical direction with respect to the image.

3.3.4 Diffusion kinetics model

To unveil the origin of the cusp formation our data was fitted using the model developed by V. G. Dubrovskii from ITMO University in St. Petersburg, Russia. For modeling of these concave profiles, the stationary diffusion equation for group III adatoms on the top nanowire facet was used:[246]

$$D \frac{d^2 n}{dx^2} + I - \frac{n}{\tau} = 0 \quad (3.3)$$

The boundary conditions were the following:

$$-D \left(\frac{dn}{dx} \right)_{x=0} = j_{\text{diff}} \quad (3.4)$$

$$\left(\frac{dn}{dx} \right)_{x=L} = 0 \quad (3.5)$$

Here, D is the effective diffusion coefficient of group III adatoms on the top nanowire facet, n is the group III adatom concentration, I is the atomic deposition flux in $\text{nm}^{-2}\text{s}^{-1}$, τ is the characteristic time of their incorporation into solid InGaAs, j_{diff} is the diffusion flux of group III adatoms to the top facet per unit length of each side of the nanowire in $\text{nm}^{-1}\text{s}^{-1}$, L is the half-width of the top facet and x is the coordinate across the nanowire. Schematics of the model is shown in Figure 3.14.

If the assumption is made that the group III adatoms do not desorb, the vertical growth rate on the nanowire top facet is equal to $\frac{dH(x,t)}{dt} = \frac{\Omega n}{\tau}$ at any point x , with Ω being the elementary volume of solid InGaAs. Integrating this, the following formulation is obtained:

$$H(x) = \frac{\Omega t}{\tau} n(x) \quad (3.6)$$

, with t being the total growth time. The solution to the Eq. (3.3) with the boundary conditions given by Eq. (3.4) and Eq. (3.5) is:

$$n(x) = It \left[1 + \frac{\lambda_0 \cosh \left[\frac{(L-x)}{\lambda} \right]}{\lambda \sinh \left(\frac{L}{\lambda} \right)} \right] \quad (3.7)$$

Which, can be further presented in terms of the normalized height:

$$\frac{H(x)}{H_{\text{max}}} = \frac{\sinh(L/\lambda) + (\lambda_0/\lambda) \cosh[(L-x)/\lambda]}{\sinh(L/\lambda) + (\lambda_0/\lambda) \cosh(L/\lambda)} \quad (3.8)$$

H_{max} is the maximum height at the edges, $\lambda = \sqrt{D\tau}$ is the effective diffusion length of group III adatoms before their incorporation into solid InGaAs, and $\lambda_0 = \frac{j_{\text{diff}}}{I}$ is the collection length of group III adatoms from the mask. In the absence of desorption, group III adatoms should be collected at the nanowire

sidewalls. Therefore, Eq. (3.8) contains only one free parameter, the diffusion length of group III adatoms λ , which can be deduced from fitting the measured profiles.

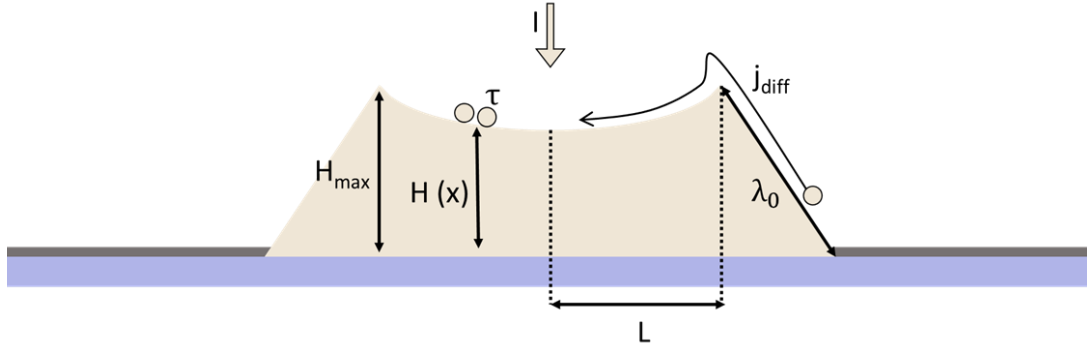


Figure 3.14 The illustration of the model showing geometry and the main parameters of the growth process. The description of the can be found in the text.

The results of fitting the ratio $H_{\max}-H(x)/H_{\max}$ with the standalone nanowire from Figure 3.5 is presented in Figure 3.15. This nanowire was chosen for the fitting for two reasons. Firstly, the non-uniformity of the SiO_2 mask was minimal and secondly, this was one of the first nanowires to be probed with a new AFM tip. As such, it was possible to accurately estimate the depth of the dip between the nanowire and the mask from the extracted profile in order to apply the appropriate correction (1.1 nm thick SiO_2) to the H_{\max} . As it can be seen from the top panel, the fitting was good and the deduced value for the diffusion length across [110]-oriented nanowire was $\lambda[1-10] = 110$ nm. However, fitting the data acquired on the nanowire in the perpendicular direction to this one did not yield good results. As it was firstly suggested by the material displacement analysis in the Figure 3.7d and later confirmed by the STM topography, the diffusion length along [1-10] should be much higher than along [110] direction due to the orientation of the As dimer rows when the (2×4) surface reconstruction occurs.

In fact, assuming that the diffusion length in [110]-direction is negligible in comparison to L , and that the growth rate expressed in the Eq.(3.6) is the same in both orientations, now having the exact value of the diffusion length for [1-10] direction allows for the estimation of the following ratio: $\frac{H(L)_{1-10}}{H(L)_{110}} \approx 1.25$. Referencing back to the values obtained experimentally $H(L)_{1-10} = 12.56$ nm and $H(L)_{110} = 10.23$ nm in Figure 3.7b, further showcases the validity of the proposed model.

In fact, we explain the observed orientation-dependent disparities in the cusp formation as follows: the adatoms which adsorb on the top (001) facet can diffuse, until they reach the edge of the nanowires. As seen in the STM images, the edge is rougher. They consist of bunches of terraces, increasing the potential barrier to overcome for further diffusion. As a result, the adatoms are incorporated there and the middle of the (001) facets grows at a smaller rate than the edge. In case of [1-10]-oriented nanowires, the profile is mostly flat as the diffusion length along [110] direction is miniscule.

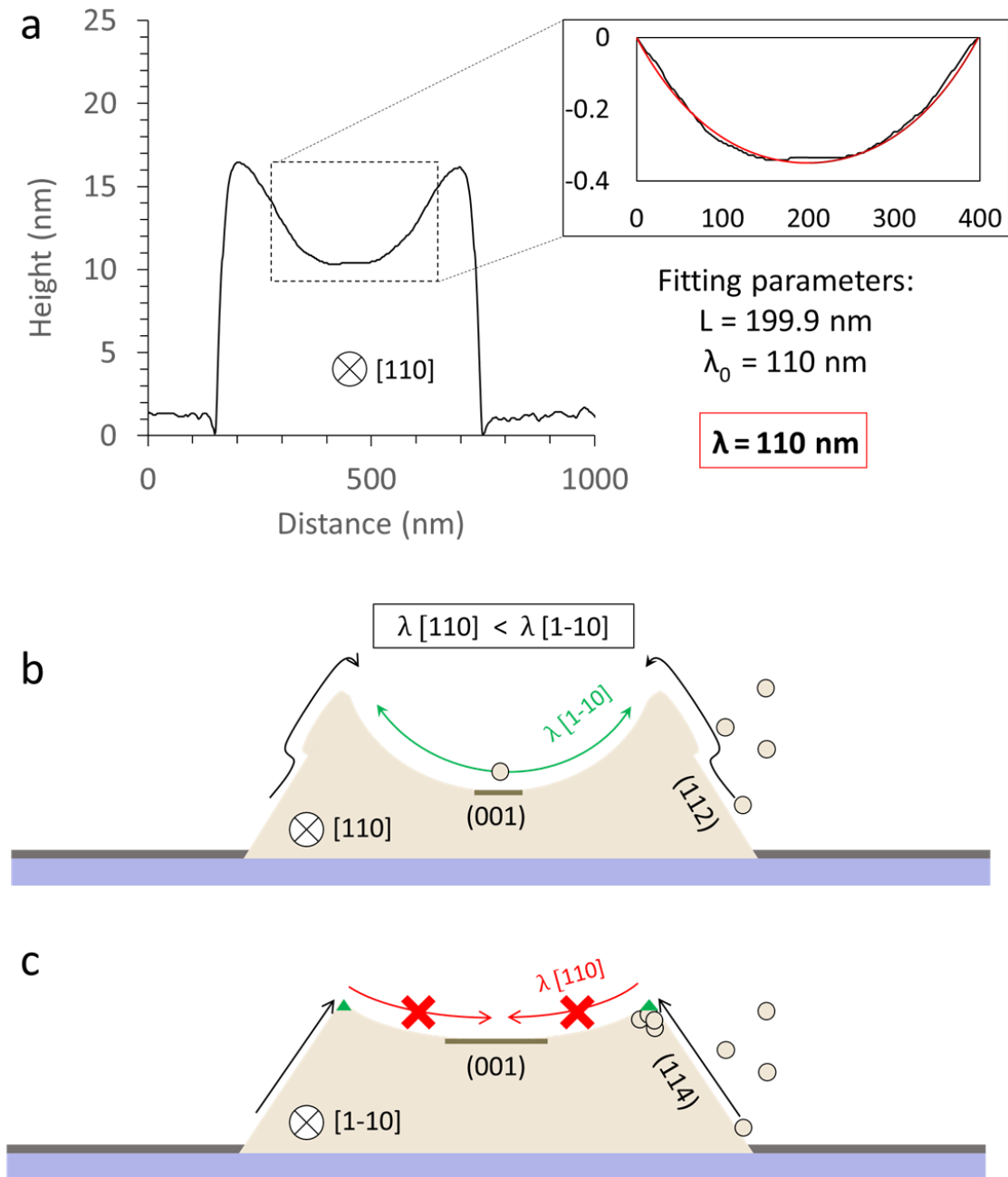


Figure 3.15 The correlation between the surface diffusion and the nanowire orientation. (a) Side by side comparison of the experimental data acquired on a standalone [110]-oriented nanowire and the theory, when the assumption is made that the atoms attach only to the nanowire sidewalls and diffuse towards the center of the structure. Illustrations of the 1D diffusion dynamics across the (b) [110]-oriented nanowires and (c) [1-10]-oriented ones.

Moreover, adatoms are also collected at the nanowire sidewalls. They can diffuse to the top edge, where they will incorporate, adding their contribution to the growth rate at the edge, forming the small ridge formations (see Figure 3.15c) for the [1-10]-oriented nanowires. Based on the orientation-dependent diffusion length of the group III adatoms, we can thus understand the larger absolute height of the [110]-oriented nanowires compared to the [1-10]-oriented nanowires and also the stronger cusp of the former nanowires. At this stage, what we do not know is the existence of small spatial variation in chemical composition, as the diffusion length of In and Ga could be different. This result calls for cross-sectional transmission electron microscopy experiments. On their own, none of these results presented so far explain the unexpected morphology of the nanowires comprising the 23 x 24 grid nanostructure along [1-10] direction (see Figure 3.10). However, together, they lead towards an interesting hypothesis.

First and foremost, as a result of the (2 x 4) surface reconstruction one could expect for the value of the diffusion length to be lower in [110] crystallographic direction because of the higher surface corrugation originating from the atomic rows (see Figure 3.11d and Figure 3.16a).

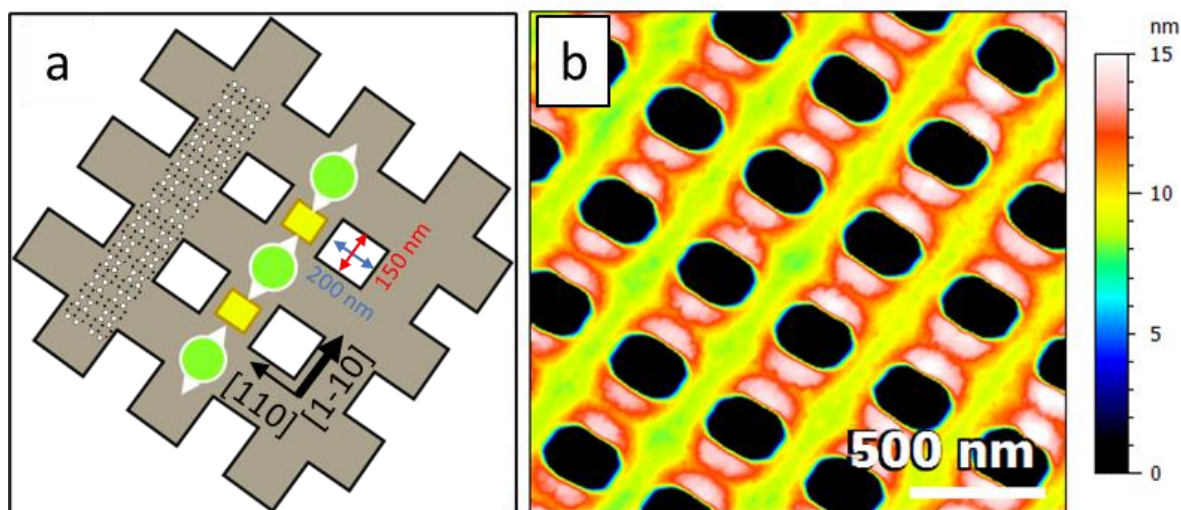


Figure 3.16 (a) The key highlights of the SEM, AFM and STM measurements summarized and applied to the case of schematically represented 23 x 24-grid nanowire structure. (b) High-resolution AFM image of the same nanostructure.

Another important factor to consider is the density of the nanowires and therefore, the number of intercepts within the nanostructure. With highly dense nanowire-based structures such as the 23 x 24-grid one, a larger fraction of its total surface area is accommodated by the intercepts which can also act as absorption sites. Due to the fact that the STM measurements have shown that the surface reconstruction across the intercept is unchanged, the diffusion dynamics in both directions should remain as expected, with $\lambda[1-10] \gg \lambda[110]$.

And indeed, by taking a closer look at the high-resolution AFM image in Figure 3.16b, the periodic contrast variations along [1-10] directions are apparent. In this image, the lowest height in the (001)

plane is represented by the green color, which can consistently be seen at the center of the nanowire intercepts. This periodicity was not observed on the larger and isolated intercepts as it was the case for the double crossbar-nanowires (see Figure 3.7). Note that the separation of the nanowires comprising the 23 x 24-grid nanostructures is comparable to the derived values of the diffusion length. Altogether, this led us to believe that building material landing on the intercepts is more likely to diffuse along [1-10], further feeding the growth of the nanowires and thus, being responsible for the observed height discrepancy.

3.4 Electronic properties of heterostructures

The characteristics of nano-heterostructure device concepts will completely depend on the type of band alignment between each component. Therefore, knowing the precise values of band offsets at the heterojunction is crucial. Over the years, there have been both theoretical and experimental approaches developed for this purpose.

We start with the work done by Anderson[247], which involves determination of conduction band offsets by utilizing electron affinity rule. In brief, the core principle of this rule is based on addressing every material on a single absolute energy scale by assigning them with a certain position within it. Thus, the conduction band offsets could be obtained from the differences in electron affinities of the two semiconductors comprising a given heterostructure, if one assumes a universal value for the energy of the vacuum level. However, this method had a major flaw. The electron affinities of materials in a heterosystem should mirror the charge redistribution at the interface and not the potential shifts at the surface of the structure in question. From here, a plethora of new theoretical approaches have been developed: starting from addressing bulk band structure at absolute energy scale, with various effective reference energy levels, such as charge neutrality, pinning of the levels and midgap states for each of the semiconductors that form the heterojunction, all the way up to the *ab initio* method and density functional theory method-based works.[248] With each new iteration, the accuracy with which the electronic band structure is calculated has been improved. For instance, the most recent scientific literature contains a report on evaluating the energetic positions of both conduction band minima and valence band maxima of alloyed semiconductors which combine into various heterosystems, by utilizing the hybrid functional HSE06 (Heyd-Scuseria-Ernzerhof).[249] Here, the authors have managed to overcome the inaccurate band gap predictions commonly associated with DFT calculations. This, if coupled with few additional improvements such as computing the accurate lattice constants and cation outermost d-orbital binding energies for the bulk III-V compound semiconductors, their methodology yields result which are much closer to the experimental data (see Figure 3.17). Unfortunately, this paper does not reflect the overall small success rate of theoretical work done in the field. Most of the calculations made on the bases of already existing experimental results have yielded correct predictions. However, calculating band offset with the satisfactory level of accuracy for the systems that have not yet been measured proves to be still a challenge. Thus, and simply put, having more and better data will not only leverage this issue, but also provide more trustworthy foundation to advance heterostructure-based applications. This two-fold motivation puts emphasis on development of new, and improvement of already existing experimental approaches for determining the band offsets.

Currently, most of the experiments involve optical and electron spectroscopies together with electrical device-based measurements.[250] However, and regardless of the approach, the viability of the resulting values is still questionable as there are inconsistencies among them. This is also true for the case of $\text{In}_{0.53}\text{Ga}_{0.47}\text{As} / \text{InP}$ heterostructures, a material combination of our own interest. For example, capacitance-voltage techniques were initially recognized as a “go-to” option for determining band offsets.[251] When this type of study was engaged on $\text{In}_{0.53}\text{Ga}_{0.47}\text{As} / \text{InP}$ heterosystems, it yielded vastly different values of conduction band offsets ranging from 190 meV all the way up to 600 meV.[251]–[255] Yet again, switching up the technique to photoluminescence excitations

spectroscopy a different number was obtained. The results of experiments performed on multilayered $\text{In}_{0.53}\text{Ga}_{0.47}\text{As}$ QW grown on InP suggested a conduction band offset of 381 meV.[256] Another example further highlighting the inconsistencies involves admittance spectroscopy, where band offsets of $\text{In}_{0.53}\text{Ga}_{0.47}\text{As}$ / InP superlattice were determined within zero-biased p-n junction, by analyzing temperature dependence of the capacitance and ac conductance. In this way the authors have managed to obtain conduction and valence band offset values of 250 ± 10 meV and 346 ± 10 meV, respectively.[257]

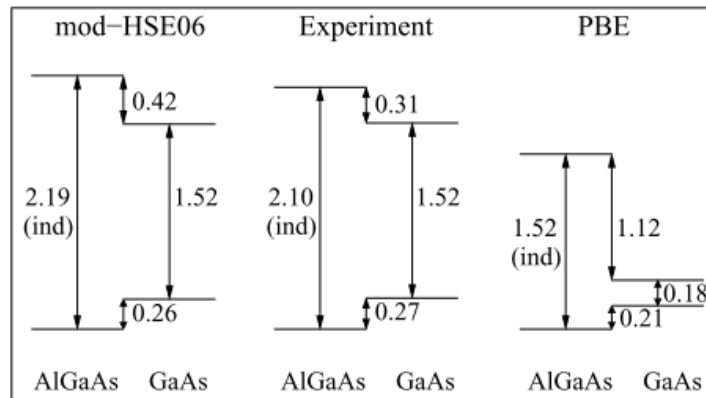


Figure 3.17. Direct comparison of the results obtained for the band alignment of $\text{Al}_{0.5}\text{Ga}_{0.5}\text{As}$ / GaAs heterostructure with experimental[258], mod-HSE06 ($\alpha = 0.30$) and more conventional PBE (Perdew-Burke-Ernzerhof[259]) approach. Figure adopted from pub.[249]

Finally, one of more recent studies incorporated the analysis of secondary electron thresholds across an in situ cleaved InP/ $\text{In}_{0.53}\text{Ga}_{0.47}\text{As}$ / InP double heterojunction and the reported value of conduction-band discontinuity was 210 meV.[260] As it is clear from examples above, having a conclusive answer for the $\text{In}_{0.53}\text{Ga}_{0.47}\text{As}$ / InP band offsets by conventional methods remains hard to overcome and at this point, a long-standing issue.

In this work we have chosen scanning probe microscopy as a lone mean to tackle this issue. In specific, a single- and two-tip scanning tunnelling microscopy (STM) and spectroscopy (STS), together with 4-probe STM transport measurements. Scientific literature does contain several reports where atomic resolution imaging and localized spectroscopy, inherent to single-tip STM, were successfully exploited and able to provide direct information on the internal electronic structure of various semiconductor heterointerfaces.[261]–[264] However, being able to probe highly localized density of states of the sample is also the major limitation of this technique. To overcome this and extend our study of electronic properties of the nanowire to a larger scale, we have complemented our investigation with a 4-probe STM system. Moreover, it was demonstrated that electrical measurements with micro-fabricated 4-contact points on the hetero-nanowires can disclose charge-transport mechanisms which occur across the heterointerface.[103] Even though this configuration enables for eradicating the effect of contact resistance on the measured current-voltage characteristics, the non-invasiveness of contact fabrication is still debatable. Thus, 4-probe STM presents itself as an ideal tool, as it allows for finer

control in establishing light ohmic contacts, but also adds an extra level of flexibility in probe positioning (more in Chapter 2).[199], [265] Finally, to the best of our knowledge, no dedicated study of band offsets has been reported on InGaAs / InP nano-heterosystems using any of the techniques listed above or even more so, the combination of them. Therefore, our single(multi)-probe STM contact/non-contact combination presents itself as a novel approach to determine the band offsets of semiconductor heterosystems.

The experiments were carried out with two complementary setups: Scanning Tunneling Microscopy (STM) and Scanning Tunneling Spectroscopy (STS) measurements were done with one and two probes on the UHV Scanning Electron Microscope (SEM)/multiprobe Low Temperature STM (LT-Nanoprobe, Scienta Omicron) operated with Matrix control system (Omicron) while the contact 4-probe measurements were done on a SEM/multiprobe STM (Nanoprobe, Omicron Nanotechnology), operated with a control system able to run the four STM tips independently (Nanonis multiprobe control system, SPECS). All measurements were performed in Ultra-High Vacuum (UHV) (base pressure lower than 5×10^{-10} mbar) and in the dark, always with the electron beam turned off.

The sample chosen for this study was the intrinsic $\text{In}_{0.53}\text{Ga}_{0.47}\text{As}$ cross-shaped nanowire selective area grown on p-type doped InP ($3 \times 10^{18} \text{ cm}^{-3}$), for which a detailed morphological description can be found in the text above. Note that the STM topography on the top (001) facet has revealed the (2x4)-surface reconstruction (see Figure 3.11). This, if coupled with the fact that substrate is highly p-doped should result in the Fermi level being pinned near the valence band as demonstrated by the recent study of the quantum well structure of the same composition.[215]

3.4.1 STS measurements of the $\text{In}_{0.53}\text{Ga}_{0.47}\text{As}$ cross-shaped nano-heterostructure

Here, the results of scanning tunnelling spectroscopy performed on the top of the InGaAs nanowire at 5 K are reported. This was achieved by first fixing the desired tip-sample distance with the STM feedback loop. Once completed, the STM feedback would be switched off and the data acquisition would be done by sweeping the chosen bias range while simultaneously recording the resulting tunneling current. In such a way one can obtain the differential conductance (dI / dV) curves which directly provide information concerning the density of states of the sample (see Chapter 2). The measurements were performed in two different system configurations. One involved two STM tips with one acting as probe, along with the other tip as ground, in contact with the nanowire (as in Figure 3.18a,b) The other configuration utilized the simple single probe STS with the sample kept at ground, as shown by the schematic in Figure 3.18d and the SEM image in panel (e).

To eliminate any potential contribution from the InP substrate below and thus, single out just the electronic response of the nanowire we had begun our study with two tip measurements (Figure 3.18a). First, one tip was approached at the distance from the nanowire at which the flow of tunneling current was feasible. As such it was kept for couple of minutes or until reaching a satisfactory degree of thermal and mechanical stability and only then, the tip was manually approach with couple of dozens of picometers at the time until the significant jump in measured current was observed. In this way the tip made light, yet stable contact with the nanowire surface. The bias voltage was set to zero, the sample was placed in floating configuration and the approach of the second tip was performed. After the approach, the planar location of the tip was evaluated to be $1.5 \mu\text{m}$ away from the priorly contacted probe, as shown in the SEM image in Figure 3.18b. In our case, each STS cycle can be treated as a sequence of forward and backwards voltage sweeps, with their respective curves presented in red and blue. In other words, the voltage was ramped from positive to negative values, within a chosen range, for the first and from negative to positive for the second, with the set raster time (20 ms) in between. The resulting dI / dV curves acquired at 5K are presented in Figure 3.18c.

Two tip configuration measurements consistently produced spectra where the zero-conductance region was measured to be 0.81 eV, which is perfectly in line with the values found in literature for the InGaAs band gap at liquid helium temperatures.[266] Taking a closer look at the curves produced during the forward and backward voltage ramps clearly display that no hysteresis was present among them. Thus, we can confidently claim that the curves obtained in this way showcase that the potential at the InGaAs surface between the position of the tunneling tip and the position of the tip in contact is constant. As a result, we were able to observe the true width of the band gap which is surrounded by InGaAs conduction band and valence band states with the expected Fermi level (0V) position close to the valence band maxima, consistent with the presence of a p-type layer underneath. At this point, we had a solid baseline for understanding the variations which would be observed in single tip measurements (see Figure 3.18d,e).

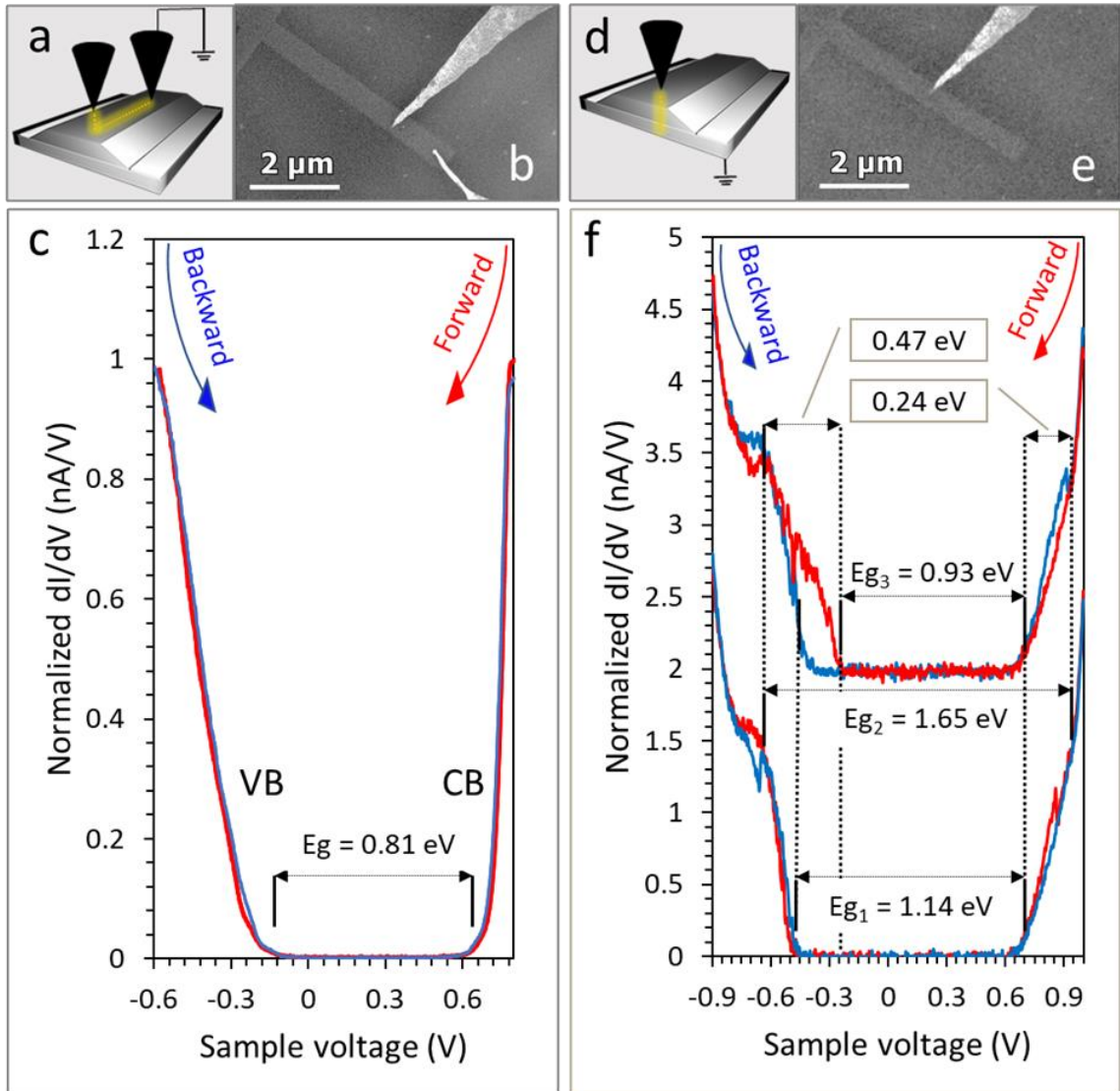


Figure 3.18 Scanning tunnelling spectroscopy on $\text{In}_{0.53}\text{Ga}_{0.47}\text{As}$ cross-shaped nanowires at 5K (a) Schematic of the two tip configuration with the sample floating: one tip is in contact with the nanowire acting as a ground, while the other was used for probing in tunnelling regime. (b) SEM image of the two-tip STS configuration. The separation between the two probes was measured to be $1.5 \mu\text{m}$ (c) Differential conductance spectra obtained in such a way. Feedback parameters: $V_{\text{bias}} = +1.3 \text{ V}$, $I_{\text{setpoint}} = 0.5 \text{ nA}$, $-z = 500 \text{ pm}$. Here, $(-z)$ is the value of vertical offset which is applied to the tip when stabilized in tunneling regime and upon switching off the feedback loop. The negative sign expresses that with this maneuver the tip is moved closer to the sample. The tip stays steady in that position throughout the whole STS cycle. Here, $(-z)$ is defined as the value of the manual offset in height, which is applied to the tip, after stabilizing it in tunneling regime and upon switching off the feedback loop. The negative

sign expresses that the tip is moved closer to the sample surface. The stays steady in this position for the whole duration of the STS cycle. Individually, the curves are comprised of two consecutive voltage sweeps presented as forward (red) and backward (blue). The sweeps differ in polarity of the starting bias with the forward scan being initiated from positive and backward from negative values of bias voltage. (d) Schematic of single-tip STS configuration with a sample grounded (e) SEM image of the cross-shaped nanowire probed in a single-tip STS configuration. (f) Two sets of differential conductance spectra. Feedback parameters: $V_{\text{bias}} = +1.3$ V, $I_{\text{setpoint}} = 0.6$ nA, $-z = 100$ pm (bottom) and 150 pm (top). Again, backward, and forward sweeps are presented in blue and red, respectively.

The results obtained from a single-tip measurement at 5K are reported in Figure 3.18f. Here, two STS cycles are Y-stacked for clearance and presented. The distinguishing parameter between the two is the variable tip-sample separation. In specific, the STS was performed as follows: once the tip was stable in tunneling regime, the feedback loop was switched off and the tip was force-approached for $-z = 100$ pm (curves below) and $-z = 150$ pm (curves above) towards the surface of the sample, where it was kept steady throughout the two consecutive sweeps. As the intensity of the tunneling current in STM has inverse exponential dependence with the tip-to-surface distance, these values can be viewed as variation of the setpoint current between the STS cycles, i.e. larger the tip-to-sample separation, smaller the setpoint current. Side-by-side comparison of the two measurements yielded a couple of key observations.

- Smaller tip-to-sample separation (curves above):
 - i) Higher noise level when compared to curves below.
 - ii) Large hysteresis present between forward and backward sweeps.
 - iii) The width of the apparent band gap for the forward sweep is measured to be $E_{g3} = 0.93$ eV.
 - iv) Apparent band gap for the backward sweep is measured to be $E_{g1} = 1.14$ eV.
 - v) The shape of the density of states reveals two distinct features which are $E_{g2} = 1.65$ eV apart.
- Larger tip-to-sample separation (curves below):
 - i) Little to no hysteresis present between forward and backward sweeps.
 - ii) The noise level is generally lower than for curves above.
 - iii) E_{g2} is missing.
 - iv) The width of the apparent band gap is measured to be $E_{g1} = 1.14$ eV.
 - v) The shape of the density of states reveals the same features at $+0.94$ V and -0.7 V.

Starting from the curves above, the hysteresis between the forward and backward sweeps is substantial. In particular, the forward sweep gives zero-conductance region of 0.93 eV, a value quite close to real width of the band gap of InGaAs previously reported in literature and measured in two-tip configuration (0.81 eV). The variation of the measured band gap between those two measurements confirms that the influence of the substrate is present when the sample is grounded, with any carrier path incorporating the 20 nm InGaAs and approximately 300 μm of the p-type doped InP below. For

the backward voltage ramp the conduction band edge is still at +0.7 V, as in the forward sweep, whereas the valence band edge shift for 0.21 eV towards negative values of sample voltage. This results in a significantly larger value of the apparent band gap of 1.14 eV. Such a large hysteresis strongly suggests charge-induced band bending inside of the nanowire valence band.

Focusing on the form of the density of states measured in the band, there are two clearly resolved features present in the spectra for both voltage ramps. The first one appears as a change in slope at 0.94 eV above the Fermi level (0V). Such features usually signify the presence of an additional pathway for the electrons. In fact, based on the previous work on $\text{In}_{0.47}\text{Ga}_{0.53}\text{As}$ quantum well grown on p-type doped InP (001) substrate, it has been shown that electrons transferred from the tip states into the lowest InGaAs conduction band states leave the conduction band by recombining with holes.[267] At higher bias, the states of the InGaAs layer become coupled with the lowest electronic states of the InP, adding a new conduction channel. Therefore, this change of slope can be attributed to the InP conduction band edge at the heterojunction between the two materials. In this sense, we could evaluate the conduction band offset between two materials of 0.24 eV. Referring to the values obtained by other techniques found in the literature, ours is close to the one expected.[260], [268] Furthermore, at negative bias, the plateau visible at -0.7 V, strongly suggests the possibility of probing the InP valence edge at the heterojunction between the two materials.

However, increasing the tip-sample distance results in the decrease of the tunneling probability between tip and nanowire, which yields a different picture from the one seen in the close tip-sample scenario. The hysteresis between the forward and backward sweeps becomes negligible. In particular, the edges of the valence and conduction bands are located at -0.43 V and +0.7 V, respectively. This translates to the much larger than expected and already mentioned zero-conductance region E_g . Furthermore, the now familiar features, assigned to InP conduction and valence band edges were again observed at the same positive and negative values of bias, respectively. However, due to the increased tip-sample distance the transmission probability is decreased. Consequently, at negative bias, the conductance signal which corresponds to the valence band edge of the InGaAs (-0.23 V) is below the noise level.[269] In contrast, and as it was previously demonstrated by Feenstra et al.[270] on the case of Si (111) 2×1 -reconstructed surface, when the sample is at positive polarity, one should expect slight lowering of the potential barrier which translates to the increase of the transmission probability and therefore, the tunneling current. As a result, the conduction band edge was clearly resolved regardless at which of the two tip-to-sample distances the STS acquisition was made.

3.4.1.1 $\text{In}_{0.53}\text{Ga}_{0.47}\text{As}$ / InP band alignment from STS

Here, we will cover in depth one complete single-probe STS cycle with the use of band diagrams in Figure 3.19. Even though the nanowire itself is intrinsic, the p-type nature of the InP substrate causes majority of the charge carriers in the InGaAs layer to be holes. This assumption is consistent with the measurement of the Fermi level position (given by the zero volt in the STS spectra) below midgap. Hence, a downward band bending imposed by the pinning of the Fermi level creates an accumulation layer of holes close to the InGaAs/InP interface.[191]

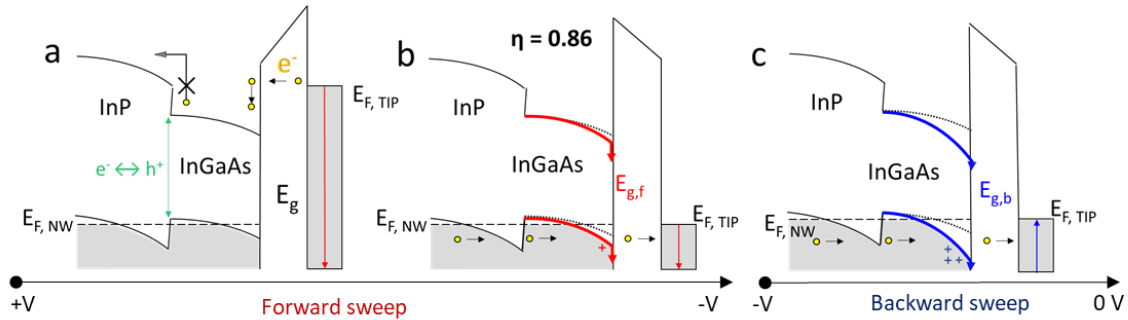


Figure 3.19 Schematic representation of the heterostructure band diagrams at different stages of the bias sweep within the single measurement cycle, performed in a single-probe configuration with the sample grounded, as demonstrated in Figure 3.18. (a) Probing at positive values of voltage within forward sweep. (b) Probing negative values of voltage within forward sweep. (c) Probing at negative values of voltage within backward sweep.

Performing STS inherently involves injection or extraction of electrons depending on the polarity of the applied bias voltage, by ascending or descending the tip Fermi level position in energy.[271] In our case, and starting from high positive values of bias voltage the Fermi level of the STM tip is resonant with the conduction band states of the InP substrate. As the voltage ramp progresses towards lower values, the electrons start tunnelling from the STM tip into conduction band states of the InGaAs nanowire, as schematically presented in Figure 3.19a. Since the added electrons do not have enough energy to proceed to conduction band of the InP substrate, the high availability of the holes in valence band makes for the electron-hole recombination process to be credible. As such the measured apparent STM band gap should remain unchanged. However, this is not what we observed in Figure 3.18f, when the bias is swept backward in the curve at the top of figure 18f. For this reason, one needs to take a closer look at the negative side of the spectrum, where major inconsistencies were found. Here, and as shown by band diagram in Figure 3.19b, the electrons are tunneling from the states below the sample Fermi level to the STM tip. This process will induce further depletion of the already scarce valence band electrons. A steady current imposes a continuous supply of electrons from the InP substrate. However, the depletion region at the InGaAs/InP layer that becomes deeper with decreasing bias makes this process less efficient. As a result, the InGaAs layer becomes positively charged which further increases the overall downward band bending at the surface. The resulting charging widens the measured zero-conductance region, since the transmission probability across the tunneling junction is reduced due to the width of the depleted region at the surface of the InGaAs layer. At this point, it is convenient to determine the

extent of charging effect by utilizing the lever-arm method. By dividing the correct value of the band gap obtained by the two-tip measurements $E_g = 0.81$ eV (Figure 3.18c) with the value measured within forward STS sweep $E_{g3} = 0.93$ eV (Figure 3.18f), we find that the lever-arm is 0.86, meaning that part of the potential applied across the junction drops into the semiconductor. However, the same methodology cannot be applied for the backwards sweep ($E_{g1} = 1.14$ eV). The reason for this can be found in the short raster time between the forward and backwards sweeps, which is responsible for keeping the nanowire in the charged state. In specific, the recovery rate of the electrons which would be transferred from the nanowire surface states to the unoccupied STM tip states is not quick enough. Therefore, initiating subsequent electron extraction at negative bias will lead to the further increase of positively charged surface states and even more pronounced downward band bending, as shown in Figure 3.19c. Finally, upon reaching positive values of bias voltage the system will rapidly discharge and the energetic positions of InGaAs and InP conduction band edges will remain unchanged. This is important, as it allows us to apply the lever-arm correction to the voltage where change of slope was observed and in such a way deduce an accurate value for the conduction band offset of 210 meV. Employing the same methodology to the plateau observed at negative bias (-0.7 eV in Figure 3.18(f)) we have also calculated a valence band offset of 400 meV. A convenient way to crosscheck these values is to apply the lever-arm correction also to the measured energy separation between the InP conduction and valence band edges ($E_{g2} = 1.65$ eV), which in our case yields a value of 1.42 eV, in agreement with the InP band gap.

3.4.2 Charge transport in the $\text{In}_{0.53}\text{Ga}_{0.47}\text{As}$ cross-shaped nano-heterostructure

Both two-probe and four-probe methods were utilized to measure the charge transport in $\text{In}_{0.53}\text{Ga}_{0.47}\text{As}$ cross-shaped nanowires on InP. As it was mentioned in the instrumental chapter of this thesis, two-probe measurements are usually a more convenient approach to obtain some preliminary information about the nano-subject of the study. In addition, just based on the fact that most of the nanowire-based electronic devices are designed with two-terminal layout (source and drain electrodes), the investigation of their intrinsic electrical properties in a comparable to real-life setup is also crucial for their future applicability.[272] Therefore, we will start this section with the results obtained for the two-probe configuration. Then, to eliminate the variable nature of the contact resistance in the measurements, and obtain a truthful picture of the transport properties at the nanoscale, the four-probe configuration will be considered.[273]

3.4.2.1 Two-probe configuration

The initial study of transport properties was performed with the two-tip technique. In a one-by-one manner, each of the tips would be automatically approached within the tunneling distance from the nanowire (001) facet. The approached tips would be stabilized whilst in tunneling regime and once attained, the tips would be manually brought closer towards the sample surface until the contact is established. The utmost caution is needed for this step, in order to avoid any damage to the surface reconstruction, but also to the contacting probes.

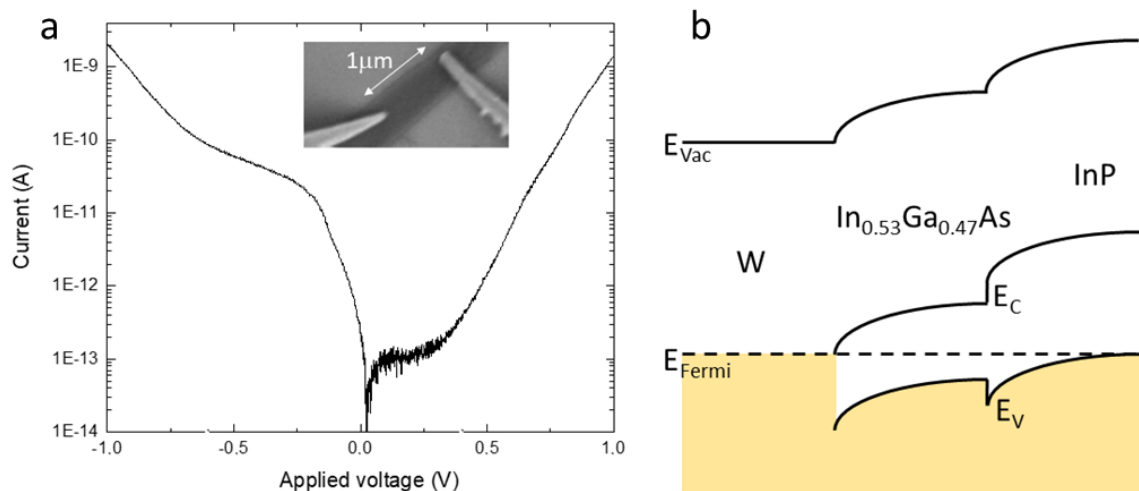


Figure 3.20 Charge transport measurements in two-tip configuration. (a) $I(V)$ characteristic measured between two W tips connected to the $\text{In}_{0.53}\text{Ga}_{0.47}\text{As}$ (001) surface of a nanowire and separated by a distance of $1\mu\text{m}$. (b) Schematic energy band diagram showing the band alignment at the interface between a W tip and a $\text{In}_{0.53}\text{Ga}_{0.47}\text{As}$ nanowire grown by selective area on a p-type doped InP (001) substrate.

With secure contacts in place, the sample would be disconnected from the ground (floating configuration) and the charge transport measurements could be performed. The voltage ramp would be applied to one of the two tips, which were kept at the constant distance of 1 μm , while the other tip would be set at 0 V and thus, act as a ground. In this configuration, the current will flow along the path of the lowest resistance between the two STM tips.

The results of this experiment are presented in Figure 3.20a. At this point it is worth mentioning that the bias voltages are defined in reference to the grounded sample, i.e. the unoccupied states are probed at (V) being negative. The I-V characteristics near the zero-bias point (Fermi level) exhibited a typical rectifying behavior. The initial non-zero current region at negative side of the spectrum is linked to steady charge injection into the conduction band of InGaAs, for reference please consult the energy band diagram in panel (b). However, upon increasing the voltage to -0.58 V, additional features can be seen. At this point, the electrons are efficiently injected from the STM tip to the InP substrate below the nanowire and thus, a new channel is opened, as indicated by a sudden change of slope in current. This is prompted by the fact that the electron affinity of $\text{In}_{0.53}\text{Ga}_{0.47}\text{As}$ is 4.5 eV[274] and that the workfunction of clean tungsten is also 4.5 eV[275]. Hence this material combination is suitable for the formation of an ohmic contact, as the Fermi level position will be at the bottom of the conduction band. As a result, the electron barrier height is negligible in this system, yielding an ohmic contact between tungsten and the clean and well-ordered $\text{In}_{0.53}\text{Ga}_{0.47}\text{As}$ (001) surface. On the positive side, the I-V trace begins with a region where no current is detected, followed by a steeper slope in current if compared to negative side, which is linked to the transport through InGaAs valence band.

This zero-current region, with significant level of noise, corresponds to the energy range of the forbidden gap of InGaAs. However, due to the p-type doped InP substrate, the downward band bending make valence band states available before the Fermi level of the tip reaches the top of the valence band at the surface of the nanowire. Indeed, the electrons can tunnel through part of the InGaAs material. Therefore, the width of the zero-current is smaller than the band gap of $\text{In}_{0.53}\text{Ga}_{0.47}\text{As}$ (0.82 eV at 5K).. While the two-probe method does not provide a direct access to the band offset and requires simulations of the current, this experiment shows that an ohmic contact is achieved between W tips and the clean and well-ordered InGaAs (001) surface.

3.4.2.2 Four-probe configuration

The variable distance DC electrical measurements of $\text{In}_{0.53}\text{Ga}_{0.47}\text{As}$ cross-shaped nanostructures were carried out with the Omicron VT-Nanoprobe system. As mentioned above, regardless of the type of contact (Ohmic or Schottky), the four-probe configuration allows for accurate measurements of the sample resistance because it circumvents any influence of contact resistance.

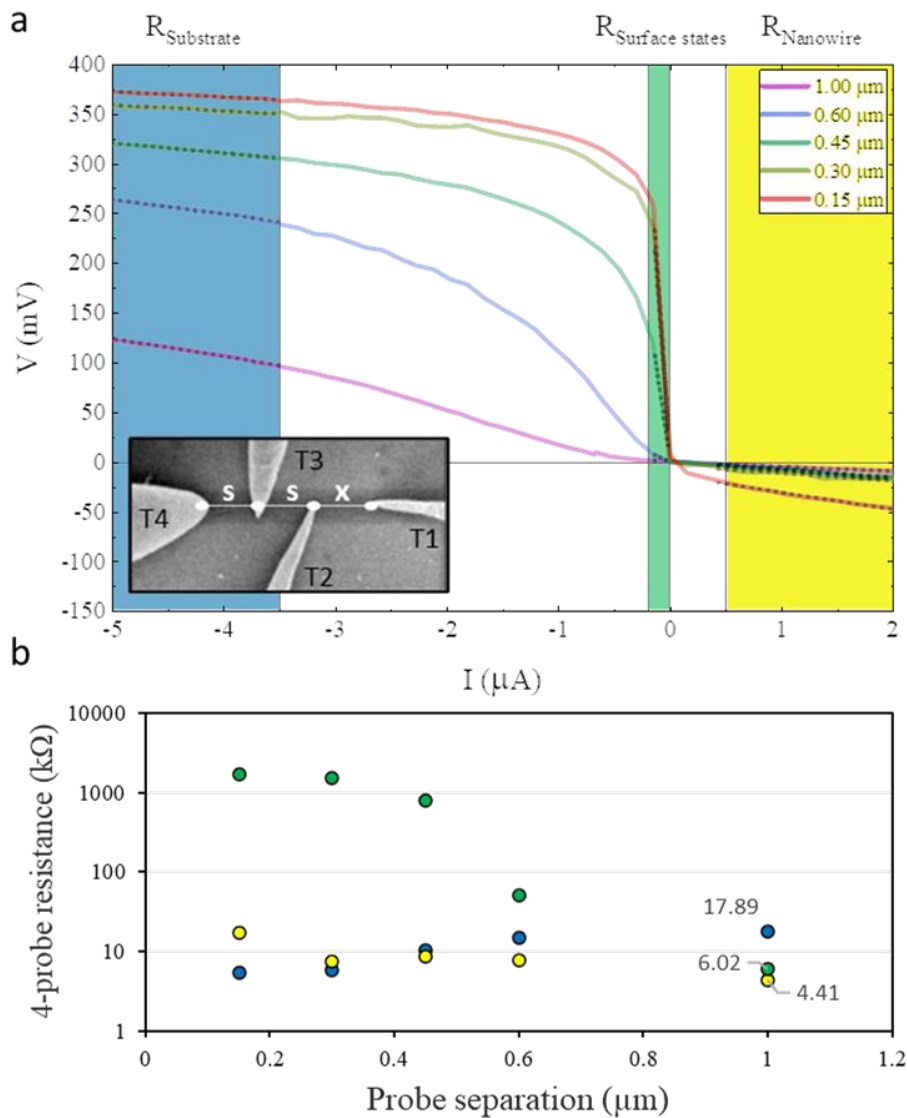


Figure 3.21 Probe-spacing dependence of the resistance of a $\text{In}_{0.53}\text{Ga}_{0.47}\text{As}$ cross-shaped nanowires measured at room temperature by four independently driven STM tips in contact with its (001) facet. (a) V-I curves at 5 different probe spacings $x = 1 \mu\text{m}$; $0.6 \mu\text{m}$; $0.45 \mu\text{m}$, $0.3 \mu\text{m}$ and $0.15 \mu\text{m}$. The inset of the panel shows a SEM image of the four tips (T1, T2, T3 and T4) which were placed in a line configuration. Three colored regions highlight the transport through the bulk of the nanowire (yellow),

its surface states (green) and the substrate (blue). (b) Resistance vs. probe separation plot deduced from the linear fits of the segmented V-I curves in panel (a).

The layout which was used in this experiment involved two outermost probes contacting the nanowire to have voltage applied between them and thus be utilized as source and drain electrodes. In the following text they are denoted as T1 and T4, respectively. Whereas for the remaining pair of inner probes, they were set at high impedance (T2 and T3) and used for voltage sensing. The inset of Figure 3.21 shows the positioning of the probes. The separation (s) of $1 \mu\text{m}$ between the T2, T3 and T4 was kept constant throughout the measurements, while the position (x) of the current sweeping probe (T1) was being varied from $1 \mu\text{m}$ to $0.15 \mu\text{m}$ apart from the T2. The data points recorded for five different values of x are presented in Figure 3.21a and show three clearly distinguishable linear zones of charge transport which are marked by dotted lines. The potential drop across the two zones at the far ends of the probed positive and negative current appears to be low and comparable throughout the series. However, the two are separated with the zone at negative values of current where there is a strong deviation of the potential drop with the change of probe separation. This is also clear from the values of the four-probe resistances in Figure 3.21b which are given by the gradient of the V-I curves ($R^{4P} = V / I$). In order to understand the origin of this behavior, it is necessary to list all the possible paths for an electron to take between T1 and T4.

The three linear segments were linked to charge transport taking place via the nanowire surface states, the nanowire bulk and the InP substrate, as illustrated by the 2D and 3D schematics in Figure 3.22. The nanowire itself is not intrinsically doped, yet the highly doped substrate artificially p-dopes it, as discussed before. As a result, injecting electrons inside of it, should result in a low potential drop (low resistance, R_{NW}). In contrast, the electron extraction process is expected to be difficult due to the low carrier density. However, one should not neglect the contribution of the surface current, a consequence of its (2 x 4) surface reconstruction and presence of missing atom/adatom defects. The surface states are the shortest physical path between the tips, but they can be quickly saturated as the electrons are extracted, resulting in high measured potential drop (R_{SS}). And lastly, at certain value of the voltage the electrons can be extracted from the InP substrate below. To determine the conductivity of each of the three channels in linear non-equidistant four-probe configuration the following relations were used[199]:

$$R_{3D}^{4P}(s, x) = \frac{\rho_{3D}}{2\pi} \left[\frac{1}{x} + \frac{1}{2s} - \frac{1}{s+x} \right] \quad (3.9)$$

$$R_{2D}^{4P}(s, x) = \frac{\rho_{2D}}{2\pi} \left[\ln\left(\frac{2s}{x}\right) - \ln\left(\frac{s}{x+s}\right) \right] \quad (3.10)$$

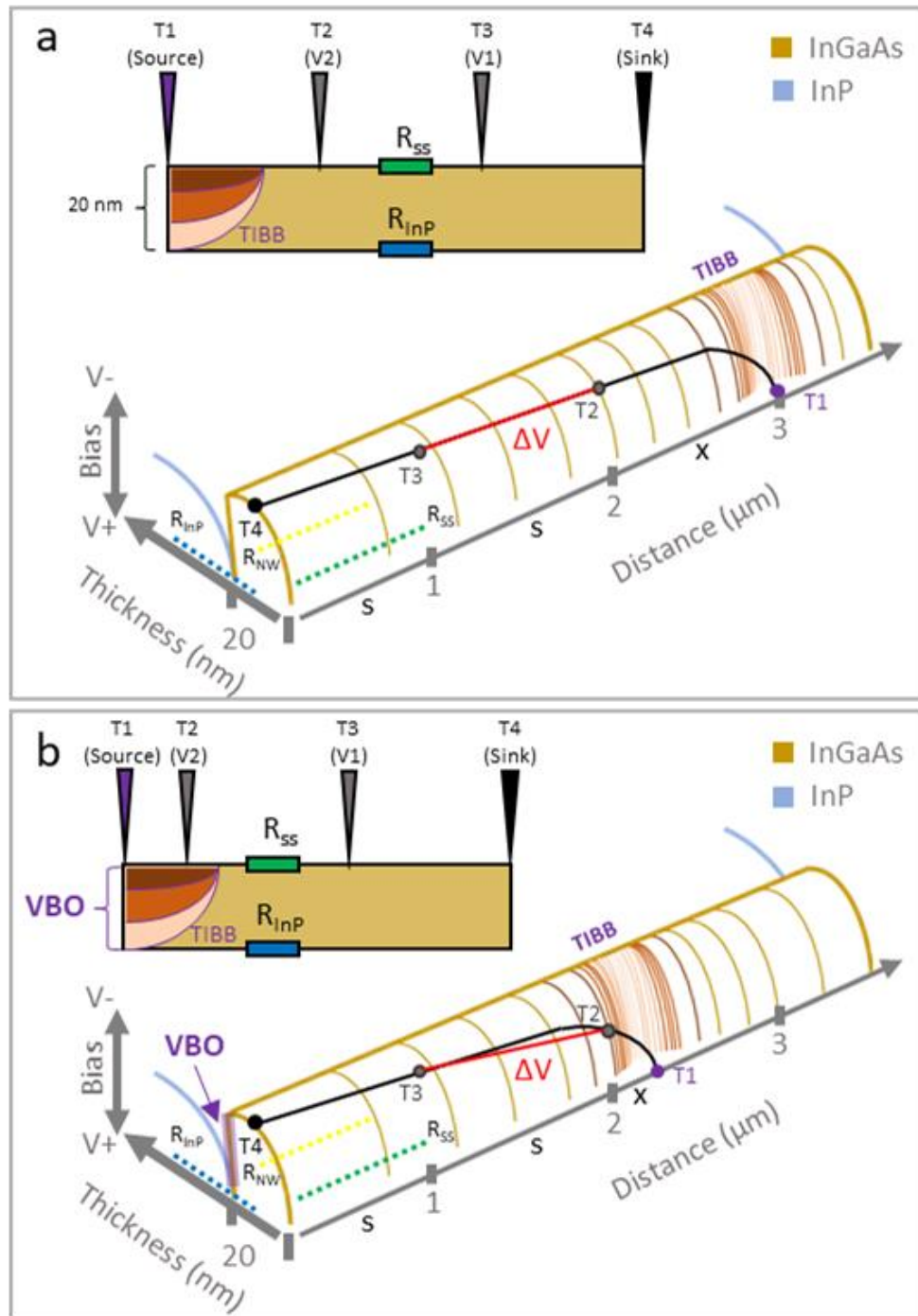


Figure 3.22 The 2D and 3D schematic representations of the In_{0.53}Ga_{0.47}As cross-shaped nanowire valence band when negative values of current are probed in four-probe configuration: (a) the tips are positioned to be equally spaced from each other and (b) when the source probe (T1) is brought in close

vicinity of the neighboring potential probe (T2). The two out of three axes are dimensional and indicate nanowire thickness and probe separation along it, while with the remaining vertical one, the polarity of the source probe is depicted. The InGaAs and InP valence bands are presented in pale yellow and blue, while the three possible carrier paths are indicated with dashed blue, yellow and green lines for R_{InP} , R_{NW} and R_{SS} , respectively. The spatial extension of the tip-induced band bending (TIBB) is illustrated by the color gradient from dark brown to light pink. VBO stands for valence band offset between the two materials and ΔV is the measured potential drop.

For the transport through the InP substrate and the nanowire, at the equidistant tip position of 1 μm , the Eq. (3.9) yielded the conductivity of 0.089 S/cm and 0.361 S/cm, respectively, while with the Eq.(3.10) the surface conductivity was calculated to be 3.67×10^{-5} S/cm. Making a simple estimate of the conductivity of 500 nm-wide and 20-nm thick InGaAs nanowire, for the highest possible carrier concentration ($3 \times 10^{18} \text{ cm}^{-3}$) and deducing the minimum of the resistance expected for the equidistant probe separation one obtains $1.73 \times 10^5 \Omega$, a value far greater than the one obtained experimentally. Therefore, in our 3 channel-layout, the resistance of the nanowire can be neglected. Furthermore, using the Eq.(3.10) to extract the conductivity of the resistance channel at 150 nm probe separation at negative current, one obtains $2.3 \times 10^{-4} \text{ S}/\square$, a value comparable to the surface conductivity ($1.6 \times 10^{-4} \text{ S}/\square$) of $\text{In}_{0.53}\text{Ga}_{0.47}\text{As}$ quantum well.[267]

With each of the electron paths identified, the probe separation dependence can be explained as follows. The increase of the negative current leads to a larger depleted region around the source, due to the saturation of the surface states. As illustrated in Figure 3.22a, this localized tip-induced band bending will not be detected when the separation between the tips is large enough. However, bringing the source probe closer and closer to the neighboring voltage sensing probe will result in the measurements of the accumulative voltage drops, but only up a certain saturation point which stays constant even with the further decrease of (x) below 300 nm, see Figure 3.22b. Since the measured voltage drop reflects both the variation of the electrostatic potential and local carrier concentration, when another channel is opened the strong deviation should dissipate. Interestingly, in our case the point of saturation was consistently measured to be around 350 meV, which is slightly smaller than the previously measured value for the valence band offset, using the single tip STS method described above. Indeed, exceeding this potential barrier results in additional electrons being transferred from the InP substrate to the InGaAs nanowire region located under the source probe.

3.5 Conclusions

In this work we have shown the ability of a combined SPM techniques to accurately measure band offsets in planar substrate-based heterostructures, in correlation with structure morphology. Together, SEM, AFM and LT-STM measurements were used to address the morphology of various $\text{In}_{0.53}\text{Ga}_{0.47}\text{As}$ selective area grown 1D nanostructures on InP (001). The initial SEM study served purpose to identify, classify and select the nanostructures which were later a subject of the SPM measurements. The overall morphology of the planar nanostructures which were comprised of nanowires extending along [110] and [1-10] directions was investigated with AFM. The images resulting from this study revealed that the hydrogen assisted MBE growth has excellent selectivity with respect to the SiO_2 mask and a large-scale nanostructure reproducibility. In addition, a strong dependence of the shape of the nanostructure with respect to its orientation on the surface was observed. The data obtained from the detailed AFM analysis of the non-homogeneous profile of the top (001) nanowire facet was modeled in order to obtain values of the surface diffusion length. The surface migration of the group III adatoms from the nanowire sidewalls towards the edge of the structure was hindered across [1-10] direction. Perpendicular to that (across [110] direction) the diffusion length was determined to be 110 nm. This description of the precursor dynamic was in a good agreement with the follow-up LT-STM study, as it revealed the As-rich (2 x 4) (001) surface reconstruction, which, due to the asymmetry of the dimer rows, give rise to anisotropic diffusion lengths. Next, the electronic properties of these nanostructures were investigated. The single- and two-probe LT-STS study was used to accurately measure conduction and valence band offsets at the $\text{In}_{0.57}\text{Ga}_{0.43}\text{As}/\text{InP}$ heterointerface, with the former being 210 meV and the latter 400 meV. The combined capabilities of two- and four-probe contact measurements gave us the information about the carrier transport properties in these nanostructures. It was determined that the tungsten probes form an ohmic contact with the InGaAs nanowires, while the carrier transport is governed over three possible channels, through the bulk nanowire (0.089 S/cm), through the nanowire surface (3.67×10^{-5} S/cm) or through the p-doped InP below (0.361 S/cm). The voltage threshold at which the lastly mentioned channel becomes accessible to the carriers was measured to be around 360 meV, further confirming the previously obtained value for the valence band offset.

Altogether, our results establish this methodology as an effective experimental platform to study the atomic scale topography and nanoscale electronic properties of the 1D semiconductor nanostructures.

Chapter 4. Quantum confinement and band alignment in CdSe NPL-based heterostructures

4.1 Introduction

With the clear goal of investigating the effects of band-alignment in conjunction with quantum confinement in one-dimensional nano-heterosystems, we have expanded our research towards nanostructures obtained by the means of colloidal synthesis. This allowed us to go beyond, or better yet, below the technological size limit of the selective area grown nanostructures (< 40 nm), while retaining high shape-control and structure quality. This has been made possible, since over the past two decades the field of colloidal semiconductor-based nanocrystals has been experiencing a steep upsurge. The growing interest can be found equally present in both academic and industrial sectors, while its main fueling agents are tunable, scalable, and cost-effective synthesis coupled with wide range of potential applications in optoelectronics. First, synthesis utilizes the flexibility of the colloidal chemistry to vary nanocrystal size, shape, and composition at a detailed level, and consequently their chemical and physical properties. Then, this field of research exploits those newly designed traits for the design of future devices, such as light emitting diodes, lasers, bio-sensors etc.[276]–[278]

As previously mentioned in the introductory part of this thesis, the nanostructures of such a small dimension are expected to exhibit the signs of quantum confinement effect. To whichever extent it is present, it will be directly reflected through heavy modification in the band structure of a given material, as previously observed in the case of quantum dots[279] and quantum rods[280]–[282]. Therefore, even the slightest morphological changes will have influence on the optical and electronic properties of certain geometries. This is the main reason why CdSe NPLs stand out among other Cd-chalcogenide-based colloidal nanostructures as the thickness of these nanocrystals can be tuned with atomic monolayer precision. However, prior to the design and study of heterointerfaces, one should first have a good grasp on the properties of each of its constituents. For example, there has been a strong belief that CdSe NPLs have electronic properties of a quasi-two-dimensional quantum well.[283], [284] Yet, optical absorbance, luminescence, and excitation spectroscopies have been mostly used to study these types of systems. Therefore, having to question and reevaluate their true electronic nature, we have moved from optical spectroscopies, which involved electron transitions between two levels, towards probing the density of states in the valence and conduction bands. This task demanded a scanning tunneling spectroscopy study, as it can probe the complete density of states in the absence of selection rules. We focused on CdSe NPLs deposited on a gold substrate and investigated their electronic structure as a function of their thickness, spatial configuration, and temperature.

4.2 Growth of CdSe NPLs

When it comes to wet chemistry synthesis of various nanostructures, the choice of materials has been mainly limited to II-VI group (CdSe, CdS, CdTe), owing to the difficulties in controlling growth and nucleation kinetics of III-V semiconductor-based systems (InP, InAs).[285] Nonetheless, this did not hinder the development of the novel synthesis protocols of metal chalcogenides semiconductors, yielding a plethora of nanostructures of various dimensionalities and geometries, in return opening the possibility to fine tune their physical and chemical properties. From the synthesis point of view the most prominent nanostructures are zinc-blende colloidal NPLs due to their anisotropic growth. This property allows for exceptionally fine control of their size and thickness. As the latter can be defined by the integer number of atomic monolayers, the nomenclature commonly used to describe these systems is defined as follows: $N \cdot A_{\text{CdSe}} / 2$, where N is an integer and A_{CdSe} is the CdSe lattice parameter for the zinc-blende crystal structure.[283] For example, the nanoplatelet comprised of three, four and five CdSe MLs will have thickness of around 1.06 nm, 4.5 MLs (≈ 1.37 nm), and 5.5 MLs (≈ 1.67 nm), respectively.[286], [287] However, in literature, it is common to find thicknesses expressed with an additional half integer number accounting for one more additional Cd-terminated plane.

In the following paragraph, the step-by-step synthesis procedure of one of our samples will be used to explain growth kinetics of these nanostructures. The sample in question is the 5.5 monolayer-thick CdSe nanoplatelets and the synthesis was performed using the protocol reported by Singh et al [138]. In general, synthesis of ZB NPLs can be sectioned into three parts. The first part involves the formation of seed particles from the precursors, the second one is associated with the growth of the nanoparticle and its lateral extension and finally, the third, which is nothing but the purification of the final product.

1st step: Cadmium myristate (0.340 g) and 25 mL of 1-octadecene (ODE) were degassed under vacuum in a three-neck round bottom flask. Following this, the temperature of the flask was raised to 250 °C under an inert atmosphere and 0.024 g of Se dispersed in 1 mL of ODE was swiftly injected into the flask. Here, abiding to the standard colloidal synthesis formula, Cd-precursor and Se powder are the main reactants which will fuel the formation of the seed particles, while the ODE acts as a solvent and ensures homogeneous reaction medium in which the precursors are soluble. The degassing step under vacuum and higher temperature is done to remove any atmospheric water trapped in the system. This is important, since the stoichiometry of the precursors controls the lateral extension and overall shape of the grown NPLs, as it was well demonstrated in the publication by Guillaume H. V. Bertrand et al.[288]

2nd step: A minute later, cadmium acetate (0.240 g) was introduced. The reaction was left to proceed for 6 min at 250 °C, after which 1.5–2 mL of Cd-oleate, preheated at 100 °C, was injected. Achieving a parallelepiped from a cubic structure requires inequivalent growth kinetics among different crystallographic surfaces. The growth kinetics are determined by temperature, facet surface energy and the type of ligands. With the injection of Cd-acetate the reaction which facilitates selective anisotropic growth by lateral extension of the NPLs is triggered. This occurs due to differences in energy required to create a full top or bottom facets and the energy needed for the formation of an extra layer on the side facets, which results in vastly different lateral and vertical growth rates.[289] A fully grown CdSe NPL is comprised of integer number of alternating Cd- and Se- atomic planes stacked together in the

[001] direction, while the outermost uncoordinated atoms are passivated with oleate ligands. This passivation is accomplished with the addition of Cd-oleate which stops the reaction by blocking all the remaining reaction sites.[290]

3rd step: The heating mantle was removed immediately after this, and the solution was allowed to cool down to 50 °C. After the synthesis, the reaction product was suspended in n-hexane and ethanol and subjected to centrifugation. The orange-red supernatant was discarded, and the precipitate was again suspended in n-hexane and centrifuged. This time the precipitate was discarded, while the supernatant was collected and diluted in n-hexane for future characterizations. For the synthesis of thicker NPL (above 3.5 ML) it is likely to have the presence of spherical quantum dots as by-products. The first purification cycle separates these from the nanoplatelets by using n-hexane and ethanol mixture. It has a role to suspend the NPLs, while the second acts as an anti-solvent. The second purification cycle is performed to remove any unreacted Cd-acetate from the final product.

Synthesis of 7.5 ML-thick NPLs:

This NPL population was synthesized by the protocol given in ref. [291] Here, 170 mg of Cd-myristate (0.3 mmol), 24 mg of Se powder and 15 mL of ODE were mixed in a 50 mL three neck flask and degassed under vacuum at 120 °C for one hour. Then the mixture was heated under argon flow, with the temperature set at 240 °C. When the solution turned deep orange (around 220 °C), 90 mg of Cd (Ac)₂ powder was added. The reaction was then maintained at 240 °C for 10 minutes. The mixture was subsequently heated up to 315 °C. Then, 1 mL of cadmium chloride/cadmium oleate solution was injected and the reaction was maintained at the same temperature for 2 hours.

4.3 Bare cadmium-selenide nanoplatelets

On the path towards attaining a good knowledge of the physical and chemical nature of colloidal NPLs, achieving a tunable and reproducible synthesis is only the first step. The next challenge is to perform reliable and accurate measurements of the NPLs, either in a stand-alone configuration or within an ensemble. For this reason, sample preparation is crucial. Dispersed in a solution or deposited on a substrate, CdSe NPLs can adopt one of the two stable spatial configurations. The first one involves individual NPLs lying flat on the given substrate, while the second entails multiple NPLs to self-assemble into long domino-like stacks. In practice, this is achieved by drop-casting or spin-coating, or even the combination of both. For the final purpose of investigating the electronic properties of these nanostructures, we have deposited NPLs of different thicknesses on a gold substrate and investigated in great detail the morphology of a single NPL or ensemble of them, using LT-STM. To have a complete picture, this comprehensive study also included other complementary techniques such as atomic force microscopy (AFM), scanning electron microscopy (SEM) and transmission electron microscopy (TEM).

Sample preparation procedure:

In our LT-STM experiments, we have focused on two NPL populations capped with oleate ligands having intended thicknesses of 5.5 ML ($d_{5.5} = 1.67$ nm) and 7.5 ML ($d_{7.5} = 2.25$ nm). Sample preparation was in large part the same for both populations. NPL that were suspended in the hexane solution were drop-casted directly from the solution onto the gold substrate. This substrate was found to be suitable for the follow-up LT-STM measurements due to its high conductivity, purity, and relatively low roughness. The number of drops was determined empirically to achieve appropriate concentration of the nanocrystals on the surface. Once each drop contacted the sample, it was swiftly dried away using nitrogen flux in order to avoid the formation of water emulsions on the surface. However, due to the presence of organic residues in 7.5 ML NPL batch an additional purification step was required. Once the NPLs were transferred to the substrate, the whole sample was slowly immersed into the dichloromethane (highly volatile organic solvent) bath for couple of seconds and subsequently again dried with nitrogen.

Before fully committing to the LT-STM measurements, it is always a good practice to have preliminary evaluation of the sample quality done with less arduous techniques, such as absorption and photoluminescence spectroscopy, scanning electron microscopy (SEM), transmission electron microscopy (TEM) and atomic force microscopy (AFM).

Absorption and photoluminescence spectroscopy:

In Figure 4.1a, the absorption spectra recorded at room temperature is shown. This study revealed two typical resonances corresponding to transitions between the electron and either light or heavy holes. Concerning the PL spectra recorded at RT and shown in Figure 4.1b, it is characterized by a single and sharp Lorentzian line where the maximum energy is compelled by the NPL thickness (2.1 eV for 7.5 ML and 2.35 eV for 5.5 ML species). It might be worth mentioning that our nanoplatelet samples did not consist of a single thickness population within one batch. As it is often the case, colloidal synthesis of these nanocrystals yields a rather sharp distribution of multiple populations in one suspension. However, with the increase NPL thickness of the dominant population this distribution broadens, which

is also evident from our PL spectra acquired from 7.5 ML batch, where there is an evident, yet miniscule presence of 6.5 ML (peak at 2.13 eV) NPL species. Nonetheless, for our experimental purpose, this effect can be neglected. The PL study at cryogenic temperature (4.2 K), revealed two additional bits of information. First one is tied to the fact that the NPLs exhibits a characteristic emission doublet for both populations. Whereas for the second, the small bump extending in the energy range below the band gap energy indicates the presence of the trap states. Far more detailed discussion of the NPL optical characteristics will be given later down in this chapter. However, at this stage, these results serve purpose to substantiate the sample identity and its adequate levels of purity and homogeneity for the follow-up STM experiments.

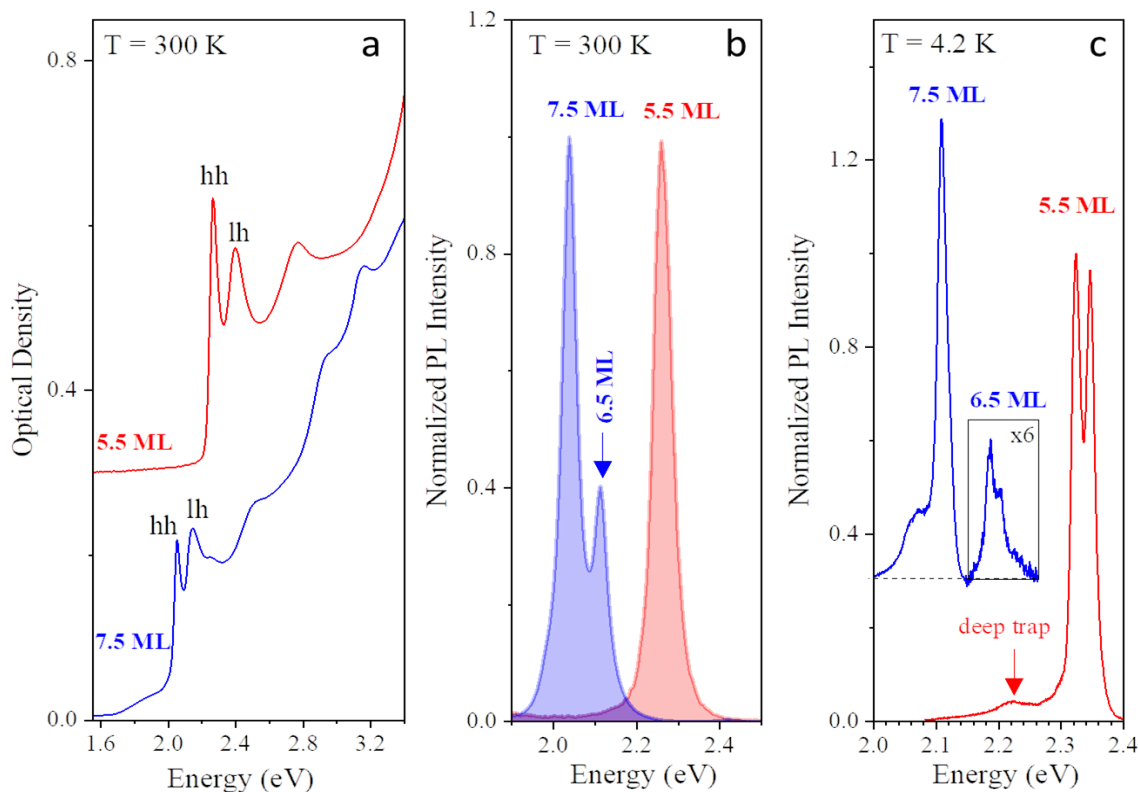


Figure 4.1 Preliminary evaluation of the sample quality of bare CdSe NPLs by means of optical spectroscopy. (a) Absorption spectra, and (b) photoluminescence spectra of 5.5 ML (red) and 7.5 ML-thick (blue) NPLs acquired at room temperature. (c) Photoluminescence spectra at $T = 4.2$ K of 5.5 ML and 7.5 ML NPLs drop-casted on glass substrate. The PL spectra are offset for clarity. The dashed line indicates the baseline for 7.5 ML NPLs. The contribution of 6.5 ML NPLs in the PL spectrum is enhanced by a factor of 6 for clarity. The arrow indicates the deep trap emission in the PL spectra of 5.5 ML NPLs.

Scanning and transmission electron microscopy:

The TEM measurements were done on both NPL species just after their synthesis, whereas SEM images were taken after sample preparation procedure. Analysis of the TEM data revealed that both NPL species have overall rectangular shape, but of different planar dimensions: $21 \pm 2 \times 7 \pm 1 \text{ nm}^2$ for the 5.5 ML-thick NPLs, and $48 \pm 3 \times 9 \pm 1 \text{ nm}^2$ for the 7.5 ML species, as reported in Figure 4.2. In terms of sample homogeneity, the TEM histograms lead to similar conclusions to the ones of optical spectroscopy. It also appears that both populations prefer to self-assemble into stacks on the TEM grid.

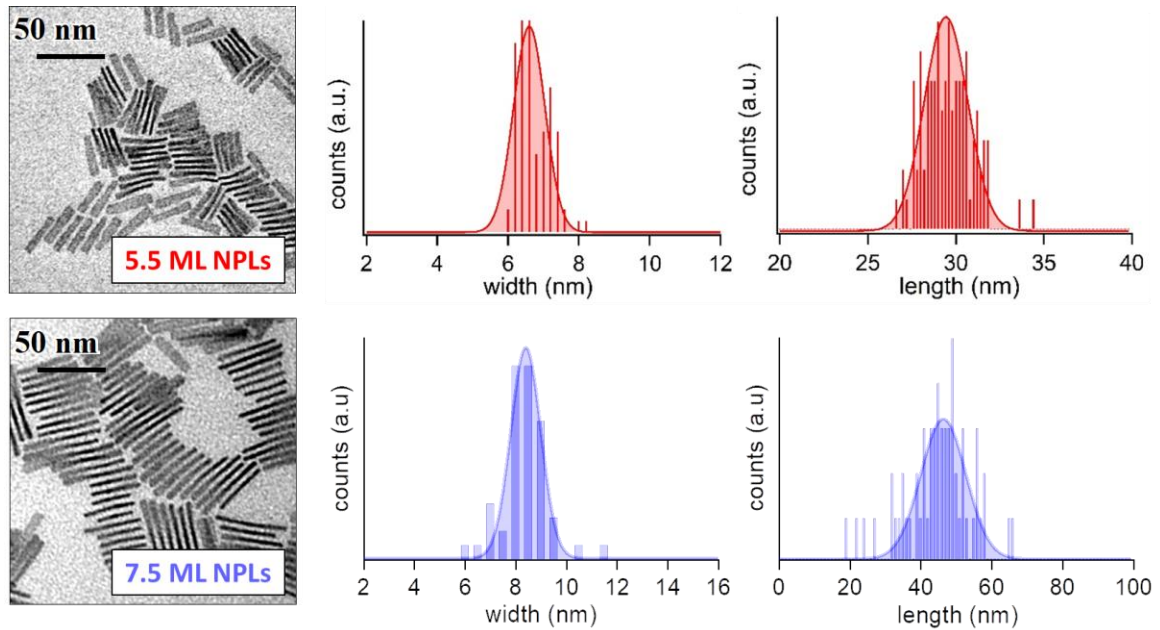


Figure 4.2 TEM morphological study of both 5.5 ML (red) and 7.5 ML-thick (blue) CdSe NPLs, including their respective images and statistics of the length and width.

After the samples have undergone the above-described preparation procedure, the quick SEM check was performed (see Figure 4.3). As expected, on the gold substrate the 5.5 ML-thick NPLs (inset (a)) preserved the predominantly stacked configuration, consistent with the TEM study. Whereas for the 7.5 ML NPL species (inset (b)), this was not the case. Even though, the purification process itself could have been deemed a success since no organic residues were observed, it is clear that their preferential spatial configuration was severely affected. After the deposition, all of the NPLs appear to be lying flat on the surface.

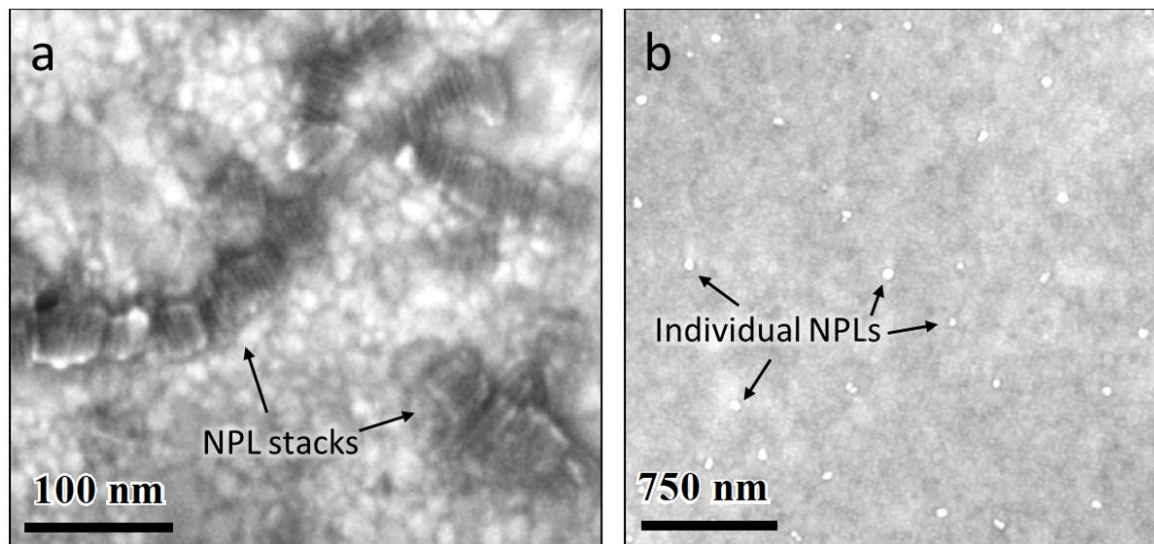


Figure 4.3 SEM images of (a) 5.5 ML-thick and (b) 7.5 ML-thick NPL populations after they have been drop-casted onto the gold substrate.

Atomic force microscopy:

In order to gain more depth perception, the same samples were further investigated with AFM. First off, the 5.5 ML NPL sample, see Figure 4.4a. With measurements performed on microscopically different areas, we have statistically confirmed that the presence of NPL stacks on the surface was much more dominant than the flat-lying individual nanocrystals. Regarding their dimensions, the NPL stacks appeared to be around 9 nm-tall and 40-nm wide, while their length could range up to even couple of hundreds of nanometers. It is clear that the width of the stack, which actually corresponds to the length of the individual NPLs far exceeds the values measured by TEM. This is also true for the height of the stack, which would translate to the single NPL width. To explain these observations, there are some key points to consider in both horizontal and vertical direction. To begin with, it should not be overlooked that the each individual NPL is effectively imbedded in the ligand layer, comprised of oleate molecules which are approximately 2 nm in length. [292] Next up, one should take into account the tip convolution effect and the consequent lateral broadening of the structure. Even then, the measured 9 nm in height does not match the expected 11 nm corresponding to twice the length of ligand molecules and the width of the NPL (7.1 nm). For this, the contact nature of the AFM technique is at fault, as the probe can induce the ligand compression or their mechanical stripping on the exposed side of the NPL. Regardless of the slightly inaccurate values of the measured dimensions, these measurements provide a good preliminary indication that the 5.5 ML-thick NPLs have their longest sides in contact with the surface whilst being in the stacked configuration. Now, concerning the sample containing 7.5 ML-thick NPLs, what was previously seen with the SEM was now also confirmed with AFM. The individual NPLs were found randomly distributed all over the gold substrate, as it can be clearly seen in Figure 4.4b. In addition, the concentration of both 5.5 ML and 7.5 ML NPLs was found to be appropriate for the follow-up LT-STM measurements. Finally, the surface morphology of the gold substrates appeared to be grainy,

but still quite flat with the surface roughness measured to be in the order of couple of angströms, much lower than the NPLs thickness.

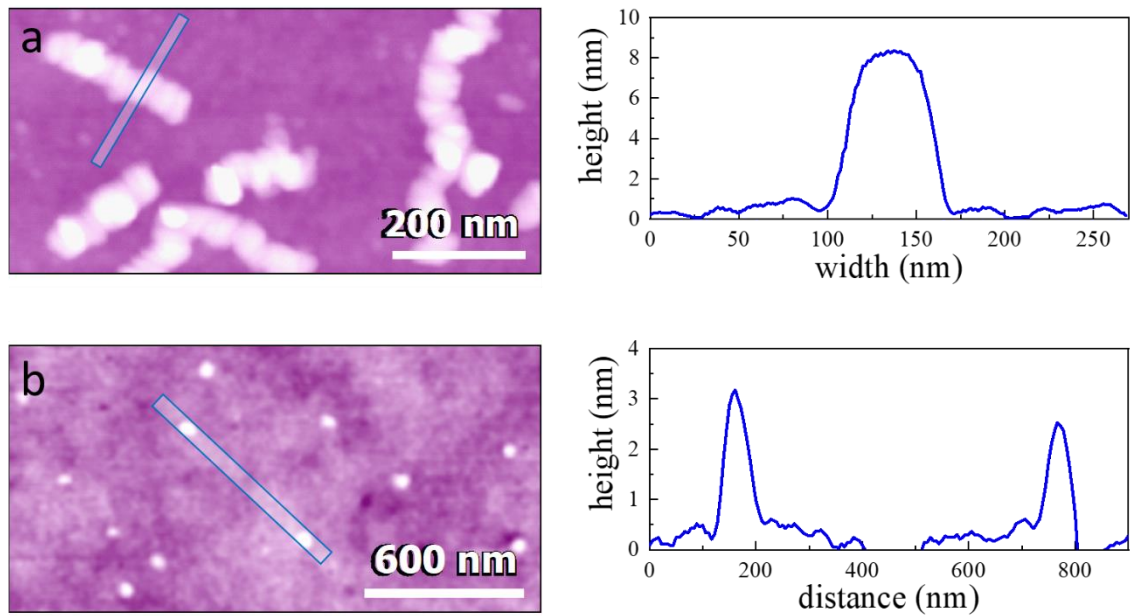


Figure 4.4 AFM study of (a) stacked 5.5 ML-thick NPLs and of (b) isolated 7.5 ML-thick NPLs, after both populations have been drop-casted on the gold substrates. Each of the images is supported with their height profiles taken across the path indicated by the blue rectangles.

4.3.1 STM investigation of the structure morphology

The morphological STM study at 77K and 5K of both NPL populations was performed, and in the following the main results of this experiment are presented.

4.3.1.1 LT-STM on 5.5 ML-thick NPLs

In Figure 4.5, a large STM overview of the 5.5 ML NPL sample is shown. Similar to the SEM and AFM images in Figure 4.3 and Figure 4.4, the surface seems to be covered with randomly distributed NPL stacks. These appear as elongated features with brighter contrast on the images and have apparent height of 10 nm. Statistically, even though their presence is scarce, individual flat lying NPLs can still be found on the surface.

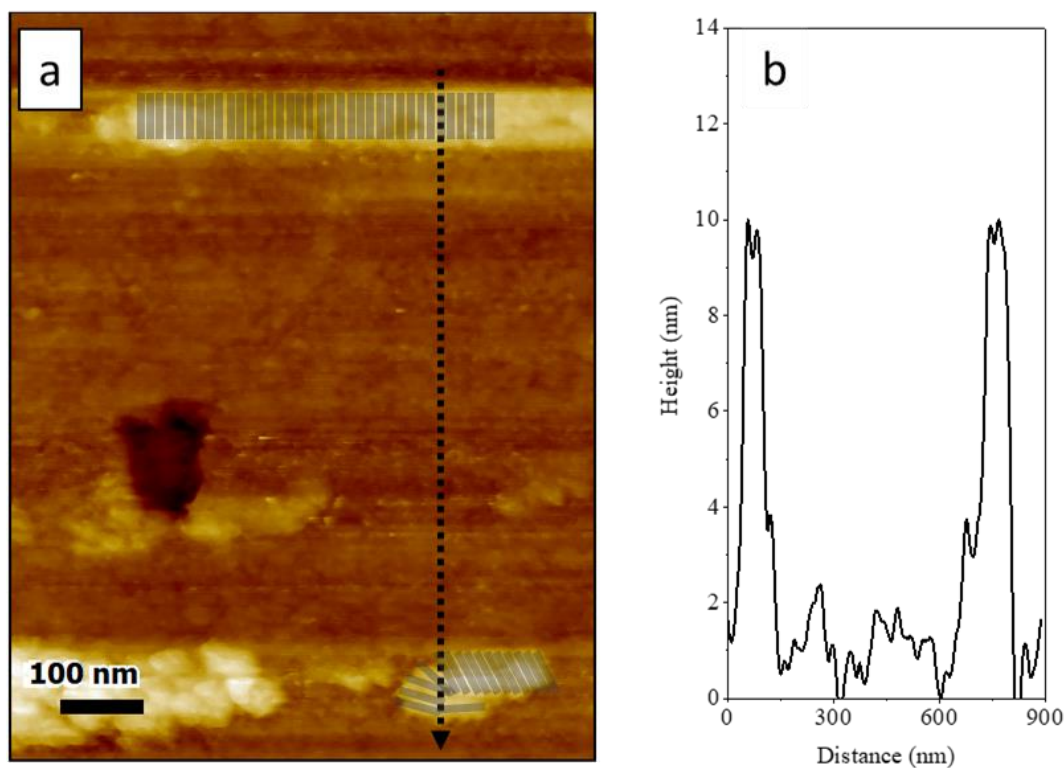


Figure 4.5 Surface overview of 5.5 ML-thick NPL sample recorded at 77K. (a) A large STM image showcasing multiple NPL stacks self-assembled on the surface with corresponding height profile in (b). Feedback parameters: $V_{\text{sample}} = -5$ V, $I_{\text{setpoint}} = 0.01$ nA.

STM on individual flat lying NPLs

The topographic LT-STM study was conducted on individual 5.5 ML-thick NPLs in the configuration illustrated in Figure 4.6a. The 3D STM image in the panel (b) shows the scanned area of the gold

substrate containing two bright protrusions which are linked to two individual NPLs lying flat on the surface. Due to the presence of ligands, unless a “just approached” STM probe is used, the only way to obtain images in which the NPLs are clearly resolved was to scan the surface with exceptionally low values of setpoint current and scanning speed, and quite high applied bias voltage ($|V| > 4V$).

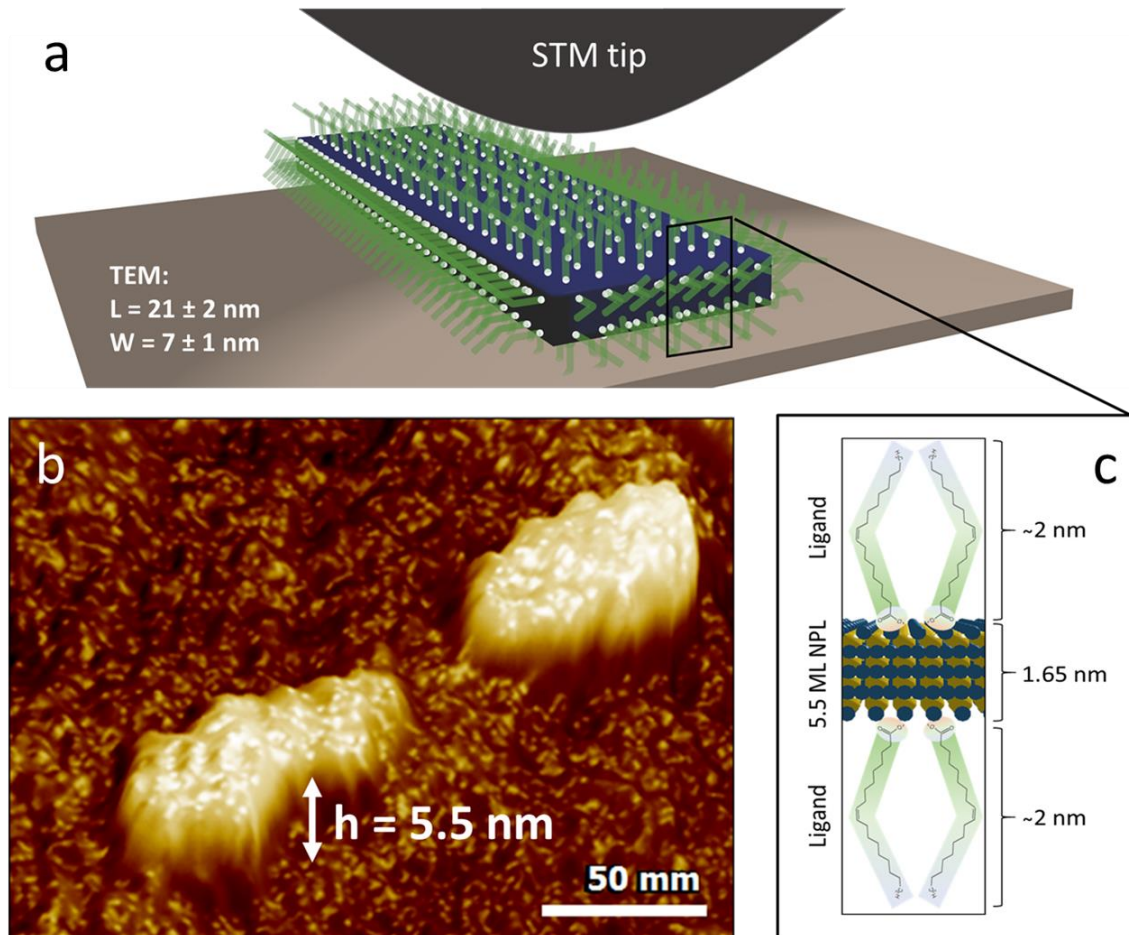


Figure 4.6 STM investigation of individual NPLs lying flat on the gold substrate. (a) Schematics of single flat lying 5.5 ML-thick NPL. (b) 3D STM image of two individual 5.5 ML-thick NPLs. Feedback parameters: $V_{\text{sample}} = -1.5 \text{ V}$, $I_{\text{setpoint}} = 0.005 \text{ nA}$. (c) Schematic representation showcasing a close-up look at the flat lying NPL structure in the vertical direction with respect to the substrate. Objects in the schematic are not in scale.

The reason for this is that the ligands that are used to passivate the NPLs showed a strong tendency to interact with the STM tip. Hence, by increasing the bias voltage, the tip-NPL distance is increased and consequently, the probability of interaction lessened. Sadly, this also has a negative impact on the resolution, which in combination with mechanical instability of nanocrystals results in them having slightly larger and more roundish appearance, instead of the rectangular one. From the height profile

taken across the NPL, we can conclude that the apparent height is measured to be 5.5 nm. If the convolution of the STM tip is taken in consideration, this value corresponds well to the thickness of the NPL (1.65 nm) and twice the value of longitudinal extension of oleate molecules (2 nm). These results also give an indication that the oleate ligand attached to the Cd-terminated NPL facets are quite robust to UHV conditions.

STM on multiple NPLs stacked up together

In this section our findings from the LT-STM investigation of the NPL stacks (illustrated in Figure 4.7a) are reported. High resolution LT-STM image as shown in Figure 4.7b, was acquired on the top of the NPL stack at 5 K, where one can clearly see individual NPLs well resolved within the ensemble.

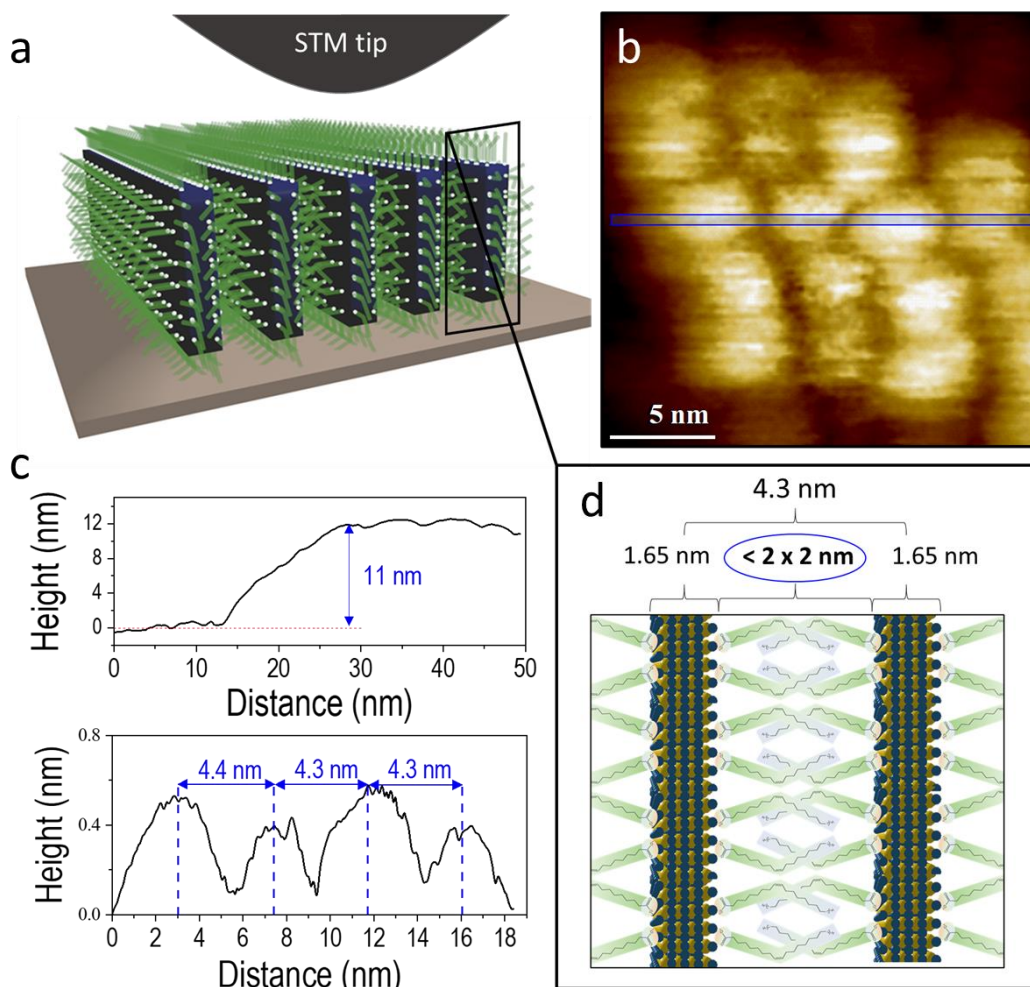


Figure 4.7 (a) Schematic representation of the NPL stack. (b) High-resolution LT-STM image of four individual 5.5 ML-thick NPLs forming a stack. $V_{\text{sample}} = -5 \text{ V}$, $I_{\text{setpoint}} = 0.01 \text{ nA}$. (c) Height profiles acquired

across the edge of the NPL stack (top panel) and on top of it in the longitudinal direction (bottom panel). (d) Schematic representation showcasing the space between two adjacent NPLs within a stack.

This is made possible, since NPL stacks are much more stable on the surface, due to their larger collective dimensions. From the profile in the top panel in Figure 4.7c, the height of stacks was measured to be 11 nm. The 1 nm height discrepancy between the STM and AFM profiles is linked to the non-contact nature of the STM technique (lack of compression of the ligand molecules).

This value is certainly in a good agreement with the prior AFM measurements (a non-contact technique this time around) and corresponds well with the width of the NPL, including the thickness of the ligand layers on the NPL edges. From here, we can conclude the NPLs form columnar ensembles, by stacking together face-to-face, while resting on the substrate on their longest side. In this configuration, NPLs are stabilized together with van der Waals attraction forces originating from ligands.[276] This higher level of stability allowed us to repeatedly scan in the direction perpendicular to nanoplatelets alignment inside the stack and in such a way obtain height profiles taken along the direction indicated by the blue line in the bottom panel in Figure 4.7c. The periodic corrugations of 4.3 ± 0.1 nm correspond to four individual NPLs within the stack. It might be noteworthy that this value is lower than the one measured across the single NPL lying flat on the surface. Such difference clearly indicates that the chains of oleate molecules of the two adjacent NPLs are interdigitated to some extent. However, the explanation behind the clearly present periodicity (Figure 4.7b), derived from lobes of brighter contrast which follow the path along the each individual NPL is still missing.

4.3.1.2 LT-STM on 7.5 ML-thick NPLs

Due to the non-stacking of the 7.5 ML NPLs accredited to the additional purification procedure described above, their STM imaging proved to be much more challenging. Their small dimensions and altered surface chemistry, resulted in them being weakly mechanically coupled to the gold substrate and thus, they would readily move during the scanning with the STM tip. One such example is shown in Figure 4.8.

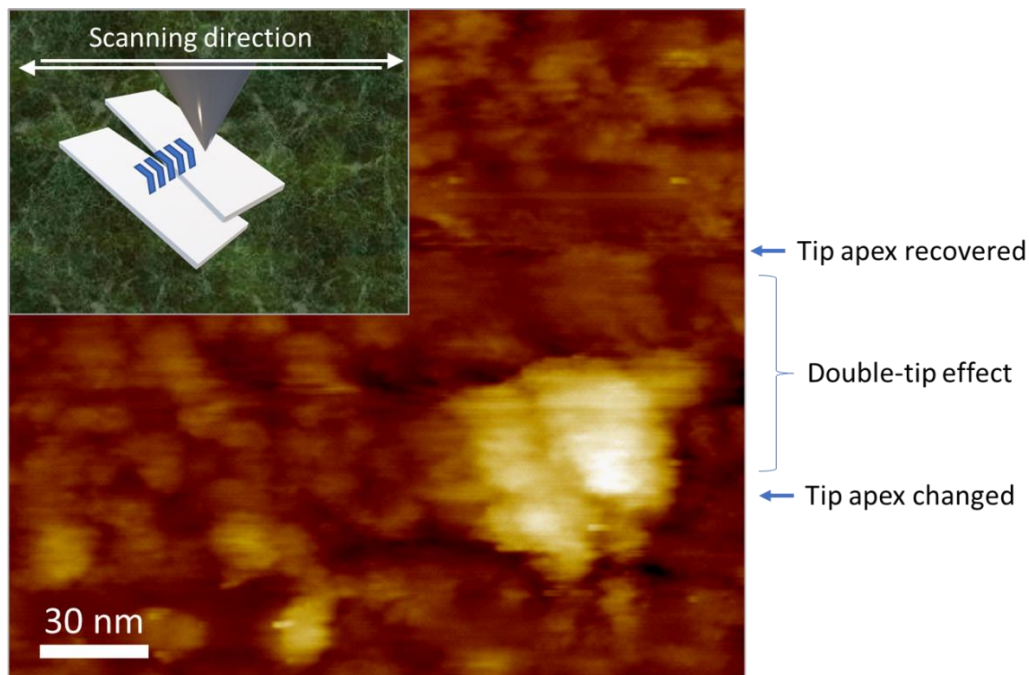


Figure 4.8 STM image showing the topography of the area containing a single flat lying 7.5 ML-thick NPL. The illustration in the inset of the figure is meant to highlight the movement of the NPL during the scan.

Here, imaging a single flat-lying NPL is challenging for two reasons. Firstly, the NPL interacts with the STM tip, changing its apex, which has an effect on the image quality. Secondly and more importantly, the NPL moves between each line scan, resulting in an image which gives the impression that two NPLs are present in the area, instead of one.

4.3.2 STS study of the electronic properties

As discussed in the First Chapter, there are plenty of works which highlight a very promising potential of colloidal nanocrystals for flexible device applications. [293] Yet, in order to take full advantage of such opportunities it is essential to have good fundamental understanding of their optical and electronic properties.

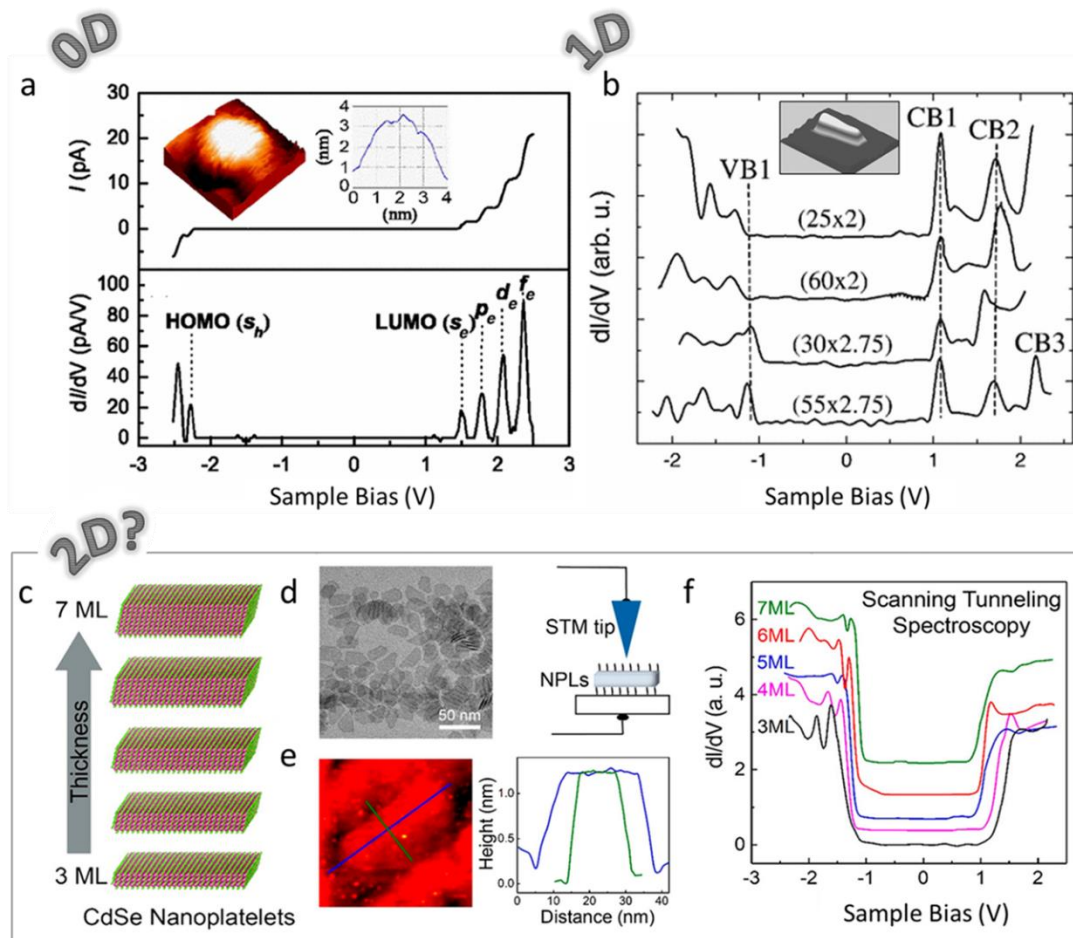


Figure 4.9 Shape-band structure relation in the semiconductor colloidal nanocrystals (a) STS performed at 4.5 K on single CdSe QD, top: I-V curve and STM image with its respective height profile; bottom: the tunnelling spectrum obtained by digitally filtering and differentiating the I-V curve above. Figure extracted from ref. [279] (b) Differential conductance tunnelling spectra acquired from CdSe QRs with different dimensions and STM image of 25 nm x 2 nm QR (inset). Figure taken and adopted from ref. [294] (c) Schematic representation of CdSe NPLs of different thicknesses studied in ref. [295] (d) TEM image 4ML-thick CdSe NPL (left) and illustration of the STS configuration with a NPL lying flat on the substrate (right). (e) STM image of the NPL of same thickness (left) with height profiles (right) taken across the paths indicated by blue and green line. (f) Differential conductance tunnelling spectra of CdSe

NPLs of different thicknesses (from 3ML to 7ML) acquired at RT. Insets (d), (e), and (f) taken and adopted from ref.[296]

With this in mind, past studies have shown that optical and tunneling spectroscopies are two complementary approaches which are suitable for this task. For the first, the allowed transitions between CB and VB states can be investigated, while the other method is able to probe electronic states without selection rules.[197] Such capabilities are necessary, as the density of states of a given colloidal nanostructure will strongly differ depending on its shape. For example, in quantum dots, or artificial atoms as they are commonly referred to, the potential is confined in spherical geometry and only depends on the radius of the particle. The origin of such descriptive sobriquet can be found in the strong quantum confinement which leads to full discretization of the energy levels into delta-function-like states, resembling a hydrogen atom.[297] A good experimental example of this behavior could be seen in the low-temperature STS (Scanning Tunneling Spectroscopy, more information in Chapter 2) measurements performed by Jdira et al.[279] on individual isolated CdSe quantum dots of different sizes. Some of the results of this study are presented in the Figure 4.9a. In the top inset the STM (Scanning Tunneling Microscopy) image shows (left) an isolated, spherical CdSe QD resting on the substrate. From the height profiles (on the right) the radius of QD is estimated to be around 3 nm. By sweeping the sample bias from -3 V to 3V, all while measuring tunneling current an I-V curve can be obtained. The curve in question exhibits step-like characteristics, with each of the steps corresponding to the peaks in digitally obtained differential conductance (dI/dV) graph shown in the bottom inset. Since dI/dV spectra gives direct insight into the density of states, the sharp peaks at negative and positive sample bias can be identified as the discrete hole and electron QD energy levels in valence and conduction band, respectively. However, if the quantum confinement is liberated in one of the three directions the electronic features differ. In Figure 4.9b, the results of STS measurements on CdSe quantum rods of different dimensions are presented. Here, the diameter of the rod is loosely fixed below 3 nm, while the length was varied from 25 nm to 55 nm. In all cases, measured differential conductance spectra did not show any significant variations in the band gap energy or any alternations of saw-tooth shaped density of states. This band structure inertness to the changes in lengths which all far exceed the CdSe Bohr radius of 5.7 nm, further highlights the quasi one-dimensional nature of these nanostructures.[294] To demonstrate further weakening of the confinement, whilst keeping the nanostructure composition the same, most of the literature will refer to the example of quasi two-dimensional CdSe nanoplatelets (NPL). Even though these nanocrystals were intensively studied by optical spectroscopies for more than ten years, [283], [298], [299] the STS measurements were still missing.

Just recently, the paper was published by Ji et al.[296] which showcased the detailed STM and STS study of CdSe NPLs of thicknesses ranging from 3ML to 7 ML as schematically presented in Figure 4.9c. As stated before in Section 4.2, the thickness of these nanostructures is expressed in terms of the number of atomic monolayers (e.g. 3 ML corresponds to ~ 1.1 nm, 4ML to ~ 1.4 nm, etc.) which build up the structure in direction of its shortest dimension. For the STM and STS measurements, the NPLs were drop-casted from a suspension onto the conductive substrates. Once on the surface the nanocrystals could be found distributed randomly and lying flat on their largest facets (see Figure 4.9d, left). Hence the proceeding STM and STS measurements were done in the configuration illustrated on the right in

Figure 4.9d. After the NPLs would be located and identified by STM (see Figure 4.9e), the dI/dV spectra were acquired. The resulting curves revealed mostly 2D-like shape of density of states on both sides of the zero-conductance region, but with a slight caveat on the positive side of the spectra. In specific, in the conduction band the authors have observed sharp rises in the density of states terminated with shallow dips (in Figure 4.9f) rather than plateau expected for typical quantum wells. This certainly leaves some open questions in terms of dimensionality of these nanocrystals. Due to the disparities in electron and hole effective masses, the quantum size effect could manifest itself differently for single particles and electron-hole quasi particles, making the assessment of dimensionality of colloidal NPLs far from a clear cut. In this regard, LT-STs measurements at 77 K and 5 K were carried out in order to shed more light into the topic.

Our STS investigation involved both 5.5 ML-thick and 7.5 ML-thick NPLs deposited on the gold substrate. However, only 5.5 ML-thick NPLs were probed in both spatial configurations (stacked and individual NPLs), for the reasons stated in the previous sections. As the NPLs are completely covered with ligands, depending on which configuration they are measured in, they can exhibit significantly different behavior. From the carrier standpoint, the NPLs are effectively embedded within a dielectric layer. Thus, the carrier path will feature two tunneling barriers, first between the tip and the nanocrystal and the second between the nanocrystal and the substrate, effectively creating double barrier tunneling junction (DBTJ).

4.3.2.1 LT-STs on individual flat-lying NPLs

In Figure 4.10a, b, the dI/dV spectra recorded on the individual flat-lying 5.5 ML and 7.5 ML-thick NPLs at both 5K and 77K are shown. The data reveal a zero-conductance region framed-in with the very sharp peaks at positive sample voltages and a broadened one at negative, both caused by the tunnelling of charge carriers through the NPLs. The measured apparent STM band gaps for 5.5 ML-thick NPL was 2.4 eV at 77 K and 2.97 eV at 5 K, while for the 7.5 ML-ones was 2.05 eV (77 K) and 2.17 (5 K). Clearly, there is an inverse dependency of the width of the band gaps on the variations in NPL thickness and temperature.

First it can be explained by the decrease of the interatomic spacing with the decrease of the temperature, hence the potential seen by the electrons will be enhanced. While for the second, the increase of quantum confinement will cause the similar result, in terms of the increase of the band gap energy. However, to avoid any ambiguities with identification of the spectral features, the real band gap should be justly evaluated. For this purpose, it is convenient to utilize the well-known concept of the lever-arm. A detailed description of this concept is given in Section XY (Second Chapter).

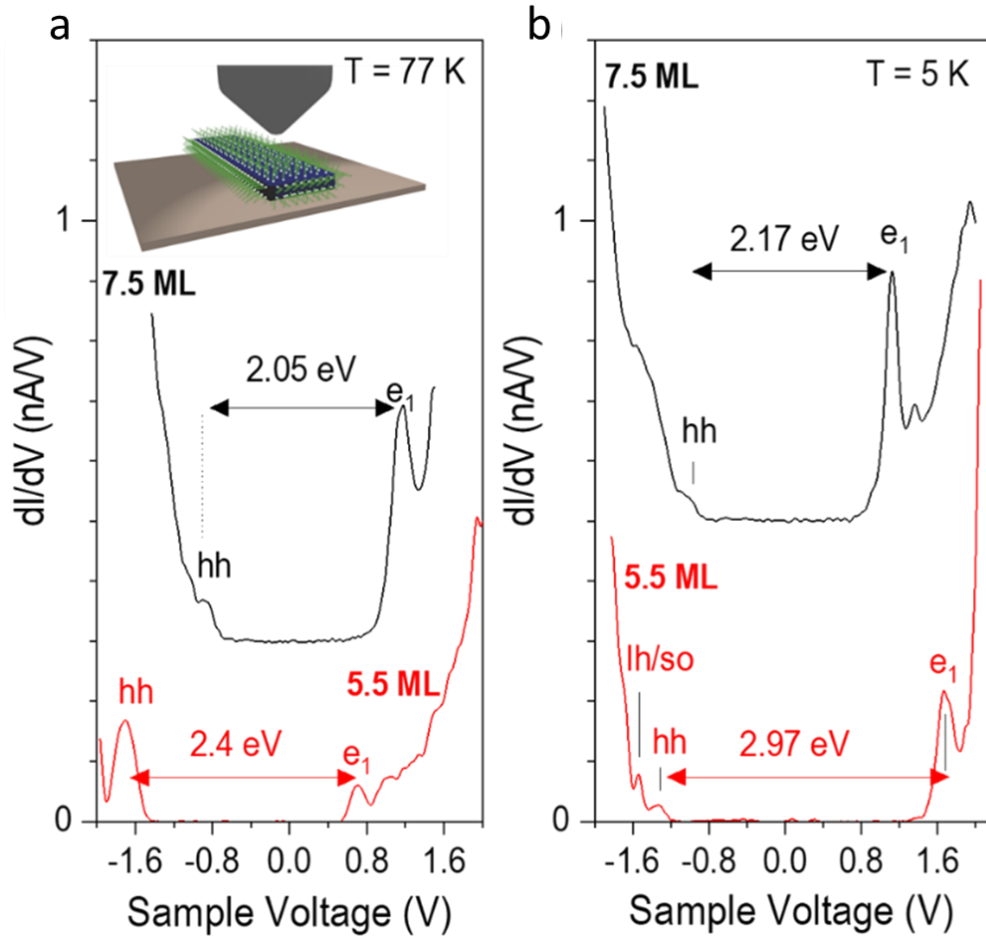


Figure 4.10 Tunneling spectroscopy of individual flat lying CdSe nanoplatelets on gold. (a) Scanning tunnelling spectroscopy of a 7.5 ML NPL (top) and of a 5.5 ML NPL (bottom) measured at 77 K. (b) Scanning tunnelling spectra acquired on a 7.5 ML NPL (top) and on a 5.5 ML NPL (bottom) at a temperature of 5 K. The separation between the lowest peak in the conduction band and the highest peak in the valence band, labelled e_1 and hh respectively, is indicated.

Now in brief, the lever-arm is best described as the ratio between the potential drop across the nanocrystal-tip junction and the voltage applied to the sample with the tip held at virtual ground,[198] or:

$$H = \frac{E_{\text{gap}}}{e(V_{e_1^+} - V_{h_1^-})} \quad (4.1)$$

Here, η is the lever-arm, $V_{e_1^+}$ and $V_{h_1^-}$ are positions in energy of conduction and valence band edge peaks, respectively. As it is the case for individual flat-lying NPLs, a large separation between the STM tip and the NPL is responsible for the transmission probability across the tip-NPL potential barrier to be much

smaller if compared to the NPL-Au junction. Therefore, the DBTJ can be labelled as asymmetric. In other words, the spectra were acquired at a distance where the bias voltage is dropped largely across the tip-NPL junction, and thus, any effects associated with charging can be dismissed.[23] If considering the relation where optical band gap is equal to the apparent STM gap minus the electron-hole attraction energy and multiplied by the lever arm, 7.5 ML NPLs showed a good agreement with the previous optical studies (2.1 eV), whereas the zero-conductance region of the 5.5 NPL was measured to be much larger than the expected value. The explanation for this discrepancy is two-fold. On one hand, the increase of the electron-hole attraction energy in the case of 5.5 ML NPLs can be accredited to the slight divergence in growth procedure, while on the other the in-plane dimensions between the two species naturally differ. More specifically, the larger 7.5 ML-thick NPLs were passivated with the combination of oleate and chloride ligands, which certainly alters the surface chemistry. As a result, one should expect the carrier transfer rate through NPL-Au junction to be more efficient as the width of the junction is reduced due to the presence of the shorter ligands. Hence, for our samples, the values of the lever arm are as estimated: for the 7.5 ML NPLs this number is close to 1, while for the 5.5 ML NPLs it is around 0.85~0.80. Therefore, we can confidently claim that the zero-conductance region (null density of states) gives access to the true information about the band gap of the semiconductor material in question. By performing the sample voltage sweeps, the Fermi level of the tip was resonant with energy levels of the nanocrystal which gave rise to the peaks in the STS spectra. Thus, the measured tunnelling current at positive and negative sample voltages can be linked to conduction band (CB) and valence band (VB) states, respectively. This, in fact indicates the truthfulness of the most important observation from this experiment, which is tied to the shape of the DOS. For both NPL populations, the DOS did not exhibit staircase-like form, a characteristic feature of 2D materials.

4.3.2.2 LT-STs on stacked up NPLs

In the Figure 4.11a, we present spectra acquired on the 5.5 ML-thick NPLs which are stacked together. It is immediately apparent that the measured spectra are characterized by sequences of distinct peaks on both sides of apparent bandgap. The width of the zero-conductance region is comparable to the one measured on individual flat-laying NPLs. As the setpoint current is increased there is a noticeable broadening of the zero-conductance region further confirming the asymmetric nature of the DBTJ system. Hence, one can safely assume that both electron and hole ground states contribute to tunnelling current at positive (CB) and negative sample voltages (VB), respectively. However, it is noteworthy that statistically not all NPL stacks exhibited the same behavior. For instance, in majority of the cases the spectra revealed behavior as in Figure 4.11b where the zero-conductance region is measured to be markedly narrower. In addition, the sharp peak position (V_{e1}^+) at the positive bias fluctuated as far as a couple of dozens of meV with every consecutive spectrum acquired over the course of 30 minutes.

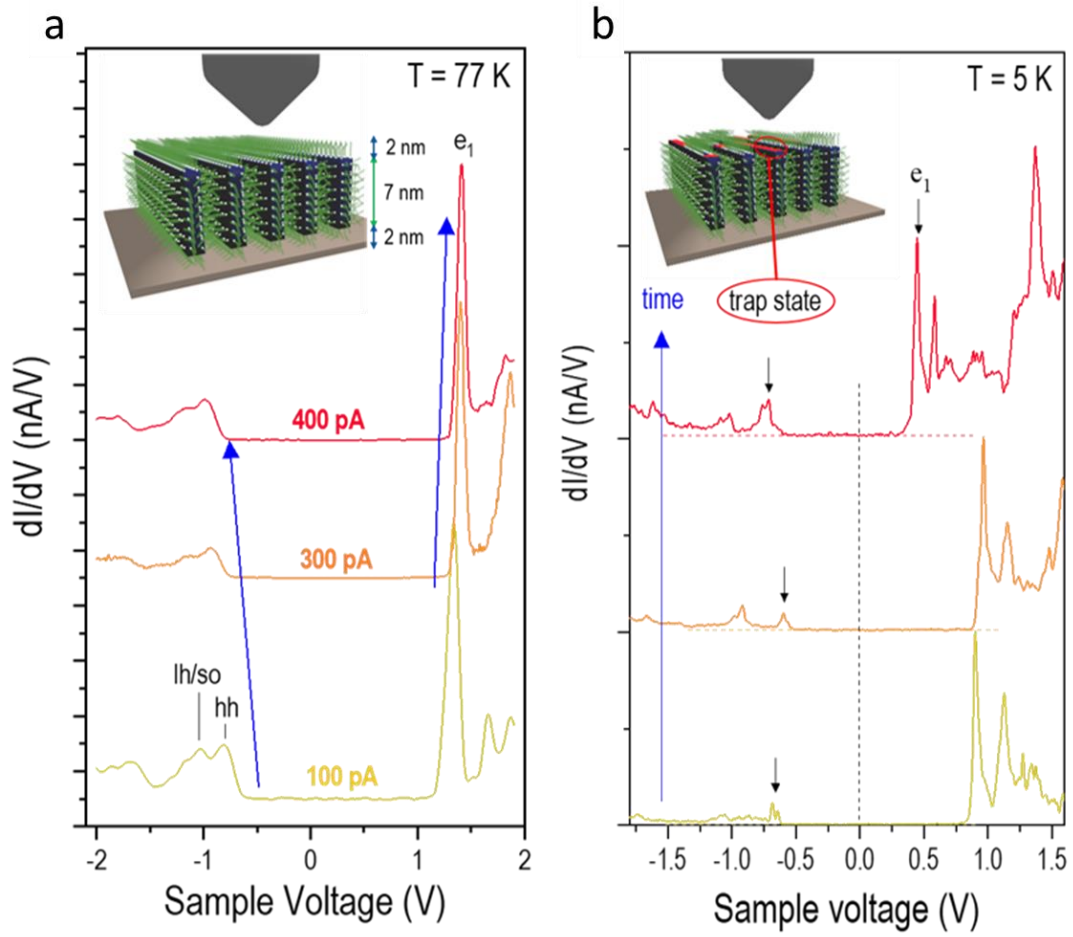


Figure 4.11 Tunneling spectroscopy of CdSe nanoplatelets within self-assembly. (a) Scanning tunnelling spectra acquired on a trap-free NPL within a stack measured at different setpoint currents as indicated in the graph. Feedback voltage: $V_{\text{sample}} = -1.5$ V. Arrows point to the shift observed with increasing setpoint currents for the lowest peak in the conduction band and the highest peak in the valence band, labelled e_1 and h_1 respectively. Inset: schematic of a stack of NPLs probed with a STM tip, where the characteristic dimensions are indicated. (b) Scanning tunnelling spectra acquired on a stacked NPL bearing a trap state at a constant setpoint current. Sequence of four differential conductance spectra that were averaged over a few successive curves between charging and discharging events. Inset: schematic of a stack of NPLs probed with a STM tip, where ligands are missing on the edge of the NPLs. e_1 indicates the position of the first electron subband, while the arrow indicates the highest trap state in the band gap of the NPL. The curves are offset for clarity. Feedback voltage: -1.8 V.

4.3.2.2.1 Temporal study of the I-V characteristics

For this reason, a thorough temporal investigation of the I-V characteristics was performed on the top of the chosen NPL stack (see Figure 4.12a). Here, three sets of I-V curves recorded at different values of setpoint current are presented.

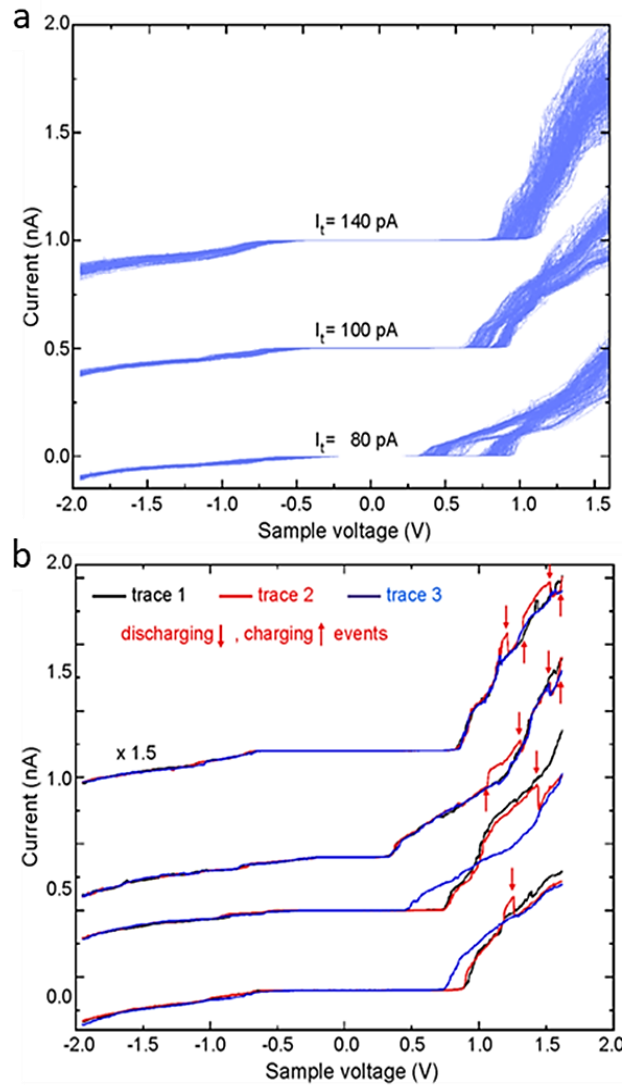


Figure 4.12 Evidence of the trap states in the I-V characteristics of stacked NPLs with a thickness of 5.5 ML. (a) Three sets of I-V traces taken at three different values of setpoint current. The curves have been shifted vertically for clarity with the setpoint currents indicated for each set of traces. (b) Four examples of three successive I-V traces showing the influence of charging and discharging events on the bias onset of the positive branch in the I-V traces.

Each set contains hundreds of traces, corresponding to consecutive voltage sweeps temporally separated by the raster time of 10 ms. It is evident that there are large shifts of the features present between different sets, but also between traces within a single set. However, from this study, two important trends were unveiled. First, as the setpoint current is increased, the collective branch in the I-Vs at positive bias shifts towards higher and higher values, evidencing a clear contribution of the conduction band states. While the second trend is present in narrowing of the mean branch with increasing setpoint currents. Both trends have been readily observed in DBTJ systems, where carrier in-and-out transfer rates are comparable, and as such create a favorable scenario for charging of the nanocrystal. This is further supported by taking a closer look at the negative side of the spectra below the Fermi level (0V). Between consecutive voltage sweeps, the tunneling junction seems to be completely unaffected, since at negative voltages no charging takes place. . Conversely, at positive bias during the next sweep, the discharging events occur. Such charging/discharging events can be identified by the sudden raises/drops in the tunneling current as presented in Figure 4.12b. Altogether, these results ruled out an intrinsic origin for the peaks seen at negative bias and instead point toward the presence of states within the band gap of CdSe NPLs.

4.3.2.2.2 Trap states in CdSe NPLs

For colloidal nanocrystals, it has been well documented that the main sources of in-gap states have been surface trap states, caused by ligand displacement. If ligands do not effectively passivate the NPL surface, trap-free bandgap scenario is highly improbable, due to unintended oxidation or reduction processes that can occur during their exposure to air or during synthesis.

This is particularly true for the Z-type group of ligands, to which oleate molecules belong. As such, they have ability to accept two electrons for the bond formation with under-coordinated surface atoms to compensate the excess charge on NPL surfaces. The NPL facets are very well defined upon their orientation with top and bottom facets being pure Cd (100) terminated and Se-rich (001) and (111) side facets. Inherently, side facets have been shown to be more reactive and therefore, decorated with more labile ligands. For CdSe nanocrystals, it has been recently predicted that selenium dangling bonds at the surface of the nanocrystal would be the main source of electrical traps.[138] This can be clearly seen by the models originating from these DFT calculations in Figure 4.13, where the incremental displacement of the ligands first leads to formation and then the increasing number of in-gap states. On this basis we can accredit low-intensity peaks localized around 0.5 eV below the Fermi level in our dI / dV spectra to trap states.

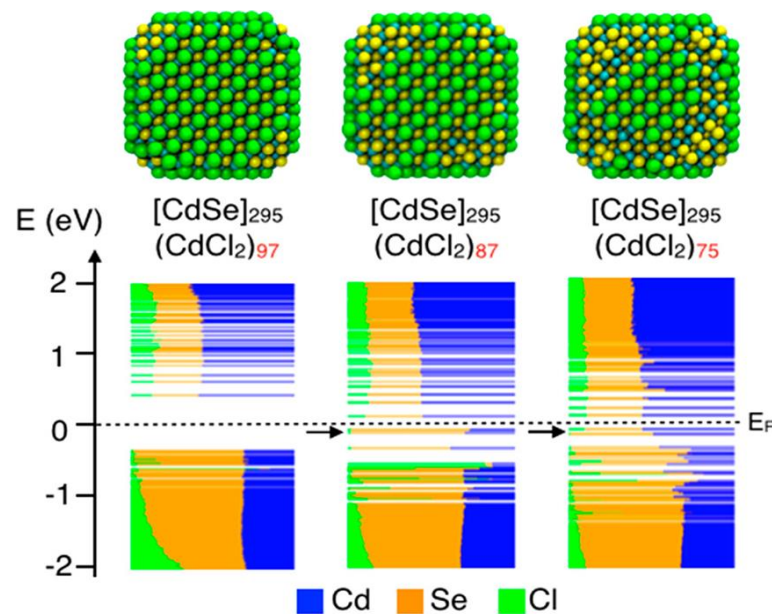


Figure 4.13 Atomistic and electronic structure of, from left to right, CdSe NPLs completely passivated with cadmium-chloride, then with 10 and finally, with 22 sites stripped of ligands. The gradual stripping of the ligands leads to formation of in-gap states marked with a black arrow. The figure is adopted from ref.[138]

Since the NPLs are resting on their longest sides within the stack, the (001) side facets are the ones exposed to the STM tip, which is certainly in line with the observations of in-gap states, or the lack

thereof in the case of individual flat-lying NPLs. As expected, trap states significantly alter carrier dynamics within the nanocrystal system, as shown by the schematics in Figure 4.14. In (a) panel, the illustration represents the electron tunneling process from the NPL to the empty STM tip states at negative sample bias.

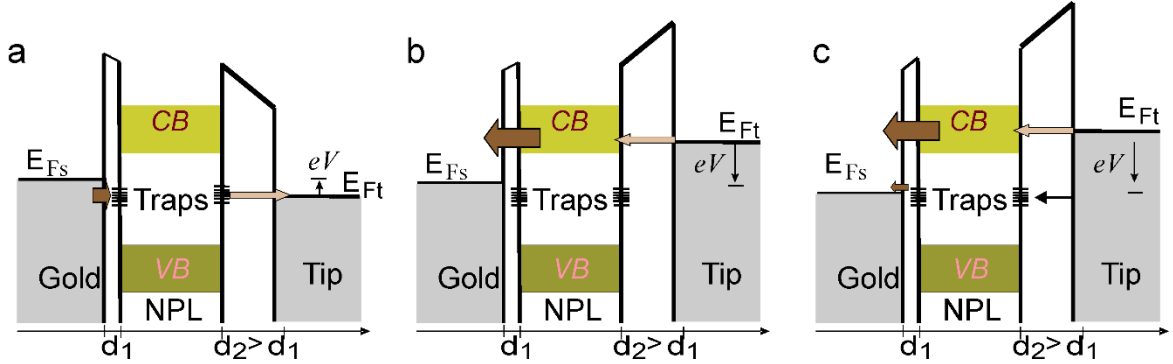


Figure 4.14 Energy-band diagrams of the double tunnelling junction with the NPL inserted in the middle of the junction for different points of the STS voltage sweep: (a) at negative, (b) positive, and (c) high positive sample bias. The widths of the NPL-gold and STM tip-NPL junctions are denoted with d_1 and d_2 , with conduction and valence bands being labelled as CB and VB, respectively.

This process entails electrons tunneling from the substrate to the nanocrystal followed by hopping from one surface trap state to another until reaching the second NPL-STM tip tunneling junction. While at positive bias, the electrons tunnel from the STM tip to the CB states of the NPL (see Figure 4.14b). However, if the positive values of bias voltage are high enough the traps states will become aligned with the Fermi level of the gold substrate, forming a favorable condition for the charging of the NPL, as showcased in Figure 4.14c. Thus, the previously mentioned drops in current in Figure 4.12 can be explained as follows: Starting with N excess of electrons, the NPL loses one electron and changes its charge state to $N-1$. The resulting shift in voltage results in a larger portion of the conduction band which becomes accessible for probing.

4.3.2.2.3 Tight binding calculations

Now, with the width of the band gap validated, and with the type of charge transport explained, the last remaining question concerned the unexpected divergence of the measured DOS from the expected 2D character. To understand the origin of the spectral features in conduction band responsible for this, tight binding calculations were performed by Christophe Delerue. This theoretical study involved calculations of the conduction band structure as a function of all three NPL dimensions. Beginning with the variation of the thickness from 2.5 ML all the way up to 8.5 ML. The DOS of infinitely long NPLs is presented in Figure 4.15a. Here, the NPL width was of 6 nm. The calculated DOS exhibited the characteristic quantum-wire-like behavior with Van Hove singularities grouped within subbands. Also, one of the signature consequences of the quantum confinement effect is on display here, in the form of shifting the energy levels towards the higher energies as the thickness of the NPL is reduced. At this point, it is safe to say that CdSe NPL are confined in two dimensions, instead of one as it was formerly conjectured. Yet, what is the threshold of the weakening the confinement in the lateral dimension of the nanocrystal, at which the DOS will resemble the one of quantum wells?

To answer this question, the calculations were extended towards the NPLs of again infinity length, but this time fixed thickness of 5.5 MLs and varying widths (4 nm, 15 nm, 30 nm, and 60 nm). The results of this study are presented in Figure 4.15b. Notably, there is a clear relation between the NPL widths and the peak spacing. As the lateral confinement is decreased, the separation between two subsequent peaks is reduced, which leads to DOS to gradually transmute into step-like function characteristic for 2D nanostructures with the increase of the NPL width. As it hits the 30 nm mark, the peak separation reaches 25 meV. At this point, the NPL DOS clearly starts to resemble the one of quantum wells. However, in practice these dimensions far exceed the ones of samples mostly studied in literature and the one covered in our work. In Figure 4.15c, we have supplemented our investigation by also studying the effects of the NPL length on the band structure. Interestingly, we have found out that by restricting the longitudinal extension of the nanocrystals up to 20-30 nm, the DOS exhibits tinier fluctuations between the previously recognized singularities.

As such, these results give us a valuable insight to where is the limit at which the electrons do start to “feel” the borders in the last free-motion direction within this quantum-box. This is evident from the calculated DOS, where upon reaching and surpassing the limit will result in more intense and far more frequent oscillations, and finally conclude with vanishing 1D DOS in favor of an oscillating DOS. For the one to one comparison of the theoretical and experimental DOS, we have selected NPLs, where tens of successive traces were measured without any stepwise changes of the current at positive bias. In this way, we avoided any charging / instability effects to have an influence on our final conceptions. Two examples of spectra acquired on the stacked 5.5 ML NPLs are shown in Figure 4.15d. In both graphs, one can clearly see sharp peaks corresponding to van Hove singularities with general, sawtooth-like form. The energy separation between the follow-up peaks with decaying intensities, discards the possibility of them being linked to polaron contribution of optical phonons (26 meV for CdSe). Instead, the experimental DOS observed here indicates a large delocalization of the electron wave function in the NPLs, where the boundaries of the NPLs act as potential barriers that laterally confine the electron wave function.

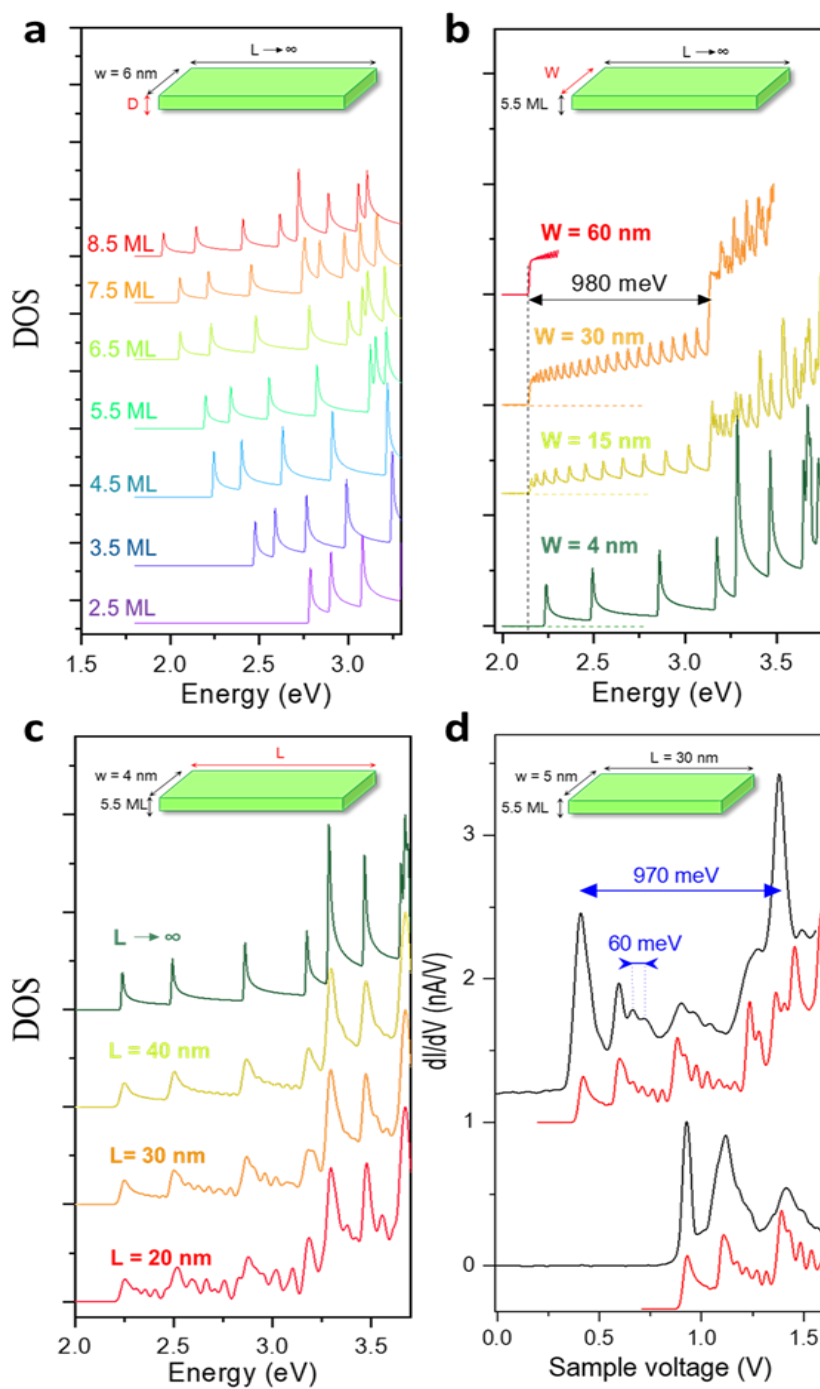


Figure 4.15 Theoretical conduction band density of states of CdSe nanoplatelets. a, DOS of infinitely long NPLs with a width of 6 nm and varying thicknesses. b DOS of infinitely long NPLs with a fixed thickness

of 5.5 ML and different widths. Due to the higher and higher number of states contributing to the DOS for larger and larger widths, the calculation becomes quickly limited to the lowest states. c DOS of NPLs with a thickness of 5.5 ML, a width of 4 nm and different lengths. d. Differential conductance of two NPL measured at $T = 5\text{K}$ (black) together with the tight binding calculation of the DOS (red) for a thickness of 5.5 ML with $L = 30\text{ nm}$ and $W = 5\text{ nm}$. The curves are offset for clarity. Feedback voltage: -1.8 V , setpoint current 100 pA .

4.4 Extensive “pre-STM” study of CdSe/CdS Core/crown NPLs

With now a good understanding of electronic properties of bare CdSe NPLs, the logical continuation of our work was to move towards CdSe NPL-based heterostructures. Based on the current state-of-the-art of the colloidal synthesis, there were two main choices: core/shell and core/crown architecture. In addition to the reasons mentioned in the first chapter of the thesis, few other factors originating from the differences in structure morphology made this an easy decision. First and foremost, the core/crown morphology allows for direct probing of the heterointerface with the STM tip, as it is completely exposed on the largest sides of the nanostructures. Secondly, unlike in the case of core/shell NPLs, the growth of the nanostructure is promoted only in the planar directions, which has some additional benefits. Keeping the thickness (the direction of the strongest confinement) uniform throughout the samples, effectively makes the quantum size effect an isolated parameter only in the lateral directions. Another advantage is connected to the dimensions of these nanocrystals. In particular, decreasing the size of the nanostructures to such small scales results in a more substantial fraction of its atoms to be located at the surfaces/interfaces. Hence, the effects of faulty passivation or material lattice mismatch are expected to become more prominent. Conveniently, the morphology of core/crown CdSe NPLs hits just the right balance, since the above-discussed STM study has shown that the Cd-terminated (100) facets are generally defect free. As a result, the inefficient passivation of the other facets can only be improved, while still keeping as low as possible fraction of the NPL subjected to heterointerface related defects. However, there is another benefit of working with CdSe NPLs, which is tied to the recent breakthroughs in understanding of their optical properties. As it was previously shown in Figure 4.1c, moving from RT towards low-temperature measurements NPLs will exhibit additional emission line, whose origin has been a part of long debate in scientific community. Multiple authors have tackled this question with obtaining vastly different conclusions. Among those, couple of them stood out, such as phonon replica,[300] p- and s-state emission,[301] excimer-like emission,[302] charged excitons (trions)[213], exciton substructure[303] etc. After a decade of intense research in the field, its origin was finally unveiled in a very recent publication[304]. The authors of this paper have turned towards optical spectroscopy measurements in high-magnetic field and in this way, they managed to provide a definite answer to this question by linking high-energy line to neutral and low-energy line to charge exciton emissions. This opened a possibility to exploit newly acquired knowledge and extend the research towards the unknown, for example, on the effects of the crown size on the optical properties of core/crown NPLs. Having selected the core/crown architecture and the core material, the next point to address is to choose the material which will comprise the crown. For our experiments we have opted for the combination of CdSe and CdS, as it exhibits characteristics commonly associated with quasi-type II band alignment (see top panel in Figure 4.16a). For instance, previous studies have shown that due to the large valence band offset of around 500 meV,[42] the hole wavefunction is localized in the core material and the electron is partially delocalized across the entire core/crown system. Even though band alignment plays a crucial role in determining optical and electronic properties of these nano-heterostructures, the exact values of both valence and conduction band offsets are still largely unknown.[305] In the end, three different NPL-based samples which were chosen for our experiments are schematically presented in the bottom panel of Figure 4.16b. These include : 4 ML-thick, 4.2 nm-wide and 32.6 nm-long bare CdSe NPLs (Figure 4.16b) and two distinct

nano-heterostructures that are comprised of the identical-sized 4 ML-thick CdSe NPLs as a core with small CdS crown extending over $6.7 \times 38.6 \text{ nm}^2$ (Figure 4.16c) and a large one, measuring up to $15 \times 56 \text{ nm}^2$ (Figure 4.16d). Structurally, the increase of crown size is mediated by the lateral extension of the CdS, while preserving the size and shape of the CdSe core. Following the same protocol as for the bare CdSe NPLs, we have started by exploring their optical properties. However, our initial findings proved to be quite interesting, which pushed our scope of research deeper towards magneto-optical studies, at high magnetic field facility in Nijmegen, Netherlands.

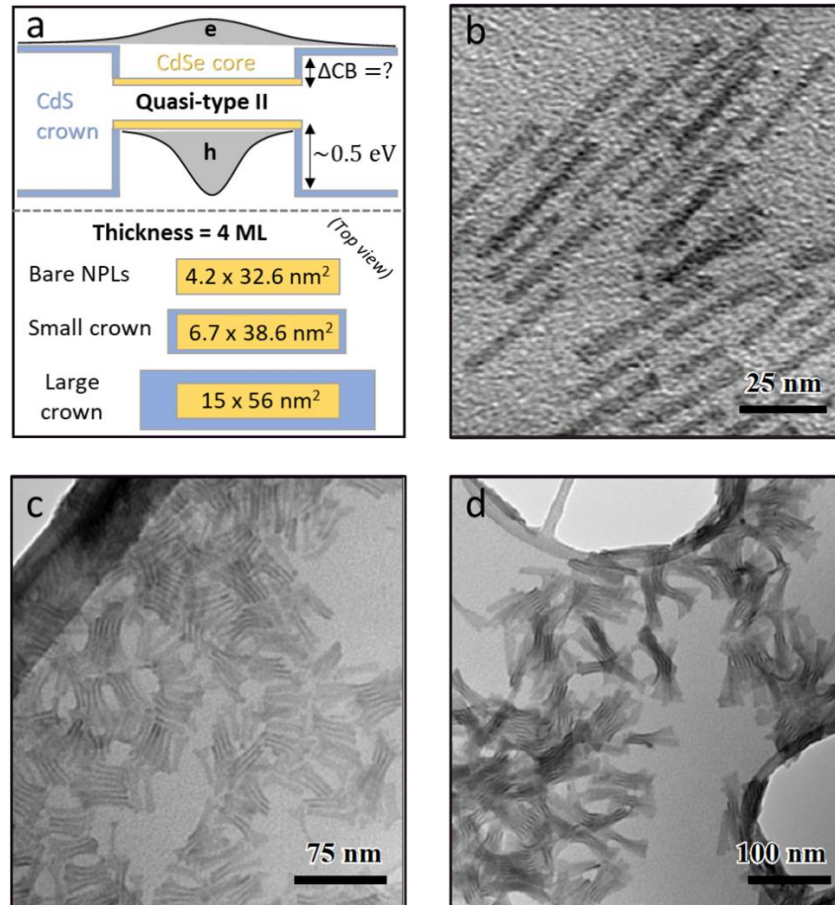


Figure 4.16 Three NPL samples used in this study with (a) their top-view schematic representations (top panel) and simple band diagram of the heterointerface (bottom panel); further accompanied with their respective TEM images: (b) bare CdSe NPLs, (c) small and (d) large-crown CdSe core/crown NPLs.

4.4.1 Influence of the crown size on optical properties

In principle, core/crown NPLs can be viewed as CdSe NPLs imbedded in larger CdS NPLs, since the thickness of both materials is identical. This structural aspect was confirmed by the initial studies of the optical properties of these nano-heterostructures where it was revealed that the exciton binding

energies of the individual materials within the nanostructure are comparable to their known standalone values. As a result one can expect that the increase in the thickness would reflect on the PL emission as it does for the case of bare CdSe NPL, since the core/crown configuration, unlike core/shell one, allows for the preservation of optical characteristics inherent to bare CdSe NPLs.[168] Yet, the optical spectroscopy data in Figure 4.17 showed a different picture. Starting from the absorption spectra in Figure 4.17a, which were recorded on small and large-crown samples. For both populations, the spectra feature two sets of two absorption lines, corresponding to the light- and heavy-hole resonances of CdSe and CdS. The heavy-hole peak positions for the small-crown NPLs were measured to be 406 nm (CdS) and 509 nm (CdSe), whereas for the large-crown 406 nm and 514 nm, respectively. There were some key observations which indicated the increase of the crown size with respect to the fixed CdSe core. For example, the CdS absorbance measured on the large-crown sample is clearly higher than the one for the small-crown NPLs. Also, the CdSe absorption line becomes slightly red-shifted as the crown size is increased, due to a larger spread of the electron wavefunction. Similar conclusions can be withdrawn from the measured photoluminescence spectra, shown in Figure 4.17b. But before that, it should be noted that the emission in these nanostructures originates only from the CdSe core. This behavior was previously reported and well explained by Tessier et al.[168] by linking it to the quasi-type II nature of the CdSe/CdS heterojunction, where the hole wavefunction is localized within CdSe. This, in combination with the large CdSe NPL exciton binding energy[306] will induce for the recombination process to be favored in the CdSe core, as it is generally the case for type I systems.[307] In fact, the easy migration of the crown-generated excitons is made possible because the Cd-terminated basal facets of zincblende NPLs allow for the formation of mostly defect-free heterointerface. Now, coming back to photoluminescence spectra. When compared to the emission of bare CdSe NPLs, a slight shift of the emission peaks towards lower energies with the increase of the crown size is evident. This further demonstrates the delocalization of the electrons to the CdS crown, which in return will experience the lessened effect of the quantum confinement. Yet this effect is not as nearly as pronounced if compared to the case of core/shell nanostructures.[308], [309] It has been suggested that the dielectric environment of the two-dimensional NPL is not significantly changed by the lateral extension of the crown, leaving CdSe large exciton binding energy practically unchanged.[307] Altogether, these results are in a good agreement with our STS studies done on bare CdSe NPLs, again showcasing the weak, yet not insignificant influence of the lateral confinement in these nanostructures. Nevertheless, the final and most important observation from these studies was the vanishing of the dual emission characteristic for bare CdSe NPLs at cryogenic temperatures, as the crown-size is increased. The origin of this effect will be the next important topic of the discussion.

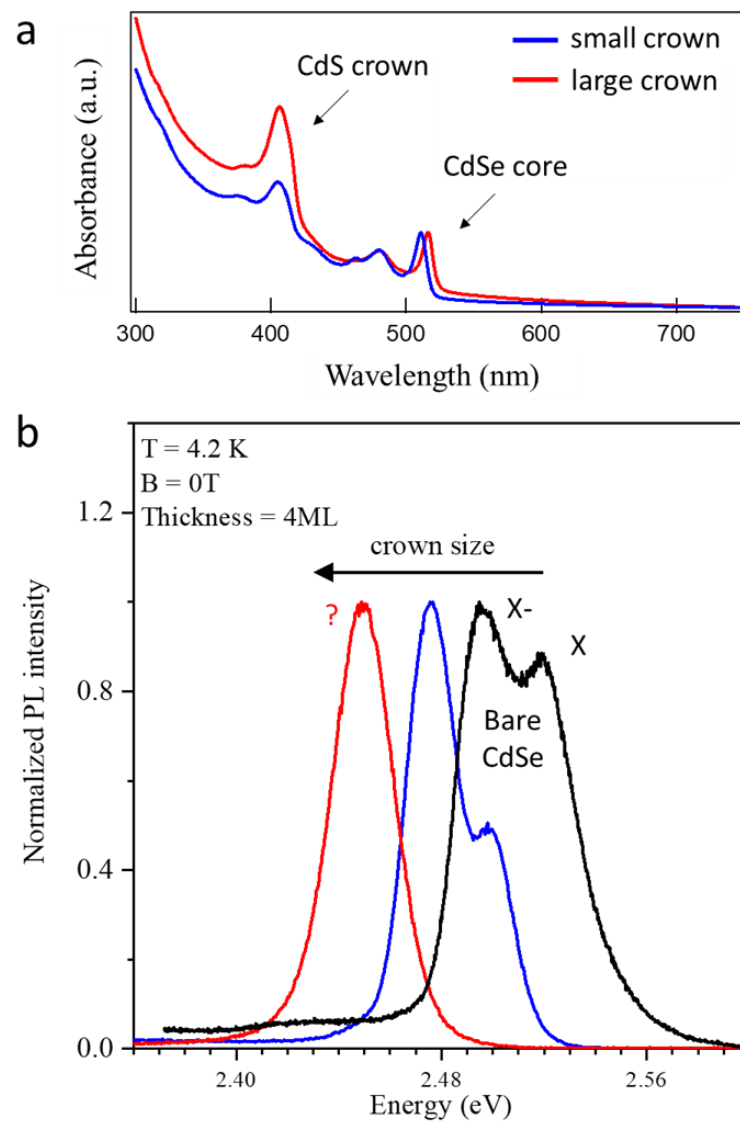


Figure 4.17 Influence of the crown size on the optical properties of CdSe/CdS core/crown NPLs. (a) The absorption spectra acquired on small and large-crown NPLs presented in blue and red, respectively. (b) Photoluminescence spectra of bare 4-ML thick NPLs (black), small and large-crown NPL samples, recorded 4.2 K.

4.4.2 CdSe exciton fine structure

To unveil the role played by the crown on the optical properties of CdSe NPLs, one should first understand and question the existing knowledge of bare CdSe NPLs. In order to achieve this, it is natural to firstly consider the CdSe band structure and resulting exciton fine structure.

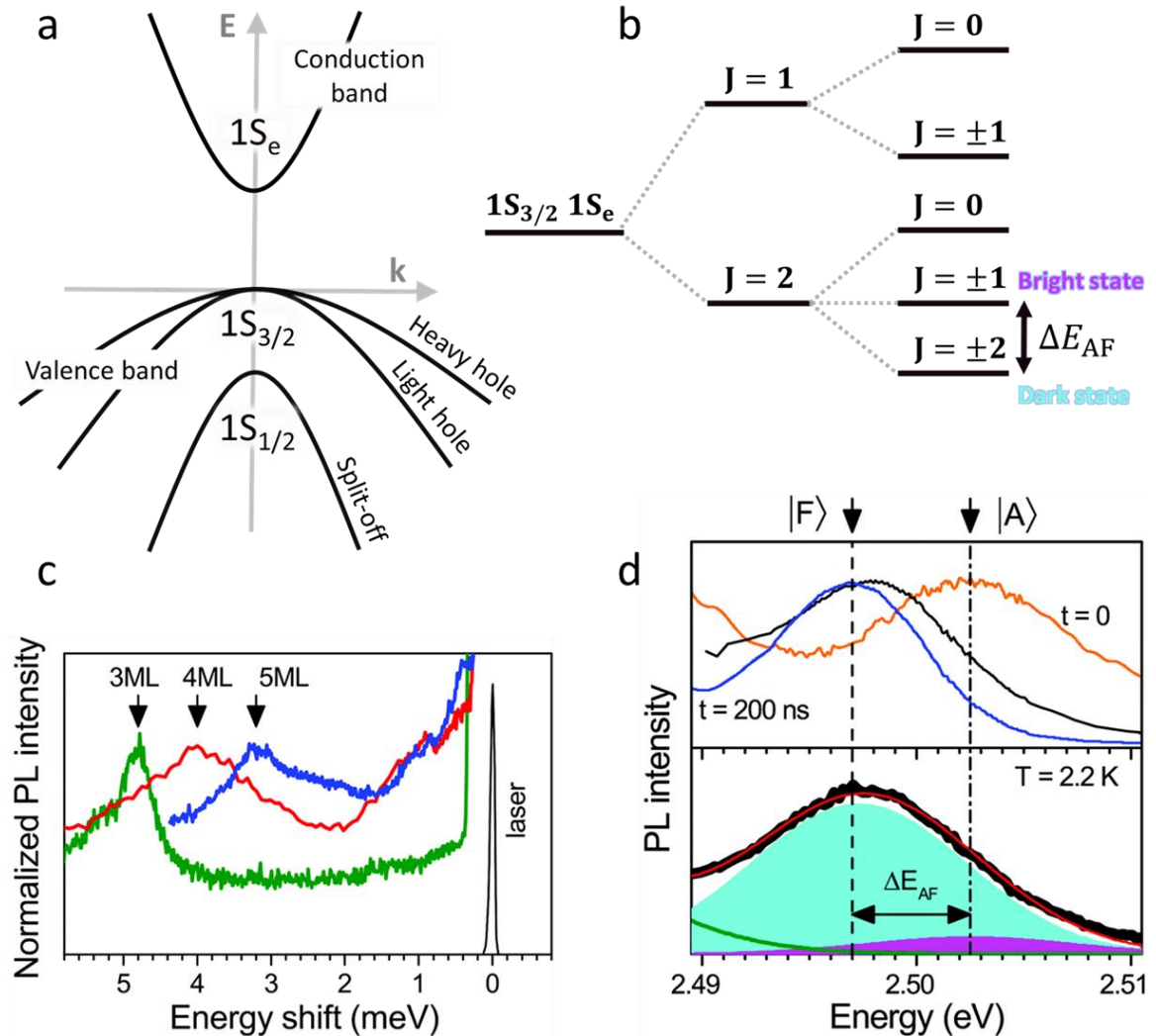


Figure 4.18 Bright and dark state energy splitting in CdSe NPLs. (a) CdSe band structure (b) CdSe exciton fine structure. (c) Fluorescence line narrowing spectra of 3ML, 4ML, and 5ML samples at laser excitation energies of 2.8076, 2.5407, and 2.3305 eV, respectively. (d) PL spectra of 4ML NPL sample recorded at $T = 2.2$ K, at different delays: $t = 0$ (orange), $t = 200$ ns (blue), and time-integrated over the laser repetition period (black). Lower panel: Time-integrated PL spectrum at $T = 2.2$ K measured with a CCD camera (black), fitted with three Gaussians corresponding to dark exciton (cyan), bright exciton (purple), and laser (black).

(magenta) and low-energy peak (green). Red line gives the resulting curve. Insets c and d taken and adopted from Ref.[213]

As it is the case for most of the II-VI semiconductors, the conduction and valence bands are defined by s-orbitals of the metal ions and p-orbitals of anions, respectively. Therefore, for CdSe the interplay between 2-fold degenerate Cd 5s-orbitals and 6-fold Se 4p-orbitals is fundamental. In this context the common notation of nQ_F is used for the description of electron and hole states, where $F = J + L$, and J is Block band edge angular momentum (1/2 for CB, 3/2 for heavy/light hole bands), and lastly, L is the angular momentum associated with the envelope function. To account for strong exchange, spin-orbit and crystal field interaction, the valence band is split into two sub-bands $p_{3/2}$ and $p_{1/2}$, while the conduction band remains unchanged. As a result, the first exciton state (8-fold degenerate) is a combination of the first electron level $1S_e$ (double degenerate) and first hole level $1S_{3/2}$ (4-fold degenerate). In this way, spin-orbit splitting defines the exciton fine structure with ground state being the dark state with momentum projection ± 2 on the quantization axis, while the first excited state is optically active and has total angular momentum of ± 1 . The energy separation between the two corresponds to bright-dark state energy splitting (ΔE_{AF}) and it is usually in the order of couple of meV.

In that regard, the work of Shornikova et al.[213], was focused on investigating the exciton fine structure of CdSe NPLs by means of fluorescence line narrowing technique and time/temperature-dependent PL emission spectra at cryogenic temperatures (see Figure 4.18d). The former technique is based on the resonant excitation of the bright exciton state with a tunable laser and the detection of the redshifted emission, namely the dark exciton PL emission. With this technique, the bright dark splitting is directly unveiled from the energy splitting between the laser line and the redshifted peak in the PL signal, which corresponds to the dark state emission (see Figure 4.18c). Here it is clear that the bright dark splitting increases as the thickness of the NPL decreases, i.e. with the quantum confinement. Whereas with the latter technique, NPLs are excited well above the band gap so that bright and dark states are equally populated right after the laser pulse. Early on (less than 1 ns), the bright exciton dominates the emission in the PL spectra due to its much larger oscillator strength. However, the radiative recombination of the bright exciton is quenched by the thermal relaxation to the dark exciton state, where the PL emission will take place. This is clearly demonstrated in Figure 4.18d, where the emission at $t=0$ (bright exciton) occurs at higher energy than at $t=200$ ns (dark exciton). Therefore, the energy splitting between the peak maximum at $t=0$ and $t=200$ ns directly shows the bright dark energy splitting. Altogether, these results and other associated reports on the fine structure of CdSe NPL showcase that the bright-dark energy splitting is correlated to NPL thickness, which can be further exploited for assessment of the quantum confinement in NPLs. However, these certainly demanding, yet powerful techniques used to disclose energy splitting caused by electron-hole exchange interaction within exciton fine structure are not in all cases applicable. For instance, to study an exciton complex such as trion, where no fine structure is expected. Indeed, in the case of negative (positive) trions, the exciton complex is formed by 2 electron (2 holes) and one hole (electron), and thus, the exchange interaction vanishes.

4.4.3 Recombination dynamics of the exciton complex

In contrast to the previous methods, the study of the exciton dynamics is a powerful technique to unveil the energy splitting within the exciton fine structure, but also the recombination dynamics of various exciton complex. While indirect, this method is commonly present in the literature, as it allows for disclosing various exciton complexes (exciton, biexciton, charged exciton) by varying external parameters such as the temperature or the magnetic field.[213] For the particular case of NPLs, these experiments can be used to unequivocally unveil the nature of the two emission peaks in the PL spectra.

The exciton dynamics in CdSe NPLs can be resumed to the thermal population of the upper bright and a lower dark exciton state. In particular, at room temperature, where the thermal energy exceeds the bright-dark energy splitting, the bright and dark states are equally populated. Because of the striking difference in their oscillator strength, the emission is dominated by the radiative recombination of the bright exciton only, and the PL decay is monoexponential. Yet, for the temperature such that $k_B \cdot T < E_{DB}$, the PL decay occurs on two markedly different timescales. It was shown that the early part of the PL decay is related to the bright exciton emission that is quenched by the non-radiative spin-flip process to the dark exciton state.[310] The fact that only a small fraction of the photons is emitted on such a short timescale clearly indicates that the spin-flip rate far exceeds the radiative relaxation rate of the bright exciton state. The slow decaying part of the PL decay is related to the radiative recombination of the dark exciton. This temperature dependence of the PL decay is a well-known behavior that has been previously observed in a plethora of colloidal nanostructures and as such, it can be used as a fingerprint to reveal the presence of an excitonic fine structure. Nevertheless, one should be aware that such a temperature dependence could be also observed by simply considering a single excitonic level and thermally activated trap. Therefore, in addition to the temperature dependence, it is useful to perform a magnetic field dependence of the PL decay as well. Note that in an ensemble measurement, the NPLs are randomly oriented. As a result, it is not possible to apply the magnetic field in a specific orientation, such as Faraday ($B_{||}$ to the quantization axis) or Voigt (B_{\perp} to quantization axis) geometry. It is worth pointing out that in the case of Faraday geometry, the magnetic field simply lifts the spin degeneracy of the bright and the dark exciton (Zeeman splitting) so no specific B-dependence of the PL decay is expected, provided that E_{DB} is far greater than the Zeeman splitting of the fine structure states. However, in any other orientation, the magnetic field will induces intermixing between the bright and the dark states which in turn leads to a shortening of the PL decay of the dark exciton (i.e. the long component of the PL decay), and a simultaneous vanishing of the fast component.[311] Coming back to the dual emission of NPLs seen in PL spectra, it is then possible to unveil the nature of the emission associated with each peak by independently studying their PL decay.[304]

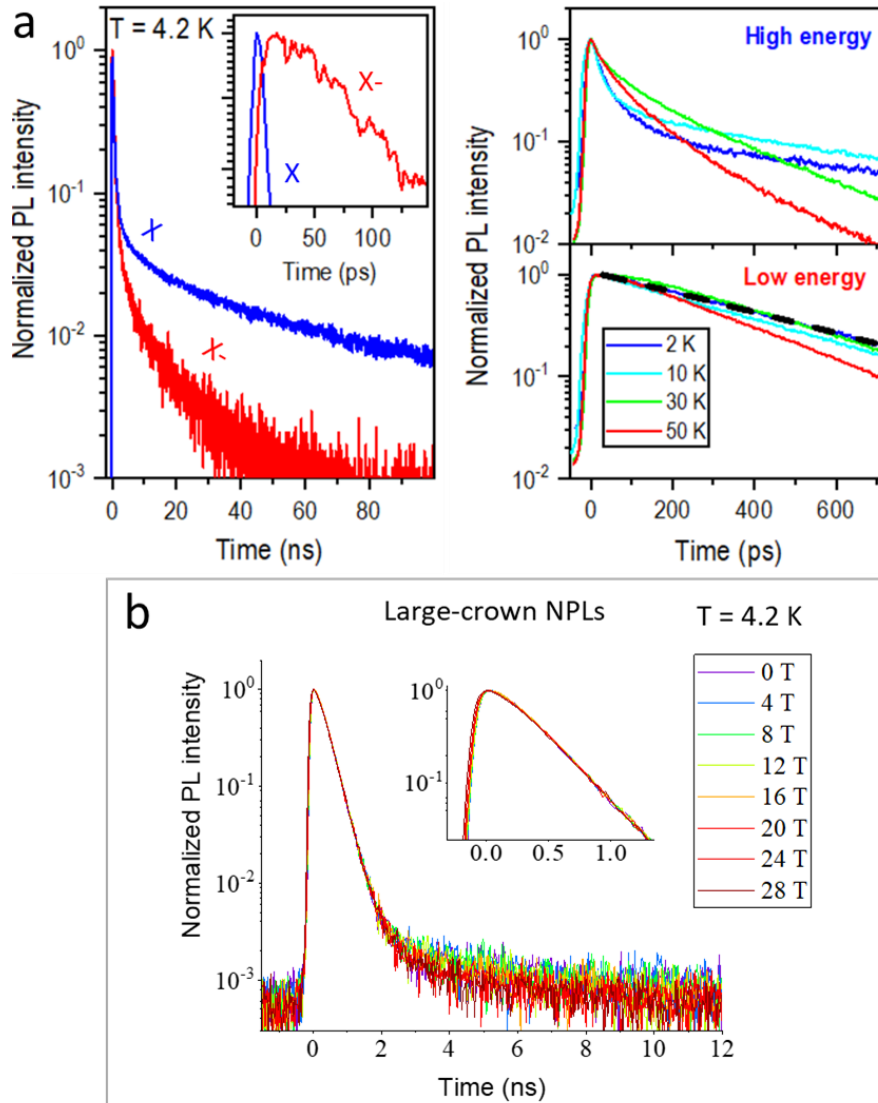


Figure 4.19 Recombination dynamics of 4.5 ML CdSe NPL and CdSe/CdS core/crown NPL. (a) In the left panel: the photoluminescence decays at $T = 4.2$ K for the exciton (blue) and negative trion (red) lines; inset: their respective initial decays. In the right panel: Normalized PL decays at various temperatures for the excitons (top) and trions (bottom), measured at the line maxima with the streak camera. Figure taken from ref.[304] (b) Magnetic field dependance of the PL decay of the single emission line of large-crown CdSe/CdS NPLs from $B = 0$ to $B = 28$ T.

As shown in Figure 4.19a, the PL decay of the high energy peak shows a pronounced temperature and magnetic dependence, hallmarks of the bright-dark state model. In contrast, the PL decay of the low energy peak progresses rather monoexponentially, with a characteristic time of 350 ps. In addition, it does not exhibit any temperature, nor magnetic field dependence between 2 and 50 K and all the way

up to 30 T (see Figure 4.19b), respectively. These results indicate that the emission at low energy stems from the radiative recombination of a bright allowed state. Altogether, these observations are characteristic for the radiative recombination of charged excitons (trions).[312] In summary, studying the temperature/magnetic field dependence of the PL decay allows for unambiguous disclosure of the origin of the emission.

We applied this approach to our core/crown CdSe/CdS NPLs that exhibit only a single peak at cryogenic temperature. As shown in Figure 19b, the PL decay of large core/crown decays monoexponentially over 3 decades with a time of 350 ps and is magnetic field independent up to 30 T. These results show that the emission of large core/crown is dominated by the radiative recombination of the trions. Therefore, our results also showcased the potential of this architecture to circumvent the known issue of large bright-dark exciton energy splitting, while still keeping the narrow emission and high quantum yield, intrinsic to bare CdSe NPLs.[313] At this point our measurements can be readily assigned to charged exciton description of the emission, yet for typifying the character of the trions an additional systematic study was required.

4.4.4 Optical properties of CdSe/CdS core/crown NPLs in high magnetic field

Disentangling the contribution of either positive or negative trions from the unpolarized PL studies (spectra or decay) is nearly impossible given that they both have the characteristics of a single bright exciton state. As depicted in Figure 4.20, the emitted photons can be either left- or right-hand polarized due to the spin degeneracy, regardless of the nature of the trions. However, investigating the polarization properties of the PL emission in magnetic field allows for determination of the sign of the trion, that is to say the nature of the minority carrier.

In magnetic field, the spin degeneracy will be lifted for the electron (e) and the hole (h) therefore the Zeeman splitting for the exciton will be $\Delta E = g_{ex} \cdot B \cdot \mu_B$, where g_{ex} is exciton g-factor, B is the intensity of external magnetic field and μ_B is Bohr magneton.[205] For the dark exciton in CdSe, the g-factor writes $g_{ex} = g_e - 3g_h$. [314] In this case, and as it can be seen in the illustration in Figure 4.20, the spin down state will be lower in energy therefore its contribution to the PL signal will steadily increase with the rise of the magnetic field strength. As a result, for magnetic field strength such that $k_B \cdot T < E_{DB}$, the PL signal will be σ^- polarized. The situation is strikingly different when considering trions. By definition, trions are described as charged excitons, a three-particle complex, where negatively charged trion is composed of a pair of electrons occupying conduction ground state in singlet configuration and a single hole in valence ground state.[315] Reciprocally, positive trions are known for having two holes in a singlet state and single conduction electron.[205] Therefore, the polarization properties in magnetic field can be directly derived from the value and the sign of the g-factor of the minority charge carrier, as shown in Figure 4.20.

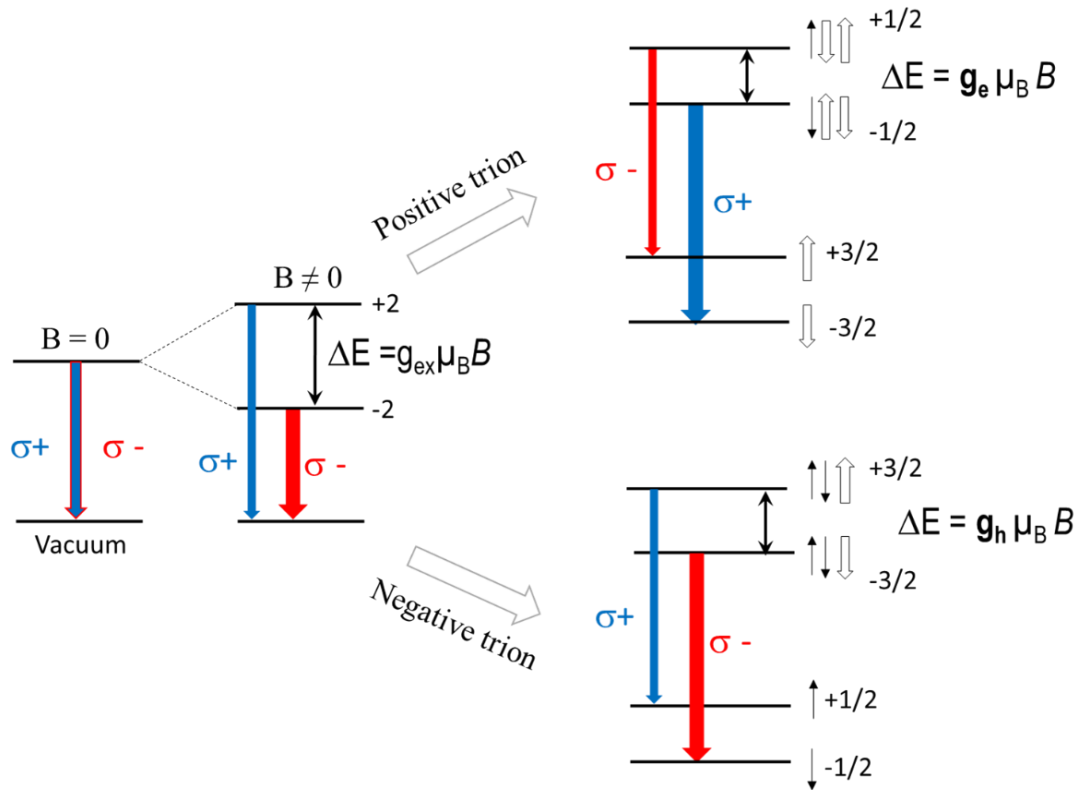


Figure 4.20 Schematic representation of the spin level structure and the optical transitions for the case of excitons and negative/positive trions in an external magnetic field. Short filled and empty arrows indicate electron and hole spins, respectively. Polarized optical transitions are shown by red ($\sigma+$) and blue ($\sigma-$) arrows. The more intense emission, shown by thicker arrow, comes from the lowest in energy trion state with spin $-3/2$ for the negative trion and with spin $-1/2$ for the positive trion. Figure taken and adopted from ref.[315]

For instance, positive trions will lead to a strong sigma $\sigma+$ polarization. A table summarizing all the possible polarization for various g-factor combination can be found in ref.[313] However, it should be noted that the energy splitting between $\sigma+$ and $\sigma-$ will always be proportional to the electron and the hole g-factor, while the PL intensity of the respective polarization will strongly depend on the charge complex considered. As shown in Figure 4.20, the difference in the PL intensity of polarized components for negative trions is solely related to the thermal population of the hole.

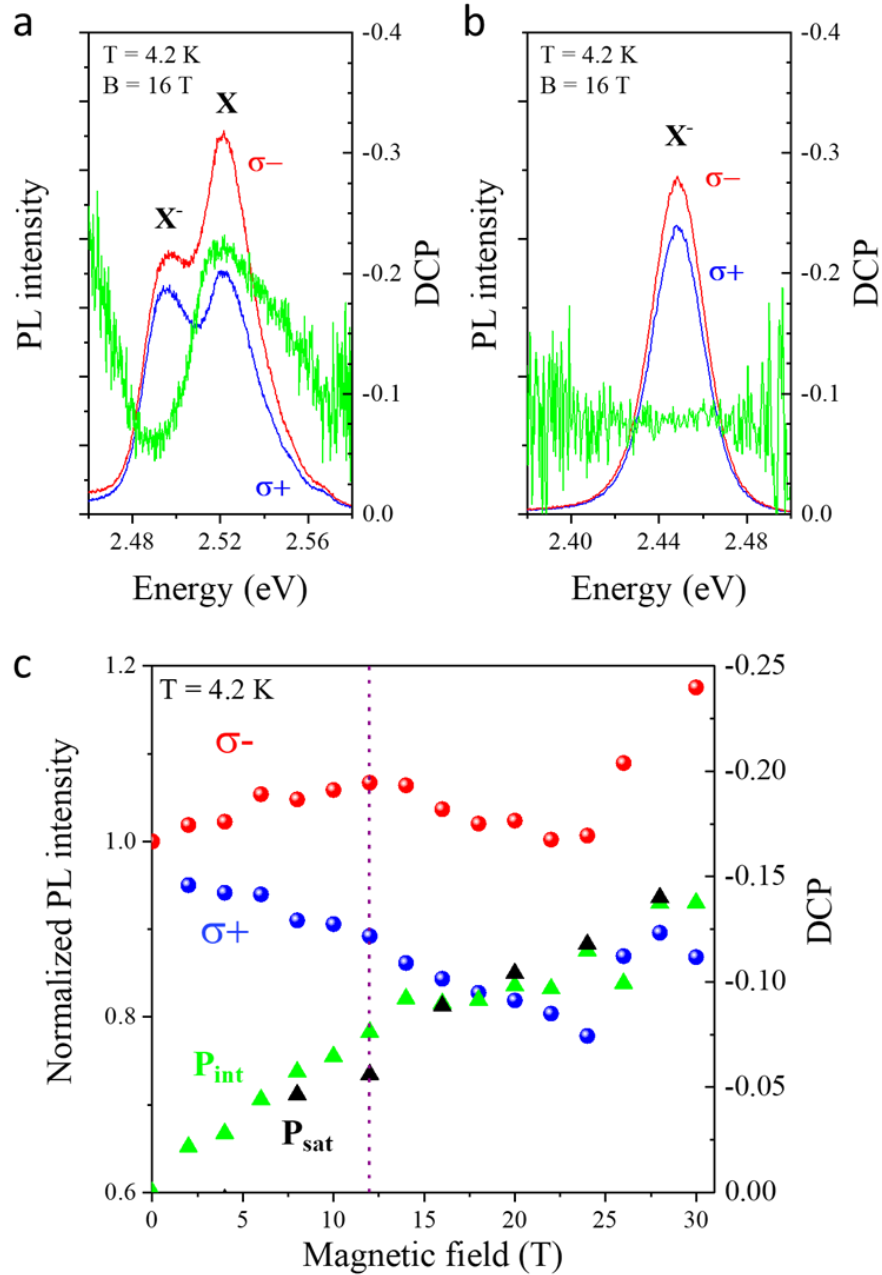


Figure 4.21 Circular PL polarization in external magnetic field. PL spectra of σ^+ (blue) and σ^- (red) circular polarization and corresponding DCP (green) of (a) 4.5 ML-thick bare CdSe NPLs and (b) large-crown CdSe/CdS NPLs at $B = 16$ T and $T = 4.2$ K. (c) Evolution of the σ^+ (blue balls)/ σ^- (red balls) polarized components and time-integrated DCP (green triangles) with respect to DCP saturation level (P_{sat} , black triangles), with the gradual increase of the magnetic field from 0 T to 30 T.

Due to selection rules dictating the polarization of emitted photons, the degree of circular polarization (DCP) is known as a useful tool to treat corresponding kinetics associated with Zeeman sublevels. [315], [316] The time-integrated DCP is best described as the relation between the intensities of left-handed polarized components I^- and right-handed polarized one I^+ , as follows:

$$P_{\text{int}} = \frac{(I^+ - I^-)}{(I^+ + I^-)} \quad (4.2)$$

If the temperature is low enough ($k_B \cdot T < \Delta E_z$), the lower spin sublevel will determine the polarization of the emitted photons.

In Figure 4.21a, the PL spectra acquired on 4.5 ML-thick NPLs at 16 T and 4.2 K is shown. As expected from the model depicted in Figure 20, the high energy peak, which corresponds to the radiative recombination of the exciton is predominantly σ^- polarized in magnetic field and has a DCP value of -0.2. Interestingly, the fact that the low energy peak is also predominantly σ^- polarized and has a weaker DCP value (-0.1), clearly indicates that the low energy peak stems from the radiative recombination of the negative trion, in agreement with previous work. [304]

Remarkably, the polarization-resolved PL characteristics of CdSe/CdS large-crown NPLs (see Figure 4.21b) evidently show that the emission is solely dominated by the radiative recombination of the negative trion. It is noteworthy that the DCP value for the negative trion in bare CdSe NPL and core/crown NPL are quantitatively the same, which indicates that in both cases the polarization properties of the trion are given by the hole g-factor in CdSe. The trion-only emission in large core/crown can be explained from a kinetics point of view. The exciton transfer process is exceptionally efficient, since 70% of excitons that are generated within CdS crown are in less than 1 ps funneled into the CdSe core. Moreover, the remaining 30% of excitons localize at the interface with the holes being trapped in CdS, while all the photogenerated CB electrons from CdS are transferred into CdSe. [317] This implies that there are significantly different transfer rates of the holes and electrons across the interface. Hence, if coupled with strong electron wavefunction overlap, the previously neutral nanocrystals are highly susceptible to photocharging. This in fact will place the nanocrystal in charge separated state and cause the generation of trions states within it. [318] More explicitly negative trions, since the electron transfer is much more efficient than the hole one. And indeed, it has been previously demonstrated that the material combination of CdSe and CdS in thick-shell core/shell nanocrystals is responsible for their negative photocharging. [29]

It is interesting to compare these results to those obtained on CdSe/CdS core/shell NPL reported in ref. [313] In this paper, the authors also evidenced a PL emission dominated by the radiative recombination of the negative trion. Even though here and in the aforementioned paper we are dealing with the same materials (CdSe and CdS) and the same exciton complex (negative trions) the PL properties are strikingly different. Indeed, for core/shell NPLs the radiative lifetime is about 3 ns, which is one order of magnitude longer than for the core/crown architecture. In addition, the broad (FWHM = 43 meV) and asymmetric shape of the PL spectra of core/shell clearly suggests the presence of

interfacial defects between the core and the shell, whereas the emission of core/crown NPLs is sharp (FWHM =25 meV), symmetric and has a Voigt profile, which suggest a monodisperse distribution. In both cases, 4.5 ML CdSe NPLs were used as seed core. The emission of the core is around 2.48 eV at T= 4.2K while the core/shell and the core/crown have emission center at 1.96 eV and 2.45 eV, respectively. The strong difference in the emission energy is insightful since it gives an idea of the electron delocalization in the CdS shell. Namely, electrons in core/shell NPL are strongly delocalized in the CdS shell which results in a reduced quantum confinement and the emission occurring at a lower energy. In contrast, the very weak change in the emission energy for core/crown, in spite of the large crown, shows that the electron does not feel the CdS crown and remain mainly confined in the CdSe core.

4.5 Conclusions

Colloidal synthesis of CdSe NPLs easily surmounts the poor scalability, rigidity, and high cost which are inherent to the epitaxial nanostructure growth, while preserving the considerable degree of control and quality of the final products. Indeed, the preliminary studies with PL, SEM, TEM, AFM images showcased the excellent homogeneity and crystal quality of our samples. Both of which were later confirmed by the LT-STM measurements. In the absence of chemical pretreatment, the NPLs prefer to stay self-assembled in stacks upon deposition. In this configuration, the detailed imaging of their side faces is made possible, and it revealed that the two neighboring NPLs have their ligand chains interpenetrated. Contrary to the expectations, we have observed electronic properties which vastly differ from the ones expected for typical 2D materials. In specific, for the typical rectangular shapes usually observed in the literature, the electron DOS displays Van Hove singularities, which are also present in our tight binding calculations. This demonstrates and therefore, confirms the strong influence of the lateral confinement in these nanostructures. Moreover, the remnants of electronic deep trap states were equally evident in our optical and STS studies. Coherently, both measurements shed the light on the NPL surface chemistry as a function of its morphology, but also the potential of addressing the trap state by NPL-based lateral heterostructures. Our experiments in high-magnetic field revealed that the emission of CdSe/CdS core/crown NPLs is dominated by negative trions.

Conclusion and Future work

The aim of this thesis was to identify an effective experimental approach to revisit some of the fundamental concepts inherent to one-dimensional semiconductor nano-heterostructures. For this purpose, a scanning probe microscopy was used to conduct a detailed study of the two samples with vastly different synthetic origins, but with a closely related underlying physics which describe their chemical and physical properties. The samples in question were $\text{In}_{0.53}\text{Ga}_{0.47}\text{As}$ nanowires grown on InP by selective area epitaxy and colloidal CdSe nanoplatelets in their bare form, but also when unified into the CdSe/CdS core/crown architecture.

Focusing on the $\text{In}_{0.53}\text{Ga}_{0.47}\text{As}$ nanowires first, the morphological characterizations were performed with the following combination of techniques: SEM, AFM and LT-STM. Nanowire-based heterostructures with different levels of structure complexity were firstly identified and classified using the SEM. Next, the large-scale morphological study of each one of the planar nano-heterostructures was investigated with AFM. The results obtained from this study demonstrated that the hydrogen-assisted MBE growth had outstanding selectivity with respect to the SiO_2 mask. Moreover, it was discovered that the cross-sectional height profiles of the nanowires were much different depending if the nanowire was extending along [110] or [1-10] direction. The significant hallmark of this behavior was the non-homogeneous profile of the nanowire (001) top facet. Further analysis of this feature was done using the LT-STM. The atomically resolved STM topography revealed As-rich (2 x 4) (001) surface reconstruction. Dimer rows spreading along [1-10] direction, were certainly accountable for the disparity in the surface roughness along two main crystallographic directions. With a newly acquired knowledge, the AFM height profiles were fitted to a model describing the surface diffusion kinetics. In this way the value of the diffusion length along [1-10] direction was determined to be 110 nm, whilst along the [110] direction it was found to be negligible. Investigation of the nanostructure electronic properties in conjunction with its morphology was the next step. The single- and two-probe STS study was successfully utilized to quantitatively determine the band alignment at the $\text{In}_{0.57}\text{Ga}_{0.43}\text{As}/\text{InP}$ heterointerface. The values of the conduction and valence band offsets between the two materials were measured to be 210 meV and 400 meV, respectively. In addition, the two- and four-probe contact measurements were performed in order to gain information about the carrier transport properties in these nanostructures. It was determined that the tungsten probes form an ohmic contact with the InGaAs nanowires, while the carrier transport is governed over three possible channels, through the bulk of the nanowire, through the nanowire surface or through the p-doped InP below. The voltage threshold at which the last mentioned channel becomes accessible to the carriers was measured to be around 360 meV, which is in a good agreement with the previously obtained value for the valence band offset. Altogether the results obtained from these experiments testify for the viability of this combination of SPM techniques for the accurate and reliable investigation of the atomic scale topography and nanoscale electronic properties of the 1D semiconductor nanostructures.

In terms of the nanostructure size, colloidal synthesis far surpasses the selective area epitaxy, as it is capable of yielding nanostructures of much smaller dimensions. At this, sub-50 nm scale, probing the

effects of quantum confinement becomes feasible. Bare 5.5-ML CdSe NPLs of two different thicknesses were firstly characterized with optical spectroscopy, SEM, TEM, AFM. With the firstly mention the thickness of the two NPL species was determined to be 5.5 ML and 7.5 ML, whereas the remaining array of techniques mainly served purpose for the measurement of the NPL lateral dimensions, but only once they were drop-casted onto the gold substrate. In the absence of chemical pretreatment, the majority of the NPLs self-assemble into stacks upon deposition. This was further confirmed by the follow-up LT-STM study, with which it was possible to image individual NPLs within a stack. The results of this study revealed that the two neighboring NPLs have their ligand chains interpenetrated. Moreover, the LT-STS study was conducted in order to investigate the electronic properties of the NPLs. In contrast to the widespread belief, the differential conductance spectra acquired from the rectangularly shaped NPLs revealed the electronic properties which vastly differ from the ones expected for typical 2D materials. The electron DOS exhibited Van Hove singularities, a finding in line with our tight binding calculations, where the extent of the lateral confinement was assessed. This demonstrates and therefore, confirms the strong influence of the lateral confinement in these nanostructures. Moreover, the remnants of electronic deep trap states were equally evident in our optical and STS studies. In order to extend our study towards CdSe NPL-based heterostructures, we have performed a preliminary, yet detailed study of the magneto-optical properties of CdSe/CdS core/crown NPLs. The highlight of the PL experiments performed in high-magnetic field was that the emission of CdSe/CdS core/crown NPLs is dominated by negative trions, a corollary of the band alignment at the heterointerface. This, if coupled with excellent growth flexibility and crystalline quality, and most importantly, easily accessible heterointerfaces makes these nano-heterostructures appealing for the future studies of the quantum confinement and band alignment with now, tested and verified, SPM methods.

Bibliography

- [1] P. Y. Yu, M. Cardona, and Y. Y. Peter, *Fundamentals of Semiconductors*. Springer, 1996.
- [2] N. S. Mohammad, "Understanding quantum confinement in nanowires: Basics, applications and possible laws," *J. Phys. Condens. Matter*, vol. 26, no. 42, 2014, doi: 10.1088/0953-8984/26/42/423202.
- [3] L. E. Brus, "Electron-electron and electron-hole interactions in small semiconductor crystallites: The size dependence of the lowest excited electronic state," *J. Chem. Phys.*, vol. 80, no. 9, pp. 4403–4409, May 1984, doi: 10.1063/1.447218.
- [4] T. J. Jacobsson and T. Edvinsson, "Absorption and fluorescence spectroscopy of growing ZnO quantum dots: Size and band gap correlation and evidence of mobile trap states," *Inorg. Chem.*, vol. 50, no. 19, pp. 9578–9586, 2011, doi: 10.1021/ic201327n.
- [5] T. Edvinsson, "Optical quantum confinement and photocatalytic properties in two-, one- and zero-dimensional nanostructures," *R. Soc. Open Sci.*, vol. 5, no. 9, 2018, doi: 10.1098/rsos.180387.
- [6] J. R. Ahn, H. W. Yeom, H. S. Yoon, and I. W. Lyo, "Metal-insulator transition in Au atomic chains on Si with two proximal bands," *Phys. Rev. Lett.*, vol. 91, no. 19, p. 196403, Nov. 2003, doi: 10.1103/PhysRevLett.91.196403.
- [7] A. Bezryadin, C. N. Lau, and M. Tinkham, "Quantum suppression of superconductivity in ultrathin nanowires," *Nature*, vol. 404, no. 6781, pp. 971–974, Apr. 2000, doi: 10.1038/35010060.
- [8] S. V. Zaitsev-Zotov, Y. A. Kumzerov, Y. A. Firsov, and P. Monceau, "Unconventional magnetoresistance in long InSb nanowires," *JETP Lett.*, vol. 77, no. 3, pp. 135–139, 2003, doi: 10.1134/1.1567775.
- [9] T. Giamarchi, "One-dimensional physics in the 21st century," *Comptes Rendus Phys.*, vol. 17, no. 3, pp. 322–331, 2016, doi: <https://doi.org/10.1016/j.crhy.2015.11.009>.
- [10] J. Voit, "Charge-spin separation and the spectral properties of Luttinger liquids," *J. Phys. Condens. Matter*, vol. 5, no. 44, pp. 8305–8336, 1993, doi: 10.1088/0953-8984/5/44/020.
- [11] H. Ishii *et al.*, "Direct observation of Tomonaga-Luttinger-liquid state in carbon nanotubes at low temperatures," *Nature*, vol. 426, no. 6966, pp. 540–544, Dec. 2003, doi: 10.1038/nature02074.
- [12] J. Lee, S. Eggert, H. Kim, S. J. Kahng, H. Shinohara, and Y. Kuk, "Real space imaging of one-dimensional standing waves: direct evidence for a Luttinger liquid," *Phys. Rev. Lett.*, vol. 93, no. 16, p. 166403, Oct. 2004, doi: 10.1103/PhysRevLett.93.166403.
- [13] Y. Xia *et al.*, "Quantum Confined Tomonaga-Luttinger Liquid in Mo₆Se₆ Nanowires Converted from an Epitaxial MoSe₂ Monolayer," *Nano Lett.*, vol. 20, no. 3, pp. 2094–2099, Mar. 2020, doi: 10.1021/acs.nanolett.0c00090.
- [14] C. Jia, Z. Lin, Y. Huang, and X. Duan, *Nanowire Electronics: From Nanoscale to Macroscale*, vol. 119, no. 15. American Chemical Society, 2019, pp. 9074–9135.
- [15] R. Landauer, "Conductance from transmission: Common sense points," *Phys. Scr.*, vol. 1992, no.

- T42, pp. 110–114, Jan. 1992, doi: 10.1088/0031-8949/1992/T42/020.
- [16] S. Chuang, Q. Gao, R. Kapadia, A. C. Ford, J. Guo, and A. Javey, “Ballistic InAs nanowire transistors,” *Nano Lett.*, vol. 13, no. 2, pp. 555–558, Feb. 2013, doi: 10.1021/nl3040674.
- [17] F. Krizek *et al.*, “Field effect enhancement in buffered quantum nanowire networks,” *Phys. Rev. Mater.*, vol. 2, no. 9, p. 093401, Sep. 2018, doi: 10.1103/PhysRevMaterials.2.093401.
- [18] G. Stan and R. F. Cook, “Mechanical properties of one-dimensional nanostructures,” in *Scanning Probe Microscopy in Nanoscience and Nanotechnology*, Springer, 2010, pp. 571–611.
- [19] B. Yuan and L. Cademartiri, “Flexible One-Dimensional Nanostructures: A Review,” *J. Mater. Sci. Technol.*, vol. 31, no. 6, pp. 607–615, 2015, doi: <https://doi.org/10.1016/j.jmst.2014.11.015>.
- [20] S. Gong and W. Cheng, “One-dimensional nanomaterials for soft electronics,” *Adv. Electron. Mater.*, vol. 3, no. 3, p. 1600314, 2017.
- [21] Z. Fan *et al.*, “Ordered Arrays of Dual-Diameter Nanopillars for Maximized Optical Absorption,” *Nano Lett.*, vol. 10, no. 10, pp. 3823–3827, Oct. 2010, doi: 10.1021/nl1010788.
- [22] C. Chen, Y. Fan, J. Gu, L. Wu, S. Passerini, and L. Mai, “One-dimensional nanomaterials for energy storage,” *Journal of Physics D: Applied Physics*, vol. 51, no. 11. Institute of Physics Publishing, p. 113002, Feb. 16, 2018, doi: 10.1088/1361-6463/aaa98d.
- [23] H. Sun, J. Deng, L. Qiu, X. Fang, and H. Peng, “Recent progress in solar cells based on one-dimensional nanomaterials,” *Energy and Environmental Science*, vol. 8, no. 4. Royal Society of Chemistry, pp. 1139–1159, Apr. 01, 2015, doi: 10.1039/c4ee03853c.
- [24] N. Lupu, *Nanowires: Science and Technology*. BoD–Books on Demand, 2010.
- [25] K. A. Dick *et al.*, “Control of III-V nanowire crystal structure by growth parameter tuning,” *Semicond. Sci. Technol.*, vol. 25, no. 2, p. 11, Jan. 2010, doi: 10.1088/0268-1242/25/2/024009.
- [26] V. G. Dubrovskii and N. V. Sibirev, “Growth thermodynamics of nanowires and its application to polytypism of zinc blende III-V nanowires,” *Phys. Rev. B - Condens. Matter Mater. Phys.*, vol. 77, no. 3, pp. 1–8, Jan. 2008, doi: 10.1103/PhysRevB.77.035414.
- [27] P. Caroff, K. A. Dick, J. Johansson, M. E. Messing, K. Deppert, and L. Samuelson, “Controlled polytypic and twin-plane superlattices in III-V nanowires,” *Nat. Nanotechnol.*, vol. 4, no. 1, pp. 50–55, Nov. 2009, doi: 10.1038/nnano.2008.359.
- [28] T. Akiyama, K. Sano, K. Nakamura, and T. Ito, “An empirical potential approach to wurtzite-zinc-blende polytypism in group III-V semiconductor nanowires,” *Japanese J. Appl. Physics, Part 2 Lett.*, vol. 45, no. 8–11, p. L275, Mar. 2006, doi: 10.1143/JJAP.45.L275.
- [29] R. S. Wagner and W. C. Ellis, “Vapor-liquid-solid mechanism of single crystal growth,” *Appl. Phys. Lett.*, vol. 4, no. 5, pp. 89–90, 1964, doi: 10.1063/1.1753975.
- [30] V. G. Dubrovskii, “Theory of VLS Growth of Compound Semiconductors,” doi: 10.1016/bs.semsem.2015.09.002.
- [31] L. J. Lauhon, M. S. Gudiksen, and C. M. Lieber, “Semiconductor Nanowire Heterostructures,” vol. 362, pp. 1247–1260, 2004, doi: 10.1098/rsta.2004.1377.
- [32] A. I. Persson, M. W. Larsson, S. Stenström, B. J. Ohlsson, L. Samuelson, and L. R. Wallenberg, “Solid-phase diffusion mechanism for GaAs nanowire growth,” *Nat. Mater.*, vol. 3, no. 10, pp. 677–681, 2004, doi: 10.1038/nmat1220.

- [33] S. N. Mohammad, "For nanowire growth, vapor-solid-solid (vapor-solid) mechanism is actually vapor-quasisolid-solid (vapor-quasiliquid-solid) mechanism For nanowire growth, vapor-solid-solid "vapor-solid... mechanism is actually vapor-quasisolid-solid "vapor-quasiliquid-soli," *Artic. J. Chem. Phys.*, 2009, doi: 10.1063/1.3246169.
- [34] K. W. Kolasinski, "Catalytic growth of nanowires: Vapor-liquid-solid, vapor-solid-solid, solution-liquid-solid and solid-liquid-solid growth," doi: 10.1016/j.cossms.2007.03.002.
- [35] J. L. Lensch-Falk, E. R. Hemesath, D. E. Perea, and L. J. Lauhon, "Alternative catalysts for VSS growth of silicon and germanium nanowires," *J. Mater. Chem.*, vol. 19, no. 7, pp. 849–857, Feb. 2009, doi: 10.1039/b817391e.
- [36] S. Kodambaka, J. Tersoff, M. C. Reuter, and F. M. Ross, "Germanium Nanowire Growth below the Eutectic Temperature," *New Ser.*, vol. 316, no. 5825, pp. 729–732, 2007, doi: 10.1126/science.ll38007.
- [37] S. Hertenberger, D. Rudolph, M. Bichler, J. J. Finley, G. Abstreiter, and G. Koblmüller, "Growth kinetics in position-controlled and catalyst-free InAs nanowire arrays on Si(111) grown by selective area molecular beam epitaxy," *J. Appl. Phys.*, vol. 108, no. 11, p. 114316, Dec. 2010, doi: 10.1063/1.3525610.
- [38] L. Gü, P. Caroff, and A. Fontcuberta I Morral, "Vapor Phase Growth of Semiconductor Nanowires: Key Developments and Open Questions," 2019, doi: 10.1021/acs.chemrev.8b00649.
- [39] T. J. Trentler, K. M. Hickman, S. C. Goel, A. M. Viano, P. C. Gibbons, and W. E. Buhro, "Solution-liquid-solid growth of crystalline III-V semiconductors: An analogy to vapor-liquid-solid growth," *Science (80-.)*, vol. 270, no. 5243, p. 1791, Dec. 1995, doi: 10.1126/science.270.5243.1791.
- [40] F. Wang, A. Dong, J. Sun, R. Tang, H. Yu, and W. E. Buhro, "Solution-liquid-solid growth of semiconductor nanowires," *Inorganic Chemistry*, vol. 45, no. 19. American Chemical Society, pp. 7511–7521, Sep. 18, 2006, doi: 10.1021/ic060498r.
- [41] S. Wang, Z. Shan, and H. Huang, "The Mechanical Properties of Nanowires," *Adv. Sci.*, vol. 4, no. 4, p. 1600332, Apr. 2017, doi: 10.1002/advs.201600332.
- [42] Y. Zhu, F. Xu, G. Qin, W. Y. Fung, and W. Lu, "Mechanical properties of vapor - Liquid - Solid synthesized silicon nanowires," *Nano Lett.*, vol. 9, no. 11, pp. 3934–3939, Dec. 2009, doi: 10.1021/nl902132w.
- [43] S. Hoffmann *et al.*, "Measurement of the bending strength of vapor-liquid-solid grown silicon nanowires," *Nano Lett.*, vol. 6, no. 4, pp. 622–625, Apr. 2006, doi: 10.1021/nl052223z.
- [44] X. D. Han, K. Zheng, Y. F. Zhang, X. N. Zhang, Z. Zhang, and Z. L. Wang, "Low-Temperature In Situ Large-Strain Plasticity of Silicon Nanowires," *Adv. Mater.*, vol. 19, no. 16, pp. 2112–2118, Aug. 2007, doi: 10.1002/adma.200602705.
- [45] G. Zhang, W. Wang, and X. Li, "Enhanced Thermoelectric Properties of Core/Shell Heterostructure Nanowire Composites," *Adv. Mater.*, vol. 20, no. 19, pp. 3654–3656, Oct. 2008, doi: 10.1002/adma.200800162.
- [46] Y. Tian *et al.*, "One-dimensional quantum confinement effect modulated thermoelectric properties in InAs nanowires," *Nano Lett.*, vol. 12, no. 12, pp. 6492–6497, Dec. 2012, doi: 10.1021/nl304194c.

- [47] G. Brönstrup, N. Jahr, C. Leiterer, A. Csäki, W. Fritzsche, and S. Christiansen, "Optical properties of individual silicon nanowires for photonic devices," *ACS Nano*, vol. 4, no. 12, pp. 7113–7122, Dec. 2010, doi: 10.1021/nn101076t.
- [48] O. Demichel, M. Heiss, J. Bleuse, H. Mariette, and I. A. Fontcuberta Morral, "Impact of surfaces on the optical properties of GaAs nanowires," *Appl. Phys. Lett.*, vol. 97, no. 20, p. 201907, Nov. 2010, doi: 10.1063/1.3519980.
- [49] L. Ahtapodov *et al.*, "A story told by a single nanowire: Optical properties of wurtzite GaAs," *Nano Lett.*, vol. 12, no. 12, pp. 6090–6095, Dec. 2012, doi: 10.1021/nl3025714.
- [50] A. V. Rodina and A. L. Efros, "Effect of dielectric confinement on optical properties of colloidal nanostructures," *J. Exp. Theor. Phys.*, vol. 122, no. 3, pp. 554–566, May 2016, doi: 10.1134/S1063776116030183.
- [51] M. Hjort *et al.*, "Direct imaging of atomic scale structure and electronic properties of GaAs wurtzite and zinc blende nanowire surfaces," *Nano Lett.*, vol. 13, no. 9, pp. 4492–4498, Sep. 2013, doi: 10.1021/nl402424x.
- [52] W. Lu and C. M. Lieber, "TOPICAL REVIEW Semiconductor nanowires," *J. Phys. D Appl. Phys.*, vol. 39, pp. 387–406, 2006, doi: 10.1088/0022-3727/39/21/R01.
- [53] H. J. Joyce, J. Wong-Leung, Q. Gao, H. H. Tan, and C. Jagadish, "Phase Perfection in Zinc Blende and Wurtzite III-V Nanowires Using Basic Growth Parameters," vol. 10, pp. 908–915, 2010, doi: 10.1021/nl903688v.
- [54] T. Mårtensson, M. Borgström, W. Seifert, B. J. Ohlsson, and L. Samuelson, "Fabrication of individually seeded nanowire arrays by vapour-liquid-solid growth," *Nanotechnology*, vol. 14, no. 12, pp. 1255–1258, 2003, doi: 10.1088/0957-4484/14/12/004.
- [55] S. Gazibegovic *et al.*, "Epitaxy of advanced nanowire quantum devices," *Nature*, vol. 548, no. 7668, pp. 434–438, Aug. 2017, doi: 10.1038/nature23468.
- [56] F. Krizek *et al.*, "Field effect enhancement in buffered quantum nanowire networks," *Phys. Rev. Mater.*, vol. 2, p. 93401, 2018, doi: 10.1103/PhysRevMaterials.2.093401.
- [57] P. Krogstrup *et al.*, "Epitaxy of semiconductor-superconductor nanowires," *Nat. Mater.*, vol. 14, no. 4, pp. 400–406, Jan. 2015, doi: 10.1038/nmat4176.
- [58] R. R. Lapierre, M. Robson, K. M. Azizur-Rahman, and P. Kuyanov, "A review of III-V nanowire infrared photodetectors and sensors," *Journal of Physics D: Applied Physics*, vol. 50, no. 12. Institute of Physics Publishing, p. 123001, Feb. 16, 2017, doi: 10.1088/1361-6463/aa5ab3.
- [59] S. W. Eaton, A. Fu, A. B. Wong, C. Z. Ning, and P. Yang, "Semiconductor nanowire lasers," *Nature Reviews Materials*, vol. 1, no. 6. Nature Publishing Group, May 04, 2016, doi: 10.1038/natrevmats.2016.28.
- [60] M. Kumar and R. Vig, "Term-frequency inverse-document frequency definition semantic (TIDS) based focused web crawler," in *Communications in Computer and Information Science*, 2012, vol. 270 CCIS, no. PART II, pp. 31–36, doi: 10.1007/978-3-642-29216-3_5.
- [61] D. M. Blei, A. Y. Ng, and M. I. Jordan, "Latent dirichlet allocation," *J. Mach. Learn. Res.*, vol. 3, no. Jan, pp. 993–1022, 2003.
- [62] S. Kaplan, "Innovation lifecycles," *Leveraging Mark. Technol. Organ. S-curves to drive Breakthr. growth. Manag. Princ. Innov. LLC*, 2007.

- [63] Z. Li, H. H. Tan, C. Jagadish, and L. Fu, "III-V Semiconductor Single Nanowire Solar Cells: A Review," *Adv. Mater. Technol.*, vol. 3, no. 9, Sep. 2018, doi: 10.1002/ADMT.201800005@10.1002/(ISSN)2365-709X.RENEWABLE-ENERGY-TECHNOLOGIES.
- [64] J. E. M. Haverkort, E. C. Garnett, and E. P. A. M. Bakkers, "Fundamentals of the nanowire solar cell: Optimization of the open circuit voltage," *Applied Physics Reviews*, vol. 5, no. 3. American Institute of Physics Inc., p. 031106, Sep. 01, 2018, doi: 10.1063/1.5028049.
- [65] E. C. Garnett, M. L. Brongersma, Y. Cui, and M. D. McGehee, "Nanowire solar cells," *Annu. Rev. Mater. Res.*, vol. 41, pp. 269–295, Aug. 2011, doi: 10.1146/annurev-matsci-062910-100434.
- [66] G. E. Moore, "Cramming More Components onto Integrated Circuits."
- [67] K. Tomioka, T. Tanaka, S. Hara, K. Hiruma, and T. Fukui, "III-V Nanowires on Si Substrate: Selective-Area Growth and Device Applications," *IEEE J. Sel. Top. QUANTUM Electron.*, vol. 17, no. 4, doi: 10.1109/JSTQE.2010.2068280.
- [68] M. C. Plante and R. R. Lapierre, "Au-assisted growth of GaAs nanowires by gas source molecular beam epitaxy: Tapering, sidewall faceting and crystal structure," *J. Cryst. Growth*, vol. 310, pp. 356–363, 2008, doi: 10.1016/j.jcrysgro.2007.10.050.
- [69] A. Biswas, I. S. Bayer, A. S. Biris, T. Wang, E. Dervishi, and F. Faupel, "Advances in top-down and bottom-up surface nanofabrication: Techniques, applications & future prospects," 2011, doi: 10.1016/j.cis.2011.11.001.
- [70] C. Zhang, X. Miao, K. D. Chabak, and X. Li, "A review of III-V planar nanowire arrays: Selective lateral VLS epitaxy and 3D transistors," *J. Phys. D. Appl. Phys.*, vol. 50, no. 39, 2017, doi: 10.1088/1361-6463/aa7e42.
- [71] P. C. McIntyre and A. Fontcuberta I Morral, *Semiconductor nanowires: to grow or not to grow?*, vol. 9. Elsevier Ltd, 2020, p. 100058.
- [72] M. Li *et al.*, "Bottom-up assembly of large-area nanowire resonator arrays," *Nat. Nanotechnol.*, vol. 3, no. 2, pp. 88–92, Jan. 2008, doi: 10.1038/nnano.2008.26.
- [73] W. Lu, P. Xie, and C. M. Lieber, "Nanowire transistor performance limits and applications," *IEEE Transactions on Electron Devices*, vol. 55, no. 11. pp. 2859–2876, 2008, doi: 10.1109/TED.2008.2005158.
- [74] P. Yang, R. Yan, and M. Fardy, "Semiconductor nanowire: Whats Next?," *Nano Lett.*, vol. 10, no. 5, pp. 1529–1536, May 2010, doi: 10.1021/nl100665r.
- [75] W. Lu and C. M. Lieber, "Nanoelectronics from the bottom up," in *Nanoscience and Technology: A Collection of Reviews from Nature Journals*, World Scientific Publishing Co., 2009, pp. 137–146.
- [76] R. G. Hobbs, N. Petkov, and J. D. Holmes, "Semiconductor nanowire fabrication by bottom-up and top-down paradigms," *Chemistry of Materials*, vol. 24, no. 11. American Chemical Society, pp. 1975–1991, Jun. 12, 2012, doi: 10.1021/cm300570n.
- [77] K. Hiruma *et al.*, "GaAs free-standing quantum-size wires," *J. Appl. Phys.*, vol. 74, no. 5, pp. 3162–3171, Sep. 1993, doi: 10.1063/1.354585.
- [78] P. Caroff, M. E. Messing, B. Mattias Borg, K. A. Dick, K. Deppert, and L. E. Wernersson, "InSb heterostructure nanowires: MOVPE growth under extreme lattice mismatch," *Nanotechnology*, vol. 20, no. 49, p. 495606, Nov. 2009, doi: 10.1088/0957-4484/20/49/495606.

- [79] T. Mårtensson *et al.*, “Epitaxial Growth of Indium Arsenide Nanowires on Silicon Using Nucleation Templates Formed by Self-Assembled Organic Coatings,” *Adv. Mater.*, vol. 19, no. 14, pp. 1801–1806, Jul. 2007, doi: 10.1002/adma.200700285.
- [80] J. Johansson and K. A. Dick, “Recent advances in semiconductor nanowire heterostructures,” *CrystEngComm*, vol. 13, no. 24, pp. 7175–7184, 2011, doi: 10.1039/c1ce05821e.
- [81] M. N. Mankin *et al.*, “Facet-Selective Epitaxy of Compound Semiconductors on Faceted Silicon Nanowires,” *Nano Lett.*, vol. 15, no. 7, pp. 4776–4782, 2015, doi: 10.1021/acs.nanolett.5b01721.
- [82] R. N. Musin and X.-Q. Q. Wang, “Structural and electronic properties of epitaxial core-shell nanowire heterostructures,” *Phys. Rev. B - Condens. Matter Mater. Phys.*, vol. 71, no. 15, p. 155318, Apr. 2005, doi: 10.1103/PhysRevB.71.155318.
- [83] Q. Gao *et al.*, “Growth and properties of III-V compound semiconductor heterostructure nanowires,” *Semicond. Sci. Technol.*, vol. 26, no. 1, pp. 14035–14045, Jan. 2011, doi: 10.1088/0268-1242/26/1/014035.
- [84] M. Royo, M. De Luca, R. Rurali, and I. Zardo, “A review on III-V core-multishell nanowires: Growth, properties, and applications,” *Journal of Physics D: Applied Physics*, vol. 50, no. 14, Institute of Physics Publishing, p. 143001, Mar. 07, 2017, doi: 10.1088/1361-6463/aa5d8e.
- [85] M. S. Gudiksen, L. J. Lauhon, J. Wang, D. C. Smith, and C. M. Lieber, “Growth of nanowire superlattice structures for nanoscale photonics and electronics,” *Nature*, vol. 415, no. 6872, pp. 617–620, Feb. 2002, doi: 10.1038/415617a.
- [86] M. T. Björk *et al.*, “One-dimensional heterostructures in semiconductor nanowhiskers,” *Appl. Phys. Lett.*, vol. 80, no. 6, pp. 1058–1060, Feb. 2002, doi: 10.1063/1.1447312.
- [87] Y. Wu, R. Fan, and P. Yang, “Block-by-Block Growth of Single-Crystalline Si/SiGe Superlattice Nanowires,” *Nano Lett.*, vol. 2, no. 2, pp. 83–86, Feb. 2002, doi: 10.1021/nl0156888.
- [88] S. Korte *et al.*, “Charge transport in GaAs nanowires: Interplay between conductivity through the interior and surface conductivity,” *J. Phys. Condens. Matter*, vol. 31, no. 7, 2019, doi: 10.1088/1361-648X/aaf515.
- [89] J. A. Goebel, R. W. Black, J. Puthussery, J. Giblin, T. H. Kosel, and M. Kuno, “Solution-Based II-VI Core/Shell Nanowire Heterostructures,” *J. Am. Chem. Soc.*, vol. 130, no. 44, pp. 14822–14833, Nov. 2008, doi: 10.1021/ja805538p.
- [90] V. L. Rideout, “A review of the theory and technology for ohmic contacts to group III-V compound semiconductors,” *Solid State Electron.*, vol. 18, no. 6, pp. 541–550, Jun. 1975, doi: 10.1016/0038-1101(75)90031-3.
- [91] A. Piotrowska, A. Guivarc’h, and G. Pelous, “Ohmic contacts to III-V compound semiconductors: A review of fabrication techniques,” *Solid State Electron.*, vol. 26, no. 3, pp. 179–197, 1983, doi: [https://doi.org/10.1016/0038-1101\(83\)90083-7](https://doi.org/10.1016/0038-1101(83)90083-7).
- [92] D. K. Schroder and D. L. Meier, “Solar Cell Contact Resistance—A Review,” *IEEE Trans. Electron Devices*, vol. 31, no. 5, pp. 637–647, 1984, doi: 10.1109/T-ED.1984.21583.
- [93] A. Agrawal *et al.*, “Fermi level depinning and contact resistivity reduction using a reduced titania interlayer in n-silicon metal-insulator-semiconductor ohmic contacts,” *Cit. Appl. Phys. Lett.*, vol. 104, p. 112101, 2014, doi: 10.1063/1.4868302.
- [94] F. Léonard and A. A. Talin, “Electrical contacts to one- and two-dimensional nanomaterials,” *Nat.*

Nanotechnol., vol. 6, no. 12, pp. 773–783, Nov. 2011, doi: 10.1038/nnano.2011.196.

- [95] H. Yu *et al.*, “Contact resistivities of metal-insulatorsemiconductor contacts and metalsemiconductor contacts,” *Appl. Phys. Lett.*, vol. 108, no. 17, p. 171602, Apr. 2016, doi: 10.1063/1.4947580.
- [96] S. Mangal, S. Adhikari, and P. Banerji, “Aluminum/polyaniline/GaAs metal-insulator-semiconductor solar cell: Effect of tunneling on device performance,” *Appl. Phys. Lett.*, vol. 94, no. 22, p. 223509, Jun. 2009, doi: 10.1063/1.3149703.
- [97] A. Nagelein *et al.*, “Comparative analysis on resistance profiling along tapered semiconductor nanowires: Multi-tip technique versus transmission line method,” *J. Phys. Condens. Matter*, vol. 29, no. 39, 2017, doi: 10.1088/1361-648X/aa801e.
- [98] X. Jiang, Q. Xiong, S. Nam, F. Qian, Y. Li, and C. M. Lieber, “InAs/InP radial nanowire heterostructures as high electron mobility devices,” *Nano Lett.*, vol. 7, no. 10, pp. 3214–3218, Oct. 2007, doi: 10.1021/nl072024a.
- [99] A. C. Ford *et al.*, “Diameter-dependent electron mobility of InAs nanowires,” *Nano Lett.*, vol. 9, no. 1, pp. 360–365, 2009, doi: 10.1021/nl803154m.
- [100] A. Javey *et al.*, “High- κ dielectrics for advanced carbon-nanotube transistors and logic gates,” *Nat. Mater.*, vol. 1, no. 4, pp. 241–246, Nov. 2002, doi: 10.1038/nmat769.
- [101] S. A. Dayeh, D. P. R. Aplin, X. Zhou, P. K. L. Yu, E. T. Yu, and D. Wang, “High electron mobility InAs nanowire field-effect transistors,” *Small*, vol. 3, no. 2, pp. 326–332, Feb. 2007, doi: 10.1002/sml.200600379.
- [102] T. Bryllert, L. E. Wernersson, L. E. Fröberg, and L. Samuelson, “Vertical high-mobility wrap-gated InAs nanowire transistor,” *IEEE Electron Device Lett.*, vol. 27, no. 5, pp. 323–325, May 2006, doi: 10.1109/LED.2006.873371.
- [103] C. Thelander, M. T. Björk, M. W. Larsson, A. E. Hansen, L. R. Wallenberg, and L. Samuelson, “Electron transport in InAs nanowires and heterostructure nanowire devices,” *Solid State Commun.*, vol. 131, no. 9-10 SPEC. ISS., pp. 573–579, Sep. 2004, doi: 10.1016/j.ssc.2004.05.033.
- [104] L. J. Lauhon, M. S. Gudlksen, D. Wang, and C. M. Lieber, “Epitaxial core-shell and core-multishell nanowire heterostructures,” *Nature*, vol. 420, no. 6911, pp. 57–61, Nov. 2002, doi: 10.1038/nature01141.
- [105] S. J. Wind, J. Appenzeller, R. Martel, V. Derycke, and P. Avouris, “Vertical scaling of carbon nanotube field-effect transistors using top gate electrodes,” *Appl. Phys. Lett.*, vol. 80, no. 20, pp. 3817–3819, May 2002, doi: 10.1063/1.1480877.
- [106] E. P. A. M. Bakkers *et al.*, “Epitaxial growth of InP nanowires on germanium,” 2004, doi: 10.1038/nmat1235.
- [107] T. Mårtensson *et al.*, “Epitaxial III-V nanowires on silicon,” *Nano Lett.*, vol. 4, no. 10, pp. 1987–1990, Oct. 2004, doi: 10.1021/nl0487267.
- [108] T. Mårtensson, P. Carlberg, M. Borgstro, L. Montelius, W. Seifert, and L. Samuelson, “Nanowire Arrays Defined by Nanoimprint Lithography,” 2004, doi: 10.1021/nl035100s.
- [109] H. Küpers *et al.*, “Surface preparation and patterning by nano imprint lithography for the selective area growth of GaAs nanowires on Si(111),” *Semicond. Sci. Technol.*, vol. 32, no. 11, p. 115003, 2017, doi: 10.1088/1361-6641/aa8c15.

- [110] C.-Y. Chi *et al.*, "Twin-Free GaAs Nanosheets by Selective Area Growth: Implications for Defect-Free Nanostructures," vol. 28, p. 14, 2013, doi: 10.1021/nl400561j.
- [111] K. Tomioka, Y. Kobayashi, J. Motohisa, S. Hara, and T. Fukui, "Selective-area growth of vertically aligned GaAs and GaAs/AlGaAs core-shell nanowires on Si(111) substrate," *Nanotechnology*, vol. 20, p. 8, 2009, doi: 10.1088/0957-4484/20/14/145302.
- [112] K. Hiruma *et al.*, "Growth and optical properties of nanometer-scale GaAs and InAs whiskers," *J. Appl. Phys.*, vol. 77, no. 2, pp. 447–462, Jan. 1995, doi: 10.1063/1.359026.
- [113] K. Tomioka, J. Motohisa, S. Hara, and T. Fukui, "Control of InAs nanowire growth directions on Si," *Nano Lett.*, vol. 8, no. 10, pp. 3475–3480, Oct. 2008, doi: 10.1021/nl802398j.
- [114] S. A. Fortuna, J. Wen, I. Su Chun, and X. Li, "Planar GaAs Nanowires on GaAs (100) Substrates: Self-Aligned, Nearly Twin-Defect Free, and Transfer-Printable," *NANO Lett.*, vol. 8, no. 12, pp. 4421–4427, 2008, doi: 10.1021/nl802331m.
- [115] K. A. Dick *et al.*, "Synthesis of branched 'nanotrees' by controlled seeding of multiple branching events," *Nat. Mater.*, vol. 3, no. 6, pp. 380–384, May 2004, doi: 10.1038/nmat1133.
- [116] S. Jin, M. J. Bierman, and S. A. Morin, "A new twist on nanowire formation: Screw-dislocation-driven growth of nanowires and nanotubes," *J. Phys. Chem. Lett.*, vol. 1, no. 9, pp. 1472–1480, May 2010, doi: 10.1021/jz100288z.
- [117] J. Wang, S. R. Plissard, M. A. Verheijen, L. F. Feiner, A. Cavalli, and E. P. A. M. Bakkers, "Reversible switching of InP nanowire growth direction by catalyst engineering," *Nano Lett.*, vol. 13, no. 8, pp. 3802–3806, Aug. 2013, doi: 10.1021/nl401767b.
- [118] K. A. Dick and P. Caroff, "Metal-seeded growth of III-V semiconductor nanowires: Towards gold-free synthesis," *Nanoscale*, vol. 6, no. 6, pp. 3006–3021, Mar. 2014, doi: 10.1039/c3nr06692d.
- [119] B. Mandl *et al.*, "Au-free epitaxial growth of InAs nanowires," *Nano Lett.*, vol. 6, no. 8, pp. 1817–1821, Aug. 2006, doi: 10.1021/nl060452v.
- [120] Y. Huang, X. Duan, Q. Wei, and C. M. Lieber, "Directed assembly of one-dimensional nanostructures into functional networks," *Science (80-.)*, vol. 291, no. 5504, pp. 630–633, Jan. 2001, doi: 10.1126/science.291.5504.630.
- [121] G. Yu, A. Cao, and C. M. Lieber, "Large-area blown bubble films of aligned nanowires and carbon nanotubes," *Nat. Nanotechnol.*, vol. 2, no. 6, pp. 372–377, May 2007, doi: 10.1038/nnano.2007.150.
- [122] D. Whang, S. Jin, Y. Wu, and C. M. Lieber, "Large-Scale Hierarchical Organization of Nanowire Arrays for Integrated Nanosystems," *NANO Lett.*, vol. 3, no. 9, pp. 1255–1259, 2003, doi: 10.1021/nl0345062.
- [123] M. Akabori, J. Takeda, J. Motohisa, and T. Fukui, "InGaAs nano-pillar array formation on partially masked InP(111)B by selective area metal-organic vapour phase epitaxial growth for two-dimensional photonic crystal application," *Nanotechnology*, vol. 14, no. 10, pp. 1071–1074, 2003, doi: 10.1088/0957-4484/14/10/303.
- [124] M. Akabori, T. Murakami, and S. Yamada, "Selective area molecular beam epitaxy of InAs on GaAs (110) masked substrates for direct fabrication of planar nanowire field-effect transistors," *J. Cryst. Growth*, vol. 345, no. 1, pp. 22–26, Apr. 2012, doi: 10.1016/j.jcrysgro.2012.02.009.
- [125] M. Friedl *et al.*, "Remote Doping of Scalable Nanowire Branches," *Nano Lett.*, vol. 20, no. 5, pp.

3577–3584, May 2020, doi: 10.1021/acs.nanolett.0c00517.

- [126] A. Bucamp, C. Coinon, J. L. Codron, D. Troadec, X. Wallart, and L. Desplanque, “Buffer free InGaAs quantum well and in-plane nanostructures on InP grown by atomic hydrogen assisted MBE,” *J. Cryst. Growth*, vol. 512, pp. 11–15, Apr. 2019, doi: 10.1016/j.jcrysgro.2019.01.033.
- [127] S. Plissard *et al.*, “Gold-free growth of GaAs nanowires on silicon: arrays and polytypism,” *Nanotechnology*, vol. 21, no. 38, p. 385602, 2010, doi: 10.1088/0957-4484/21/38/385602.
- [128] J. Treu *et al.*, “Widely tunable alloy composition and crystal structure in catalyst-free InGaAs nanowire arrays grown by selective area molecular beam epitaxy,” *Appl. Phys. Lett.*, vol. 108, no. 5, p. 053110, Feb. 2016, doi: 10.1063/1.4941407.
- [129] G. Tutuncuoglu *et al.*, “Towards defect-free 1-D GaAs/AlGaAs heterostructures based on GaAs nanomembranes,” *Nanoscale*, vol. 7, no. 46, pp. 19453–19460, Dec. 2015, doi: 10.1039/c5nr04821d.
- [130] M. Friedl *et al.*, “Template-Assisted Scalable Nanowire Networks,” 2018, doi: 10.1021/acs.nanolett.8b00554.
- [131] A. Bucamp, “Selective growth and characterization of nanostructures of III-V materials developed by epitaxia by molecular jets,” University of Lille, 2019.
- [132] M. Nasilowski, B. Mahler, E. Lhuillier, S. Ithurria, and B. Dubertret, “Two-Dimensional Colloidal Nanocrystals,” *Dimens. Colloid. Nanocrystals. Chem. Rev.*, vol. 116, no. 18, pp. 10934–10982, 2016, doi: 10.1021/acs.chemrev.6b00164i.
- [133] P. W. Voorhees, “The theory of Ostwald ripening,” *J. Stat. Phys.*, vol. 38, no. 1–2, pp. 231–252, Jan. 1985, doi: 10.1007/BF01017860.
- [134] M. Yarema *et al.*, “Upscaling Colloidal Nanocrystal Hot-Injection Syntheses via Reactor Underpressure,” *Chem. Mater.*, vol. 29, no. 2, pp. 796–803, Jan. 2017, doi: 10.1021/acs.chemmater.6b04789.
- [135] J. Van Embden, A. S. R. Chesman, and J. J. Jasieniak, “The heat-up synthesis of colloidal nanocrystals,” *Chemistry of Materials*, vol. 27, no. 7. American Chemical Society, pp. 2246–2285, Apr. 14, 2015, doi: 10.1021/cm5028964.
- [136] S. G. Kwon and T. Hyeon, “Formation mechanisms of uniform nanocrystals via hot-injection and heat-up methods,” *Small*, vol. 7, no. 19. John Wiley & Sons, Ltd, pp. 2685–2702, Oct. 04, 2011, doi: 10.1002/sml.201002022.
- [137] A. J. Houtepen, Z. Hens, J. S. Owen, and I. Infante, “On the Origin of Surface Traps in Colloidal II-VI Semiconductor Nanocrystals,” *Chem. Mater.*, vol. 29, no. 2, pp. 752–761, Jan. 2017, doi: 10.1021/acs.chemmater.6b04648.
- [138] S. Singh *et al.*, “Colloidal CdSe Nanoplatelets, A Model for Surface Chemistry/Optoelectronic Property Relations in Semiconductor Nanocrystals,” *J. Am. Chem. Soc.*, vol. 140, no. 41, pp. 13292–13300, 2018, doi: 10.1021/jacs.8b07566.
- [139] C. Livache *et al.*, “A colloidal quantum dot infrared photodetector and its use for intraband detection,” *Nat. Commun.*, vol. 10, no. 1, pp. 1–10, Dec. 2019, doi: 10.1038/s41467-019-10170-8.
- [140] S. Keuleyan, E. Lhuillier, V. Brajuskovic, and P. Guyot-Sionnest, “Mid-infrared HgTe colloidal quantum dot photodetectors,” *Nat. Photonics*, vol. 5, no. 8, pp. 489–493, Aug. 2011, doi:

10.1038/nphoton.2011.142.

- [141] G. Konstantatos and E. H. Sargent, "Colloidal quantum dot photodetectors," in *Infrared Physics and Technology*, May 2011, vol. 54, no. 3, pp. 278–282, doi: 10.1016/j.infrared.2010.12.029.
- [142] B. Guzelturk, Y. Kelestemur, M. Olutas, S. Delikanli, and H. V. Demir, "Amplified spontaneous emission and lasing in colloidal nanoplatelets," *ACS Nano*, vol. 8, no. 7, pp. 6599–6605, Jul. 2014, doi: 10.1021/nn5022296.
- [143] G. Manfredi, P. Lova, F. Di Stasio, P. Rastogi, R. Krahne, and D. Comoretto, "Lasing from dot-in-rod nanocrystals in planar polymer microcavities," *RSC Adv.*, vol. 8, no. 23, pp. 13026–13033, Apr. 2018, doi: 10.1039/c8ra01282b.
- [144] M. Kazes, D. Y. Y. Lewis, Y. Ebenstein, T. Mokari, and U. Banin, "Lasing from Semiconductor Quantum Rods in a Cylindrical Microcavity," *Adv. Mater.*, vol. 14, no. 4, p. 317, Feb. 2002, doi: 10.1002/1521-4095(20020219)14:4<317::aid-adma317>3.3.co;2-l.
- [145] P. S. Weiss, "Molecules join the assembly line," *Nature*, vol. 413, no. 6856. Nature Publishing Group, pp. 585–586, Oct. 11, 2001, doi: 10.1038/35098175.
- [146] W. C. W. Chan and S. Nie, "Quantum dot bioconjugates for ultrasensitive nonisotopic detection," *Science (80-.)*, vol. 281, no. 5385, pp. 2016–2018, Sep. 1998, doi: 10.1126/science.281.5385.2016.
- [147] M. Dahan, S. Lévi, C. Luccardini, P. Rostaing, B. Riveau, and A. Triller, "Diffusion Dynamics of Glycine Receptors Revealed by Single-Quantum Dot Tracking," *Science (80-.)*, vol. 302, no. 5644, pp. 442–445, Oct. 2003, doi: 10.1126/science.1088525.
- [148] H. W. Hillhouse and M. C. Beard, "Solar cells from colloidal nanocrystals: Fundamentals, materials, devices, and economics," *Current Opinion in Colloid and Interface Science*, vol. 14, no. 4. Elsevier, pp. 245–259, Aug. 01, 2009, doi: 10.1016/j.cocis.2009.05.002.
- [149] M. Wu *et al.*, "Solid-state infrared-to-visible upconversion sensitized by colloidal nanocrystals," *Nat. Photonics*, vol. 10, no. 1, pp. 31–34, Jan. 2016, doi: 10.1038/nphoton.2015.226.
- [150] J. H. Choi *et al.*, "Exploiting the colloidal nanocrystal library to construct electronic devices," *Science (80-.)*, vol. 352, no. 6282, pp. 205–208, Apr. 2016, doi: 10.1126/science.aad0371.
- [151] C. R. Kagan, "Flexible colloidal nanocrystal electronics," *Chemical Society Reviews*, vol. 48, no. 6. Royal Society of Chemistry, pp. 1626–1641, Mar. 21, 2019, doi: 10.1039/c8cs00629f.
- [152] D. V. Talapin, J. S. Lee, M. V. Kovalenko, and E. V. Shevchenko, "Prospects of colloidal nanocrystals for electronic and optoelectronic applications," *Chem. Rev.*, vol. 110, no. 1, pp. 389–458, Jan. 2010, doi: 10.1021/cr900137k.
- [153] R. Komatsu *et al.*, "Repeatedly foldable AMOLED display," *J. Soc. Inf. Disp.*, vol. 23, no. 2, pp. 41–49, Feb. 2015, doi: 10.1002/jsid.276.
- [154] D.-U. Jin *et al.*, "65.2: Distinguished Paper: World-Largest (6.5") Flexible Full Color Top Emission AMOLED Display on Plastic Film and Its Bending Properties," *SID Symp. Dig. Tech. Pap.*, vol. 40, no. 1, p. 983, Jun. 2009, doi: 10.1889/1.3256964.
- [155] H. Ohmae *et al.*, "9.4: Stretchable 45 × 80 RGB LED Display Using Meander Wiring Technology," *SID Symp. Dig. Tech. Pap.*, vol. 46, no. 1, pp. 102–105, Jun. 2015, doi: 10.1002/sdtp.10298.
- [156] Y. E. Panfil, M. Oded, and U. Banin, "Colloidal Quantum Nanostructures: Emerging Materials for

- Display Applications," *Angewandte Chemie - International Edition*, vol. 57, no. 16. Wiley-VCH Verlag, pp. 4274–4295, Apr. 09, 2018, doi: 10.1002/anie.201708510.
- [157] Z. Tan *et al.*, "Colloidal nanocrystal-based light-emitting diodes fabricated on plastic toward flexible quantum dot optoelectronics," *J. Appl. Phys.*, vol. 105, no. 3, p. 034312, Feb. 2009, doi: 10.1063/1.3074335.
- [158] J. H. Choi *et al.*, "Bandlike transport in strongly coupled and doped quantum dot solids: A route to high-performance thin-film electronics," *Nano Lett.*, vol. 12, no. 5, pp. 2631–2638, May 2012, doi: 10.1021/nl301104z.
- [159] D. V. Talapin and C. B. Murray, "PbSe nanocrystal solids for n- and p-channel thin film field-effect transistors," *Science (80-.)*, vol. 310, no. 5745, pp. 86–89, Oct. 2005, doi: 10.1126/science.1116703.
- [160] J. Yang, M. K. Choi, D. H. Kim, and T. Hyeon, "Designed Assembly and Integration of Colloidal Nanocrystals for Device Applications," *Advanced Materials*, vol. 28, no. 6. Wiley-VCH Verlag, pp. 1176–1207, Feb. 10, 2016, doi: 10.1002/adma.201502851.
- [161] J. F. Miethe, A. Schlosser, J. G. Eckert, F. Lübke, and N. C. Bigall, "Electronic transport in CdSe nanoplatelet based polymer fibres," *J. Mater. Chem. C*, vol. 6, no. 40, pp. 10916–10923, Oct. 2018, doi: 10.1039/c8tc03879a.
- [162] E. Lhuillier, J. F. Dayen, D. O. Thomas, A. Robin, B. Doudin, and B. Dubertret, "Nanoplatelets bridging a nanotrench: A new architecture for photodetectors with increased sensitivity," *Nano Lett.*, vol. 15, no. 3, pp. 1736–1742, Mar. 2015, doi: 10.1021/nl504414g.
- [163] S. Z. Bisri, C. Piliago, M. Yarema, W. Heiss, and M. A. Loi, "Low Driving Voltage and High Mobility Ambipolar Field-Effect Transistors with PbS Colloidal Nanocrystals," *Adv. Mater.*, vol. 25, no. 31, pp. 4309–4314, Aug. 2013, doi: 10.1002/adma.201205041.
- [164] E. Lhuillier *et al.*, "Investigating the n- and p-Type Electrolytic Charging of Colloidal Nanoplatelets," *J. Phys. Chem. C*, vol. 119, no. 38, pp. 21795–21799, Sep. 2015, doi: 10.1021/acs.jpcc.5b05296.
- [165] S. Ithurria and B. Dubertret, "Quasi 2D colloidal CdSe platelets with thicknesses controlled at the atomic level," *J. Am. Chem. Soc.*, vol. 130, no. 49, pp. 16504–16505, 2008, doi: 10.1021/ja807724e.
- [166] V. Dzhanov *et al.*, "Morphology-induced phonon spectra of CdSe/ CdS nanoplatelets: core/shell vs. core-crown," vol. 8, p. 17204, 2016, doi: 10.1039/c6nr06949e.
- [167] B. Mahler, B. Nadal, C. Bouet, G. Patriarche, and B. Dubertret, "Core/Shell Colloidal Semiconductor Nanoplatelets," 2012, doi: 10.1021/ja307944d.
- [168] D. Tessier *et al.*, "Efficient exciton concentrators built from colloidal core/crown CdSe/CdS semiconductor nanoplatelets," *Nano Lett.*, vol. 14, no. 1, pp. 207–213, 2014, doi: 10.1021/nl403746p.
- [169] H. K. Wickramasinghe, "Progress in scanning probe microscopy," *Acta Mater.*, vol. 48, no. 1, pp. 347–358, Jan. 2000, doi: 10.1016/S1359-6454(99)00303-1.
- [170] M. A. Poggi, E. D. Gadsby, L. A. Bottomley, W. P. King, E. Oroudjev, and H. Hansma, "Scanning probe microscopy," *Analytical Chemistry*, vol. 76, no. 12. American Chemical Society, pp. 3429–3444, Jun. 15, 2004, doi: 10.1021/ac0400818.

- [171] K. Kaiser, L. Gross, and F. Schulz, "A Single-Molecule Chemical Reaction Studied by High-Resolution Atomic Force Microscopy and Scanning Tunneling Microscopy Induced Light Emission," *ACS Nano*, vol. 13, 2019, doi: 10.1021/acsnano.9b01852.
- [172] E. Meyer, H. J. Hug, and R. Bennewitz, *Scanning probe microscopy: the lab on a tip*. Springer Science & Business Media, 2003.
- [173] G. Binnig, H. Rohrer, C. Gerber, and E. Weibel, "Surface studies by scanning tunneling microscopy," *Phys. Rev. Lett.*, vol. 49, no. 1, pp. 57–61, Jul. 1982, doi: 10.1103/PhysRevLett.49.57.
- [174] G. Binnig, H. Rohrer, C. Gerber, and E. Weibel, "Tunneling through a controllable vacuum gap," *Appl. Phys. Lett.*, vol. 40, no. 2, pp. 178–180, Jan. 1982, doi: 10.1063/1.92999.
- [175] G. Binnig and H. Rohrer, "Scanning Tunneling Microscopy—from Birth to Adolescence (Nobel Lecture)," *Angew. Chemie Int. Ed. English*, vol. 26, no. 7, pp. 606–614, 1987, doi: 10.1002/anie.198706061.
- [176] K. W. Hipps, "Scanning tunneling spectroscopy (STS)," in *Handbook of Applied Solid State Spectroscopy*, Springer, 2006, pp. 305–350.
- [177] D. J. Griffiths, "Introduction to quantum mechanics," 2nd, Pearson, Chapter 2. time-independent schrodinger Equ., pp. 90–91, 2005.
- [178] W. Greiner, *Quantum mechanics: an introduction*. Springer Science & Business Media, 2011.
- [179] J. Tersoff and D. R. Hamann, "Theory and application for the scanning tunneling microscope," *Phys. Rev. Lett.*, vol. 50, no. 25, pp. 1998–2001, Jun. 1983, doi: 10.1103/PhysRevLett.50.1998.
- [180] J. Bardeen, "Tunnelling from a many-particle point of view," *Phys. Rev. Lett.*, vol. 6, no. 2, pp. 57–59, Jan. 1961, doi: 10.1103/PhysRevLett.6.57.
- [181] A. Selloni, P. Carnevali, E. Tosatti, and C. D. Chen, "Voltage-dependent scanning-tunneling microscopy of a crystal surface: Graphite," Springer, Dordrecht, 1985, pp. 168–171.
- [182] R. J. Hamers, "Atomic-resolution surface spectroscopy with the scanning tunneling microscope," *Annu. Rev. Phys. Chem.*, vol. 40, no. 1, pp. 531–559, Oct. 1989, doi: 10.1146/annurev.pc.40.100189.002531.
- [183] D. R. Vij, *Handbook of applied solid state spectroscopy*. Springer Science & Business Media, 2007.
- [184] M. Berthe, "Electronic transport in quantum confined systems," Université des Sciences et Technologies de Lille, 2007.
- [185] K. M. Bastiaans *et al.*, "Amplifier for scanning tunneling microscopy at MHz frequencies," *Rev. Sci. Instrum.*, vol. 89, no. 9, p. 093709, Sep. 2018, doi: 10.1063/1.5043267.
- [186] J. Yang, D. Sordes, M. Kolmer, D. Martrou, and C. Joachim, "Imaging, single atom contact and single atom manipulations at low temperature using the new ScientaOmicron LT-UHV-4 STM," *EPJ Applied Physics*, vol. 73, no. 1. EDP Sciences, p. 10702, Jan. 01, 2016, doi: 10.1051/epjap/2015150489.
- [187] C. Joachim *et al.*, "Multiple atomic scale solid surface interconnects for atom circuits and molecule logic gates," *J. Phys. Condens. Matter*, vol. 22, no. 8, p. 084025, Feb. 2010, doi: 10.1088/0953-8984/22/8/084025.
- [188] R. M. Feenstra, Y. Dong, M. P. Semtsiv, and W. T. Masselink, "Influence of tip-induced band bending on tunnelling spectra of semiconductor surfaces," *Nanotechnology*, vol. 18, no. 4, p.

044015, Jan. 2007, doi: 10.1088/0957-4484/18/4/044015.

- [189] R. M. Feenstra, "Electrostatic potential for a hyperbolic probe tip near a semiconductor," *J. Vac. Sci. Technol. B Microelectron. Nanom. Struct.*, vol. 21, no. 5, p. 2080, Sep. 2003, doi: 10.1116/1.1606466.
- [190] N. Ishida, K. Sueoka, and R. M. Feenstra, "Influence of surface states on tunneling spectra of n - type GaAs(110) surfaces," *Phys. Rev. B - Condens. Matter Mater. Phys.*, vol. 80, no. 7, p. 075320, Aug. 2009, doi: 10.1103/PhysRevB.80.075320.
- [191] Z. Zhang and J. T. Yates, "Band Bending in Semiconductors: Chemical and Physical Consequences at Surfaces and Interfaces," *Chem. Rev.*, vol. 112, no. 10, pp. 5520–5551, Oct. 2012, doi: 10.1021/cr3000626.
- [192] M. McEllistrem, G. Haase, D. Chen, and R. J. Hamers, "Electrostatic sample-tip interactions in the scanning tunneling microscope," *Phys. Rev. Lett.*, vol. 70, no. 16, pp. 2471–2474, Apr. 1993, doi: 10.1103/PhysRevLett.70.2471.
- [193] R. Dombrowski, C. Steinebach, C. Wittneven, M. Morgenstern, and R. Wiesendanger, "Tip-induced band bending by scanning tunneling spectroscopy of the states of the tip-induced quantum dot on InAs(110)," *Phys. Rev. B - Condens. Matter Mater. Phys.*, vol. 59, no. 12, pp. 8043–8048, Mar. 1999, doi: 10.1103/PhysRevB.59.8043.
- [194] G. J. De Raad, D. M. Bruls, P. M. Koenraad, and J. H. Wolter, "Interplay between tip-induced band bending and voltage-dependent surface corrugation on GaAs(110) surfaces," *Phys. Rev. B - Condens. Matter Mater. Phys.*, vol. 66, no. 19, pp. 1–14, Nov. 2002, doi: 10.1103/PhysRevB.66.195306.
- [195] I. Swart, P. Liljeroth, and D. Vanmaekelbergh, "Scanning probe microscopy and spectroscopy of colloidal semiconductor nanocrystals and assembled structures," *Chemical Reviews*, vol. 116, no. 18. American Chemical Society, pp. 11181–11219, Sep. 28, 2016, doi: 10.1021/acs.chemrev.5b00678.
- [196] C. de Mello Donegá, *Nanoparticles: workhorses of nanoscience*. Springer, 2014.
- [197] U. Banin and O. Millo, "Tunneling and optical spectroscopy of semiconductor nanocrystals," *Annu. Rev. Phys. Chem.*, vol. 54, no. 7, pp. 465–492, 2003, doi: 10.1146/annurev.physchem.54.011002.103838.
- [198] T. H. Nguyen *et al.*, "Charge carrier identification in tunneling spectroscopy of core-shell nanocrystals," *Phys. Rev. B - Condens. Matter Mater. Phys.*, vol. 84, no. 19, 2011, doi: 10.1103/PhysRevB.84.195133.
- [199] B. Voigtländer *et al.*, "Invited Review Article: Multi-tip scanning tunneling microscopy: Experimental techniques and data analysis," *Rev. Sci. Instrum.*, vol. 89, no. 10, p. 101101, Oct. 2018, doi: 10.1063/1.5042346.
- [200] S. Morita, F. J. Giessibl, E. Meyer, and R. Wiesendanger, *Noncontact Atomic Force Microscopy: Volume 3*. Springer, 2015.
- [201] D. Rugar and P. Hansma, "Atomic force microscopy," *Phys. Today*, vol. 43, no. 10, pp. 23–30, 1990.
- [202] F. J. Giessibl, "Advances in atomic force microscopy," *Reviews of Modern Physics*, vol. 75, no. 3. American Physical Society, pp. 949–983, Jul. 29, 2003, doi: 10.1103/RevModPhys.75.949.
- [203] Y. Gan, "Atomic and subnanometer resolution in ambient conditions by atomic force

- microscopy," *Surface Science Reports*, vol. 64, no. 3. North-Holland, pp. 99–121, Mar. 01, 2009, doi: 10.1016/j.surfrep.2008.12.001.
- [204] S. Shionoya, "Photoluminescence," in *Luminescence of Solids*, Springer US, 1998, pp. 95–133.
- [205] M. I. Dyakonov and A. V. Khaetskii, *Spin physics in semiconductors*, vol. 1. Springer, 2008.
- [206] T. H. Gfroerer, "Photoluminescence in Analysis of Surfaces and Interfaces," in *Encyclopedia of Analytical Chemistry*, Chichester, UK: John Wiley & Sons, Ltd, 2006.
- [207] D. Budker, W. Gawlik, D. F. Kimball, S. M. Rochester, V. V. Yashchuk, and A. Weis, "Resonant nonlinear magneto-optical effects in atoms," *Reviews of Modern Physics*, vol. 74, no. 4. American Physical Society, pp. 1153–1201, Oct. 20, 2002, doi: 10.1103/RevModPhys.74.1153.
- [208] Z. Q. Qiu and S. D. Bader, "Surface magneto-optic Kerr effect," *Review of Scientific Instruments*, vol. 71, no. 3. American Institute of Physics Inc., pp. 1243–1255, Mar. 03, 2000, doi: 10.1063/1.1150496.
- [209] F. L. Pedrotti and P. Bandettini, "Faraday rotation in the undergraduate advanced laboratory," *Am. J. Phys.*, vol. 58, no. 6, pp. 542–545, Jun. 1990, doi: 10.1119/1.16445.
- [210] F. J. P. Wijnen *et al.*, "Construction and Performance of a 38-T Resistive Magnet at the Nijmegen High Field Magnet Laboratory," *IEEE Trans. Appl. Supercond.*, vol. 26, no. 4, Jun. 2016, doi: 10.1109/TASC.2016.2537141.
- [211] S. A. J. Wieggers, J. Rook, A. Den Ouden, J. A. A. J. Perenboom, and J. C. Maan, "Design and construction of a 38 t resistive magnet at the Nijmegen high field magnet laboratory," *IEEE Trans. Appl. Supercond.*, vol. 22, no. 3, 2012, doi: 10.1109/TASC.2011.2177432.
- [212] R. Pandya *et al.*, "Fine Structure and Spin Dynamics of Linearly Polarized Indirect Excitons in Two-Dimensional CdSe/CdTe Colloidal Heterostructures," *ACS Nano*, vol. 13, no. 9, pp. 10140–10153, Sep. 2019, doi: 10.1021/acsnano.9b03252.
- [213] E. V. Shornikova *et al.*, "Addressing the exciton fine structure in colloidal nanocrystals: The case of CdSe nanoplatelets," *Nanoscale*, vol. 10, no. 2, pp. 646–656, Jan. 2018, doi: 10.1039/c7nr07206f.
- [214] C. Weedbrook *et al.*, "Gaussian Quantum Information," 2011.
- [215] N. A. F. Vergel *et al.*, "Criteria for the direct observation of a two-dimensional density of states in InGaAs / InP (001) heterostructures with scanning tunneling spectroscopy," no. 001, pp. 1–23.
- [216] B. J. Ohlsson, J. O. Malm, A. Gustafsson, and L. Samuelson, "Anti-domain-free GaP, grown in atomically flat (001) Si sub- μ m-sized openings," *Appl. Phys. Lett.*, vol. 80, no. 24, pp. 4546–4548, Jun. 2002, doi: 10.1063/1.1485311.
- [217] S. Ando "i," N. Kobayashi, and H. Ando, "Selective area metalorganic chemical vapor deposition growth for hexagonal-facet lasers," 1994.
- [218] N. Mejid Elsiiti *et al.*, "New Technique for Fabrication of Two-Dimensional Photonic Bandgap Crystals by Selective Epitaxy Related content Fabrication of high aspect ratio micro electrode by using EDM A Novel Polarizer Made from Two-Dimensional Photonic Bandgap Materials GaAs and InP Nanohole Arrays Fabricated by Reactive Beam Etching Using Highly Ordered Alumina Membranes Recent citations," 1997.

- [219] K. Tomioka, J. Motohisa, S. Hara, and T. Fukui, "Control of InAs Nanowire Growth Directions on Si," vol. 18, p. 34, 2020, doi: 10.1021/nl802398j.
- [220] "Monolithic GaAs/InGaP nanowire light emitting diodes on silicon - IOPscience." <https://iopscience-iop-org.ressources-electroniques.univ-lille.fr/article/10.1088/0957-4484/19/30/305201> (accessed May 31, 2020).
- [221] B. Tian *et al.*, "Coaxial silicon nanowires as solar cells and nanoelectronic power sources," *Nature*, vol. 449, no. 7164, pp. 885–889, Oct. 2007, doi: 10.1038/nature06181.
- [222] C. Thelander *et al.*, "Development of a vertical wrap-gated InAs FET," *IEEE Trans. Electron Devices*, vol. 55, no. 11, pp. 3030–3036, 2008, doi: 10.1109/TED.2008.2005151.
- [223] Q. T. Do, K. Blekker, I. Regolin, W. Prost, and F. J. Tegude, "High transconductance MISFET with a single InAs nanowire channel," *IEEE Electron Device Lett.*, vol. 28, no. 8, pp. 682–684, Aug. 2007, doi: 10.1109/LED.2007.902082.
- [224] M. Zeghouane *et al.*, "Formation of voids in selective area growth of InN nanorods in SiN x on GaN templates," doi: 10.1088/2399-1984/ab8450.
- [225] W. T. Tsang and E. F. Schubert, "Extremely high quality Ga_{0.47}In_{0.53}As/InP quantum wells grown by chemical beam epitaxy," *Appl. Phys. Lett.*, vol. 49, no. 4, pp. 220–222, 1986, doi: 10.1063/1.97177.
- [226] K. Tomioka, M. Yoshimura, and T. Fukui, "A III-V nanowire channel on silicon for high-performance vertical transistors," *Nature*, vol. 488, no. 7410, pp. 189–192, 2012, doi: 10.1038/nature11293.
- [227] Y. Kohashi, T. Sato, K. Ikejiri, K. Tomioka, S. Hara, and J. Motohisa, "Influence of growth temperature on growth of InGaAs nanowires in selective-area metal-organic vapor-phase epitaxy," 2011, doi: 10.1016/j.jcrysgr.2011.10.041.
- [228] D. G. Coronell and K. F. Jensen, "Analysis of MOCVD of GaAs on patterned substrates," *J. Cryst. Growth*, vol. 114, no. 4, pp. 581–592, Dec. 1991, doi: 10.1016/0022-0248(91)90404-S.
- [229] B. Korgel and R. F. Hicks, "A diffusion model for selective-area epitaxy by metalorganic chemical vapor deposition," *J. Cryst. Growth*, vol. 151, no. 1–2, pp. 204–212, May 1995, doi: 10.1016/0022-0248(95)00008-9.
- [230] M. Fahed, L. Desplanque, C. Coinon, D. Troadec, and X. Wallart, "Impact of P/In flux ratio and epilayer thickness on faceting for nanoscale selective area growth of InP by molecular beam epitaxy," *Nanotechnology*, vol. 26, no. 29, p. 295301, Jul. 2015, doi: 10.1088/0957-4484/26/29/295301.
- [231] J. S. Lee *et al.*, "Selective-area chemical beam epitaxy of in-plane InAs one-dimensional channels grown on InP(001), InP(111)B, and InP(011) surfaces," *Phys. Rev. Mater.*, vol. 3, no. 8, p. 084606, Aug. 2019, doi: 10.1103/PhysRevMaterials.3.084606.
- [232] T. Ujihara, Y. Yoshida, W. Sik Lee, and Y. Takeda, "Pattern size effect on source supply process for sub-micrometer scale selective area growth by organometallic vapor phase epitaxy," *J. Cryst. Growth*, vol. 289, no. 1, pp. 89–95, Mar. 2006, doi: 10.1016/j.jcrysgr.2005.11.088.
- [233] X. Q. Shen, D. Kishimoto, and T. Nishinaga, "Arsenic pressure dependence of surface diffusion of Ga on nonplanar GaAs substrates," *Jpn. J. Appl. Phys.*, vol. 33, no. 1R, p. 11, 1994, doi: 10.1143/JJAP.33.11.

- [234] J. E. Greenspan, C. Blaauw, B. Emmerstorfer, R. W. Glew, and I. Shih, "Analysis of a time-dependent supply mechanism in selective area growth by MOCVD," in *Journal of Crystal Growth*, Feb. 2003, vol. 248, no. SUPPL., pp. 405–410, doi: 10.1016/S0022-0248(02)01845-6.
- [235] S. Nagata and T. Tanaka, "Self-masking selective epitaxy by molecular-beam method," *J. Appl. Phys.*, vol. 48, no. 3, pp. 940–942, Mar. 1977, doi: 10.1063/1.323712.
- [236] M. Kawabe and T. Sugaya, "Anisotropic lateral growth of GaAs by molecular beam epitaxy," *Jpn. J. Appl. Phys.*, vol. 28, no. 7 A, pp. L1077–L1079, Jul. 1989, doi: 10.1143/JJAP.28.L1077.
- [237] Y. Okuno, H. Asahi, T. Kaneko, T. W. Kang, and S. ichi Gonda, "Surface diffusion lengths of Ga molecules during GaAs MOMBE (metalorganic molecular beam epitaxy) growth," *J. Cryst. Growth*, vol. 105, no. 1–4, pp. 185–190, Oct. 1990, doi: 10.1016/0022-0248(90)90358-R.
- [238] M. Hata, T. Isu, A. Watanabe, Y. Kajikawa, and Y. Katayama, "Surface diffusion and sticking coefficient of adatoms to atomic steps during molecular beam epitaxy growth," *J. Cryst. Growth*, vol. 114, no. 1–2, pp. 203–208, Oct. 1991, doi: 10.1016/0022-0248(91)90694-Z.
- [239] N. Grandjean and J. Massies, "Epitaxial growth of highly strained In_xGa_{1-x}As on GaAs(001): the role of surface diffusion length," *J. Cryst. Growth*, vol. 134, no. 1–2, pp. 51–62, Nov. 1993, doi: 10.1016/0022-0248(93)90008-K.
- [240] J. Tersoff and R. M. Tromp, "Shape transition in growth of strained islands: Spontaneous formation of quantum wires," *Phys. Rev. Lett.*, vol. 70, no. 18, pp. 2782–2785, May 1993, doi: 10.1103/PhysRevLett.70.2782.
- [241] B. G. Orr, D. Kessler, C. W. Snyder, and L. Sander, "A model for strain-induced roughening and coherent island growth," *EPL*, vol. 19, no. 1. IOP Publishing, pp. 33–38, May 01, 1992, doi: 10.1209/0295-5075/19/1/006.
- [242] D. A. Reed and G. Ehrlich, "Surface diffusion, atomic jump rates and thermodynamics," *Surf. Sci.*, vol. 102, no. 2–3, pp. 588–609, Jan. 1981, doi: 10.1016/0039-6028(81)90048-0.
- [243] T. Fujii, M. Ekawa, and S. Yamazaki, "A theory for metalorganic vapor phase epitaxial selective growth on planar patterned substrates," *J. Cryst. Growth*, vol. 146, no. 1–4, pp. 475–481, Jan. 1995, doi: 10.1016/0022-0248(94)00498-6.
- [244] O. Kayser, R. Westphalen, B. Opitz, and P. Balk, "Control of selective area growth of InP," *J. Cryst. Growth*, vol. 112, no. 1, pp. 111–122, May 1991, doi: 10.1016/0022-0248(91)90916-S.
- [245] J. Décobert *et al.*, "Modeling and characterization of AlGaInAs and related materials using selective area growth by metal-organic vapor-phase epitaxy," *J. Cryst. Growth*, vol. 298, no. SPEC. ISS, pp. 28–31, Jan. 2007, doi: 10.1016/j.jcrysgro.2006.10.005.
- [246] M. Sobanska, Z. R. Zytkeiwicz, M. Ekielski, K. Klosek, A. S. Sokolovskii, and V. G. Dubrovskii, "Surface Diffusion of Gallium as the Origin of Inhomogeneity in Selective Area Growth of GaN Nanowires on Al_xO_yNucleation Stripes," *Cryst. Growth Des.*, vol. 20, no. 7, pp. 4770–4778, Jul. 2020, doi: 10.1021/acs.cgd.0c00530.
- [247] R. L. Anderson, "Experiments on Ge-GaAs heterojunctions," *Solid State Electron.*, vol. 5, no. 5, pp. 341–351, Sep. 1962, doi: 10.1016/0038-1101(62)90115-6.
- [248] H. Ehrenreich and D. Turnbull, *Solid State Physics*. Elsevier Science, 1992.
- [249] A. Wadehra, J. W. Nicklas, and J. W. Wilkins, "Band offsets of semiconductor heterostructures: A hybrid density functional study," *Appl. Phys. Lett.*, vol. 97, no. 9, pp. 6–8, 2010, doi:

10.1063/1.3487776.

- [250] E. T. Yu, J. O. McCaldin, and T. C. McGill, *Band Offsets in Semiconductor Heterojunctions*, vol. 46, no. C. 1992.
- [251] L. Y. Leu and S. R. Forrest, "The determination of heterojunction energy band discontinuities in the presence of interface states using capacitance-voltage techniques," *J. Appl. Phys.*, vol. 64, p. 5030, 1988, doi: 10.1063/1.342456.
- [252] S. R. Forrest and O. K. Kim, "An n-In_{0.53}Ga_{0.47}As/n-InP rectifier," *J. Appl. Phys.*, vol. 52, no. 9, pp. 5838–5842, Sep. 1981, doi: 10.1063/1.329479.
- [253] M. A. Haase, N. Pan, and G. E. Stillman, "(No Title)," *Appl. Phys. Lett.*, vol. 54, p. 1457, 1989, doi: 10.1063/1.100696.
- [254] M. T. Furtado, M. S. S. Loural, A. C. Sachs, and P. J. Shieh, "Band offset in GaAlAs and InGaAs: InP heterojunctions by electrochemical CV profiling," *Superlattices Microstruct.*, vol. 5, no. 4, pp. 507–510, Jan. 1989, doi: 10.1016/0749-6036(89)90373-X.
- [255] S. R. Forrest, P. H. Schmidt, R. B. Wilson, and M. L. Kaplan, "Cite as," *Appl. Phys. Lett.*, vol. 45, p. 1199, 1984, doi: 10.1063/1.95096.
- [256] R. Sauer, T. D. Harris, and T. Tsang, "Spectroscopy of excited states in In_{0.53}Ga_{0.47}As-Inp single quantum wells grown by chemical-beam epitaxy," *J. Vac. Sci. Technol. B*, vol. 4, p. 07974, 1986.
- [257] D. V. Lang, M. B. Panish, F. Capasso, J. Allam, and R. A. Hamm, "Measurement of heterojunction band offsets by admittance spectroscopy: InP/Ga_{0.47}In_{0.53}As Related Articles," *Cit. Appl. Phys. Lett.*, vol. 50, p. 736, 1987, doi: 10.1063/1.98083.
- [258] I. Vurgaftman, J. R. Meyer, and L. R. Ram-Mohan, "Band parameters for III-V compound semiconductors and their alloys," *J. Appl. Phys.*, vol. 89, no. 11, pp. 5815–5875, 2001, doi: 10.1063/1.1368156.
- [259] J. P. Perdew, K. Burke, and M. Ernzerhof, "Generalized Gradient Approximation Made Simple," 1996.
- [260] P. E. Smith *et al.*, "Atomic diffusion and band lineups at In_{0.53}Ga_{0.47}As-on-InP heterointerfaces," *J. Vac. Sci. Technol. B Microelectron. Nanom. Struct.*, vol. 23, no. 4, pp. 1832–1837, Jul. 2005, doi: 10.1116/1.1949218.
- [261] Y. Dong, R. M. Feenstra, M. P. Semtsiv, and W. T. Masselink, "Band offsets of InGaP/GaAs heterojunctions by scanning tunneling spectroscopy," *J. Appl. Phys.*, vol. 103, no. 7, p. 073704, Apr. 2008, doi: 10.1063/1.2902828.
- [262] H. W. M. Salemink, O. Albrechtsen, and P. Koenraad, "Tunneling spectroscopy across GaAs/Al_xGa_{1-x}As interfaces at nanometer resolution," *Phys. Rev. B*, vol. 45, no. 12, pp. 6946–6949, Mar. 1992, doi: 10.1103/PhysRevB.45.6946.
- [263] D. Steiner, D. Dorfs, U. Banin, F. Della Sala, L. Manna, and O. Millo, "Determination of Band Offsets in Heterostructured Colloidal Nanorods Using Scanning Tunneling Spectroscopy," vol. 58, p. 59, 2020, doi: 10.1021/nl801848x.
- [264] Y. Dong, R. M. Feenstra, M. P. Semtsiv, and W. T. Masselink, "Cross-sectional scanning tunneling microscopy and spectroscopy of InGaP/GaAs heterojunctions," *Appl. Phys. Lett.*, vol. 84, no. 2, pp. 227–229, Jan. 2004, doi: 10.1063/1.1638637.

- [265] M. Berthe, C. Durand, T. Xu, J. P. Nys, P. Caroff, and B. Grandidier, "Combined STM and Four-Probe Resistivity Measurements on Single Semiconductor Nanowires," Springer, Berlin, Heidelberg, 2012, pp. 107–118.
- [266] P. K. Bhattacharya, M. V Rao, and M. Tsai, "Growth and photoluminescence spectra of high-purity liquid phase epitaxial $\text{In}_{0.53}\text{Ga}_{0.47}\text{As}$," *J. Appl. Phys.*, vol. 54, no. 9, pp. 5096–5102, Sep. 1983, doi: 10.1063/1.332784.
- [267] N. A. Franchina Vergel *et al.*, "Influence of doping level and surface states in tunneling spectroscopy of an $\text{In}_{0.53}\text{Ga}_{0.47}\text{As}$ quantum well grown on p-type doped $\text{InP}(001)$," *Phys. Rev. Mater.*, vol. 3, no. 9, p. 094604, Sep. 2019, doi: 10.1103/PhysRevMaterials.3.094604.
- [268] J. R. Waldrop, E. A. Kraut, C. W. Farley, and R. W. Grant, "Measurement of $\text{InP}/\text{In}_{0.53}\text{Ga}_{0.47}\text{As}$ and $\text{In}_{0.53}\text{Ga}_{0.47}\text{As}/\text{In}_{0.52}\text{Al}_{0.48}\text{As}$ heterojunction band offsets by x-ray photoemission spectroscopy," *J. Appl. Phys.*, vol. 69, no. 1, pp. 372–378, Jan. 1991, doi: 10.1063/1.347724.
- [269] R. M. Feenstra, "Tunneling spectroscopy of the (110) surface of direct-gap III-V semiconductors," *Phys. Rev. B*, vol. 50, no. 7, pp. 4561–4570, Aug. 1994, doi: 10.1103/PhysRevB.50.4561.
- [270] R. M. Feenstra, J. A. Stroscio, and A. P. Fein, "Tunneling spectroscopy of the $\text{Si}(111)2 \times 1$ surface," *Surf. Sci.*, vol. 181, no. 1–2, pp. 295–306, Mar. 1987, doi: 10.1016/0039-6028(87)90170-1.
- [271] R. M. Feenstra, "Scanning tunneling spectroscopy," *Surf. Sci.*, vol. 299–300, no. C, pp. 965–979, Jan. 1994, doi: 10.1016/0039-6028(94)90710-2.
- [272] Y. F. Lin *et al.*, "Electron transport in high-resistance semiconductor nanowires through two-probe measurements," *Phys. Chem. Chem. Phys.*, vol. 12, no. 36, pp. 10928–10932, Sep. 2010, doi: 10.1039/c0cp00038h.
- [273] A.-P. Li, K. W. Clark, X.-G. Zhang, and A. P. Baddorf, "Electron Transport at the Nanometer-Scale Spatially Revealed by Four-Probe Scanning Tunneling Microscopy," *Adv. Funct. Mater.*, vol. 23, no. 20, pp. 2509–2524, May 2013, doi: 10.1002/adfm.201203423.
- [274] S. H. Kim, G. S. Kim, S. W. Kim, and H. Y. Yu, "Effective Schottky barrier height lowering technique for InGaAs contact scheme: D MIGS and D it reduction and interfacial dipole formation," *Appl. Surf. Sci.*, vol. 453, pp. 48–55, Sep. 2018, doi: 10.1016/j.apsusc.2018.05.070.
- [275] C. Davisson and L. H. Germer, "The thermionic work function of tungsten," *Phys. Rev.*, vol. 20, no. 4, pp. 300–330, Oct. 1922, doi: 10.1103/PhysRev.20.300.
- [276] S. Jana *et al.*, "Stacking and Colloidal Stability of CdSe Nanoplatelets," *Langmuir*, vol. 31, no. 38, pp. 10532–10539, 2015, doi: 10.1021/acs.langmuir.5b02152.
- [277] L. Biadala, F. Liu, M. D. Tessier, D. R. Yakovlev, B. Dubertret, and M. Bayer, "Recombination dynamics of band edge excitons in quasi-two-dimensional CdSe nanoplatelets," *Nano Lett.*, vol. 14, no. 3, pp. 1134–1139, 2014, doi: 10.1021/nl403311n.
- [278] J. Joo, J. S. Son, S. G. Kwon, J. H. Yu, and T. Hyeon, "Low-temperature solution-phase synthesis of quantum well structured CdSe nanoribbons," *J. Am. Chem. Soc.*, vol. 128, no. 17, pp. 5632–5633, 2006, doi: 10.1021/ja0601686.
- [279] L. Jdira, P. Liljeroth, E. Stoffels, D. Vanmaekelbergh, and S. Speller, "Size-dependent single-particle energy levels and interparticle Coulomb interactions in CdSe quantum dots measured by scanning tunneling spectroscopy," *Phys. Rev. B - Condens. Matter Mater. Phys.*, vol. 73, no. 11,

- pp. 1–6, 2006, doi: 10.1103/PhysRevB.73.115305.
- [280] H. Talaat, T. Abdallah, M. B. Mohamed, S. Negm, and M. A. El-Sayed, “The sensitivity of the energy band gap to changes in the dimensions of the CdSe quantum rods at room temperature: STM and theoretical studies,” *Chem. Phys. Lett.*, vol. 473, no. 4–6, pp. 288–292, 2009, doi: 10.1016/j.cplett.2008.11.025.
- [281] O. Millo *et al.*, “Charging and quantum size effects in tunnelling and optical spectroscopy of CdSe nanorods,” *Nanotechnology*, vol. 15, no. 1, pp. 1–6, 2004, doi: 10.1088/0957-4484/15/1/R01.
- [282] D. Steiner, T. Mokari, U. Banin, and O. Millo, “Electronic structure of metal-semiconductor nanojunctions in gold CdSe nanodumbbells,” *Phys. Rev. Lett.*, vol. 95, no. 5, pp. 2–5, 2005, doi: 10.1103/PhysRevLett.95.056805.
- [283] S. Ithurria, M. D. Tessier, B. Mahler, R. P. S. M. Lobo, B. Dubertret, and A. L. Efros, “Colloidal nanoplatelets with two-dimensional electronic structure,” *Nat. Mater.*, vol. 10, no. 12, pp. 936–941, 2011, doi: 10.1038/nmat3145.
- [284] E. Lhuillier, S. Pedetti, S. Ithurria, B. Nadal, H. Heuclin, and B. Dubertret, “Two-Dimensional colloidal metal chalcogenides semiconductors: Synthesis, spectroscopy, and applications,” *Acc. Chem. Res.*, vol. 48, no. 1, pp. 22–30, 2015, doi: 10.1021/ar500326c.
- [285] X. Peng, J. Wickham, and A. P. Alivisatos, “Kinetics of II-VI and III-V colloidal semiconductor nanocrystal growth: ‘Focusing’ of size distributions [15],” *J. Am. Chem. Soc.*, vol. 120, no. 21, pp. 5343–5344, 1998, doi: 10.1021/ja9805425.
- [286] B. Abécassis, M. D. Tessier, P. Davidson, and B. Dubertret, “Self-assembly of CdSe nanoplatelets into giant micrometer-scale needles emitting polarized light,” *Nano Lett.*, vol. 14, no. 2, pp. 710–715, 2014, doi: 10.1021/nl4039746.
- [287] A. W. Achtstein, A. Antanovich, A. Prudnikau, R. Scott, U. Woggon, and M. Artemyev, “Linear Absorption in CdSe Nanoplates: Thickness and Lateral Size Dependency of the Intrinsic Absorption,” *J. Phys. Chem. C*, vol. 119, no. 34, pp. 20156–20161, Aug. 2015, doi: 10.1021/acs.jpcc.5b06208.
- [288] G. H. V. Bertrand, A. Polovitsyn, S. Christodoulou, A. H. Khan, and I. Moreels, “Shape control of zincblende CdSe nanoplatelets,” *Chem. Commun.*, vol. 52, no. 80, pp. 11975–11978, 2016, doi: 10.1039/c6cc05705e.
- [289] A. Riedinger *et al.*, “An intrinsic growth instability in isotropic materials leads to quasi-two-dimensional nanoplatelets Europe PMC Funders Group,” *Nat Mater*, vol. 16, no. 7, pp. 743–748, 2017, doi: 10.1038/nmat4889.
- [290] M. Nasilowski *et al.*, “Two-Dimensional Colloidal Nanocrystals,” *Hal*, vol. 116, no. 18, pp. 10934–10982, Sep. 2016, Accessed: Sep. 01, 2020. [Online]. Available: <https://pubs.acs.org/doi/abs/10.1021/acs.chemrev.6b00164>.
- [291] S. Christodoulou *et al.*, “Chloride-Induced Thickness Control in CdSe Nanoplatelets,” *Nano Lett.*, vol. 18, no. 10, pp. 6248–6254, 2018, doi: 10.1021/acs.nanolett.8b02361.
- [292] X. Miao, C. Chen, J. Zhou, and W. Deng, “Influence of hydrogen bonds and double bonds on the alkane and alkene derivatives self-assembled monolayers on HOPG surface: STM observation and computer simulation,” *Appl. Surf. Sci.*, vol. 256, no. 14, pp. 4647–4655, 2010, doi: 10.1016/j.apsusc.2010.02.065.

- [293] M. K. Choi, J. Yang, T. Hyeon, and D. H. Kim, "Flexible quantum dot light-emitting diodes for next-generation displays," *npj Flexible Electronics*, vol. 2, no. 1. Nature Research, p. 10, Dec. 01, 2018, doi: 10.1038/s41528-018-0023-3.
- [294] D. Katz, T. Wizansky, O. Millo, E. Rothenberg, T. Mokari, and U. Banin, "Size-Dependent Tunneling and Optical Spectroscopy of CdSe Quantum Rods," *Phys. Rev. Lett.*, vol. 89, no. 8, pp. 1–4, 2002, doi: 10.1103/PhysRevLett.89.086801.
- [295] B. Ji *et al.*, "Dielectric Confinement and Excitonic Effects in Two-Dimensional Nanoplatelets," *ACS Nano*, vol. 14, no. 7, pp. 8257–8265, Jul. 2020, doi: 10.1021/acsnano.0c01950.
- [296] B. Ji *et al.*, "Dielectric Confinement and Excitonic Effects in Two-Dimensional Nanoplatelets," *ACS Nano*, vol. 14, 2020, doi: 10.1021/acsnano.0c01950.
- [297] J. C. Norman *et al.*, "A review of high-performance quantum dot lasers on silicon," *IEEE Journal of Quantum Electronics*, vol. 55, no. 2. Institute of Electrical and Electronics Engineers Inc., Apr. 01, 2019, doi: 10.1109/JQE.2019.2901508.
- [298] S. A. Cherevko, A. V. Baranov, A. V. Fedorov, A. P. Litvin, M. V. Artemyev, and A. V. Prudnikau, "Optical properties of two-dimensional (2D) CdSe nanostructures," *Nanophotonic Mater. X*, vol. 8807, no. December 2016, p. 88070A, 2013, doi: 10.1117/12.2023586.
- [299] G. B. Griffin, S. Ithurria, D. S. Dolzhenkov, A. Linkin, D. V. Talapin, and G. S. Engel, "Two-dimensional electronic spectroscopy of CdSe nanoparticles at very low pulse power," *J. Chem. Phys.*, vol. 138, no. 1, 2013, doi: 10.1063/1.4772465.
- [300] M. D. Tessier, L. Biadala, C. Bouet, S. Ithurria, B. Abecassis, and B. Dubertret, "Phonon line emission revealed by self-assembly of colloidal nanoplatelets," *ACS Nano*, vol. 7, no. 4, pp. 3332–3340, 2013, doi: 10.1021/nn400833d.
- [301] A. W. Achtstein *et al.*, "P-State Luminescence in CdSe Nanoplatelets: Role of Lateral Confinement and a Longitudinal Optical Phonon Bottleneck," *Phys. Rev. Lett.*, vol. 116, no. 11, pp. 1–4, 2016, doi: 10.1103/PhysRevLett.116.116802.
- [302] B. T. Diroll *et al.*, "Semiconductor Nanoplatelet Excimers," *Nano Lett*, vol. 18, p. 40, 2018, doi: 10.1021/acs.nanolett.8b02865.
- [303] J. F. Specht *et al.*, "Size-dependent exciton substructure in CdSe nanoplatelets and its relation to photoluminescence dynamics †," *Nanoscale*, vol. 11, 2019, doi: 10.1039/c9nr03161h.
- [304] E. V. Shornikova *et al.*, "Negatively Charged Excitons in CdSe Nanoplatelets," *Nano Lett.*, vol. 20, no. 2, pp. 1370–1377, 2020, doi: 10.1021/acs.nanolett.9b04907.
- [305] C. Javaux *et al.*, "Thermal activation of non-radiative Auger recombination in charged colloidal nanocrystals," *Nat. Nanotechnol.*, vol. 8, no. 3, pp. 206–212, Feb. 2013, doi: 10.1038/nnano.2012.260.
- [306] O. Erdem *et al.*, "Orientation-Controlled Nonradiative Energy Transfer to Colloidal Nanoplatelets: Engineering Dipole Orientation Factor," *Nano Lett.*, vol. 19, no. 7, pp. 4297–4305, Jul. 2019, doi: 10.1021/acs.nanolett.9b00681.
- [307] D. Tessier, P. Spinicelli, D. Dupont, G. Patriarche, S. Ithurria, and B. Dubertret, "Efficient Exciton Concentrators Built from Colloidal Core/Crown CdSe/CdS Semiconductor Nanoplatelets," *Nano Lett*, vol. 14, pp. 207–213, 2014, doi: 10.1021/nl403746p.
- [308] A. W. Achtstein *et al.*, "Impact of Shell Growth on Recombination Dynamics and Exciton-Phonon

- Interaction in CdSe-CdS Core-Shell Nanoplatelets,” *ACS Nano*, vol. 12, no. 9, pp. 9476–9483, Sep. 2018, doi: 10.1021/acsnano.8b04803.
- [309] A. A. Rossinelli, A. Riedinger, P. Marqués-Gallego, P. N. Knüsel, F. V. Antolinez, and D. J. Norris, “High-temperature growth of thick-shell CdSe/CdS core/shell nanoplatelets,” *Chem. Commun.*, vol. 53, no. 71, pp. 9938–9941, Aug. 2017, doi: 10.1039/c7cc04503d.
- [310] D. Oron, A. Aharoni, C. D. M. Donega, J. Van Rijssel, A. Meijerink, and U. Banin, “Universal Role of Discrete Acoustic Phonons in the Low-Temperature Optical Emission of Colloidal Quantum Dots,” vol. 177402, no. May, pp. 1–4, 2009, doi: 10.1103/PhysRevLett.102.177402.
- [311] A. L. Efros, M. Rosen, M. Kuno, M. Nirmal, D. Norris, and M. Bawendi, “Band-edge exciton in quantum dots of semiconductors with a degenerate valence band: Dark and bright exciton states,” *Phys. Rev. B - Condens. Matter Mater. Phys.*, vol. 54, no. 7, pp. 4843–4856, Aug. 1996, doi: 10.1103/PhysRevB.54.4843.
- [312] E. V. Shornikova *et al.*, “Electron and Hole g-Factors and Spin Dynamics of Negatively Charged Excitons in CdSe/CdS Colloidal Nanoplatelets with Thick Shells,” *Nano Lett.*, vol. 18, no. 1, pp. 373–380, Jan. 2018, doi: 10.1021/acsnanolett.7b04203.
- [313] E. V. Shornikova *et al.*, “Electron and hole g-factors and spin dynamics of negatively charged excitons in CdSe/CdS colloidal nanoplatelets with thick shells,” 2017.
- [314] E. Johnston-Halperin *et al.*, “Spin spectroscopy of dark excitons in CdSe quantum dots to 60 T,” *Phys. Rev. B - Condens. Matter Mater. Phys.*, vol. 63, no. 20, p. 205309, Apr. 2001, doi: 10.1103/PhysRevB.63.205309.
- [315] F. Liu *et al.*, “Spin dynamics of negatively charged excitons in CdSe/CdS colloidal nanocrystals,” *Phys. Rev. B - Condens. Matter Mater. Phys.*, vol. 88, no. 3, p. 35302, Jul. 2013, doi: 10.1103/PhysRevB.88.035302.
- [316] E. V. Shornikova *et al.*, “Surface spin magnetism controls the polarized exciton emission from CdSe nanoplatelets,” *Nat. Nanotechnol.*, vol. 15, no. 4, pp. 277–282, Apr. 2020, doi: 10.1038/s41565-019-0631-7.
- [317] Q. Li, K. Wu, J. Chen, Z. Chen, J. R. McBride, and T. Lian, “Size-Independent Exciton Localization Efficiency in Colloidal CdSe/CdS Core/Crown Nanosheet Type-I Heterostructures,” *ACS Nano*, vol. 10, no. 3, pp. 3843–3851, Mar. 2016, doi: 10.1021/acsnano.6b00787.
- [318] P. P. Jha and P. Guyot-Sionnest, “Trion Decay in Colloidal Quantum Dots,” vol. 3, no. 1, pp. 1–4, 2009, doi: 10.1021/nn9001177.

List of publications

Díaz Álvarez, A., **Peric, N.**, Franchina Vergel, N. A., Nys, J.-P., Berthe, M., Patriarche, G., Harmand, J.-C., Caroff, P., Plissard, S., Ebert, P., Xu, T., & Grandidier, B. (2019). Importance of point defect reactions for the atomic-scale roughness of III-V nanowire sidewalls. *Nanotechnology*, 30(32).
<https://doi.org/10.1088/1361-6528/ab1a4e>

Kaliteevskii, V., Deder, A., **Peric, N.**, & Chechurin, L. (2020). Conceptual Semantic Analysis of Patents and Scientific Publications Based on TRIZ Tools. In *IFIP Advances in Information and Communication Technology*: Vol. 597 IFIP. https://doi.org/10.1007/978-3-030-61295-5_5

Peric, N., Lambert, Y., Singh, S., Khan, A. H., Franchina Vergel, N. A., Deresmes, D., Berthe, M., Hens, Z., Moreels, I., Delerue, C., Grandidier, B., & Biadala, L. (2021). Van Hove Singularities and Trap States in Two-Dimensional CdSe Nanoplatelets. *Nano Letters*, 21(4), 1702–1708.
<https://doi.org/10.1021/acs.nanolett.0c04509>

Sciacca, D., **Peric, N.**, Berthe, M., Biadala, L., Pirri, C., Derivaz, M., Massara, N., Diener, P., & Grandidier, B. (2020). Account of the diversity of tunneling spectra at the germanene/Al(1 1 1) interface. *Journal of Physics Condensed Matter*, 32(5). <https://doi.org/10.1088/1361-648X/ab4d15>

PAPER

Importance of point defect reactions for the atomic-scale roughness of III–V nanowire sidewalls

To cite this article: Adrian Díaz Álvarez *et al* 2019 *Nanotechnology* **30** 324002

View the [article online](#) for updates and enhancements.





IOP | ebooks™

Bringing together innovative digital publishing with leading authors from the global scientific community.

Start exploring the collection—download the first chapter of every title for free.

Importance of point defect reactions for the atomic-scale roughness of III–V nanowire sidewalls

Adrian Díaz Álvarez^{1,5}, Nemanja Peric¹,
Nathali Alexandra Franchina Vergel¹, Jean-Philippe Nys¹, Maxime Berthe¹,
Gilles Patriarche², Jean-Christophe Harmand², Philippe Caroff^{1,6},
Sébastien Plissard^{1,7} , Philipp Ebert³, Tao Xu^{1,4} and Bruno Grandidier¹ 

¹ Univ. Lille, CNRS, Centrale Lille, ISEN, Univ. Valenciennes, UMR 8520—IEMN, F-59000 Lille, France

² Centre de Nanosciences et de Nanotechnologies (C2N), UMR 9001 CNRS, University Paris Sud, University Paris-Saclay, avenue de la Vauve, F-91120 Palaiseau, France

³ Peter Grünberg Institut, Forschungszentrum Jülich GmbH, D-52425 Jülich, Germany

⁴ Key Laboratory of Advanced Display and System Application, Shanghai University, Shanghai 200072, People's Republic of China

E-mail: xtld@shu.edu.cn and bruno.grandidier@isen.iemn.univ-lille1.fr

Received 23 January 2019, revised 29 March 2019

Accepted for publication 17 April 2019

Published 13 May 2019



CrossMark

Abstract

The surface morphology of III–V semiconductor nanowires (NWs) protected by an arsenic cap and subsequently evaporated in ultrahigh vacuum is investigated with scanning tunneling microscopy and scanning transmission electron microscopy. We show that the changes of the surface morphology as a function of the NW composition and the nature of the seed particles are intimately related to the formation and reaction of surface point defects. Langmuir evaporation close to the congruent evaporation temperature causes the formation of vacancies which nucleate and form vacancy islands on {110} sidewalls of self-catalyzed InAs NWs. However, for annealing temperatures much smaller than the congruent temperature, a new phenomenon occurs: group III vacancies form and are filled by excess As atoms, leading to surface As_{Ga} antisites. The resulting Ga adatoms nucleate with excess As atoms at the NW edges, producing monoatomic-step islands on the {110} sidewalls of GaAs NWs. Finally, when gold atoms diffuse from the seed particle onto the {110} sidewalls during evaporation of the protective As cap, Langmuir evaporation does not take place, leaving the sidewalls of InAsSb NWs atomically flat.

Keywords: III–V semiconductor nanowires, {110} sidewall, surface morphology, roughness, point defect, scanning tunneling microscopy

(Some figures may appear in colour only in the online journal)

1. Introduction

Compound semiconductor nanowires (NWs) have attracted wide interest for optoelectronic and photovoltaic applications, due to their unique ability to relax strain and hence enabling the realization of a much wider range of non-lattice matched heterostructures and polytypes than in planar growth. Numerous examples of heterogeneous integrations have been demonstrated, either axially with III–V NWs directly grown

⁵ Present address: International Center for Materials Nanoarchitectonics, National Institute for Materials Science, Tsukuba, Ibaraki 305-0044, Japan.

⁶ Present address: Microsoft Quantum Lab Delft, Delft University of Technology, 2600 GA Delft, The Netherlands.

⁷ Present address: CNRS-Laboratoire d'Analyse et d'Architecture des Systèmes (LAAS), Univ. de Toulouse, 7 Avenue du Colonel Roche, F-31400 Toulouse, France.

on Si substrates [1, 2] or radially with semiconductor–semiconductor, semiconductor–ferroelectric and semiconductor metal core–shell NWs [3–6]. However, the quality of the interface, in particular in the radial configuration, where the surface to volume ratio is high, critically affects the NW properties. Hence, controlling the surface morphology and chemistry of NWs is becoming of utmost importance for tuning manifold NW properties, not only for the growth of core–shell structures, but also to prepare NWs with strong confinement effects [7] or enhanced luminescence [8].

Indeed, apparently small surface effects can have a strong impact on the physical properties of semiconductor heterostructures. For example, a pronounced roughness of the sidewall facets will reduce the sharpness of radial interfaces and increase the scattering of electrons and phonons, influencing their propagation. Also, surface steps induce a Fermi-level pinning at the NW sidewall facets, which modifies the band offsets between different axially arranged polytypes or heteromaterials [9, 10], hence influencing greatly the axial electrical conductivity and optical emission of NWs. Moreover, this pinning governs the incorporation of defects and isoelectronic impurities during lateral overgrowth, affecting the electronic properties of core–shell heterostructures.

These effects are likely to occur when the growth processes require the evaporation of chemical elements that take place in separate growth systems, implying stringent conditions to preserve the interfacial layer from contamination accumulated during the sample transfer [11]. For III–V semiconductor NWs, a smart protection scheme relies on the use of a thin arsenic amorphous layer to cap the NW sidewalls [12, 13], that can then be easily sublimated once the sample has been transferred in a different growth system. However, it is still not clear how the protective cap affects the morphology of the NW sidewalls. This is even more important in the light of very different surface morphologies observed by scanning tunneling microscopy, ranging from very rough to atomically smooth facets [14], but without good understanding thus far.

In this work, we examine clean and well-ordered (110) sidewalls of III–V semiconductor NWs with scanning tunneling microscopy (STM) and spectroscopy (STS) after the sublimation of an As protective cap. We find pronounced differences in the morphology and roughness of NW sidewalls of different III–V compounds. The morphologies are shown to correlate with point defect formation and reaction processes during the sublimation of the As protective cap. These point defect-based processes lead to sidewall morphologies characterized by nucleated islands, vacancy clusters, atomically smooth sidewalls, as well as to highly off-stoichiometric or perfectly stoichiometric surfaces depending on annealing and Fermi-level position at the NW surface.

2. Methods

For the experiments, InAs, GaAs and InAs_{1-x}Sb_x NWs were synthesized by molecular beam epitaxy with seed particles to drive the NW growth in the vapor–liquid–solid regime. In and

Ga droplets were used for the growth of self-catalyzed InAs and GaAs NWs on [111]-oriented Si substrates covered with a native oxide layer at the surface. As described in [15], optimized conditions with oxide thickness of 0.9 nm were chosen to obtain the highest yield of vertical growth. The growth of InAs NWs was done at 0.02 monolayer per second, given as equivalent to the growth rate on planar GaAs, with an As₄ partial pressure of 3.6×10^{-7} mbar, an In partial pressure of 4.1×10^{-8} mbar and a temperature of 420 °C. The growth of GaAs NWs was carried out at a nominal growth rate of 0.3 \AA s^{-1} , with an As₄ partial pressure of 2.5×10^{-6} mbar, a Ga partial pressure of 1.4×10^{-7} mbar and a temperature of 620 °C. At the end of the growth, the In and Ga droplets were consumed by closing the In or Ga shutter for 30 min under As₄ flux. Then, the As₄ flux was stopped, what reduced the As-related pressure substantially, and the temperature was lowered to room temperature. At room temperature, the As₄ flux was opened again and the NWs were capped with a 10–20 nm thick amorphous As layer for protection against air exposure (oxidation). A high yield of vertical NWs grown along the $\langle 111 \rangle$ direction was obtained, with a diameter distribution between 60 and 90 nm [16]. InAs_{1-x}Sb_x NWs and GaAs NWs were also grown with gold seed particles, as thoroughly described in [12] and [17]. The capping procedure was similar except that the gold seed particle was left at the end of the growth and embedded in the As capping layer.

After the growth, the NWs were investigated with a Jeol 2200 FS scanning transmission electron microscope (STEM) operating at 200 keV and with a low-temperature scanning tunneling microscope working at 77 K in ultrahigh vacuum (UHV). The STEM analysis required to work with cleaved and dispersed NWs in toluene that were dropcasted onto E-chip supports (Protochips). The annealing of the NWs to sublimate the As-capping layer was performed *in situ* and the temperature of the E-chip in the STEM was measured with a thermocouple. For the STM characterization, the sublimation process was performed in the preparation chamber connected to a low-temperature scanning tunneling microscope with a base pressure lower than 10^{-10} mbar. The substrate that was used to grow the NWs was annealed by direct current heating. The As desorption was monitored by mass spectrometry and the temperature of the sample was probed with a pyrometer, yielding an uncertainty of ± 10 °C on the substrate temperature. While the pressure increased around $2\text{--}5 \times 10^{-10}$ mbar for a few tens of seconds and then decreased, we usually kept the sample heating for 30 min. At the end of this process, the NWs were transferred to a *n*-type Si(111) substrate coated with a thin layer of Ag. The transfer was performed by mechanical cleavage of the NWs without interruption of UHV [18], to have one of the sidewalls parallel to the host substrate and accessible to the tungsten STM tip. For the STM study, we did not consider the base or the top region of the NWs, since the morphology of these regions can be different from the rest of the NWs. Tunneling spectroscopic curves were acquired with an open feedback loop at constant tip-sample separation.

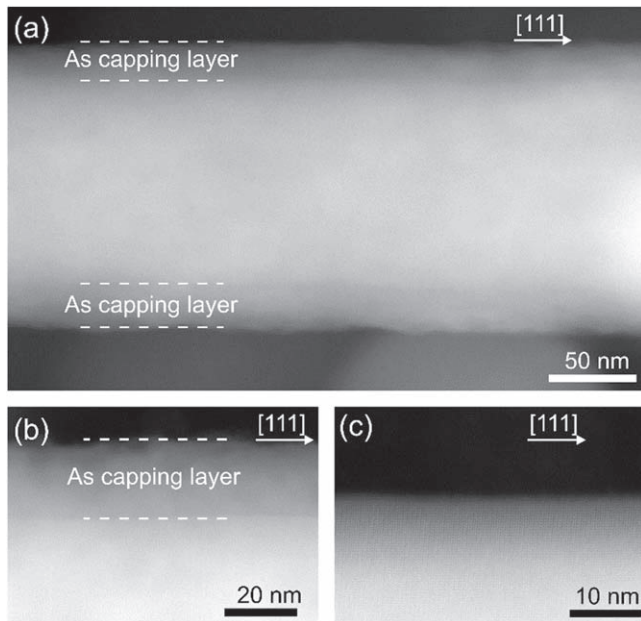


Figure 1. (a) STEM image of a self-catalyzed GaAs NW capped with a thin protective layer of amorphous As. (b) and (c) TEM images of the same GaAs NW after the annealing of the sample at 250 °C for 10 min and then 270 °C for 10 min. At 250 °C, the amorphous As cap is still present and blurs the NW's atomic structure (b). In contrast, at 270 °C the As cap evaporated fully (c), revealing the underlying atomic structure of the NW.

3. Results

In order to determine the range of temperatures that enable the complete sublimation of the As protective cap, temperature-dependent STEM experiments were first performed with self-catalyzed GaAs NWs. Figure 1(a) shows a typical STEM image of such a GaAs NW capped by an amorphous As capping layer. The capping layer is identified from its slightly darker contrast in the upper and lower parts of the NW in comparison with the GaAs core. The thickness of the capping layer is 20 nm. Heating the NW at 250 °C for 10 min does not produce any significant modification of the protective cap (figure 1(b)). Further annealing at 270 °C for 10 min leads to the disappearance of the dark As shell and the appearance of the NW atomic lattice in the STEM image, as shown in figure 1(c). Both observations indicate the sublimation of the protecting As cap. However, annealing at this temperature was found to leave a lot of defective areas in the STM images of the NWs sidewalls. Therefore, for the subsequent STM analyses, the As capping layer was always sublimated above 310 °C–320 °C and below 370 °C–380 °C. The upper limit corresponds to the congruent evaporation temperature of InAs [19].

Figure 2 shows an overview of STM images for three different III–V NWs after the sublimation of the As-capping layer at the maximum temperature of 370 °C–380 °C allowed for this study. The morphologies of the sidewalls for the NWs appear different, despite the same $\langle 110 \rangle$ orientation of the sidewalls and similar conditions to sublimate the capping layer. First, the InAs and GaAs NWs have straight sidewalls

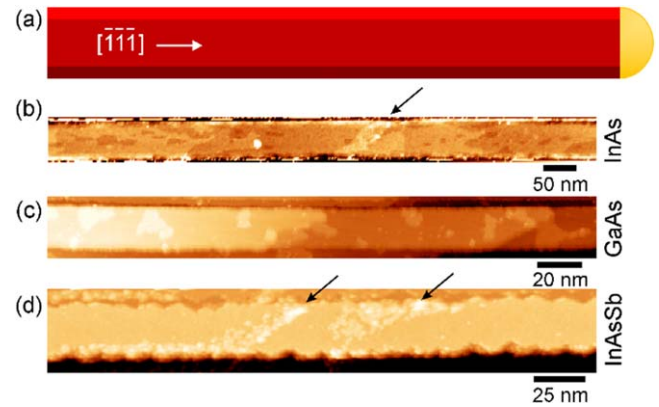


Figure 2. STM images of the $\{110\}$ sidewall of (a) an In-catalyzed InAs NW, (b) a Ga-catalyzed GaAs NW and (c) a Au-catalyzed InAs_{0.9}Sb_{0.1} NW obtained after the sublimation of the As capping layer at 370 °C–380 °C, tunneling conditions: (a) $V_{\text{sample}} = +3.0 \text{ V} / I_{\text{tunneling}} = 10 \text{ pA}$, (b) $V_{\text{sample}} = -4.0 \text{ V} / I_{\text{tunneling}} = 20 \text{ pA}$, (c) $V_{\text{sample}} = -3.0 \text{ V} / I_{\text{tunneling}} = 10 \text{ pA}$. The arrows point to defective areas.

while the InAs_{1-x}Sb_x NW appear with sawtooth-like sidewalls. This difference has been explained by the epitaxial overgrowth of the sidewalls [20]. $\langle 111 \rangle$ -oriented NWs have initially twelve alternating $\{110\}$ and $\{112\}$ sidewalls. However, if overgrowth takes place, the grooves induced by the $\{111\}$ -A and B-type facets in the $\{112\}$ planes, which give rise to the sawtooth-like shape, are filled in and the $\{112\}$ planes becomes narrower. As a result, the $\{110\}$ sidewalls almost connect with each other giving rise to straight edges along the growth axis.

More importantly for this study, we compare the roughness of the $\{110\}$ sidewalls. The InAs NW sidewall consists of propagating terraces along the growth direction, with pits sparsely distributed into the terraces (figure 2(b)). We note the presence of a small defective area, which is presumably a damaged region that might affect the complete removal of the As capping layer in its vicinity. The GaAs NW sidewalls exhibit terraces also. But opposite to the pits observed on the InAs NW sidewalls, islands appear on top of these terraces (figure 2(c)). Interestingly, the majority of the islands are connected to the sidewall and terrace edges, whereas the pits seem to be randomly distributed on a terrace. In contrast to the InAs and GaAs NWs, the InAs_{1-x}Sb_x NW sidewall is atomically flat, except in two small defective areas (figure 2(d)). While the absence of terraces might be related to the limited duration of the lateral overgrowth process as compared with the InAs and GaAs NWs, this third example shows that the $\{110\}$ sidewalls can also exist without any pits or islands.

In order to get further insight into the origin of the formation of these clusters and islands, figure 3 highlights the height profiles measured on the sidewalls of the self-catalyzed InAs and GaAs NWs. At the surface of the InAs NW, the pits have a depth of about 2 Å, whereas the islands that are found on the GaAs NWs show a height of 2 Å. These heights correspond to the separation of single atomic (110) planes in

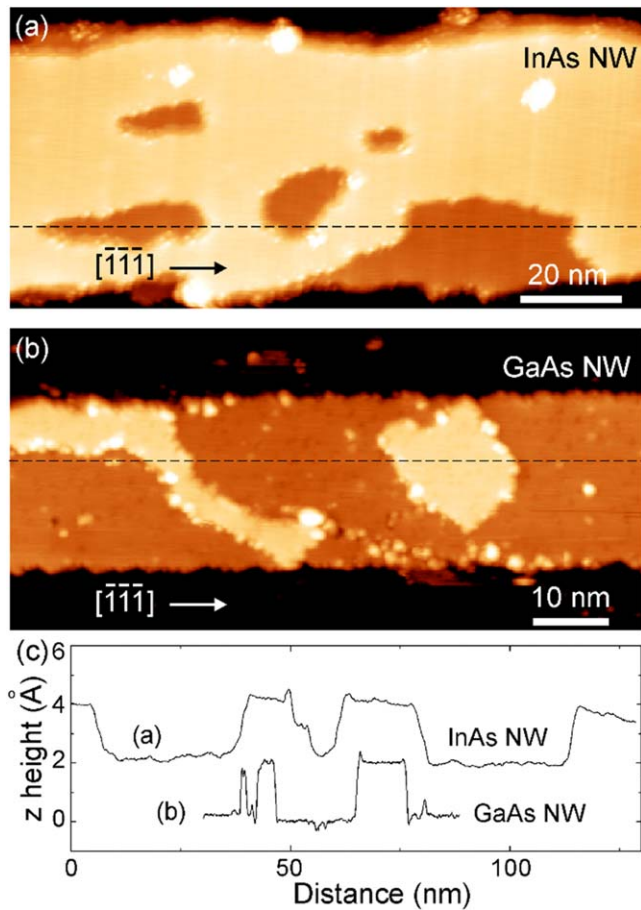


Figure 3. STM images of the {110} sidewall of self-catalyzed (a) InAs and (b) GaAs NWs after the removal of the As capping layer at 370 °C–380 °C. (c) Height profiles measured along the horizontal lines in (a) and (b). Tunneling conditions: $V_{\text{sample}} = +2.0$ V (a)/ -3.5 V (b), $I_{\text{tunneling}} = 20$ pA. Vacancy islands are found to form on InAs NW sidewalls, whereas islands nucleate on GaAs NW sidewall at edges.

InAs and GaAs crystals, meaning that single-layer vacancy clusters or islands with monoatomic step height were formed.

In order to get further insight into the origin of the formation of these clusters and islands, we examined surfaces of III–V semiconductor bulk crystals. Figures 4(a)–(c) shows atomically flat (110) surfaces of a cleaved *p*-type InP crystal, a cleaved *p*-type GaAs crystal and a cleaved *n*-type GaAs crystal respectively. All three crystals show single vacancies, but depending on the doping of the crystals, the nature of the vacancies is different. Group V vacancies are observed in the filled state images of figures 4(a) and (b), while Ga (group III) vacancies are visible in the unoccupied state image of figure 4(c), consistent with previous studies [21–23]. We note that the STM image of the *p*-type InP surface was acquired after sample annealing at 205 °C for 42 h in UHV. Upon further annealing at 300 °C for 6 h, the *p*-type InP surface shows the formation of pits (figure 4(d)), similar to those produced upon exposure to electrons, photons or ions [24–26].

For surfaces initially covered with a thin As capping layer and then annealed to desorb the capping layer, such as

the InAs (001) surface in figure 4(e) and the GaAs (110) surface in figure 4(f), the same pits are also found. Once the amorphous capping layer has been desorbed, desorption of atoms from the crystal occurs and gives rise to the holey surface seen on the InAs NW sidewalls. The surface morphology is fully consistent with the formation of vacancy clusters resulting from stoichiometric Langmuir evaporation of group III and group V elements. Both elements leave the surface at equal fluxes because the annealing temperature is lower than the congruent temperature [27].

In contrast, the GaAs NW sidewalls do not show a pit-dominated morphology, but rather an island morphology. Understanding this requires a deeper examination of the possible presence of defects on the GaAs NW sidewalls. The atomically resolved STM image of figure 5(a) corresponds to a filled state image and shows rows of As atoms on the {110} sidewall of the NW. Interestingly, atomically confined protrusions at Ga lattice sites are seen between the As rows. Counting their number yields a surface density of protrusions of $4 \times 10^{13} \text{ cm}^{-2}$. These defects do not cause a change of contrast in their surroundings and can be found next to each other in the same row, suggesting that they are uncharged. We anticipate that the protrusions correspond to As atoms substituted to Ga atoms. This is supported by their comparison with the STM image of an As_{Ga} antisite defect in the surface layer simulated with density functional calculations of the integrated filled local density of states [28]. As we do not observe any contrast associated with subsurface As_{Ga} antisite defects as found previously in low-temperature grown GaAs planar layers as well as GaAs NWs [29–31], our result suggests that the antisites are exclusively formed at the GaAs surface during the post-growth decapping process.

An additional insight into the post-growth mechanism is provided by the statistical analysis of the one-monolayer-height islands. The Abbott curve calculated with the STM image shown in the inset of figure 5(c) reveals that 18% of the sidewall is covered with islands. As the cation concentration at the GaAs (110) surface is $2.2 \times 10^{14} \text{ cm}^{-2}$, it means that $4 \times 10^{13} \text{ cm}^{-2}$ Ga atoms are necessary to form these islands. This quantity corresponds exactly to the Ga atoms substituted by the As_{Ga} antisites.

4. Discussion

In order to explain the different morphologies obtained for the InAs NWs and the GaAs NWs despite identical post-growth treatments, we recall that the morphology is governed by the atomic processes occurring during the annealing procedure used to desorb the As cap from the NWs. These atomic processes are intimately related to point defects at the sidewall surfaces. It is well known that the types of point defects formed on III–V (110) surfaces are highly sensitive to the position of the Fermi level [32–34]. Since the formation process of point defects during desorption is a kinetically limited process, we cannot base the discussion on equilibrium energies of point defects, but rather need to consider the formation barriers. Experimentally it has been shown that

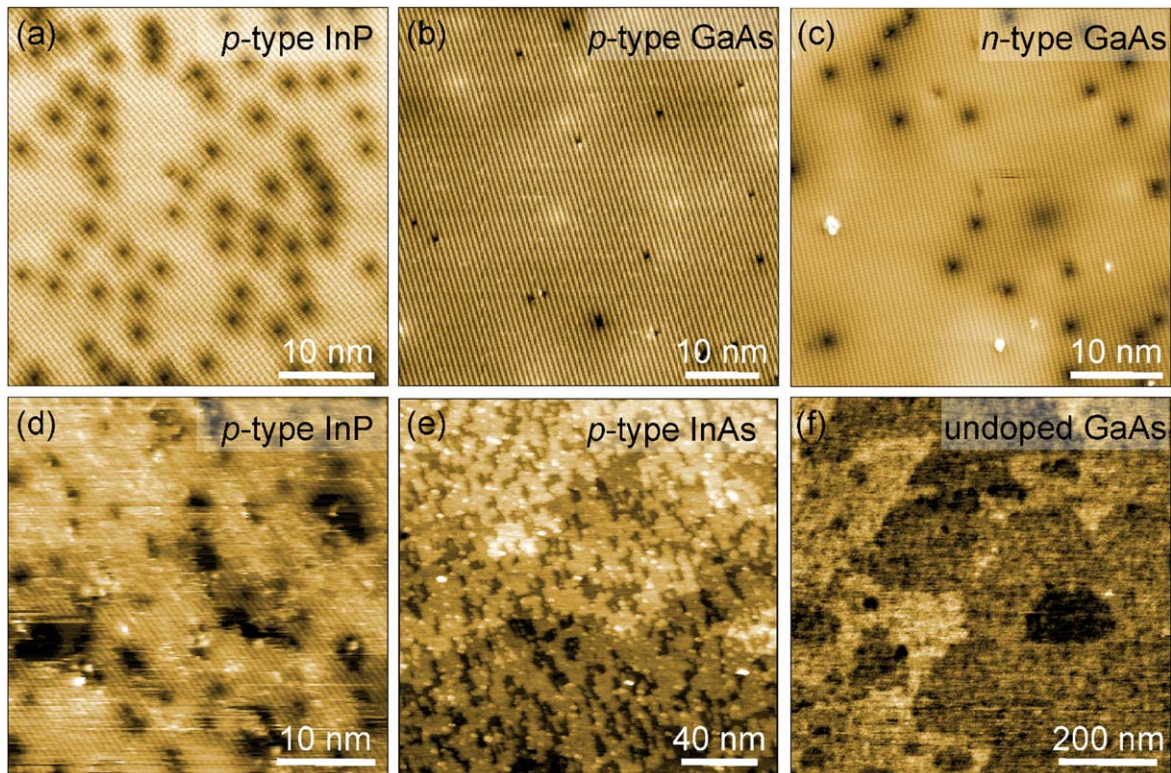


Figure 4. STM images of (a) a *p*-type InP(110) crystal annealed at 200 °C for 42 h in UHV, (b) a *p*-type GaAs (110) crystal, (c) a *n*-type GaAs (110) surface, (d) a *p*-type InP (110) surface annealed at 300 °C for 6 h in UHV, (e) a *p*-type InAs(001) crystal, initially capped with As and annealed at 400 °C for 2 h, (f) an undoped GaAs (110) crystal initially capped with As and annealed at 450 °C for 4 h in UHV. Tunneling conditions: $V_{\text{sample}} = -2.7$ V (a), -2.6 V (b), $+1.2$ V (c), -2.8 V (d), $+1.5$ V (e), $+2.0$ V (b); $I_{\text{tunneling}} = 800$ pA (a), 600 pA (b), 300 pA (c), 600 pA (d), 10 pA (e), 10 pA.

negatively charged group III (positively charged group V) vacancies form kinetically on *n*-type (*p*-type) surfaces even at room temperature [21–23]. No other point defect, such as antisite or adatom, is experimentally found to form thermally in significant concentrations on (110) surfaces. This is confirmed by the defects visible in figures 4(a) and (c).

Therefore, we performed tunneling spectroscopy measurements on sidewalls of the self-catalyzed InAs and GaAs NWs in order to determine the electrical nature of the sidewalls. For the GaAs NWs, the band edges are clearly resolved in figure 6: at negative (positive) sample voltages, the branches of the current correspond to a tunneling out of (into) the valence (conduction) band states. The Fermi level position, measured at 0 V, is found midgap, 0.75 eV above the valence band edge, in agreement with a previous study which attributed this position to a pinning induced by the surface steps [9]. For the InAs NWs, three regions of tunneling current are also observed. In this case, the central component turning on at 0 V and extending to negative voltages is not equal to zero. This component arises from electrons tunneling out of the partially occupied conduction band, due to a pinning slightly above the conduction band minimum. This Fermi level position within the conduction band is in agreement with measurements performed on the planar InAs(110) surface [35] and InAs NW sidewall [36]. It is caused by the formation of an electron accumulation layer near the NW sidewalls, giving a *n*-type character to the sidewall.

On this basis, one can explain the atomic processes on the (110) InAs sidewall facet: during the post-growth annealing, the amorphous As cap is progressively removed. Once crystalline (110) facets become uncovered, In vacancies form. Since the annealing temperature of 380 °C is close enough to the InAs congruent sublimation temperature of 387 °C [19], the In adatoms desorb and leave behind negatively charged In vacancies [32], with weakly bonded neighboring As atoms. These neighboring As atoms can detach and form As adatoms, which desorb by forming As_2 molecules [21]. As a result, uncharged divacancies form, which, due to the lack of repulsive Coulomb interactions, migrate and agglomerate to form pits of one monolayer depth on the whole sidewall of the InAs NW. The fact that the majority of the pits do not touch the sidewall edges indicates that their nucleation occurs randomly on the sidewall facets. Note that during these processes no charging of the surface by point defects occur. Similar effects can be expected to occur when the oxidized sidewalls of InAs NWs are cleaned with atomic hydrogen at 370 °C. Indeed the morphology observed on such prepared InAs NW sidewall facets is also dominated by holes of one monolayer depth elongated along the [111] direction [37]. It should be noted that the fraction of holes on the sidewall facet is essentially determined by the annealing time, the longer the more holes.

For the GaAs NWs an analogous effect may occur: as soon as the stoichiometric GaAs surface becomes uncovered

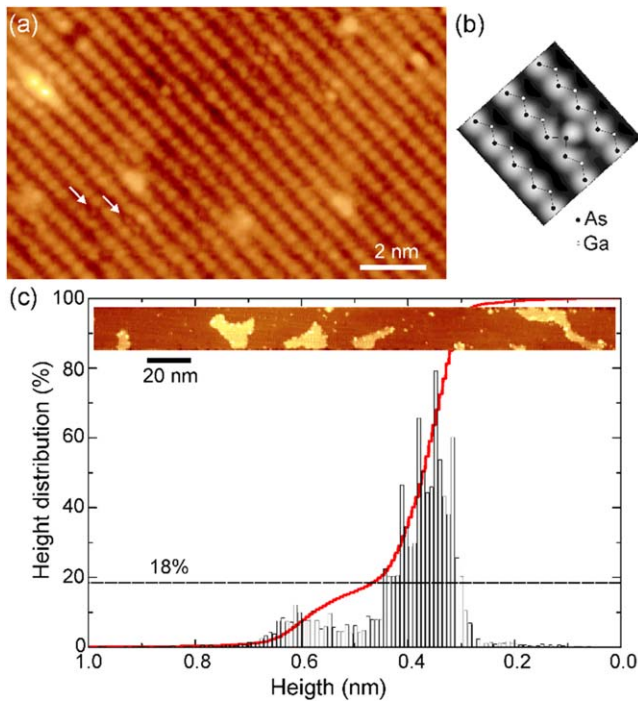


Figure 5. (a) Atomic scale STM image of the {110} sidewall of a Ga-catalyzed GaAs NW. Tunneling conditions: $V_{\text{sample}} = -3.5$ V, $I_{\text{tunneling}} = 20$ pA. The arrows point to protrusions at Ga lattice sites that correspond to a single surface As_{Ga} antisite and a pair of surface As_{Ga} antisites. (b) Calculated filled state STM image of the GaAs {110} surface including states over an energy range of 0.7 eV below the top of the valence band reproduced from [28] (c) height distribution and Abbott curve obtained for the {110} sidewall of the GaAs NW shown in the inset (tunneling conditions: $V_{\text{sample}} = -4.0$ V, $I_{\text{tunneling}} = 20$ pA). The horizontal dashed line indicates the fraction of the total area that corresponds to the bright islands seen in the STM image of the inset.

during As decapping, negatively charged Ga vacancies form for undoped and n -type materials [22, 38]. However, in contrast to InAs, the annealing temperature used to desorb the As capping layer is much lower than the congruent sublimation temperature of GaAs [7, 27, 39], preventing the Ga adatoms to desorb. As a result, for the following discussion, we need to take into account the presence of negatively charged Ga vacancies and Ga adatoms combined with high concentrations of As adatoms originating from the amorphous As cap. Their joint presence inevitably leads to point defect reactions: a simple formation of negatively charged Ga vacancies would lead to a negative charging of the NW sidewall facets, which would quickly undermine further vacancy formation, due to repulsive Coulomb interactions. The observation of surface antisite defects in the STM image of figure 5(a) indicates that the negative charge of a Ga vacancy can be removed by inserting an As adatom on a Ga lattice site to form an uncharged As_{Ga} antisite defect in the surface layer. This point defect reaction is very likely to happen, due to the As rich conditions created by the As cap and also energetic reasons. For midgap Fermi energies in our case, the formation energy of a V_{Ga} , a negatively charged As adatom, and an uncharged As_{Ga} antisite are 1.2, 1, 0, and -0.25 eV, respectively [38], hence freeing about 2.5 eV per

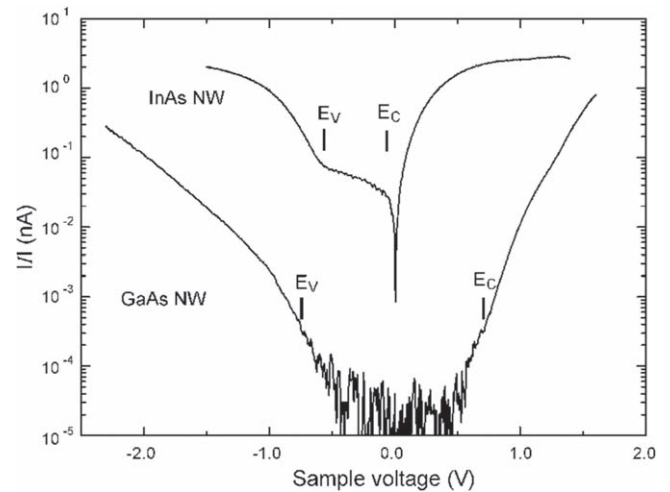


Figure 6. Tunneling spectra acquired on the {110} sidewall of self-catalyzed InAs and GaAs NWs. E_V and E_C indicate the position of the valence and conduction band edges respectively. The spectrum of the InAs NW has been shifted vertically for clarity.

formed surface antisite defect. In addition, this reaction results in charge neutrality. These antisite defects remain in the surface layer, as the barrier for inward diffusion is too high [38]. The lack of subsurface antisite defects corroborates this formation mechanism.

At this stage, we consider the Ga adatoms created during vacancy formation. Once the vacancy is filled by an As adatom, the Ga adatoms cannot jump back into the Ga vacancy nor desorb, since the temperature is too low. Hence they remain diffusing over the sidewall surface until they nucleate with As adatoms, preferentially at the NW edges, forming GaAs islands on the sidewalls. This effect is responsible for the distribution of one-monolayer-height islands observed on the sidewalls of the self-catalyzed GaAs NWs.

An intriguing aspect of this result is the degree of non-stoichiometry achievable at NW sidewall facets without formation of precipitates. In bulk GaAs, the equilibrium phase diagram only permits very small deviations from stoichiometry in the range of $\sim 10^{-3}\%$ at 700 °C, before precipitation occurs. The single phase area narrows even further at lower temperatures [40, 41]. Under non-equilibrium conditions in low-temperature GaAs growth, As antisite concentrations of up to 1% are reachable, but annealing leads to As precipitation [30, 42]. Here on the NW sidewall, a deviation from stoichiometry of 18% is observed at 370 °C–380 °C and no precipitate forms during annealing.

We also note that the formation of the surface antisites occurs at relatively low temperature in comparison with the congruent temperature of GaAs. This effect is not observed on the planar GaAs {110} surface which was annealed at 450 °C. Similarly, under realistic annealing temperatures, holes cannot be avoided for InAs NWs. For example, at temperatures as low as 315 °C–325 °C, As-capped self-catalyzed InAs NWs exhibit a holey surface, as shown in figure 7, meaning that the In surface atoms already desorb rather than diffuse on the sidewalls at this temperature.

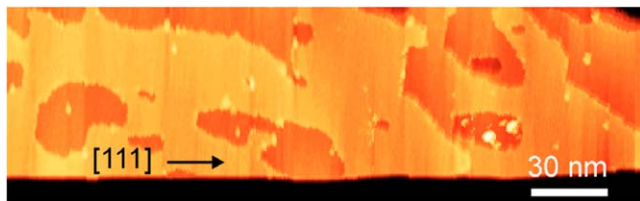


Figure 7. STM image of the {110} sidewall of a In-catalyzed InAs NWs after the removal of the As capping layer at 315 °C–325 °C. Tunneling conditions: V sample = +2.5 V, I tunneling = 10 pA.

Finally, due to the lower congruent temperature of InSb with respect to InAs [43], similar post-growth treatments should have produced a holey surface at the sidewall of the InAsSb NWs. Instead, the sidewalls are atomically flat. Although Sb behaves as a surfactant in the growth of III–V semiconductor alloys [44], we do not believe that it plays a role during the sublimation of the As layer, since it has been shown to preferentially incorporate into the surface lattice and substitute to As than diffusing at the NW surface [45]. Instead, our previous study of InAs_{1-x}Sb_x NWs with STM and x-ray energy-dispersive spectroscopy analysis operated in the high-angle annular dark field STEM mode have revealed the presence of gold clusters on the NW sidewalls [12]. This result is confirmed by *in situ* temperature-dependent STEM experiments of GaAs NWs grown with Au seed particles that were protected by an As cap. Figure 8 shows a STEM image of a GaAs NW with the Au particle on top. At first, the NW and the seed particle are surrounded by the amorphous capping layer. By increasing the temperature at 250 °C, the capping layer roughens and the interface between the Au droplet and the top of the NW widens drastically, indicating the interdiffusion of As and Au atoms. In fact, the droplet becomes gradually an AsAu alloy. In concomitance, as the annealing time increases, dark features appear on the sidewall, diffusing from the Au seed particle towards the bottom of the NW. Therefore, the desorption of the As capping layer from Au-catalyzed NWs inevitably leads to the presence of gold atoms and clusters on the sidewalls. We suspect these impurities to modify the Fermi level position and to prevent the formation of vacancies, keeping the {110} sidewalls atomically flat.

5. Conclusion

We have investigated the sidewall morphology of III–V semiconductor NWs after the desorption of a protective As cap. The desorption of the As cap for self-catalyzed NWs produces two types of morphology arising from Fermi-level-dependent point defect formation and reaction. For annealing temperatures close to the congruent evaporation temperature, the formation of vacancies from the evaporation of group III and group IV elements leads to sidewalls with pits nucleating within the sidewalls. However, when the annealing temperature is much smaller than the congruent evaporation temperature, group III vacancies are formed and substituted by the excess of As atoms on the surface of the NW. The resulting

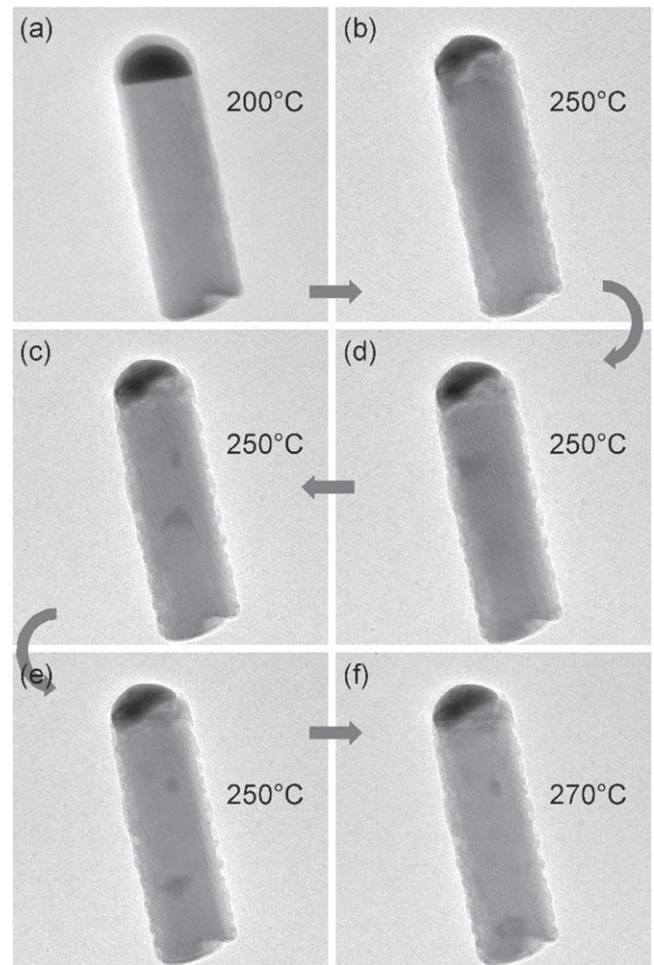


Figure 8. Sequence of temperature-dependent STEM images of an Au-catalyzed GaAs NW capped with a thin As cap. The annealing temperature is indicated in the images.

group III adatoms nucleate with excess As adatoms in islands, preferentially at the sidewall edges. We have furthermore found that a strongly enhanced solubility of excess As is achieved through these surface point defect reactions. Hence, besides the ability to relax strain much more efficiently than in planar growth, NW can also accommodate much larger deviations from stoichiometry at least at their surfaces. Finally, for gold-catalyzed NWs, Au from the seed is redistributed on the sidewalls upon desorption of the protective As cap. The Au induces a midgap pinning of the sidewalls which is anticipated to suppress vacancy formation, and thereby blocks the formation of islands or vacancy pits. The results highlight the critical impact, which point defect formation and reactions have on the sidewall morphology of NWs.

Acknowledgments

This work was financially supported by the European Community's Seventh Framework Program (Grant No. PITN-GA-2012-316751, Nanoembrace project), the H2020 program (Grant No. PITN-GA-2016-722176, Indeed Project), the French state funds managed by the ANR within the

Investissements d'Avenir programme (Grant No. ANR-11-EQPX-0015, EQUIPEX Excelsior; Grant No. ANR-10-EQPX-0050), EQUIPEX Tempos), the French National Research Agency (ANR-16-CE24-0007-01, Dirac III-V project) and the RENATECH network and the Deutsche Forschungsgemeinschaft (Grant No. 390247238). T Xu acknowledges the supports of the National Natural Science Foundation of China (Grant No. 61775130). The authors thank C Coinon and X Wallart for the growth of the As capped bulk samples and C Domke, M Heinrich, M Simon, and C Dzeja for participating in some of the measurements leading to figure 4.

ORCID iDs

Sébastien Plissard  <https://orcid.org/0000-0002-0769-5429>

Bruno Grandidier  <https://orcid.org/0000-0001-6131-7309>

References

- [1] Svensson C P T, Mårtensson T, Trägårdh J, Larsson C, Rask M, Hessman D, Samuelson L and Ohlsson J 2008 *Nanotechnology* **19** 305201
- [2] Tomioka K, Yoshimura M and Fukui T 2012 *Nature* **488** 189
- [3] Dayeh S A et al 2012 *Nano. Lett.* **13** 1869–76
- [4] Royo M, De Luca M, Rurali R and Zardo I 2017 *J. Phys. D: Appl. Phys.* **50** 143001
- [5] Guan X et al 2016 *Nano. Lett.* **16** 2393–9
- [6] Yang M, Dvorak D, Leistner K, Damm C, Watkins S P and Kavanagh K L 2019 *Nanotechnology* **30** 025701
- [7] Loisch B et al 2015 *Adv. Mater.* **27** 2195–202
- [8] Cirlin G E, Thernycheva M, Patriarche G and Harmand J C 2012 *Semiconductor* **46** 175–8
- [9] Capiod P et al 2013 *Appl. Phys. Lett.* **103** 122104
- [10] Xu T et al 2015 *Appl. Phys. Lett.* **107** 112102
- [11] Guan X et al 2016 *Nanoscale* **8** 15637
- [12] Xu T, Dick K A, Plissard S, Nguyen T H, Makoudi Y, Berthe M, Nys J P, Wallart X, Grandidier B and Caroff P 2012 *Nanotechnology* **23** 095702
- [13] Fanetti M, Ambrosini S, Amati M, Gregoratti L, Abyaneh M K, Franciosi A, Chia A C E, LaPierre R R and Rubini S 2013 *J. Appl. Phys.* **114** 154308
- [14] Arbiol J and Xiong Q (ed) 2015 *Semiconductor Nanowires: Materials, Synthesis, Characterization and Applications* (New York: Elsevier)
- [15] Matteini F, Tütüncüoğlu G, Potts H, Jabeen F, Fontcuberta I and Morral A 2015 *Crys. Growth Des.* **15** 3105–9
- [16] Dubrovskii V G, Xu T, Díaz Álvarez A, Plissard S R, Caroff P, Glas F and Grandidier B 2015 *Nano Lett.* **15** 5580–4
- [17] Harmand J C, Patriarche G, Péré-Laperne N, Merat-Combes M N, Travers L and Glas F 2005 *Appl. Phys. Lett.* **87** 203101
- [18] Xu T, Nys J P, Addad A, Lebedev O I, Urbietta A, Salhi B, Berthe M, Grandidier B and Stiévenard D 2010 *Phys. Rev. B* **81** 115403
- [19] Lenrick F, Ek M, Deppert K, Samuelson L and Wallenberg L R 2014 *Nano Res.* **7** 1188–94
- [20] Knutsson J V, Lehmann S, Hjort M, Reinke P, Lundgren E, Dick K A, Timm R and Mikkelsen A 2015 *ACS Appl. Mater. Interfaces* **7** 5748–55
- [21] Ebert P, Heinrich M, Simon M, Urban K and Lagally M G 1995 *Phys. Rev. B* **51** 9696–701
- [22] Domke C, Ebert P, Heinrich M and Urban K 1996 *Phys. Rev. B* **54** 10288–91
- [23] Semmler U, Simon M, Ebert P and Urban K 2001 *J. Chem. Phys.* **114** 445–51
- [24] Han B Y, Nakayama K and Weaver J H 1999 *Phys. Rev. B* **60** 13846–53
- [25] Tanimura K and Kanasaki J I 2008 *Surf. Sci.* **602** 3162–71
- [26] Pechman R J, Wang X S and Weaver J H 1995 *Phys. Rev. B* **51** 10929–36
- [27] Heyn Ch and Jesson D E 2015 *Appl. Phys. Lett.* **107** 161601
- [28] Ebert P, Quadbeck P, Urban K, Henninger B, Horn K, Schwarz G, Neugebauer J and Scheffler M 2001 *Appl. Phys. Lett.* **79** 2877–9
- [29] Feenstra R M, Woodall J M and Pettit G D 1993 *Phys. Rev. Lett.* **71** 1176–9
- [30] Demonchaux T et al 2018 *Phys. Rev. Mater.* **2** 104601
- [31] Diaz A et al 2015 *Nano Lett.* **15** 6440–5
- [32] Ebert P 1999 *Surf. Sci. Rep.* **33** 121–303
- [33] Speckbacher M et al 2016 *Nano Lett.* **16** 5135–42
- [34] Alekseev P A, Dunaevskiy M S, Cirlin G E, Reznik R R, Smirnov A N, Kirilenko D A, Davydov V Y and Berkovits V L 2018 *Nanotechnology* **29** 314003
- [35] Morgenstern M, Haude D, Gudmundsson V, Wittneven C, Dombrowski R, Steinebach C and Wiesendanger R 2000 *J. Electron Spectrosc. Relat. Phenom.* **109** 127–45
- [36] Hjort M et al 2014 *ACS Nano* **8** 12346–55
- [37] Hjort M, Knutsson J V, Mandl B, Deppert K, Lundgren E, Timm R and Mikkelsen A 2015 *Nanoscale* **7** 9998–10004
- [38] Schwarz G 2002 Untersuchungen zu Defekten auf und nahe der (110) Oberfläche von GaAs und weiteren III–V–Halbleitern *PhD Thesis* Technischen Universität Berlin
- [39] Chatillon C and Chatain D 1995 *J. Cryst. Growth* **151** 91–101
- [40] Wenzl H, Dahlen A, Fattah A, Petersen S, Mika K and Henkel D 1991 *J. Cryst. Growth* **109** 191–204
- [41] Morozov A N, Bublik V T and Morozova O Y 1986 *Cryst. Res. Technol.* **21** 749–54
- [42] Melloch M R, Woodall J M, Harmon E S, Otsuka N, Pollak F H, Nolte D D, Feenstra R M and Lutz M A 1995 *Annu. Rev. Mater. Sci.* **25** 547–600
- [43] Haworth L, Lu J, Westwood D I and Macdonald J E 2000 *Appl. Surf. Sci.* **166** 253–8
- [44] Borg B M and Wernersson L-E 2013 *Nanotechnology* **24** 202001
- [45] Hjort M, Kratzer P, Lehmann S, Patel S J, Dick K A, Palmstrøm C J, Timm R and Mikkelsen A 2017 *Nano Lett.* **17** 3634–40

PAPER

Account of the diversity of tunneling spectra at the germanene/Al(1 1 1) interface

To cite this article: Davide Sciacca *et al* 2020 *J. Phys.: Condens. Matter* **32** 055002

View the [article online](#) for updates and enhancements.






IOP | ebooks™

Bringing together innovative digital publishing with leading authors from the global scientific community.

Start exploring the collection—download the first chapter of every title for free.

Account of the diversity of tunneling spectra at the germanene/Al(1 1 1) interface

Davide Sciacca¹, Nemanja Peric¹, Maxime Berthe¹, Louis Biadala¹, Carmelo Pirri^{2,3} , Mickael Derivaz^{2,3}, Natalia Massara^{2,3}, Pascale Diener¹  and Bruno Granddier¹ 

¹ Institut d'Electronique, de Microélectronique et de Nanotechnologie, UMR 8520, 59650 Villeneuve d'Ascq, France

² Institut de Science des Matériaux de Mulhouse IS2M UMR 7361 CNRS-Université de Haute Alsace, 3 bis rue Alfred Werner, 68057, Mulhouse, France

³ Université de Strasbourg, 67081 Strasbourg, France

E-mail: pascale.diener@isen.iemn.univ-lille1.fr

Received 23 July 2019, revised 30 September 2019

Accepted for publication 11 October 2019

Published 1 November 2019



CrossMark

Abstract

Despite the wealth of tunneling spectroscopic studies performed on silicene and germanene, the observation of a well-defined Dirac cone in these materials remains elusive. Here, we study germanene grown on Al(1 1 1) at submonolayer coverages with low temperature scanning tunneling spectroscopy. We show that the tunnelling spectra of the Al(1 1 1) surface and the germanene nanosheets are identical. They exhibit a clear metallic behaviour at the beginning of the experiments, that highlights the strong electronic coupling between the adlayer and the substrate. Over the course of the experiments, the spectra deviate from this initial behaviour, although consecutive spectra measured on the Al(1 1 1) surface and germanene nanosheets are still similar. This spectral diversity is explained by modifications of the tip apex, that arise from the erratic manipulation of the germanium adlayer. The origin of the characteristic features such as a wide band gap, coherence-like peaks or zero-bias anomalies are tentatively discussed in light of the physical properties of Ge and AlGe alloy clusters, that are likely to adsorb at the tip apex.

Keywords: germanene, STM/S, 2D materials

(Some figures may appear in colour only in the online journal)

1. Introduction

Dirac cones in the band structure of graphene provides massless fermions, at the origin of outstanding physical properties such as the half-integer quantum hall effects, ultrahigh carrier mobility and minimum conductivity [1, 2]. Their existence can be readily determined with scanning tunnelling spectroscopy (STS), where the measurement of the differential conductance in the vicinity of the Fermi level is proportional to the density of states (DOS). For example, when graphene flakes are decoupled from a highly oriented pyrolytic graphite, a typical V-shaped DOS, vanishing at the Dirac point, signature of a Dirac cone, is usually measured with STS [3]. Similar to graphene, silicene and germanene should exhibit Dirac cones because of the honeycomb structure of their lattice [4, 5]. Nevertheless, the longer bond lengths in silicene

and germanene yields a buckled structure, which slightly modifies their electronic structure. As the spin-orbit coupling increases with the degree of buckling, a small band gap has been predicted in addition to the linear energy dispersion [6]. So far, the presence of a small band gap has never been reported and only a few works have observed a differential conductance with a V-shape centred at the Fermi level [7–10]. Although the Dirac fermion nature of the charge carriers has yet to be proved in these examples, where the spectra should develop into a sequence of Landau levels with a square root dependence on the magnetic field, the majority of the experimental works has nonetheless reported tunnelling spectra that differ from the V-shape characteristic in the region of the Fermi level [11–20]. This behaviour has been attributed to the strong electronic coupling between the silicene and germanene sheets with the host substrates. Moreover, a careful

inspection of all the experimental spectra reported for a given system reveals significant deviations between the measured characteristics. For example, if we consider the (4×4) phase of silicene grown on the Ag(111) surface, [11] and [12] show differential conductance curves consisting of two symmetric branches increasing with bias at both polarities, whereas the curves displayed in [13–15] have a clear asymmetric shape. Moreover, the Fermi level is inconsistently positioned close to the negative branch [11, 13] or to the positive branch [14, 15]. Also, some spectra are featureless around the Fermi level [11, 12, 16], while others show many peaks [14, 15, 17, 18]. Similar variations have been found for germanene grown on Pt/Ge(110) islands [7, 21, 22]. Different reasons were invoked to explain these variations, among them, the temperature of the measurements, spatial fluctuations of the electronic coupling between the sheet and the underlying substrate, and the electronic structure of the tip used in scanning tunnelling microscopy (STM). Indeed, the local density of states (LDOS) of a silicene or germanene sheet measured in tunnelling spectroscopy is always influenced by the bias-dependent transmission probability and the LDOS of the STM tip. Usually, the LDOS of a tungsten tip is considered as constant over a wide range of energy [23]. This flat LDOS tip leads to a differential conductance proportional to the LDOS of the sample. However many experiments have shown the key role of the tip LDOS in STS measurement [24–28].

Here, we report STS measurements performed on the (3×3) phase of germanene grown on the Al(111) surface [20, 29, 30]. Comparison of the tunnelling spectra with the ones obtained on clean Al islands reveals a similar metallic behaviour, when the measurements are performed with fresh and clean STM tips. As the tips are used, the spectra are found to deviate from this initial behaviour, although they still show a very good similarity between the germanene and Al islands. Some spectra show a V-shape, that are also observed on the surrounding Al islands, whereas other spectra depart from this characteristic. We explain the variability of the spectral features by the fortuitous manipulation of the surface during the course of the experiments. Germanene nanosheets can be scraped, resulting in the formation of clusters on the surface or in the deposition of new germanene islands. While these spurious modifications of the germanene adlayer show the weak mechanical coupling between the germanene nanosheet and the Al(111) surface, they also involve a contamination of the STM tips by Ge and Al atoms. Based on the electronic structures of numerous Ge and AlGe alloy clusters, that have been predicted in the literature, we speculate on the origin of the broad spectral diversity observed when the germanene/Al(111) interface is characterized with STS.

2. Experiment

Sample preparation and experiments were carried out in an ultrahigh vacuum chamber (UHV) with a base pressure lower than 5×10^{-11} Torr. Germanene was synthesized following the recipe of Derivaz *et al* [29]: clean and well-ordered Al(111) surfaces were first prepared by Ne bombardment

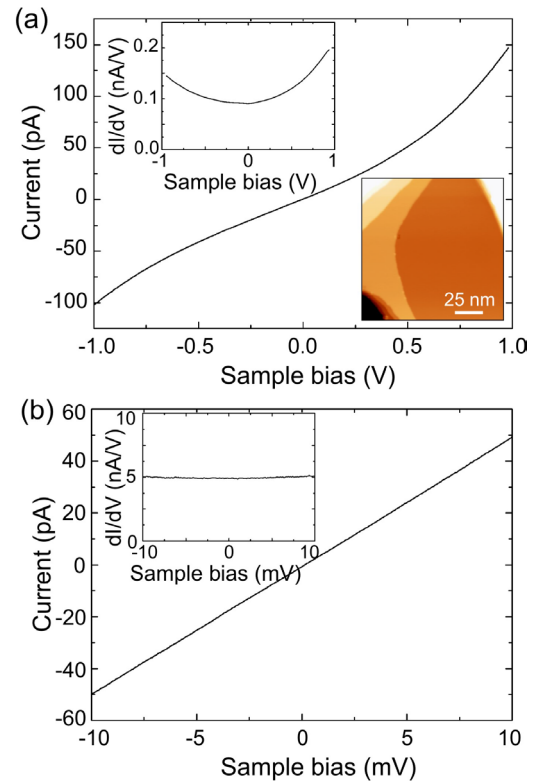


Figure 1. I-V curves and the related dI/dV spectra (upper insets) measured on the clean Al(111) for feedback conditions of (a) $V = -1.0$ V, $I = 100$ pA, and (b) $V = -10$ mV, $I = 50$ pA. Lower inset: STM image of the clean Al(111) surface acquired at a temperature of 5 K.

(800 V, 5×10^{-6} Torr) and subsequent annealing at 450 °C for 1 h; then atomic Ge was evaporated from a Ge(001) crystal onto the clean and well-ordered Al(111) surface heated at a temperature between 80 and 100 °C. The deposited film was then characterized with an Omicron low-temperature scanning tunnelling microscope (LT-STM) at liquid nitrogen (77 K) and liquid helium (5 K) temperatures. Atomically sharp tips were obtained via chemical etching of a tungsten wire in NaOH solution. The wires were thoroughly heated in UHV to obtain clean tips, the final cleaning step involving a cycle of flashes with a duration of 10 s at temperatures higher than 2000 K, to ensure a high purity of the tungsten material at the apex [31, 32]. Such flashes were also repeated in the course of the STM experiments to get rid of the adsorbed species and recover an apex free of contaminants. Typical STM imaging conditions with these tips were obtained for sample bias ranging between -2.0 and 2.0 V and with tunnelling set-point currents smaller than 400 pA.

STS measurements were performed by recording both $I(V)$ curves and the analog derivative dI/dV curves with a Signal Recovery lock-in amplifier, using a modulating frequency of 480 Hz, a variable modulating amplitude between 1 and 7 mV RMS and a variable RC time constant between 10 and 20 ms. Prior to the STM experiments with the germanene sample, the tips were tested on a clean Al(111) surface to make sure that the tunnelling spectra were featureless between -1 and $+1$ V and in particular around the Fermi level. As shown in figure 1,

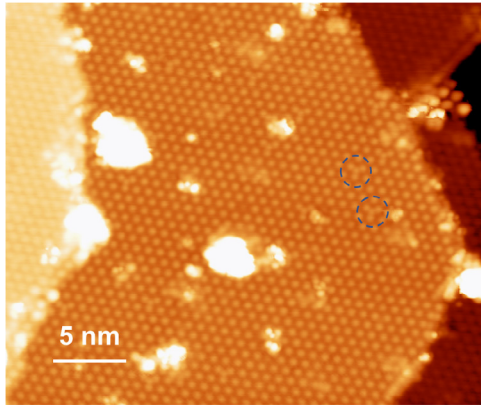


Figure 2. Large scale filled-state STM image of monolayer germanene on Al(1 1 1). Typical Y-shape defects are shown in dashed circles. Image parameters: sample bias $V = -1$ V, current $I = 50$ pA, temperature $T = 77$ K.

the absence of any features in the $I(V)$ and $dI(V)/dV$ curves is consistent with a constant LDOS for the tip apex. The acquisition of local spectra measured at constant tip-sample separation can also be extended to a grid of pixel in a STM image. The method, denoted current imaging tunneling spectroscopy (CITS), was performed by acquiring a 64×64 grid of spectra simultaneously with the STM images consisting of a grid of 256×256 pixels. Between the measurements of two consecutive spectra, a constant stabilization voltage was applied to the sample and the feedback loop was active, so that the tip height was adjusted to maintain a constant tunnelling current and safely moved to the next pixel.

3. Results

Figure 2 shows a large scale STM image obtained for a full coverage of the Al(1 1 1) surface with germanium. Multiple terraces are visible. They are separated with a step height of 2.3 \AA , which compares well with the Al(1 1 1) step height. All the terraces are covered with the same periodic array of bright protrusions showing a hexagonal symmetry. The distance between two neighbouring protrusions is $8.7 \pm 0.2 \text{ \AA}$. The observed structure is compatible with the previously reported 3×3 reconstruction of germanene compared to the periodicity of the Al(1 1 1) lattice [20, 30, 33]. In this configuration, previous theoretical calculations showed that the protrusions correspond to a Ge atom that is uplifted by $1.5\text{--}2.1 \text{ \AA}$ compared to the other atoms in the unit cell, producing a hexagonal lattice in the STM image [30, 33]. We also note the presence of a few Y-shape structures characterized by three bright protrusions and a fourth one in the hollow site between the three top Ge atoms (two of these Y-shape structures are highlighted by dashed circles in figure 2). For this sample, the concentration of the Y-shape defects was $9 \times 10^{11} \text{ cm}^{-2}$. Finally, bright clusters are seen here and there, that we attribute to the slight extra amount of germanium adsorbed on the surface.

STS measurements were performed on this surface, with particular attention to the spatial dependence of the $I(V)$ characteristics. Figure 3(a) shows spatially resolved

tunnelling spectra on an area which includes a Y-shaped defect. A sequence of twelve dI/dV spectra selected either on the top Ge atoms, in the hollow sites or on the Y-shaped defect are displayed in figure 3(b). Remarkably, they all show the same characteristics with two peaks at -0.18 V and $+0.20$ V and a small dip at zero bias, corresponding to the Fermi level position in the sample. The position of the peaks and the minimum at the Fermi level are not affected by the local environment. Although the spectra show a high spatial reproducibility, we have found that subsequent tunneling measurements performed on similar clean and well-ordered areas with the same tip over the course of the experiments do not exhibit the same spectral features. Figures 3(c)–(f) show a representative set of differential conductance measurements. In spectrum (c), the differential conductance has a finite value when the bias approaches zero, indicating a metallic behaviour. Conversely, in spectrum (d), the differential conductance exhibits a zero-conductance gap about 500 mV around the Fermi level. Much smaller zero-conductance gaps are also found such as the one visible in figure 3(e), with a width of 35 meV. Significant variations also exist in the number and shape of the measured peaks and plateau, figure 3(f) exhibiting coherence peaks-like around the Fermi level, for example.

Due the large variety of spectra encountered on the germanene surface, it is important to make sure that the LDOS of the STM tip is constant over a wide range of energy prior to the interpretation of the spectral features. As a result, samples with sub-monolayer coverage were also grown, so that bare Al areas can be probed to provide reference spectra. Figure 4 shows an example of a germanene nanosheet, that grew on an Al(1 1 1) terrace. The 3×3 reconstruction is still observed, with interatomic distances and step heights that match the ones measured at monolayer coverage. Based on the height profile shown in figure 4, the average height of the island appears at the same level as the rest of the Al terrace, the top Ge atoms protruding 0.30 \AA above this mean level for the best tip conditions. While small defective areas decorated possibly with Ge atoms and clusters are also seen in the STM image, a large part of the Al terrace is unaffected by the growth, allowing to acquire reference tunnelling spectra.

Measurements shown in figure 5 were obtained with a fresh and clean STM tip at a temperature of 5 K. In the reduced range of bias between -0.1 V and $+0.1$ V, the $I(V)$ curves measured on the bare Al surface are all linear whatever the set-point current is. This behaviour is also found on a larger bias range, extending from -1.0 V to $+1.0$ V. It is consistent with the spectra obtained on the clean Al(1 1 1) surface in figure 1 and agrees with the metallic nature of the substrate and the tip. It indicates that the contribution of any surface states of the Al surface is negligible, in particular those positioned at the K point, 0.7 eV below the Fermi level in the band gap of the three-dimensional Al band structure projected onto the two-dimensional Brillouin zone [34]. Indeed, these states having a high parallel wave-vector should strongly decay into vacuum, implying a small transmission probability. Therefore, the linear characteristic found on an Al(1 1 1) terrace shows that the LDOS of the STM tip can be considered constant over

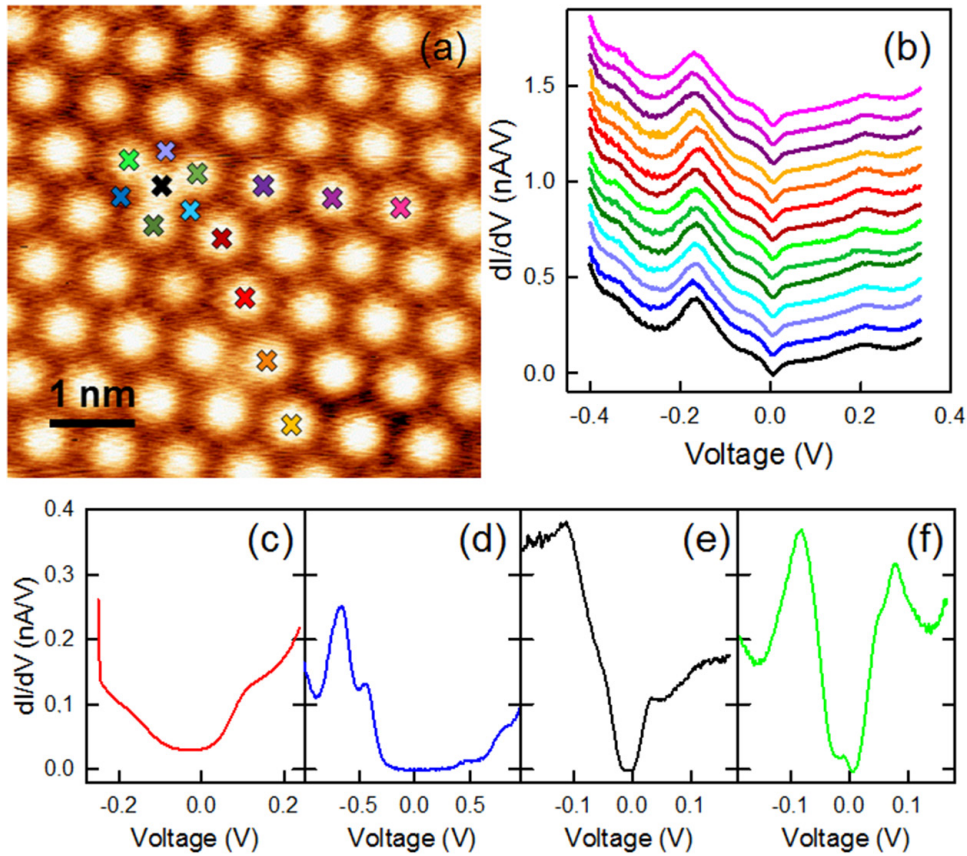


Figure 3. (a) Spatially-resolved tunneling spectra of a germanene area with an Y-shape defect, $V = -0.4$ V, $I = 100$ pA, $T = 5$ K. (b) Different spectra acquired at the location highlighted in (a). (c)–(f) Different dI/dV acquired on monolayer 3×3 germanene on Al(111), measured at different temperatures with different setpoint bias and currents. (c) 77 K, -0.25 V, 100 pA. (d) 77 K, -0.75 V, 100 pA. (e) 5 K, -0.2 V, 90 pA. (f) 5 K, -0.2 V, 60 pA.

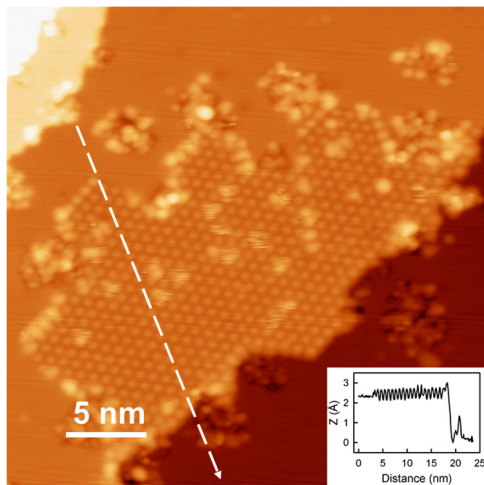


Figure 4. STM image of submonolayer germanene growth on Al(111). $V = -1.5$ V, $I = 50$ pA. $T = 77$ K. Inset: height profile measured across the germanene island along the dashed line.

the whole energy range. Reference spectra being established, the same tip was used to probe the germanene island located nearby, as pointed out in the STM image of figure 5. Again, $I(V)$ were recorded with different set-point currents to assess any influence of the tip-sample distance as the tip becomes closer to the surface with increasing currents. Remarkably, all $I(V)$ curves measured on the germanene island match the $I(V)$

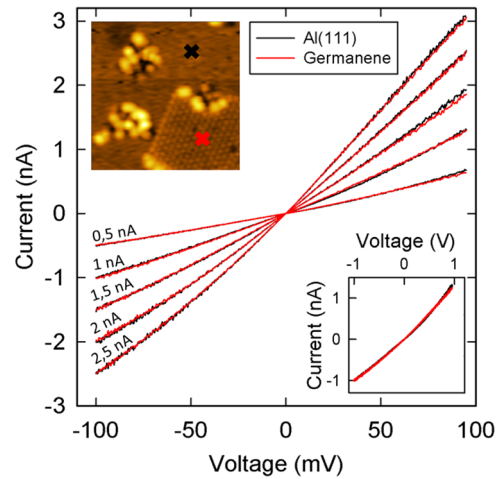


Figure 5. I - V curve measured as a function of setpoint current on Al(111) and germanene areas indicated by crosses in the STM image of the upper inset at 5 K. Inset: similar $I(V)$ curves measured on a wider bias range with a setpoint current of 1 nA.

curves measured on the Al(111) surface, These measurements show a clear metallic behaviour, which highlights the strong electronic coupling between germanene and aluminium, preventing the formation of a small band gap in germanene.

During the run of the experiments with the same tip, the acquisition of the additional spectra in other areas confirmed

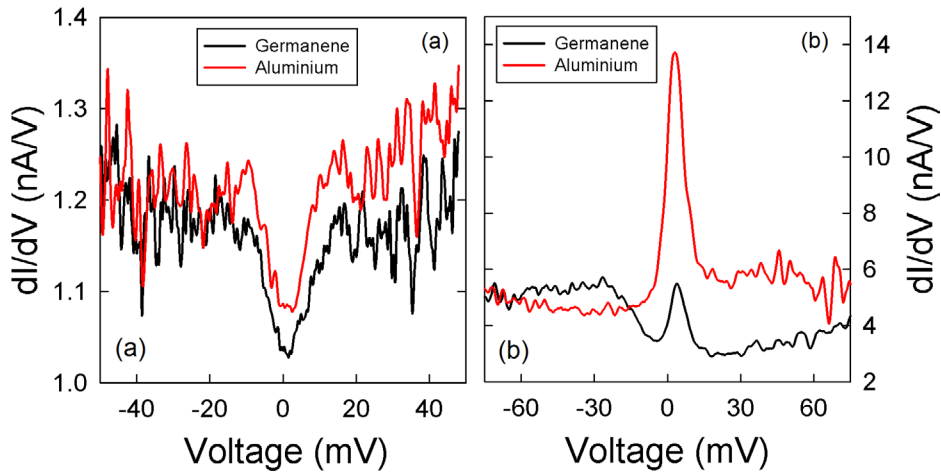


Figure 6. Two different example of dI/dV spectra measured on Al(1 1 1) and germanene of non-trivial interpretation. Both couple of spectra have been acquired at 5 K, (a) $V = -0.5$ V, $I = 60$ pA, (b) $V = -0.1$ V, 500 pA.

the similarity of the spectra acquired on the bare Al(1 1 1) surface and the germanene islands. However, the shape of the spectra was different from the initial linear behaviour. Two examples are shown in figure 6. In figure 6(a), a dip, that could be approximated with a V-shape-like function, is clearly seen in the differential conductance of both entities. Since this feature centred at the Fermi level is not expected for the Al(1 1 1) surface, we dismiss its origin to be related to the existence of a Dirac cone in the germanene nanosheet. Alternatively, figure 6(b) exhibits a strong peak, which is slightly shifted by 3.5 mV above the Fermi level. Again, the STS measurements between the Al surface and the germanene islands show the same peak, albeit to a modification of the peak intensity. As such a peak is not expected for the Al(1 1 1) surface, we rule out it to be caused by the electronic structure of the germanene nanosheet. Therefore, the diversity of the spectra obtained as the tip becomes used points to its crucial contribution to produce the spectral features visible in figures 3 and 6. These change of behaviors with time suggests that the tip gets contaminated as it probes the sample.

So far, in the literature has been shown that the STM tip can induce a change of the germanene structure at room temperature, switching between a honeycomb lattice to a hexagonal lattice [33]. However, we have encountered more dramatic events at low temperatures. As shown in figure 7, a germanene island can be disrupted when the tip is scanning on top of the nanosheet. The lower part of the island visible in figure 7(a), that exhibits a typical 3×3 reconstruction and the characteristic step height (see figure 7(b)), has disappeared in figure 7(c), leaving behind a large cluster with a height of 2.1 nm at the bottom right of the island. At the place of the island, the bare Al surface is partially recovered, but sparsely decorated with small clusters. Moreover, a narrow crack appears in the surface, as shown in figure 7(d), and its existence suggests that some Al atoms have been stripped off during the manipulation of the Ge adlayer. While most of the Ge and Al atoms, that were removed, have certainly been incorporated in the clusters seen on the surface, we cannot rule out the adsorption of atoms and clusters on the tip apex also. Figure 8 reveals another example of the surface

modification under scanning conditions. The topographic and current images in figures 8(a) and (b) show an isolated germanene island. Upon the measurement of an $I(V)$ curve with a close feedback loop in the top left part of the STM image, a germanene island appears in figures 8(c) and (d). During the next scans with constant feedback conditions, the surface is found to evolve to the final arrangement of the terraces seen in figures 8(e) and (f). Surprisingly, some new terraces show the 3×3 structure of germanene, meaning that nanosheets have been redeposited or displaced under the action of the STM tip. Although the occurrence of such events is the exception rather than the rule, they emphasize on the fragility of the germanene adlayer. This is consistent with the weak adsorption energy calculated for Ge atoms on the Al(1 1 1) surface [33, 35].

As an additional hint for the key role of adsorbed species at the tip apex in STS, we show CITS result in figure 9. The high resolution STM image of the 3×3 reconstruction of germanene simultaneously acquired with the grid of $I(V)$ and $dI(V)/dV$ curves, reveals sequences of topographic lines with a high density of glitches. Two types of regions exist, one with a low level of noise and one with a higher level of noise. The analysis of the spectra reveals the existence of two sets of spectra, consistent with the absence or presence of noise in the STM image. The lower spectrum in figure 9(b) shows a peak at negative bias and an apparent band gap of 50 mV, that extends more above the Fermi level. The upper spectrum of figure 9(b) resembles the lower one, but the peak is shifted towards the Fermi level and the apparent band gap is almost closed. The change of the image quality is therefore correlated with the change observed in the differential conductance. At a bias of -20 mV, which corresponds to the bias of the peak seen in the lower spectrum, the differential conductance is the highest in the topographic areas free of glitches (figure 9(c)). Such a correlation is emphasized when a line of spectra is plotted along the dashed line indicated in the STM image (figure 9(d)). As the area probed by the tip is clean and well-ordered, such measurements demonstrate the STM tip is at the origin of these sudden but repeatable changes in the tunnelling spectra. Based on these three examples, we believe that, despite the low temperature of the experiments, the STM

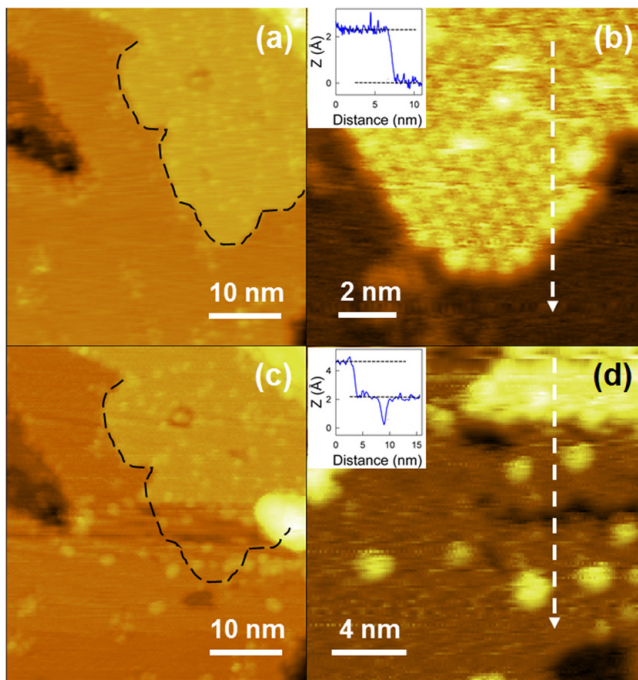


Figure 7. (a) Initial STM topography of a germanene island. (b) Atomically resolved image of the lower edge of germanene island, showing the typical 3×3 structure. Inset: height profile across the germanene island along the dashed line. (c) STM topography of the island after its unintentional manipulation. (d) Zoom on the removed area, with height profile in the inset. All the images were acquired at 77 K, $V = -1$ V, $I = 50$ pA.

tip can be easily contaminated by single atoms or clusters of Ge or/and Al atoms, resulting in characteristics with complex shapes.

4. Discussion

The similarity of the spectra measured on the bare Al(111) islands and on the germanene nanosheets indicates a tunnelling current dominated by the band structure of the Al crystal close to the Fermi level. We attribute this effect to the significant charge transfer calculated between the Ge atoms in contact with the Al(111) surface [30, 36], that certainly keeps the transmission probability high across the tunnelling junction. However, with continuous scanning of the surface over time, the spectra deviate from this linear behaviour around the Fermi level and show apparent gaps and peaks. We attribute the presence of these features to the formation of a nonconstant tip LDOS. Although the existence of tips with a nonuniform density of states has been reported in the literature [24–28], we note that the probability to get such a tip is rather high with a germanene sample. Due to the weak bonding of the Ge adlayer that arises from the jellium-like character of the electron distribution at the Al(111) surface [29], the germanene nanosheets can easily lose atoms or clusters, that adsorb on the tip apex resulting in nonconstant tip LDOS. Opposite to graphene, where small flakes have been displaced on a surface without any alteration [37, 38], we have always failed in controlling the manipulation of a germanene nanosheet to slide on the Al(111) surface. Manipulation have always led to a

drastic transformation of the sheet, causing either the formation of clusters on the surface (figure 7) or the reshaping of the terraces to produce new germanene islands (figure 8). This observation is in agreement with the difficulty to maintain Ge atoms in a plane, as observed with high-resolution transmission electron microscopy where two-dimensional Ge clusters have been found to morph into stable three dimensional clusters [39].

Based on the different apex termination that are likely to occur, we can speculate on their impact on the tunnelling spectra. For example, the weak attachment of a small Ge crystallite at the end of the tip could give rise to a double tunnelling junction structure, where electrons would be transferred through the states of the nanocrystals. As a result, the tunnelling spectra exhibit a zero conductance gap, which is caused by the band gap of the nanocrystal. This configuration accounts for the spectra with the largest apparent band gap, like the one seen in figure 3(d), the width of the band gap being consistent with the one reported in the literature for Ge nanocrystals [40]. Smaller Ge crystallites can also exist. In particular, a wide range of Ge clusters have been predicted to exist [41]. Depending on the Ge cluster size, theoretical calculations of the separation between the highest occupied and lowest unoccupied molecular orbitals yield value in the range of the apparent band gap found by the STS measurements [42, 43]. Instead of crystallites, amorphous Ge clusters could also self-assemble at the tip apex. They might have a density of states that can be relatively high in the vicinity of the Fermi level. Tunnelling through such a quasi-metallic cluster also results in an apparent band gap in the spectra due to electron-electron interaction. This Coulomb gap was estimated by Efros [44] and can explain the observation of spectra with small apparent band gap of a few mV to tens of mV, as the ones seen in figures 3(e) and (f). Similar behaviour should arise when Ge clusters are doped with W atoms of the tip or Al atoms of the surface [45, 46]. Missing areas of the Al surface were observed after the manipulation of the germanene islands (figure 7(d)), suggesting that Ge clusters containing Al atoms could exist at the tip apex. In this case, the observation of a Fano resonance is possible, similar to the peak seen in figure 6(b), since interference effects between direct tunnelling from the tip to the surface and tunnelling through the energy level of the Al impurity might occur [47]. Clusters with different stoichiometry may exist and we could even imagine to stabilize Al-rich clusters. Depending on the number of Al atoms, it has been shown that some clusters become more stable with a magic number of Al and Ge atoms. A typical example is Al icosahedral clusters consisting of 13 atoms, whose stability increases by substituting an Al atom with a Ge atom [48]. If weakly bound to the tip, such a cluster, could give rise to an apparent band gap in the tunnelling spectra [49]. It is interesting to note that mixture of Al and Ge films were found to show an enhanced superconductivity [50, 51], above the critical temperature of Al. Thus, we cannot rule out that these clusters show similar properties. The existence of superconducting clusters at the end of the tip could account for a vanishing DOS at the Fermi level or the observation of coherence peaks-like, similar to the spectra

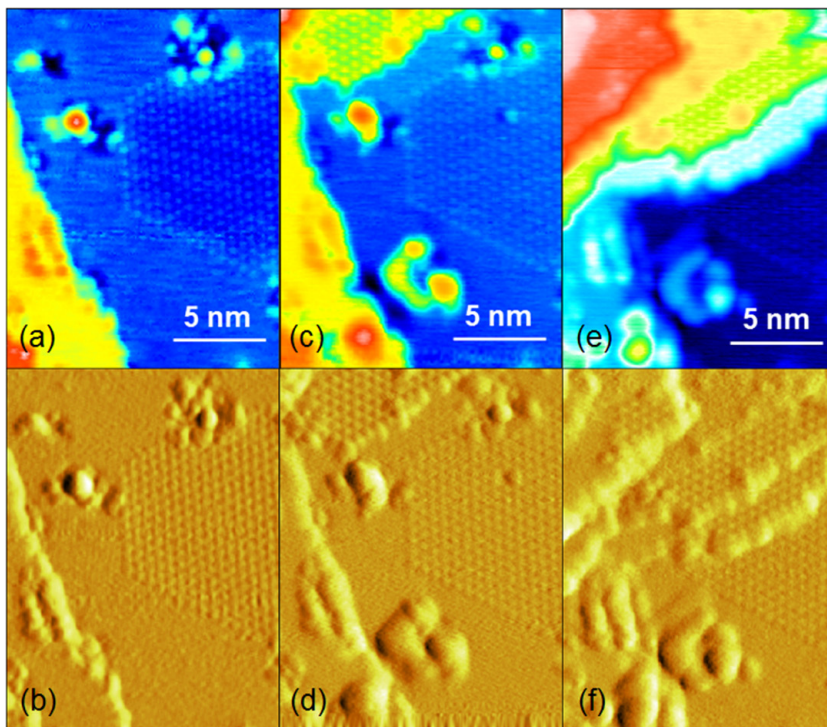


Figure 8. Sequence of STM images showing the real time appearance of germanene island. (a) Initial configuration of a hexagonal germanene island, with the related current image (b). (c) and (d) Modified configuration. The new terrace is a monolayer germanene step as shown in (d). (e)–(f) Final equilibrium position, with a bilayer+monolayer. All the images have been acquired at 77 K, $V = -1$ V, $I = 5$ pA.

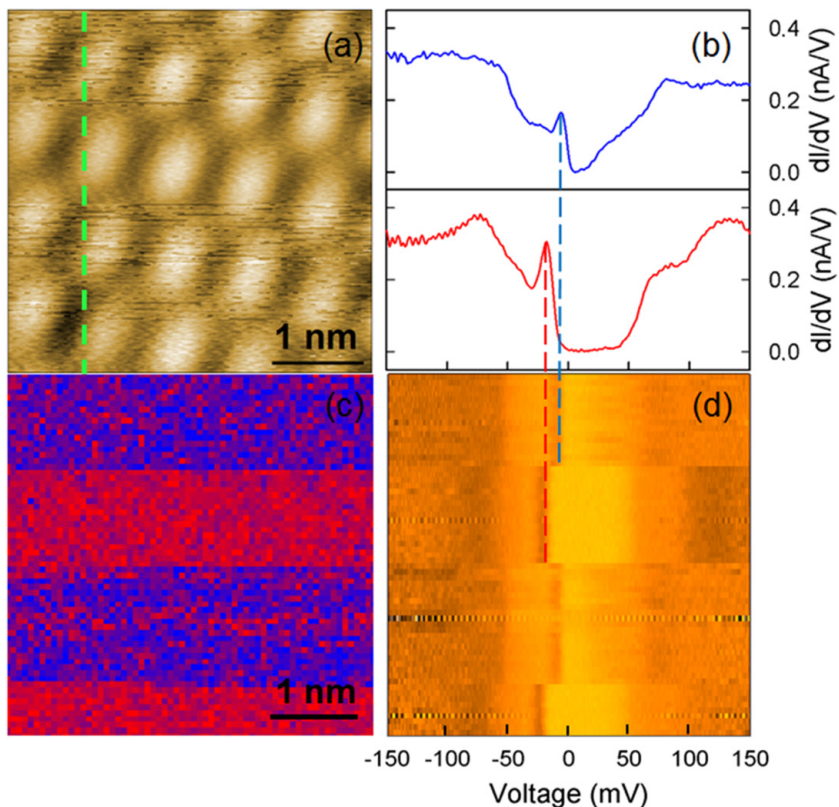


Figure 9. (a) Topography of a defect-free germanene area, $V = -0.15$ V, $I = 50$ pA, $T = 5$ K. (b) The two classes of spectra measured during the CITS. (c) Differential conductance map, measured at -20 mV, blue and red as in (b). (d) Strips view representation of the 64 spectra along the green line in (a).

observed in figures 3(f) and 6(a). Finally, as mentioned above, examination of Ge clusters with transmission electron microscopy have revealed the transformation of the clusters under the electron beam. These transformations can reach different equilibrium geometries or even lead to the fragmentation of the clusters with time, causing the appearance of different features in the tunnelling spectra. They could also explain the glitches observed in figure 9 [39].

5. Conclusion

In summary, we have performed intensive tunnelling spectroscopic measurements of the germanene surface, taking care of comparing the spectra with reference spectra obtained on the bare Al(1 1 1) surface. When clean STM tips are used, a linear behaviour of the I(V) characteristics is found and indicates a metallic surface. However, as the tips become used, significant changes in the shape of the spectra occur, even though the spectra are spatially and temporally reproducible over a few hours. We attribute these changes to the weak bonding of the germanene layer with the Al(1 1 1) surface and the ease for the tip to capture Ge, Al or Ge-Al clusters. The vast zoology of these clusters explains the diversity of the spectra observed during the experiments. Our results highlight the instability of the germanene sheet when it loses contact with the Al substrate underneath, consistent with the lack of two-dimensional Ge crystallites in the gas phase. While they call for a greater care in the interpretation of tunnelling spectra acquired on fragile two-dimensional atomic crystals that do not exist in nature, they also bespeak the unforeseen richness of the electronic structure of Ge and Al clusters.

Acknowledgments

This study was financially supported by the French National Research Agency (Germanene project ANR-17-CE09-0021-03), the EQUIPEX program Excelsior (Grant No. ANR-11-EQPX-0015) and the RENATECH network.

ORCID iDs

Carmelo Pirri  <https://orcid.org/0000-0002-3629-1044>
 Pascale Diener  <https://orcid.org/0000-0002-9685-2982>
 Bruno Grandidier  <https://orcid.org/0000-0001-6131-7309>

References

- [1] Novoselov K S, Geim A K, Morozov S, Jiang D, Katsnelson M, Grigorieva I, Dubonos S and Firsov A A 2005 *Nature* **438** 197
- [2] Zhang Y, Tan Y W, Stormer H L and Kim P 2005 *Nature* **438** 201
- [3] Li G, Luican A and Andrei E Y 2009 *Phys. Rev. Lett.* **102** 176804
- [4] Acun A *et al* 2015 *J. Phys.: Condens. Matter* **27** 443002
- [5] Cahangirov S, Topsakal M, Aktürk E, Şahin H and Ciraci S 2009 *Phys. Rev. Lett.* **102** 236804
- [6] Liu C C, Feng W and Yao Y 2011 *Phys. Rev. Lett.* **107** 076802
- [7] Walhout C, Acun A, Zhang L, Ezawa M and Zandvliet H J 2016 *J. Phys.: Condens. Matter* **28** 284006
- [8] Zhang L, Bampoulis P, Rudenko A, Yao Q V, Van Houselt A, Poelsema B, Katsnelson M and Zandvliet H 2016 *Phys. Rev. Lett.* **116** 256804
- [9] Qin Z, Pan J, Lu S, Shao Y, Wang Y, Du S, Gao H J and Cao G 2017 *Adv. Mater.* **29** 1606046
- [10] Zhuang J *et al* 2018 *Adv. Sci.* **5** 1800207
- [11] Chiappe D, Grazianetti C, Tallarida G, Fanciulli M and Molle A 2012 *Adv. Mater.* **24** 5088
- [12] Du Y *et al* 2014 *ACS Nano* **8** 10019
- [13] Feng B, Ding Z, Meng S, Yao Y, He X, Cheng P, Chen L and Wu K 2012 *Nano Lett.* **12** 3507
- [14] Álvarez A D, Zhu T, Nys J, Berthe M, Empis M, Schreiber J, Grandidier B and Xu T 2016 *Surf. Sci.* **653** 92
- [15] Lin C L, Arafune R, Kawai M and Takagi N 2015 *Chin. Phys. B* **24** 087307
- [16] Grazianetti C, Chiappe D, Cinquanta E, Tallarida G, Fanciulli M and Molle A 2014 *Appl. Surf. Sci.* **291** 109
- [17] Lin C L, Arafune R, Kawahara K, Kanno M, Tsukahara N, Minamitani E, Kim Y, Kawai M and Takagi N 2013 *Phys. Rev. Lett.* **110** 076801
- [18] De Padova P *et al* 2017 *J. Phys. Chem. C* **121** 27182
- [19] Volders C, Monazami E, Ramalingam G and Reinke P 2016 *Nano Lett.* **17** 299
- [20] Endo S, Kubo O, Nakashima N, Iwaguma S, Yamamoto R, Kamakura Y, Tabata H and Katayama M 2017 *Appl. Phys. Express* **11** 015502
- [21] Bampoulis P, Zhang L, Safaei A, van Gastel R, Poelsema B and Zandvliet H J W 2014 *J. Phys.: Condens. Matter* **26** 442001
- [22] Zhang L, Bampoulis P, van Houselt A and Zandvliet H J 2015 *Appl. Phys. Lett.* **107** 111605
- [23] Stroschio J A, Feenstra R and Fein A 1986 *Phys. Rev. Lett.* **57** 2579
- [24] Klitsner T, Becker R and Vickers J 1990 *Phys. Rev. B* **41** 3837
- [25] Pelz J 1991 *Phys. Rev. B* **43** 6746
- [26] Dombrowski R, Steinebach C, Wittneven C, Morgenstern M and Wiesendanger R 1999 *Phys. Rev. B* **59** 8043
- [27] Passoni M, Donati F, Bassi A L, Casari C S and Bottani C E 2009 *Phys. Rev. B* **79** 045404
- [28] Kwapiński T and Jałochowski M 2010 *Surf. Sci.* **604** 1752
- [29] Derivaz M, Dentel D, Stephan R, Hanf M C, Mehdaoui A, Sonnet P and Pirri C 2015 *Nano Lett.* **15** 2510
- [30] Wang W and Uhrberg R I 2017 *Beilstein J. Nanotechnol.* **8** 1946
- [31] Albrektsen O, Salemkink H, Mo/rch K and Thölen A 1994 *J. Vac. Sci. Technol. B* **12** 3187
- [32] Yu Z, Wang C M, Du Y, Thevuthasan S and Lyubinetsky I 2008 *Ultramicroscopy* **108** 873
- [33] Stephan R, Derivaz M, Hanf M C, Dentel D, Massara N, Mehdaoui A, Sonnet P and Pirri C 2017 *J. Phys. Chem. Lett.* **8** 4587
- [34] Kevan S, Stoffel N and Smith N 1985 *Phys. Rev. B* **31** 1788
- [35] Gao N, Liu H, Zhou S, Bai Y and Zhao J 2017 *J. Phys. Chem. C* **121** 5123
- [36] Stephan R, Hanf M, Derivaz M, Dentel D, Asensio M, Avila J, Mehdaoui A, Sonnet P and Pirri C 2016 *J. Phys. Chem. C* **120** 1580
- [37] Kawai S *et al* 2016 *Science* **351** 957
- [38] Feng X, Kwon S, Park J Y and Salmeron M 2013 *ACS Nano* **7** 1718
- [39] Bals S, Van Aert S, Romero C, Lauwaet K, Van Bael M J, Schoeters B, Partoens B, Yücelen E, Lievens P and Van Tendeloo G 2012 *Nat. Commun.* **3** 897

- [40] Nakamura Y, Watanabe K, Fukuzawa Y and Ichikawa M 2005 *Appl. Phys. Lett.* **87** 133119
- [41] Lu W C, Wang C, Zhao L Z, Zhang W, Qin W and Ho K 2010 *Phys. Chem. Chem. Phys.* **12** 8551
- [42] Negishi Y, Kawamata H, Hayakawa F, Nakajima A and Kaya K 1998 *Chem. Phys. Lett.* **294** 370
- [43] Wang J, Wang G and Zhao J 2001 *Phys. Rev. B* **64** 205411
- [44] Efros A and Shklovskii B I 1975 *J. Phys. C: Solid State Phys.* **8** L49
- [45] Wang J and Han J G 2006 *J. Phys. Chem. A* **110** 12670
- [46] Chambouleyron I and Comedi D 1998 *J. Non Cryst. Solids* **227** 411
- [47] Mantsevich V N and Maslova N S 2010 *JETP Lett.* **91** 139
- [48] Gong X and Kumar V 1993 *Phys. Rev. Lett.* **70** 2078
- [49] Li X and Wang L S 2002 *Phys. Rev. B* **65** 153404
- [50] Hauser J 1971 *Phys. Rev. B* **3** 1611
- [51] Fontaine A and Meunier F 1972 *Z. Phys. B* **14** 119

Van Hove Singularities and Trap States in Two-Dimensional CdSe Nanoplatelets

Nemanja Peric, Yannick Lambert, Shalini Singh, Ali Hossain Khan, Nathali Alexandra Franchina Vergel, Dominique Deresmes, Maxime Berthe, Zeger Hens, Iwan Moreels, Christophe Delerue, Bruno Grandidier,* and Louis Biadala*

Cite This: *Nano Lett.* 2021, 21, 1702–1708

Read Online

ACCESS |

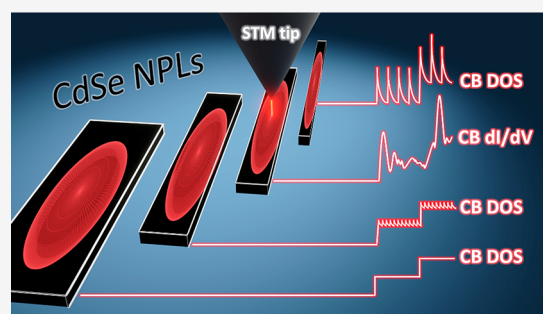
Metrics & More

Article Recommendations

Supporting Information

ABSTRACT: Semiconductor nanoplatelets, which offer a compelling combination of the flatness of two-dimensional semiconductors and the inherent richness brought about by colloidal nanostructure synthesis, form an ideal and general testbed to investigate fundamental physical effects related to the dimensionality of semiconductors. With low temperature scanning tunnelling spectroscopy and tight binding calculations, we investigate the conduction band density of states of individual CdSe nanoplatelets. We find an occurrence of peaks instead of the typical steplike function associated with a quantum well, that rule out a free in-plane electron motion, in agreement with the theoretical density of states. This finding, along with the detection of deep trap states located on the edge facets, which also restrict the electron motion, provides a detailed picture of the actual lateral confinement in quantum wells with finite length and width.

KEYWORDS: CdSe nanoplatelets, nanocrystals, quantum confinement, dimensionality, scanning tunneling spectroscopy, traps



In condensed matter physics, a stepwise reduction of the dimensionality from bulk to the nanoscale is known to lead to striking electronic and optical properties such as the giant oscillator strength transition for two-dimensional (2D) semiconductor quantum wells¹ and the spin-charge separation in one-dimensional (1D) systems.² However, in contrast to metals, the lateral confinement in semiconductor materials competes with the exciton Coulomb interaction, which can be magnified by dielectric mismatch. Due to the complexity of these interactions,³ the degree of freedom in the electron motion remains poorly understood, whereas its clear circumscription could significantly improve the optoelectronic performances of quasi-2D systems such as CdSe colloidal nanoplatelets (NPLs).

Since the distribution of the quantized states, the so-called density of states (DOS), reflects the restrictions of the electron motion with dimensionality, it can serve as a genuine fingerprint to unambiguously disclose the confinement experienced by the charge carriers. A unique way to probe the DOS consists in measuring single-particle excitation spectra with scanning tunnelling spectroscopy (STS).^{4–7} Here we used this technique to study electron confinement in colloidal CdSe nanoplatelets (NPLs), which have a quantized thickness d due to a discrete number of monolayers (MLs) and a rectangular shape with finite length L and width W . Recently, Ji et al. have demonstrated that the hole DOS is consistent with a free in-plane motion, while the electrons have

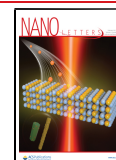
a more complex DOS that deviates from the simple 2D model.⁸ When W or/and L are smaller than ten to five times the exciton Bohr radius, the electron behavior, which has a smaller effective mass than the hole, becomes affected, with a significant impact on its interaction with the hole and the dielectric image charges. The already present complexity in understanding electron–hole correlation in these box-shaped nanostructures is further enhanced with the existence of electrical surface traps, which are caused by the sporadic absence of ligands. It makes the electron confinement in the NPLs still unknown, leading to intense debates about their true dimensionality.^{9,10}

In this study, two sets of CdSe NPLs capped with oleate ligands having thicknesses of 5.5 ML ($d_{5.5} = 1.65$ nm) and 7.5 ML ($d_{7.5} = 2.25$ nm) were synthesized.^{11,12} While transmission electron microscopy (TEM) shows the overall rectangular shapes of the NPLs and yields their lateral sizes, $(21 \pm 2) \times (7 \pm 1)$ nm² for the 5.5-ML-thick NPLs and $(45 \pm 10) \times (9 \pm 1)$ nm² for the 7.5-ML-thick NPLs (Figure 1a and Figure S1), the

Received: November 13, 2020

Revised: February 3, 2021

Published: February 5, 2021



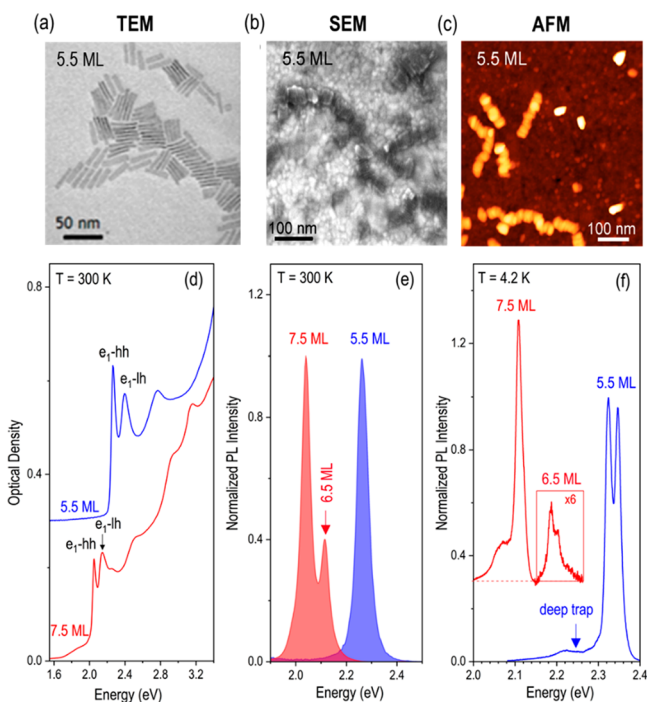


Figure 1. a) TEM, b) SEM, and c) AFM images of 5.5-ML-thick NPLs deposited on the Au surface. d) Absorption and e) photoluminescence spectra at room temperature of 5.5 and 7.5 ML NPLs in solution. f) Photoluminescence spectra at $T = 4.2$ K of 5.5 and 7.5 ML NPLs drop-casted on glass substrate. Spectra are offset for clarity. The dashed line indicates the baseline for 7.5 ML. The contribution of 6.5 ML NPLs in the PL spectrum is enhanced by a factor of 6 for clarity. The arrow indicates the deep trap emission in the PL spectra of 5.5 ML NPLs.

thickness of the NPLs is directly obtained from their optical properties. The optical absorption spectra measured at room temperature are dominated by two absorption lines (Figure

1d), attributed to the formation of excitons composed of the 1S electron (e_1) in the conduction band (CB) and the $1S_{3/2}$ heavy holes (hh) and light holes (lh) in the valence band.¹³ At room temperature, the photoluminescence (PL) spectra consist of a single sharp Lorentzian line from the radiative recombination of hh excitons (Figure 1e). As the NPL thickness decreases, the hh exciton energy steadily increases because of stronger vertical quantum confinement.¹³ The additional feature observed at 2.13 eV in the PL spectra of 7.5 ML NPLs is due to the presence of a small fraction of 6.5 ML NPLs. At cryogenic temperature (Figure 1f), the PL spectra of the NPLs exhibit an emission doublet, with decreasing separation for larger NPL thicknesses, which is attributed to the radiative recombination of the hh exciton (high energy peak) and its negative trion (low energy peak).¹⁴ The PL spectra measured at $T = 4.2$ K reveals the presence of a small and broad band in an energy range extending below the band gap energy. It is attributed to the recombination through trap states in the band gap,¹⁵ which are caused by the incomplete passivation of surface dangling bonds (DB) with organic ligands.

While insightful, optical transitions do not provide a direct access to the energy levels of the NPLs. In particular, the relative positions of the trap states with respect to the Fermi level remain unknown. To this aim, the NPLs were drop-casted on gold surfaces to be studied with STS. Their arrangement was first observed with scanning electron microscopy (SEM) and atomic force microscopy (AFM). As shown in Figure 1b,c, the 5.5 ML NPLs stack to form columnar assemblies. Only a small number of 5.5 ML NPLs adsorb in a flat-lying geometry. For this configuration, the apparent height measured from the scanning tunnelling microscopy (STM) image yields 4.2 nm (Figure 2b,c). This value is consistent with a NPL thickness of 1.65 nm surrounded by tilted oleate ligands (around 2 nm in length) on top and bottom Cd-rich (100) facets. In contrast to the 5.5 ML NPLs, the majority of the 7.5 ML NPLs was found flat on the Au surface (Figure S2). We attribute this change to

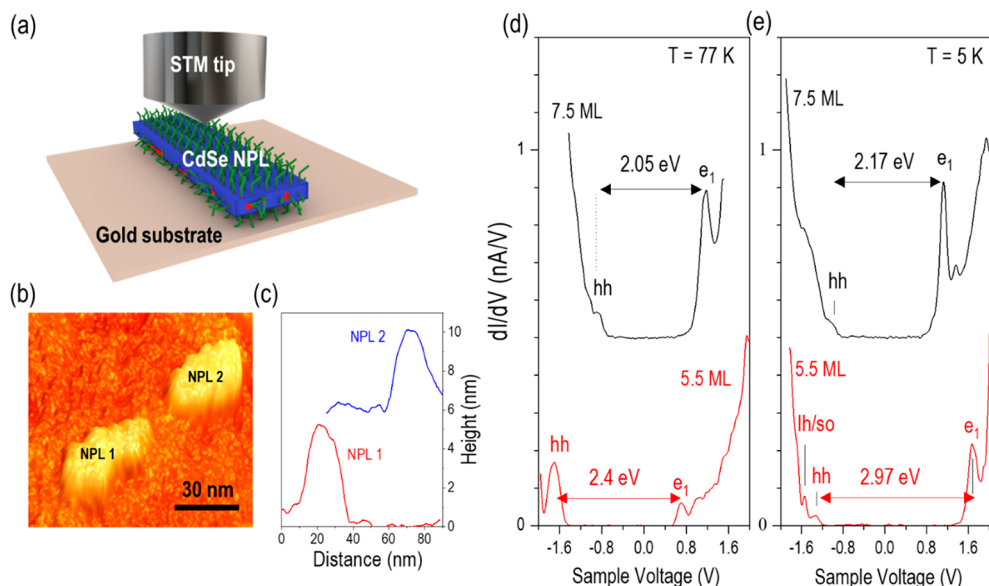


Figure 2. a) Illustration of the STS on individual flat-lying NPL. b) STM image of two flat-lying CdSe NPLs with a thickness of 5.5 ML and c) corresponding height profiles. Tunneling conditions: $V_{\text{sample}} = -1.5$ V, $I_t = 5$ pA. STS of a 7.5 ML NPL (black) and a 5.5 ML NPL (red) measured at d) $T = 77$ K and e) 5 K, respectively. The separation between the lowest peak in the conduction band and the highest peak in the valence band, labeled e_1 and hh, respectively, is indicated. The light hole/split-off state is labeled lh/so.

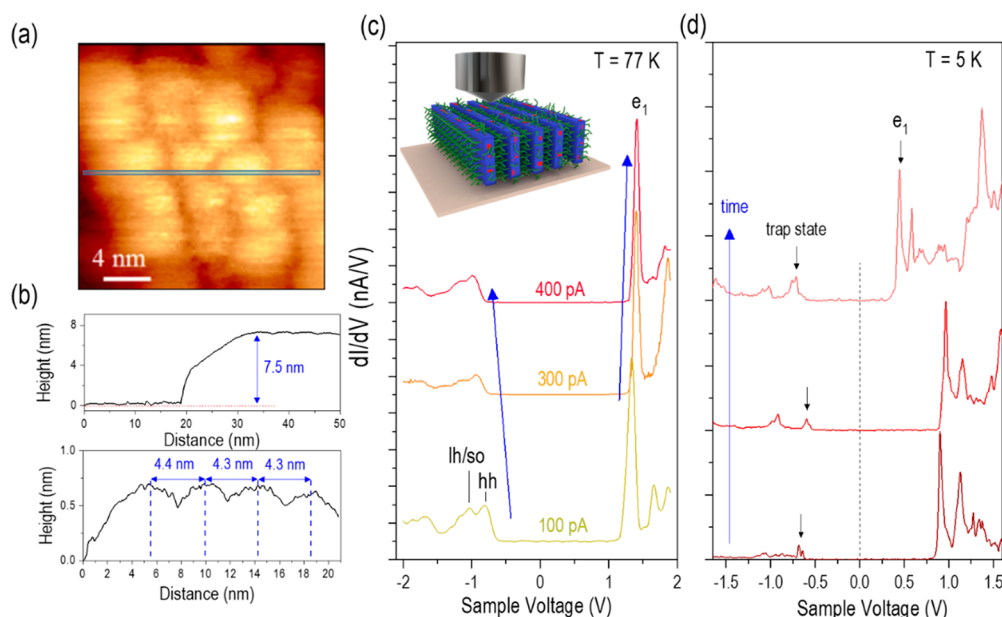


Figure 3. a) STM image of a stack of CdSe 5.5 ML NPLs. Tunneling conditions: $V_{\text{sample}} = -5.0$ V, $I_t = 10$ pA. b) (top) Height profile measured at the position of the horizontal segment in a), across a larger area image than the one shown in the STM image. (Bottom) Height profile on top of the stack pointing out the inter NPL distance. c) STS of a trap-free NPL within a stack measured at different set point currents as indicated in the graph. Feedback voltage: $V_{\text{sample}} = -1.5$ V. Arrows point to the shift observed with increasing set point currents for the lowest peak in the conduction band e_1 , and the highest peaks in the valence band labeled hh and lh/so, respectively. Inset: schematic of a stack of NPLs probed with a STM tip. d) Sequence of three differential conductance spectra acquired on a stacked NPL bearing a trap state and averaged over a few successive curves between charging and discharging events. e_1 indicates the position of the first electron sub-band, while the downward arrow indicates the highest trap state in the band gap of the NPL. The curves are offset for clarity. Feedback conditions: $V_{\text{sample}} = -1.8$ V, $I_t = 80$ pA.

dichloromethane that was used as a solvent for the 7.5 ML NPLs to reduce clustering effects.

For the sake of clarity in the data interpretation, tunnelling spectroscopic measurements were first acquired on the isolated and flat-lying NPLs (Figure 2a), which show the typical configuration of resonant tunneling across a double tunneling junction. In this geometry, by choosing tunnelling currents smaller than 100 pA as set points, the width of the STM tip-NPL junction is usually larger than the one of the NPL-gold junction and limits the current. In such a situation, where an electron tunneling from the tip to the NPL leaves the NPL before a second electron arrives, the zero-conductance region (ZCR), surrounded by peaks at positive and negative sample voltages, gives access to the quasiparticle band gap of the NPLs.^{16,17} The peaks occur at voltages that correspond to the energy levels of the NPLs plus the polarization energy of the charge carriers divided by the capacitance ratio of the two junctions, the so-called lever arm.¹⁸ Examination of the ZCRs in Figure 2d,e shows larger apparent band gaps for thinner NPLs, with values consistent with those measured in ref 8. While the lever arm is close to one for the 7.5 ML NPLs with partially chloride-passivated facets, smaller lever arms of 0.80–0.85 are occasionally found for 5.5 ML NPLs, due to the smaller in-plane dimensions and the thicker NPL-gold junction consisting of long oleic acid ligands only. For these few spectra exhibiting apparent band gaps much larger than the optical gap, two neighboring peaks, separated by 200 mV, are clearly seen at negative bias (Figure 2d, 5.5 ML NPL). They are attributed to the heavy hole (hh) and light hole/split-off (lh/so) states, the mixing between the lh and so bands arising from a 2D confinement.⁸ Most importantly, whatever the size of the NPLs that are probed, the STS measurements consistently reveal the presence of one or several peaks in CB, in agreement

with a recent STS work.⁸ This behavior clearly departs from the typical steplike function observed in the tunneling spectra of semiconductor quantum wells.^{7,19} Its observation rules out the simple picture of an electron moving freely in two dimensions.

We now turn to the tunnelling spectra measured on the stacks. As shown in the STM topography of Figure 3a, the NPLs are individually resolved within a stack. An average separation of 4.3 ± 0.1 nm between the NPLs (Figure 3b) suggests an entwinement of the ligands for the largest facets which are face-to-face. The thickness of the whole junction reaches about 7.5 nm in STM, in agreement with the average width of the NPLs and a disordered layer of ligands on the side facets (inset Figure 3c). Based on the height profiles (see also Figure S2), the NPLs lie along their longest edge,^{20,21} providing another access to the DOS from the side facets. Tunneling spectra fall into two classes. Some NPLs show a ZCR similar to the one observed for the flat-lying NPLs (Figure 3c). In this case, the gap is surrounded by an intense peak at positive bias and a doublet peak at negative bias. As the ZCR increases with higher set point current,^{18,22,23} we unambiguously identify the intense peak as an electron level in CB and the doublet peak in VB as the hh and lh/so states. Notice that the peaks in CB are usually more intense in comparison with the peaks found for the flat-lying NPLs, while the apparent band gap is unchanged, as discussed in the Supporting Information. In other cases, the spectra still exhibit the highly intense peak at positive bias, yet the ZCR is inconsistently smaller than the optical gap of the 5.5 ML NPLs. For example, in Figure 3d, the ZCR is a mere 1.63 eV, while the optical gap measured in Figure 1f was 2.33 eV. Such a behavior was not seen for the flat-lying NPLs. Moreover, recording hundreds of consecutive spectra over 30 min with

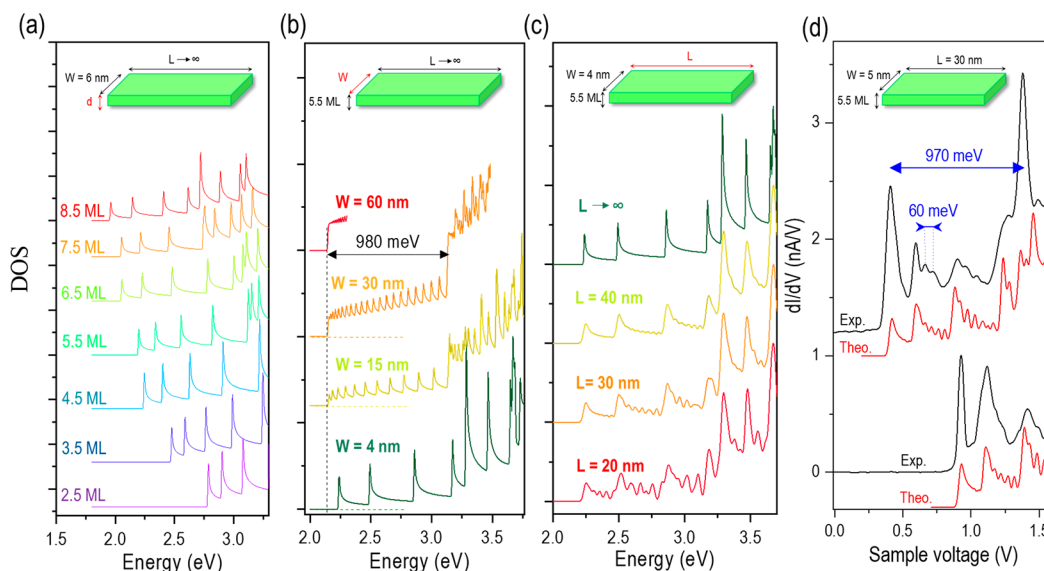


Figure 4. Theoretical conduction band density of states of CdSe nanoplatelets. a) DOS of infinitely long NPLs with a width of 6 nm and varying thicknesses. b) DOS of infinitely long NPLs with a fixed thickness of 5.5 ML and different widths. Due to the higher number of states contributing to the DOS for larger widths, the calculation becomes quickly limited to the lowest states. c) DOS of NPLs with a thickness of 5.5 ML, a width of 4 nm and different lengths. d) Comparison between two differential conductance spectra (black, labeled Exp.) and the theoretical DOS (red, labeled Theo.) of 5.5 ML NPLs with $L = 30$ nm and $W = 5$ nm. Experimental conditions: $V_{\text{sample}} = -1.8$ V, $I_t = 100$ pA, temperature 5 K. The curves are offset for clarity.

the same feedback parameters reveals the occurrence of sudden shifts in the onset of the current at positive bias (Figure S3). This result mirrors the typical spectral diffusion phenomenon obtained on the PL emission line width of individual nanocrystals attributed to charge fluctuation in the local environment of the NCs.^{24,25} Altogether, these results point toward the presence of states within the band gap of CdSe NPLs (Figure S4).

In the literature, the trap states at the surface of colloidal semiconductor nanocrystals have been designated as the main source of in-gap states.^{26,27} These trap states stem from the DBs of unpassivated atoms at the nanoparticle surface. For CdSe nanocrystals, it has been predicted that selenium DBs at the surface of the nanocrystal would be the main source of electrical traps.^{11,28,29} In contrast with spherical nanocrystals, NPL facets are very well-defined upon their orientation. Top and bottom facets are pure Cd {100} facets, while the side facets can consist of Se rich facets. Here, the comparison between the spectra acquired on the flat-lying NPLs and those acquired on NPL within stacks indicates that traps states are only detected when NPLs rest on their edge. This finding is consistent with conclusions drawn from macroscopic analyses of the NPLs, which pinpointed a preferred localization of trap states at the NPL edges. On these facets, the ligands are the most labile, and their desorption favors the formation of two-coordinated selenium surface atoms.^{11,28} The nature of the DBs in CdSe NPLs is further supported by the relative energetic position of the trap state in the band gap. These deep states, that lie below the Fermi level, are found almost midgap, in agreement with DFT calculations assuming Se DBs.¹¹

When tunnelling charge carriers are captured or released by a deep level, clear stepwise changes occur in single real-traces signatures of charging or discharging events (Figure S3). These sudden variations of the tunnelling current are seen at positive bias only, and they are found to be distributed over a few hundreds of meV. Several charging events can even take place

during the same trace. These charges dramatically affect the potential distribution between the tip and the Au surface, which has been shown to result in a substantial shift of the CB states.^{30,31} Similar to ref 30, we attribute a sudden decrease of the current to the release of one electron by a trap state to the gold substrate, since the next trace shows a clear shift toward smaller positive bias. Starting with N excess of electrons, the NPL loses one electron and changes its charge state to $N-1$. As a result, a larger portion of the CB becomes accessible. For electrostatic shifts exceeding 500 meV, the differential conductance unveils a wealth of features that, again, are not compatible with the ones of a 2D quantum well.

In order to get deeper insight into these features, tight binding calculations were performed to determine the CB structure of the NPLs (see Supporting Information). Starting with the geometry of an infinitely long NPL and a finite width ($W = 6$ nm), the calculations yield the typical DOS of a quantum wire for any NPL thickness from 2.5 to 8.5 ML (Figure 4a). It consists of Van Hove singularities, that can be gathered within sub-bands. The transitions between the lowest sub-bands are clearly identified when the band structure is plotted in the Brillouin zone (Figure S5). They correspond to a change of the peak intensity and spacing in the DOS. As expected, the position of the first peak, which corresponds to the lowest sub-band, shifts toward higher energy as the thickness of the NPL decreases because of strong confinement (Figure 4a).

In contrast, the energy difference between subsequent peaks is directly linked to the width of the NPL (Figure 4b). For increasing widths and consequent reduction of lateral confinement, the peak spacing decreases, revealing a steplike function modulated by closer and closer singularities. Ultimately, the DOS converges to a pure steplike function, the fingerprint of a quantum well. Based on our calculations, a peak spacing of the order of 25 meV is obtained for the lowest sub-bands of infinitely long NPLs with a width of 30 nm. While such NPLs

could be approximated as 2D systems at room temperature, the NPLs that are considered here, and more generally in the literature, definitely deviate from this simple picture. The tight binding calculations also reveal a strong influence of the NPL length. Reducing the length to realistic lengths of 20–30 nm leads to the formation of oscillations in the DOS between the reciprocal square root singularities (Figure 4c). This feature indicates the loss of a free electron motion in the plane of the NPLs. As the motion becomes more and more restricted, the 1D DOS vanishes in favor of an oscillating DOS. Therefore, the Van Hove singularities and the strength of the oscillating DOS are the signature of the electron behavior in the NPLs: their respective contribution to the DOS provides direct insight into the lateral extension of the electron wave function.

In order to compare the theoretical DOS with experiments, we selected NPLs, where tens of successive traces were measured without any stepwise changes of the current at positive bias. This condition ensures the absence of any significant electrostatic change in the environment of the NPLs. Two examples of spectra acquired on the stacked 5.5 ML NPLs are shown in Figure 4d. They exhibit both features of the calculated DOS: the singularities superimposed to a small oscillation. Note that the energy difference between the maxima of amplitude in the small oscillation is too large to be attributed to a polaron contribution of optical phonons (26 meV for CdSe) as measured on nanocrystals.³² Instead, the experimental DOS observed here indicates a large delocalization of the electron wave function in the NPLs, where the boundaries of the NPLs act as potential barriers that laterally confine the electron wave function.

Notwithstanding the qualitative agreement with the experimental results, the tight binding calculations quantitatively reproduce the experimental data for realistic dimensions of NPLs ($d = 5.5$ ML; $W = 5$ nm; $L = 30$ nm). As the calculations do not include any corrections for the self-energy, our results suggest a weak self-energy of the tunnelling electron. We explain this effect by the substantial dielectric screening that arises from the proximity of the NPLs in the stack and the presence of top and bottom metal electrodes. This quantitative agreement further emphasizes the structural quality of NPLs: any localization potential, scattering with phonons, or defect in the lattice would dramatically alter the DOS by notably inducing a strong broadening or even the vanishing of the Van Hove singularities. We note, however, that the degree of delocalization must be slightly alleviated. The agreement between the experimental spectra and the theoretical DOS shown in Figure 4d is only obtained when comparing the DOS of 5-nm-wide NPLs with STS spectra recorded on 7-nm-wide NPLs. This difference indicates that the electron wave function does not fully extend up to the boundaries. Despite the presence of traps on the edge of the NPLs that modify the confining potential when they are negatively charged, we assign the existence of the small depleted layer along the side facets of the NPLs to a dipole layer arising from ligands and/or surface reconstruction, which can account for a very localized potential.³³

In summary, the CB structure of CdSe NPLs has been investigated with STS. The observation of Van Hove singularities implies a paradigm shift on the electronic structure of typical CdSe NPLs considered in the literature. As the electron DOS exhibits a striking modulation that is directly related to the length of the NPLs, delineating the in-plane electron motion at low temperature has important con-

sequences for a deeper understanding of the exciton dissociation, diffusive transport, and annihilation in NPLs. Moreover, it is shown that the side facets of NPLs host electronic deep trap states, which cause a Coulomb blockade in the tunnelling current. As they could be fully removed by the formation of core-crown NPL, our results anticipate a genuine boost for NPL-based lateral heterostructures that will notably allow for the mixing of the dimensionalities to favor specific electronic or optical properties.

■ ASSOCIATED CONTENT

Supporting Information

The Supporting Information is available free of charge at <https://pubs.acs.org/doi/10.1021/acs.nanolett.0c04509>.

Methods for synthesis, structural and optical analysis, STM experiments, and tight binding calculations and additional data (PDF)

■ AUTHOR INFORMATION

Corresponding Authors

Louis Biadala – Université de Lille, CNRS, Centrale Lille, Université Polytechnique Hauts-de-France, Junia-ISEN, Centrale Lille, UMR 8520 - IEMN, F-59000 Lille, France; orcid.org/0000-0002-1953-9095; Email: louis.biadala@iemn.fr

Bruno Grandidier – Université de Lille, CNRS, Centrale Lille, Université Polytechnique Hauts-de-France, Junia-ISEN, Centrale Lille, UMR 8520 - IEMN, F-59000 Lille, France; Email: bruno.grandidier@iemn.fr

Authors

Nemanja Peric – Université de Lille, CNRS, Centrale Lille, Université Polytechnique Hauts-de-France, Junia-ISEN, Centrale Lille, UMR 8520 - IEMN, F-59000 Lille, France

Yannick Lambert – Université de Lille, CNRS, Centrale Lille, Université Polytechnique Hauts-de-France, Junia-ISEN, Centrale Lille, UMR 8520 - IEMN, F-59000 Lille, France

Shalini Singh – Physics and Chemistry of Nanostructures, Ghent University, 9000 Ghent, Belgium; orcid.org/0000-0001-8607-8383

Ali Hossain Khan – Physics and Chemistry of Nanostructures, Ghent University, 9000 Ghent, Belgium; orcid.org/0000-0001-7155-0200

Nathali Alexandra Franchina Vergel – Université de Lille, CNRS, Centrale Lille, Université Polytechnique Hauts-de-France, Junia-ISEN, Centrale Lille, UMR 8520 - IEMN, F-59000 Lille, France

Dominique Deresmes – Université de Lille, CNRS, Centrale Lille, Université Polytechnique Hauts-de-France, Junia-ISEN, Centrale Lille, UMR 8520 - IEMN, F-59000 Lille, France

Maxime Berthe – Université de Lille, CNRS, Centrale Lille, Université Polytechnique Hauts-de-France, Junia-ISEN, Centrale Lille, UMR 8520 - IEMN, F-59000 Lille, France

Zeger Hens – Physics and Chemistry of Nanostructures, Ghent University, 9000 Ghent, Belgium; orcid.org/0000-0002-7041-3375

Iwan Moreels – Physics and Chemistry of Nanostructures, Ghent University, 9000 Ghent, Belgium; orcid.org/0000-0003-3998-7618

Christophe Delerue – Université de Lille, CNRS, Centrale Lille, Université Polytechnique Hauts-de-France, Junia-ISEN,

Centrale Lille, UMR 8520 - IEMN, F-59000 Lille, France;
orcid.org/0000-0002-0427-3001

Complete contact information is available at:
<https://pubs.acs.org/10.1021/acs.nanolett.0c04509>

Author Contributions

L.B. conceived and designed the experiments. A.K. and S.S. synthesized the NPLs and performed the TEM experiments and the room temperature optical characterization under the supervision of Z.H. and I.M. N.P. and L.B. performed the STM measurements under the guidance of B.G. and M.B. L.B. and N.P. performed the optical characterization at cryogenic temperature. D.D. and Y.L. performed the AFM. N.F.V. and N.P. did the SEM experiments. C.D. performed the tight binding calculations. L.B., C.D., and B.G. interpreted the data. B.G. and L.B. wrote the manuscript.

Notes

The authors declare no competing financial interest.

ACKNOWLEDGMENTS

This study was financially supported by the European Community's H2020 Program (Grant No. PITN-GA-2016-722176, "Indeed" Project), the EQUIPEX program Excelsior (Grant No. ANR-11-EQPX-0015), the RENATECH network, the Agence National de la Recherche (Grant No. ANR-19-CE09-0022, "TROPICAL" Project), and I-SITE ("PRIVET" project). This project has also received funding from the European Research Council (ERC) under the European Union's Horizon 2020 research and innovation programme (grant agreement No. 714876 PHOCONA). We also acknowledge the TEM facility of the Nematology Research Unit, member of the UGent TEM-Expertise Centre (life sciences).

REFERENCES

- (1) Naeem, A.; Masia, F.; Christodoulou, S.; Moreels, I.; Borri, P.; Langbein, W. Giant Exciton Oscillator Strength and Radiatively Limited Dephasing in Two-Dimensional Platelets. *Phys. Rev. B: Condens. Matter Mater. Phys.* **2015**, *91* (12), 121302.
- (2) Jompol, Y.; Ford, C. J. B.; Griffiths, J. P.; Farrer, I.; Jones, G. A. C.; Anderson, D.; Ritchie, D. A.; Silk, T. W.; Schofield, A. J. Probing Spin-Charge Separation in a Tomonaga-Luttinger Liquid. *Science* **2009**, *325* (5940), 597–601.
- (3) Failla, M.; García Flórez, F.; Salzmann, B. B. V.; Vanmaekelbergh, D.; Stoof, H. T. C.; Siebbeles, L. D. A. Observation of the Quantized Motion of Excitons in CdSe Nanoplatelets. *Phys. Rev. B: Condens. Matter Mater. Phys.* **2020**, *102* (19), 195405.
- (4) Banin, U.; Cao, Y. W.; Katz, D.; Millo, O. Identification of Atomic-like Electronic States in Indium Arsenide Nanocrystal Quantum Dots. *Nature* **1999**, *400* (6744), 542–544.
- (5) Urbietta, A.; Grandidier, B.; Nys, J. P.; Deresmes, D.; Stiévenard, D.; Lemaître, A.; Patriarche, G.; Niquet, Y. M. Scanning Tunneling Spectroscopy of Cleaved InAs/GaAs Quantum Dots at Low Temperatures. *Phys. Rev. B: Condens. Matter Mater. Phys.* **2008**, *77* (15), 155313.
- (6) Ma, D. D. D.; Lee, C. S.; Au, F. C. K.; Tong, S. Y.; Lee, S. T. Small-Diameter Silicon Nanowire Surfaces. *Science* **2003**, *299* (5614), 1874–1877.
- (7) Franchina Vergel, N. A.; Tadjine, A.; Notot, V.; Mohr, M.; Kouassi N'Guissan, A.; Coinon, C.; Berthe, M.; Biadala, L.; Sossoe, K. K.; Dzagli, M. M.; et al. Influence of Doping Level and Surface States in Tunneling Spectroscopy of an In 0.53 G a 0.47 As Quantum Well Grown on p-Type Doped InP(001). *Phys. Rev. Mater.* **2019**, *3* (9), 094604.
- (8) Ji, B.; Rabani, E.; Efros, A. L.; Vaxenburg, R.; Ashkenazi, O.; Azulay, D.; Banin, U.; Millo, O. Dielectric Confinement and Excitonic

Effects in Two-Dimensional Nanoplatelets. *ACS Nano* **2020**, *14* (7), 8257–8265.

(9) Scott, R.; Heckmann, J.; Prudnikau, A. V.; Antanovich, A.; Mikhailov, A.; Owschimikow, N.; Artemyev, M.; Climente, J. I.; Woggon, U.; Grosse, N. B.; et al. Directed Emission of CdSe Nanoplatelets Originating from Strongly Anisotropic 2D Electronic Structure. *Nat. Nanotechnol.* **2017**, *12* (12), 1155–1160.

(10) Brumberg, A.; Harvey, S. M.; Philbin, J. P.; Diroll, B. T.; Lee, B.; Crooker, S. A.; Wasielewski, M. R.; Rabani, E.; Schaller, R. D. Determination of the In-Plane Exciton Radius in 2D CdSe Nanoplatelets via Magneto-Optical Spectroscopy. *ACS Nano* **2019**, *13* (8), 8589–8596.

(11) Singh, S.; Tomar, R.; ten Brinck, S.; De Roo, J.; Geiregat, P.; Martins, J. C.; Infante, I.; Hens, Z. Colloidal CdSe Nanoplatelets, A Model for Surface Chemistry/Optoelectronic Property Relations in Semiconductor Nanocrystals. *J. Am. Chem. Soc.* **2018**, *140* (41), 13292–13300.

(12) Christodoulou, S.; Climente, J. I.; Planelles, J.; Brescia, R.; Prato, M.; Martín-García, B.; Khan, A. H.; Moreels, I. Chloride-Induced Thickness Control in CdSe Nanoplatelets. *Nano Lett.* **2018**, *18* (10), 6248–6254.

(13) Ithurria, S.; Tessier, M. D.; Mahler, B.; Lobo, R. P. S. M.; Dubertret, B.; Efros, A. L. Colloidal Nanoplatelets with Two-Dimensional Electronic Structure. *Nat. Mater.* **2011**, *10* (12), 936–941.

(14) Shornikova, E. V.; Biadala, L.; Yakovlev, D. R.; Sapega, V. F.; Kusrayev, Y. G.; Mitioglu, A. A.; Ballottin, M. V.; Christianen, P. C. M.; Belykh, V. V.; Kochiev, M. V.; et al. Addressing the Exciton Fine Structure in Colloidal Nanocrystals: The Case of CdSe Nanoplatelets. *Nanoscale* **2018**, *10* (2), 646–656.

(15) She, C.; Fedin, I.; Dolzhanov, D. S.; Dahlberg, P. D.; Engel, G. S.; Schaller, R. D.; Talpin, D. V. Red, Yellow, Green, and Blue Amplified Spontaneous Emission and Lasing Using Colloidal CdSe Nanoplatelets. *ACS Nano* **2015**, *9* (10), 9475–9485.

(16) Liljeroth, P.; van Emmichoven, P.; Hickey, S.; Weller, H.; Grandidier, B.; Allan, G.; Vanmaekelbergh, D. Density of States Measured by Scanning-Tunneling Spectroscopy Sheds New Light on the Optical Transitions in PbSe Nanocrystals. *Phys. Rev. Lett.* **2005**, *95* (8), 086801.

(17) Banin, U.; Millo, O. Tunneling and Optical Spectroscopy of Semiconductor Nanocrystals. *Annu. Rev. Phys. Chem.* **2003**, *54* (1), 465–492.

(18) Niquet, Y. M.; Delerue, C.; Allan, G.; Lannoo, M. Interpretation and Theory of Tunneling Experiments on Single Nanostructures. *Phys. Rev. B: Condens. Matter Mater. Phys.* **2002**, *65* (16), 165334.

(19) Hashimoto, K.; Sohrmann, C.; Wiebe, J.; Inaoka, T.; Meier, F.; Hirayama, Y.; Römer, R. A.; Wiesendanger, R.; Morgenstern, M. Quantum Hall Transition in Real Space: From Localized to Extended States. *Phys. Rev. Lett.* **2008**, *101* (25), 256802.

(20) Ithurria, S.; Bousquet, G.; Dubertret, B. Continuous Transition from 3D to 1D Confinement Observed during the Formation of CdSe Nanoplatelets. *J. Am. Chem. Soc.* **2011**, *133* (9), 3070–3077.

(21) Bertrand, G. H. V.; Polovitsyn, A.; Christodoulou, S.; Khan, A. H.; Moreels, I. Shape Control of Zincblende CdSe Nanoplatelets. *Chem. Commun.* **2016**, *52* (80), 11975–11978.

(22) Liljeroth, P.; Van Emmichoven, P. A. Z.; Hickey, S. G.; Weller, H.; Grandidier, B.; Allan, G.; Vanmaekelbergh, D. Density of States Measured by Scanning-Tunneling Spectroscopy Sheds New Light on the Optical Transitions in PbSe Nanocrystals. *Phys. Rev. Lett.* **2005**, *95* (8), 086801.

(23) Nguyen, T. H.; Habinshuti, J.; Justo, Y.; Gomes, R.; Mahieu, G.; Godey, S.; Nys, J. P.; Carrillo, S.; Hens, Z.; Robbe, O. Charge Carrier Identification in Tunneling Spectroscopy of Core-Shell Nanocrystals. *Phys. Rev. B: Condens. Matter Mater. Phys.* **2011**, *84* (19), 195133.

(24) Tessier, M. D.; Javaux, C.; Maksimovic, I.; Lorientte, V.; Dubertret, B. Spectroscopy of Single CdSe Nanoplatelets. *ACS Nano* **2012**, *6* (8), 6751–6758.

(25) Biadala, L.; Louyer, Y.; Tamarat, P.; Lounis, B. Direct Observation of the Two Lowest Exciton Zero-Phonon Lines in Single CdSe/ZnS Nanocrystals. *Phys. Rev. Lett.* **2009**, *103* (3), 037404.

(26) Ip, A. H.; Thon, S. M.; Hoogland, S.; Voznyy, O.; Zhitomirsky, D.; Debnath, R.; Levina, L.; Rollny, L. R.; Carey, G. H.; Fischer, A.; et al. Hybrid Passivated Colloidal Quantum Dot Solids. *Nat. Nanotechnol.* **2012**, *7* (9), 577–582.

(27) Bozyigit, D.; Volk, S.; Yarema, O.; Wood, V. Quantification of Deep Traps in Nanocrystal Solids, Their Electronic Properties, and Their Influence on Device Behavior. *Nano Lett.* **2013**, *13* (11), 5284–5288.

(28) Pokrant, S.; Whaley, K. B. Tight-Binding Studies of Surface Effects on Electronic Structure of CdSe Nanocrystals: The Role of Organic Ligands, Surface Reconstruction, and Inorganic Capping Shells. *Eur. Phys. J. D* **1999**, *6* (2), 255–267.

(29) Houtepen, A. J.; Hens, Z.; Owen, J. S.; Infante, I. On the Origin of Surface Traps in Colloidal II-VI Semiconductor Nanocrystals. *Chem. Mater.* **2017**, *29* (2), 752–761.

(30) Hummon, M. R.; Stollenwerk, A. J.; Narayanamurti, V.; Anikeeva, P. O.; Panzer, M. J.; Wood, V.; Bulović, V. Measuring Charge Trap Occupation and Energy Level in CdSe/ZnS Quantum Dots Using a Scanning Tunneling Microscope. *Phys. Rev. B - Condens. Matter Mater. Phys.* **2010**, *81* (11), 115439.

(31) Biadala, L.; Peng, W.; Lambert, Y.; Kim, J. H.; Cannesson, D.; Houppé, A.; Berthe, M.; Troadec, D.; Deresmes, D.; Patriarche, G.; et al. Trap-Free Heterostructure of PbS Nanoplatelets on InP(001) by Chemical Epitaxy. *ACS Nano* **2019**, *13* (3), 1961–1967.

(32) Sun, Z.; Swart, I.; Delerue, C.; Vanmaekelbergh, D.; Liljeroth, P. Orbital and Charge-Resolved Polaron States in CdSe Dots and Rods Probed by Scanning Tunneling Spectroscopy. *Phys. Rev. Lett.* **2009**, *102* (19), 196401.

(33) Niquet, Y. M.; Delerue, C. Band Offsets, Wells, and Barriers at Nanoscale Semiconductor Heterojunctions. *Phys. Rev. B: Condens. Matter Mater. Phys.* **2011**, *84* (7), 075478.